DESIGN AND ANALYSIS OF PHOTONIC CRYSTAL FIBER FOR WAVEGUIDING AND ANALYTE SENSING IN THz PLATFORM

By

Md. Moshiur Rahman

A thesis submitted to the Department of Electrical and Electronic Engineering in partial fulfillment of the requirements for the degree of

DOCTOR OF PHILOSOPHY

Bangladesh University of Engineering and Technology (BUET)
Dhaka-1205, Bangladesh

7 June 2023

Statement of Originality

Date: **7 June 2023**

Author: **Md. Moshiur Rahman**

Title: **DESIGN AND ANALYSIS OF PHOTONIC CRYSTAL FIBER FOR WAVEGUIDING AND ANALYTE SENSING IN THz PLATFORM**

Department: **Electrical and Electronic Engineering**

University: **Bangladesh University of Engineering and Technology (BUET)**

I hereby declare that this work contains no material which has been accepted for the award of any other degree or diploma in my name, in any university or other tertiary institution and, to the best of my knowledge and belief, contains no material previously published or written by another person, except where due reference has been made in the text.
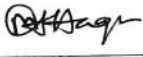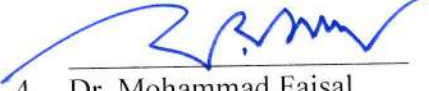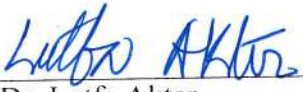
Signature of Author
Md. Moshiur Rahman
Student No. 0416064005
Session: April 2016

The dissertation entitled **"Design and Analysis of Photonic Crystal Fiber for Waveguiding and Analyte Sensing in THz Platform"** submitted by Md. Moshiur Rahman, Student ID # 0416064005, Session: April 2016 has been accepted as satisfactory in partial fulfilment of the requirements for the degree of **Doctor of Philosophy in Electrical and Electronic Engineering** on 7th **June 2023**.

BOARD OF EXAMINERS

1. Dr. Mohammed Imamul Hassan Bhuiyan
    Professor, EEE, BUET, Dhaka

    Chairman
    (Supervisor)

2. Dr. Md. Aynal Haque
    Professor and Head, EEE, BUET, Dhaka

    Member
    (Ex-officio)

3. Dr. Mohammad Ariful Haque
    Professor, EEE, BUET, Dhaka

    Member

4. Dr. Mohammad Faisal
    Professor, EEE, BUET, Dhaka

    Member

5. Dr. Lutfa Akter
    Professor, EEE, BUET, Dhaka

    Member

6. Dr. Mohammad Rakibul Islam
    Professor
    Electrical and Electronic Engineering, IUT, Board Bazar, Gazipur-1704

    Member

7. Dr. S M Abdur Razzak
    Professor
    Electrical and Electronic Engineering, Rajshahi University of Engineering and Technology, Rajshahi

    Member
    (External)

iii

Acknowledgement

I would like to thank the almighty Allah first for the completion of this research work. At the outset, I would like to convey my sincere gratitude to my thesis supervisor, **Dr. Mohammed Imamul Hassan Bhuiyan**, Professor, Department of Electrical and Electronic Engineering, Bangladesh University of Engineering & Technology (BUET) for his continuous supervision and support throughout my thesis with patience and knowledge. I would like to extend my sincere thanks to him for his constant guidance, encouragement, and kind cooperation, particularly in justifying the proper research direction of the thesis and ensuring that the research aims and objectives are fulfilled over the past few years. Completion of this research work would not be possible without his stimulating inspiration and cooperation.

I would like to convey my sincere thanks to **Dr. Mohammad Rakibul Islam**, Professor & Head, Department of EEE, IUT for his constant help, valuable suggestions, and guideline, which motivated and contributed to completing this work properly.

I would like to convey my special thanks to **Dr. Mohammad Faisal**, Professor, Department of EEE, BUET for his continuous suggestions, guidelines, and valuable time to enrich this research.

Furthermore, I also would like to convey my special thanks to **Dr. Lutfa Akter**, Professor, Department of EEE, BUET for her continuous encouragement to make this research an exceptional one by adding supportive information and through proper presentation.

Additionally, I would like to express my thanks to **Dr. Mohammad Ariful Haque** Professor, Department of EEE, BUET, and **Dr. Md. Aynal Haque**, Professor & Head, Department of EEE, BUET, for their valuable suggestions. I would also like to convey my sincere thanks to **Dr. S M Abdur Razzak**, Professor, Department of Electrical and Electronic Engineering RUET, for being the external member of this thesis examination committee and giving consent for evaluating this work. His suggestions were instrumental in shaping and enriching this thesis.

I greatly acknowledged the Institute for Energy, Environment, Research, and Development (IEERD), University of Asia Pacific (UAP) for the financial support to present my works at international conferences in India, Indonesia, and Bangladesh.

My wholehearted thanks should go to my parents for their principles and unconditional love for me and teaching me the objectives and aim in life.

Last, but not the least, I am deeply thankful to my beloved wife, **Farhana Akter Mou**, who has persistently accompanied me in completing this journey, sharing my tears and cries, and showering me with love, joy, and laughter. I would also like to express my endless love to my son, **Shaahzin Mehshid** who always cherished me in every moment of my life with the sacrifices of his needs.

Dedication

This work is dedicated to my parents, my wife, my son, and my respected teachers for their constant support and patience throughout my academic life.

Table of Contents

List of Tables

List of Figures

with respect to core size.

μm *strut* size.

List of Abbreviations

Abbreviation	Definition
CL	Confinement Loss
COC	Cyclic-Olefin Copolymer
COP	Cyclo-Olefin Polymer
dB	Decibel
ERI	Effective Refractive Index
EML	Effective Material Loss
FEM	Finite Element Method
FET	Field Effect Transistor
FIR	Far Infrared
HCF	Hollow Core Fiber
MMF	Multi-Mode Fiber
MOFs	Microstructure Optical Fibers
NA	Numerical Aperture
PML	Perfectly Matched Layer
PCF	Photonic Crystal Fiber
PMD	Polarization Mode Dispersion
PBG	Photonic Band Gap
PC	Porous Core
PTFE	polytetrafluoroethylene
PMMA	Poly Methyl Methacrylate
RI	Refractive Index
RIU	Refractive Index Unit
SMF	Single Mode Fiber
SPR	Surface Plasmon Resonance
THz	Terahertz
TDS	Time Domain Spectroscopy
Teflon	Tetrafluoroethylene

List of Symbols

Abbreviation	Definition
α_{eff}	Effective material loss
ϵ_0	Relative permeability
n_{mat}	Refractive index
α_{mat}	Bulk absorption loss
S_z	Z-component of the Poynting vector
E	Electric field component
H	Magnetic field component
L_c	Confinement loss
f	Operating frequency
c	Speed of light
$Im(n_{eff})$	Imaginary part of the complex effective refractive index
A_{eff}	Effective area
x	Area of the region of interest
n_{eff}	Effective refractive index
n_1	Effective refractive index core region
n_2	Effective refractive index cladding region
$I(f)$	Intensities of light with the presence of the analyte needed to be detected
I_0	Intensities of light without the presence of the analyte needed to be detected
r	Relative sensitivity
α_m	Absorption coefficient
l_c	Channel length
n_r	Refractive index of the sample
k	Light interaction
B	Birefringence
n_x	Effective refractive index of the x polarization mode
n_y	Effective refractive index of the y polarization mode

R	Radius of the lattice
w_{eff}	Spot size
γ	Nonlinearities
θ_{radian}	Beam Divergence
η	Core Power Fraction
$\boldsymbol{\alpha_{BL}}$	Bending Loss
$\mathbf{R_b}$	Bending Radius

Abstract

In present times, Photonic Crystal Fiber (PCF) has emerged as a strong contender for THz waveguiding and analyte sensing. Major benefits of a porous-core PCF include minimum absorption loss due to unique light-guiding process through a guided air medium, lower confinement loss, near-zero flattened dispersion, extensive detecting potential, faster response with precise results, and geometry design flexibility. Most importantly, the optical behaviors of the PCF can be controlled by the geometrical specifications for both waveguiding and sensing cases.

In this research, different novel geometries of PCF are proposed and numerically analyzed. Necessary optical properties are evaluated in the Terahertz (THz) platform for waveguiding and analyte sensing. The purpose is not only to provide high-quality THz transmission but also to render the ability for sensing different unknown analytes, basically several harmful and well-known liquid chemicals, biological components, and air pollutants, with high sensitivity. The various geometrical parameters of the PCFs have been optimized and the optical properties of the tuned PCFs are numerically investigated for wave propagation and sensing cases. The full vector analysis-based Finite Element Method (FEM) with COMSOL Multiphysics software (v. 5.3a) is employed to design, and evaluate the optical properties. As compared to existing works, a superior performance in terms of low losses, flattened waveguide dispersion, high core power fraction, and large effective area are obtained for THz wave guidance. For the liquid chemicals, biological components, and air pollutant analytes, a number of improvements are demonstrated that include higher sensitivity, negligible confinement loss, ultra-low effective material loss (EML), and moderate effective area, as compared to several recently reported results. Furthermore, in the context of current developments in fabrications, recommendations are provided regarding the potential for fabricating the proposed PCFs. Overall, the designed PCFs have a good degree of potential for diverse applications in the THz domain including wave transmission and sensing of different substances.

Chapter 1

Introduction

1.1 Introduction

Currently, the THz signal is positioning itself as a potential candidate for various versatile and improved applications in sensing [1-2], security [3] telecommunication [4-6], pharmaceutical drug testing [7], biomedical sensing [8], imaging [9], environmental applications [10], etc. An unguided air medium for THz transmission has a number of problems such as unpredictable absorption loss caused by the atmospheric situation, alignment complexity between transmitter and receiver, etc. Various types of guided media are proposed, most of these demonstrated high absorption, high weight, and ohmic loss in THz wave propagation [11-15]. The photonic crystal fiber (PCF) provides a highly promising solution due to its remarkable wave-guiding capability with reduced absorption loss, near-zero flattened dispersion, and lower confinement loss [16-19]. In addition, presently PCF has attained acceptance in sensing areas because of good sensitivity in detection, low weight, tiny size, etc. [1, 2, 10, 20-22]. Moreover, versatility in geometrical parameter selection and most importantly optical properties optimization flexibility by regulating the structural specifications have attracted researchers' attention [1, 2, 10, 16-34]. Proper PCF designing and optimization thus is a vibrant research domain. This Chapter offers a brief description regarding the background and present state of the problem, motivation, research objective, and outline of the thesis.

1.2 Background and present state of the problem

Considering the potential of PCF devices in waveguiding and sensing cases, as well as the scopes of improving performance by the proper geometry development, several PCF geometries have been proposed over the last decades by different researchers.

For efficient use of PCF in THz wave guidance, several PCFs have been designed in recent years. M. S. Islam *et al.* have proposed an elliptical-shaped porous core with Kagome structured cladding PCF for THz wave transmission, and report a very low EML of 0.056 cm^{-1}at specified design condition and operation frequency of 1 THz in *y*-polarization. The practical implementation of the presented PCF geometry is quite complex using existing fabrication methods due to Kagome structure cladding and elliptical core [26]. B. K. Paul *et al.* have presented a hexahedron-shaped core PCF for efficient wave guiding with a modest EML of 0.051 cm^{-1} for a working frequency of 0.6 THz. The waveguide dispersion characteristic of this PCF is ± 0.6 ps/THz/cm in the frequency range of (0.8-1.4) THz [27]. A honeycomb cladding and hexagonal slotted core structured PCF is presented in [28] that exhibits 0.095 cm^{-1} EML with a birefringence of 0.083 at 1.5 THz. A quasi-pattern PCF design is developed by B. K. Paul *et al.* for the THz waveguiding application; this PCF provides an EML of 0.038 cm^{-1} at 1 THz but suffers from a quite high waveguide dispersion [6]. I. K. Yakasai *et al.* present a PCF geometry with elliptical air holes set up in the core and circular air holes arrangement in a hexagonal manner in the cladding. This PCF shows a moderate material loss of 0.03 cm^{-1} at 1.3 THz with a peak waveguide dispersion of 3 ± 1.2 ps/THz/cm in y-polarization [29]. In 2017 S. Sen *et al.* suggested a circular-shaped core and cladding PCF structure which shows an effective material loss of 0.04 per centimeter with an effective area of $2.80 \times 10\text{-}7\text{m}^2$ for 1THz operating frequency but they ignored an important property characterization which is waveguide dispersion. Near zero flattened dispersion is very important for effective THz pulse transmission [35]. In the same year M. A. Habib *et al.* proposed an asymmetrical rectangular slotted air core and a rectangular-shaped cladding that was filled with circular air holes. The outcomes of this presented PCF structure exhibit the lowest value of EML of 0.035 cm^{-1} at optimum parameters. This proposed design shows very high confinement loss and they avoid the calculation of effective area, although a large effective area is necessary to minimize the nonlinear effects [36]. M.S. Islam *et al.* presented an asymmetrical rectangular slotted air cladding with elliptical array core PCF, where zeonex is used as background material. The numerical analysis of the PCF reveals an EML of 0.06 cm^{-1} at 1THz [37]. A modified cladding structure with enlarged core geometry of the previously proposed design [37] is suggested by M.S. Islam *et al.* in 2018. This

modified design shows an improved birefringence but increases the EML of 0.06 cm^{-1} to 0.065 cm^{-1}, which causes more light absorption by zeonex [38]. An elliptical-shaped core filled by slotted rectangular air holes with an EML of 0.047 cm^{-1} is reported by M. Faisal *et al.* in 2018 [39]. A complex kagome structured cladding and hexagonal-shaped core inserted by multiple numbers of hexagonal air holes are reported by S. Rana *et al.* Although their numerical report presents a low EML of 0.029 cm^{-1} at 1.3 THz frequency a kagome-structured PCF fabrication is very perplexing compared to a circular structured PCF [40]. Recently in 2019, M.S. Islam *et al.* modified the PCF structure which was previously reported by S. Rana *et al.* They modified only the core section with an elliptical core structure instead of a hexagonal core and the core filled with slotted air holes. The outcome of their modified PCF structure is not suitable for EML reduction, which provides an EML of 0.056 cm^{-1} for 1 THz operating frequency [41]. F. Ahmed *et al.* introduced a PCF with a spiral-founded cladding and circular-shaped core formed by circular air holes. They achieved an EML 0.0167 cm^{-1} which is low compared to recently published articles, but because of the spiral cladding structure, practical implementation is completed when compared with a circular sectored cladding PCF [42]. K. Ahmed *et al.* presented an octagonal core structured PC-PCF which exhibits an effective material loss of 0.049 cm^{-1} at 1 Terahertz operating frequency, but ignored two necessary properties which are confinement loss and dispersion. Characterization of these properties is very essential for long-distance THz wave propagation with low bit error [43]. B. K. Paul *et al.* in 2018, a hexagonal core-cladding structured PC-PCF is proposed to minimize the effective material loss that exhibits an EML of 0.030 cm^{-1} with a high confinement loss of 20×10^{-2} cm^{-1} at an operating frequency of 1 THz [44].

Besides, efficient THz wave guidance, already PCF has proved the potentiality in sensing platform due to its highly promising guiding features, versatile diversity for applications, and faster response with precise results for detection approaches. Already, several types of PCF geometries have been developed and numerically analyzed for different analytes detection cases. Recently, M. S. Islam *et al.* has introduced a Kagome structure cladding and hexagonal core PCF for chemical identification with absolute sensitivity of 85.7 %. This PCF also shows a low confinement loss of 1.7×10^{-9} cm^{-1}.

Due to the overlapping of rectangles in structure, fabrication is a big challenge for this type of geometry [22]. B. K. Paul *et al.* have presented a slotted core PCF for sensing purposes. This PCF design attains 48.28 % sensitivity and confinement loss of 1.26×10^{-5} cm^{-1} at an operating wavelength of 1.33 μm [43]. Alongside, M. S. Islam *et al.* proposed a cyanide detection mechanism using a hexagonal core and sectored cladding PCF. The proposed PCF structure shows a sensitivity of 85.8 % and a low confinement loss of 1.62×10^{-9} cm^{-1} [1]. Using circular air holes with a hexagonal arrangement in the cladding area and elliptical lattices in the core region constitute, a PCF geometry by E. Poddar *et al.* is reported for sulfuric acid detection in liquid samples, which gives a sensitivity of 63.5 % [31]. S. Sen et al. proposed a rotated-hexacore and circular cladding structured PCF for detecting liquid chemicals in the THz regime. The maximum sensitivity reported is 76.44 % for Benzene detection at 1 THz [44]. S. R. Tahhan *et al.* have presented a PCF structure with circular lattices in core and cladding in a pentagonal fashion that renders maximum sensitivity of 82% for Ketamine identification in liquid drugs [45]. A symmetrical core-cladding structure is introduced in [33] for gas sensing application in the THz regime. But, different sizes of air holes are used in the core that increases the fabrication complexity, while the birefringence profile is not considered for developing this PCF geometry. Recently, B. K. Paul *et al.* proposed a quasi-fiber for liquid chemical detection and shows 73.78 % sensitivity for particular design parameters [2]. S. Singh and V. Kaur have proposed [46] a PCF structure with a sensing ring around the solid core region for detecting major constituents of blood. Their demonstrated the sensitivity of 66.46978 % for hemoglobin sensing at 1.4 μm with a confinement loss of 8.1343×10^{-9} (dB/m) obtained for RBCs detection cases. Later they have reinvestigated their previous work and achieved improved sensitivity of 55.82 %, 58.047 %, 62.721 %, 65.054 %, and 66.469 % for RBCs, hemoglobin, WBCs, plasma, and water respectively with reduced confinement loss [47]. It should be mentioned that except sensitivity and confinement loss, no other crucial sensing properties are examined in both works. A PCF geometry is proposed by K. Ahmed *et al.* [21] consists of type-b crystalline core, and gives a maximum sensitivity of 80.93 % for RBC detection at 1.5 THz. A very low confinement loss of 1.23×10^{-11} dB/cm is also attained for the same substance and at the same THz operating point. However, absorption loss by the background material is not considered

in this investigation. M. B. Hossain *et al.* [48] presents a hollow core PCF with asymmetrical slotted cladding for the detection of blood components. The authors report sensitivity upto 93.5 % through geometrical optimization for identifying RBCs. However, performance of the PCF regarding effective material loss (EML), dispersion and numerical aperture are not studied in this work. M. B. Hossain *et al.* [49] have designed a rectangular hollow-core PCF geometry for bane chemical identification. The highest sensitivity achieved 94.4 % is achieved and confinement loss is 1.71×10^{-14} cm^{-1} at 1.8 THz frequency. Still, some necessary properties such as dispersion, NA, and effective area are not addressed in this research. Besides, fabrication possibilities using the existing techniques is not addressed properly. In 2019, M. M. Hasan *et al.* developed a heptagonal shape PCF-based sensor for chemical sensing and achieved maximum sensitivity of 63.24% in benzene sensing [50]. Absorption experience by the background material and some crucial sensing properties are not included in this study. Previously, B. K. Paul *et al.* have been presented a chemical sensor based on PCF, and the numerical outcome showed the sensitivity of 66.73% for pentanol detection [51]. A Zeonex-based PCF for ethanol sensing is introduced by J. Sultana *et al.* to improve the sensitivity and they obtained 68.87% sensitivity at 1 THz frequency [52]. A rhombic shape core PCF has been proposed by M. S. Islam *et al.* [53] for aqueous analytes' sensing application, and they reported 69% sensitivity. M. S. Islam *et al.* have presented a hollow core PCF-based THz sensor for chemical sensing and the developed sensor exhibits a maximum 96.8% sensitivity for 1.4 THz frequency [20].

Based on the above discussion, one can see that there is a good scope of research toward developing a PCF for efficient THz waveguiding as well as for the detection of various analytes with ultra-high sensitivity.

1.3 Motivation

Several PCF geometries have been proposed over the last decades by different researchers. Square [20], circular [32], hexagonal [1, 23], suspended [19], rectangular [34], quasi-pattern [6], elliptical [26], Oligoporous [25] etc. shaped core PCF have been developed and tested for waveguiding and sensing applications in the THz spectrum. For efficient use of PCF for THz wave guidance several PCF structures have been

proposed [6, 17, 19, 23-26, 28, 31]. It is to be noted that some of these works do not analyze many crucial optical properties [23, 26, 24, 28], while some works have comparatively higher losses, higher dispersion, lower effective area, lower core power fraction, etc. [24-26, 28].

Apart from designing efficient PCF structures for THZ wave guidance, sensing with PCF in diverse applications has a great potential especially for the detection of harmful liquid chemicals, biological components and evanescent substances. In recent times, various PCF-based THz sensors have been proposed by researchers for detecting different analytes for example water, methanol, ethanol, benzene, Sulfuric acid, Cyanide, blood components etc. [1, 10, 20-22, 31, 32, 34] as discussed before. However, considering the harmfulness of different air pollutants for example dioxin, nitrogen dioxide, hydrogen sulfide etc. and for diagnosis of hematologic diseases different biological components in blood (blood cholesterol, blood protein etc.) and urine (albumin) need to be considered as a targeted analyte. Additionally, lower sensitivity, and higher confinement loss as well as lack of elaboration for possible fabrication using existing fabrication techniques of their developed complex PCF geometries need to be addressed.

The present research works lack in some cases, selection of improper core cladding geometry, inappropriate development of core type without considering the purpose of uses, complex core cladding structure selection, absence of crucial optical properties evaluation, non-consideration of a number of analytes, higher losses, lower sensitivity whereas in general the issue of fabrication for practical implementation is not properly elaborated. Thus, there is ample scope to improve the performances of PCF by proper geometry selection and fine design parameters regulation in both wave propagation and sensing applications alike.

1.4 Objectives

The main objectives of the research work are as follows:

i. To design and characterization of new PCF geometries for THz waveguiding with improved performance.

6

ii. To develop PCF-based sensors for different analytes' (Chemical, Gas and Biological) identification with high sensitivity.

iii. To develop suitable PCF geometry that is able to perform both THz waveguiding as well as analyte sensing application with improved performance.

iv. To study and compare the performance of the developed PCFs geometry in THz wave propagation and sensing of analytes with those of contemporary research works.

1.5 Outline of the Thesis

This thesis contains total eight (08) Chapters. The detailed description of each Chapter is as follows-

Chapter 1 presents the overview of this thesis including background and current states of the problem, objectives, and motivation of this thesis.

Chapter 2 provides the details regarding photonic crystal fiber, PCF types and its applications. Guiding mechanism of PCF is also delineated in this Chapter. Terahertz frequency and its application are also discussed in detail.

Chapter 3 describes several necessary optical properties of PCF for waveguiding and sensing. Methods for evaluating their properties are also briefly described.

Chapter 4 provides proposed PCF geometries for THz waveguiding and their design process, and result analysis.

Chapter 5 provides proposed PCF geometries for analytes sensing and their design process, and result analysis.

Chapter 6 provides the proposed PCF geometry for THz waveguiding and analytes sensing. Design process, and result analysis are discussed here.

Chapter 7 discussed on current developments of PCF fabrications and the potential for fabricating the proposed PCFs in the context of current development.

Chapter 8 summarizes the major outcomes of the thesis. It also describes some limitations and further scopes of works in the PCF field and beyond.

Chapter 2

Photonic Crystal Fiber and Terahertz Spectrum

2.1 Introduction

Recently microstructure fibers have gained enormous attention for several applications in THz spectrum for various significant fields such as high frequency waveguiding, non-invasive medical imaging, sensing, security, spectroscopy, oral healthcare, cancer cell detection, bio-technology, telecommunication, military, environmental applications, detection of defects in solar panels, characterization of dielectric materials, pharmaceutical drug testing and astronomy with a huge range of frequency between IR and microwave. THz generator and detector are commercially available in everywhere but a guided medium for THz wave still big challenges since several losses associated with it and it is influenced by different parameters. Terahertz sensing technology already has shown numerous breakthroughs in various fields especially biological sensing and it allows the measurement of dispersion and losses. This Chapter offers the details of PCF, PCF types, its application, and Terahertz spectrum.

2.2 Photonic Crystal Fiber (PCF)

Photonic crystal fiber (PCF) is constructed with the combination of the properties of photonic crystal and the optical fiber. The PCF is a unique class of fiber with unique cladding structure. The PCF exhibits exceptional optical properties these are not available in the conventional optical fiber. The core-cladding structure of conventional optical fiber is also fixed in classical fiber, on the contrary in PCF has core-cladding design flexibility. Depending on the core type PCF basically characterized in three category namely solid core PCF, porous core PCF and hollow core PCF. These three types of PCF will be discussed in details in the following sections.

2.2.1 Solid Core PCF

Solid core PCF is basically a class of index guided PCF which constructed with solid material in the core section and air holes in the cladding region [54]. A basic solid core PCF is displayed in the Figure 2.1. The suitable application of this type of PCF is that where small core size PCF is needed as well as highly birefringence characteristic is essential. Because of solid host material on the core region excessive material absorption loss is rendered in this type of PCF. So, for long distance communication solid core PCF is a not a good choice.
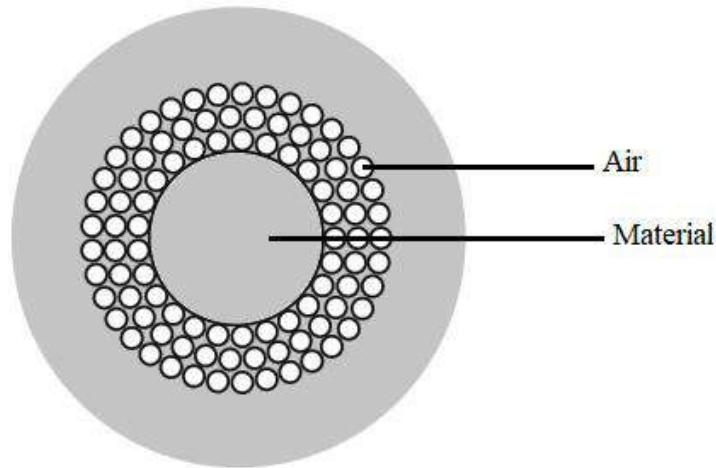
Figure 2.1: Solid Core PCF [54].

2.2.2 Porous Core PCF

In the year of 2008 the researchers have introduced a new type of PCF with subwavelength small air holes in the PCF core region for THz applications [54]. A typical porous core fiber is displayed in Figure 2.2. Because of several tiny air holes placing in the solid core its termed as porous core fiber. The ratio of total solid area and the total air area in the core called porosity of the fiber core. By increasing or decreasing the core porosity the material area can arrange in the core. The material absorption of the fiber in the core area can be controlled by controlling the porosity of the fiber and this is a unique feature of the porous core fiber. The core of the porous core fiber constructed with a significant amount of host material that helps to provide structural strength than a hollow core fiber. There is a huge scope to design the geometrical parameters in the core as well as in the cladding by changing the holes shapes, sizes, pitch sizes etc. for enhancing the performances. Due to the low absorption loss and

single mode profile characteristics the porous core fiber renders excellent performances for long distance waveguiding. Because of low material absorption, single mode profile, design flexibility for controlling loss and other optical parameters in this thesis we have chosen porous core fiber for THz wave guidance, more details regarding the porous core fiber, its design process, and performances are discussed in Chapter 4.
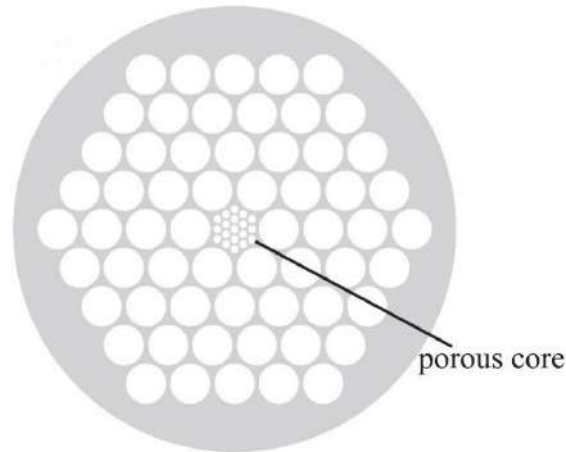
Figure 2.2: Porous Core Fiber [54].

2.2.3 Hollow Core PCF

Hollow-core photonic bandgap fibers turn conventional fiber technology inside out by guiding the light in a hollow-core. A typical hollow core fiber is shown in Figure 2.3. This unique structure of hollow core with highly porous cladding, as PGB fiber the refractive index varies in both propagation and transverse direction periodically [55]. This unique fiber core is filled with lossless air which opens for sensing, imaging, short distance communication, and ultrashort pulse applications. The hollow core PCF contains greater analyte volume inside the core area compared to a porous core. Alongside, hollow core PCF minimizes the requirements of bulk material that helps to reduce the material absorption loss. Furthermore, due to the absence of solid material in the core and porous structure in the cladding section makes it damage prone in the long-distance installation. Because of aforementioned reason for sensing applications, we have chosen hollow core fiber. More details regarding the hollow core fiber, design process, and sensing performances for different anlytes sensing application are discussed in Chapter 5.
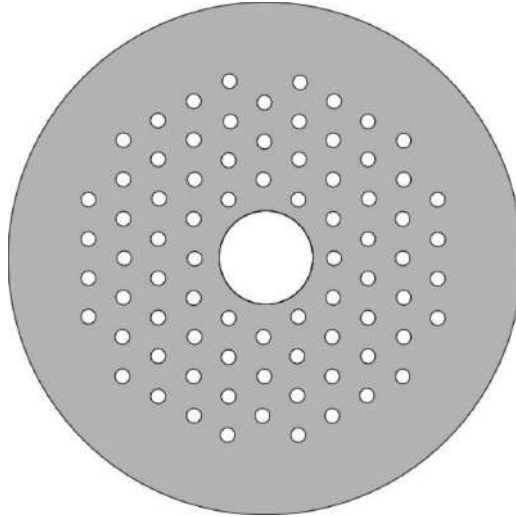
Figure 2.3: Hollow Core Fiber [55].

2.3 PCF's Characteristics

Due to several advantageous nature in the PCF platform over conventional optical fiber, waveguiding as well as a sensor PCF can be utilized. Low index contras, absence of design flexibility, high losses etc. are the major limitations of conventional optical fiber these pitfalls can be utilized by the PCF. The optical behaviors of PCF rely on two things namely intrinsic properties of host material and geometrical structure. The optical behavior cannot be changed for a specific material but all the optical behaviors can be tunned by the geometrical specifications. The PCF perform with single mode characteristics for a wide range of wavelength by small ratio of air holes size and air hole spacing [56]. Asymmetrical hole structure in the core and cladding renders highly birefringence nature that leads to a polarization maintaining fiber. It is possible to achieve extremely large or extremely low mode area in the PCF whose helps to minimize or extend the PCF nonlinearities. PCF can be constructed with low sensitivity setup to bend losses also for large mode area [56]. Wave guidance is possible in photonic bandgap fiber (even hollow core fiber) with the certain air holes arrangement. Higher refractive index material in the inner section of the fiber is no longer required in PCF platform. This kind of hollow core waveguide is highly suitable for dispersive pulse compression at high pulse energy level. For analyte sensing, nonlinear spectral broadening or for variable power attenuator, lager holes PCF can be exploited.

Multicore development is very possible in regular shape PCF where coupling between the cores may or may not be required. Furthermore, it shows high index contrast and the most unique matter is that it is a single material fiber.

2.4 Waveguiding Mechanism of PCF

Waveguiding mechanism in the PCF depends on the type of the fiber. For index guided fiber the waveguiding properties almost same as conventional optical fiber [57]. There is a simple difference from conventional optical fiber is that the refractive index of the PCF is not fixed, which depends on the wavelength. Depending on the wavelength the filed expands or scale down to the cladding which changes the refractive index of the cladding. For this reason, the light is guided in the PCF by MTIR process instead of TIR. For low index guided or hollow core fiber light is guided by PBG [58] or anti-resonant effect [59] due to low refractive index material in the core than cladding.

2.5 Sensing Mechanism using PCF

The sensing mechanisms in the PCF platforms can be shortly illustrated as below:

Absorbance	→ Measured in a transparent medium
Reflectance	→ Measured in non-transparent media, usually using an immobilized indicator
Luminescence	→ Based on the measurement of the intensity of light emitted by a chemical reaction in the receptor
Fluorescence	→ Measured as the positive emission effect caused by irradiation
Refractive index	→ Measured as the result of a change in solution composition
Opto-thermal effect	→ Based on a measurement of the thermal effect caused by light absorption
Light scattering	→ Based on effects caused by particles of definite size present in the sample

13

2.6 Terahertz Spectrum

The electromagnetic wave spectrum from 0.1 to 10 THz range frequency is defined as the THz frequency band which occupies the middle ground between microwaves and infrared [2]. Although some researchers suggested to setup it 0.3 THz to 3.0 THz [60, 61]. The electromagnetic spectrum and its application areas are displayed in Figure 2.4(a), where the magnified view near the THz band is exhibited in Figure 2.4 (b). From Figure 2.4 (b) it is visualized that the THz band is overlapping with the longer wavelength end of the EHF band and the shorter wavelength end of the FIR band. It is seen that from Figure 2.4 (b) the EHF band ends at closely 0.3 THz but the THz band starts from 0.1 THz, similarly on the other side the THz band ends at 10THz but the FIR starts from 1.0 THz. So, the overlapping is identified on both ends. Since this type of overlapping is not a usual situation but there is also another such type of overlapping already exists between x-ray and gamma-ray bands. Using several units, the researchers specified the THz band. In this thesis, we have considered THz as a spectral unit. Except for the frequency range the THz can be expressed in other forms including,

- Angular frequency: $w = 2\pi f = (0.628 - 62.8)$ rad/s.
- Time: $t = 1/f = (0.1 – 10)$ ps.
- Wavelength: $\lambda = c/f = 30\ \mu m–3$ mm.
- Wavenumber: $\bar{k} = 1/\lambda = (3.3–333)$ cm^{-1}.
- Photon energy: $hf = \hbar w = 410\ \mu eV - 41$ meV, where, $h = 2\pi\hbar$, indicates Planck's constant.

Due to the unavailability of materials or devices, the expansion of THz technology is lagging for effective utilization compared to other frequency bands like microwaves and optics. A very limited number of commercial products are currently operating in the THz band, on the contrary, a massive number of products are utilized in commercial and many other sectors. However, already several pieces of research have been able to prove the potentiality of THz band in several applications as we as on the societal impact.
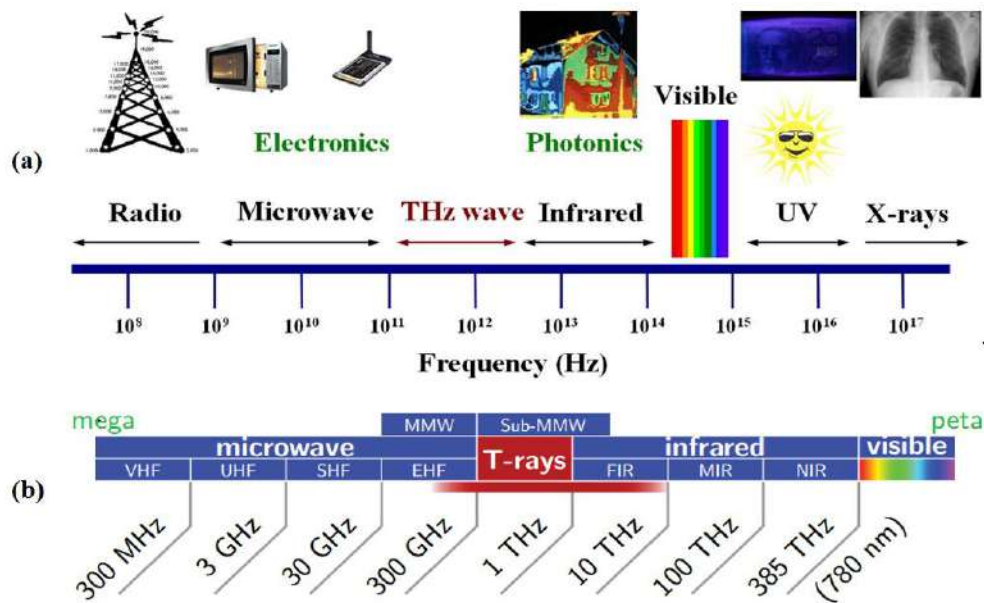
Figure 2.4: Electromagnetic spectrum (a) Electromagnetic spectrum with application areas, (b) Expanded view of the neighborhood of the THz band [61].

2.7 THz Sources and Detectors

For THz band communication, besides designing of a waveguide, THz sources and THz detectors are the two important components. Several THz sources and detectors are currently available in the market [62]. So, the challenge is to design a proper waveguide with low losses. Some available THz sources and detectors are discussed in the following sections.

2.7.1 THz Sources

A good numbers of THz wave generator are available now. In the laboratory carborundum heated rod and mercury lamp are generally utilized as a THz sources [63]. Both mentioned THz sources are from high power laser including klystrons [64], travelling-wave tubes [65], and free-electron lasers [66]. Apart from these solid-state electronics is another source for THz wave generation. Gunn diode [67] and high frequency oscillators [68] are the two solid-state electronics THz sources. Ge-Si can be a potential source for efficient THz wave generation [69]. Some gas laser also able to generate THz wave [70]. Optical sampling method also been utilized to produce THz radiation by using conductive dipole antenna [71].

2.7.2 THz Detectors

It is very hard to detect the THz band signal by using conventional by means electronics, which only can able to access the lower end of the THz spectrum. Photoinductive antenna, and bolometer are the most useable THz detectors. THz radiation detection with nonlinear crystal is another popular technique. Besides THz wave detection the photoinductive antenna also can perform as a THz source which consists of two metallic strips with a photoconductive switch between them. It performed like as pump-probe measurement where optical probe pulse works alike photoconductive switch. The THz radiation to be detected when it passes the photoconductive switch [72]. The process also known as electro-optic sampling. Thermal detection method is used in bolometer technique. In this process the radiation is detected depends on the heat generation during absorption. Indium antimonide (InSb) bolometer can be used as a THz wave detector [72]. In non-linear crystals a terahertz wave and electric field can interact [73]. One can exploit to isolate THz radiation from this interaction by interferometrically changes of optical phase.

2.8 THz Applications

The electromagnetic radiation in the THz band interacts strongly with the system which renders the lifetimes behavior in picosecond and/or meV range energy. Several systems can be considered as such types of system, for example bound electrical charges (74), free charge plasmas (75), strongly confined charge plasmas (76), transient molecular dipoles (77), phonons in crystalline solids (78), hydrogen bonds in chemicals (79), intermolecular forces in liquids (80), and biological matter (81). The THz frequency spectrum has gained enormous attention, not only for communication also for several diverse application such as sensing, medical imaging, drug testing, security, spectroscopy, oral healthcare, cancer cell detection, bio- technology, military, environmental applications, detection of defects in solar panels, characterization of dielectric materials and astronomy [22, 82-85]. THz spectrum have significant uses in the nonmetallic materials such as wood, ceramics, paper, plastics, and fabrics for quality control of products and surveillance imaging. Several studies already shown THz frequency also can be used for material characterization. One of the most

limitation of THz rays is that it loses a significant amount of energy by water absorption. Due to strong absorption characteristics of THz radiation by the water molecules it is suitable for sensing of hydration level of biological tissue which enhance the interest of skin cancer detection in the THz frequencies. Furthermore, THz frequency also applicable for medical and dental diagnostics because of ono-ionizing and non-invasive nature.

2.9 Summary

Different types of PCF and their characteristics are discussed in this Chapter. As per natural behaviors of microstructure fibers, it can be said that porous core fiber will be preferable for long-distance communication compared to solid core and hollow core fiber in terms of EML and long-distance wave guidance respectively. On the contrary, hollow PCF offers higher sensing capability for analyte sensing applications. THz spectrum, available THz sources, and THz detectors are also discussed here. The above discussion indicates that THz frequency offers several diverse applications including communication and sensing. Several optical properties should be evaluated for a PCF to ensure its performance in waveguiding and sensing applications. The necessary optical properties for both waveguiding and sensing applications and their analysis methods will be discussed in the next Chapter.

Chapter 3

Optical Properties and Methods of Numerical Analysis

3.1 Introduction

The optical behaviors of PCF can be controlled by the geometrical specifications. There is the freedom to change the geometrical size and shape in the PCF platform. The optical properties can be measured by the simulation process. During the simulation process, PCF geometry can be modified until fulfilling the requirements. On the contrary, after producing a prototype geometrical modification is a challenging task, in some cases, it is impossible to modify further. So, before making a prototype extensive analysis is required through simulation. For such analysis, FEM is an excellent method and can be executed in the COMSOL Multiphysics software. PCF design process, simulation process, and necessary optical properties are discussed in this Chapter.

3.2 PCF design and Analysis Methodology

Considering the purpose of uses and fabrication complexity, different PCFs geometry has been developed in COMSOL Multiphysics software v.5.3a. Different optical properties for both waveguiding and sensing cases are assessed using Finite Element Method (FEM) in COMSOL Multiphysics by tuning the geometrical parameters. By comparing the measured results an optimum geometrical condition is identified for better attainment. Both porous and hollow-core PCF has been considered for the design of THz wave guide and sensing application, respectively. Circular, octagonal, hexagonal, square etc. core structures are also investigated.

For ensuring the efficient THz wave guidance by the developed PCF structures, several optical properties including effective material loss (EML), confinement loss (CL), dispersion, effective area, core power fraction, V-parameter, birefringence, bending loss, etc. are evaluated in FEM. Different toxic chemicals (ethanol, methanol, benzene,

18

etc.), air pollutants (dioxin, nitrogen dioxide, sodium cyanide, hydrogen sulfide, etc.) and biological components (RBC, WBC, hemoglobin, plasma, cholesterol, albumin, etc.) are considered for testing the performance of the developed PCFs as sensor. Different optical properties such as sensitivity, confinement loss, effective material loss, numerical aperture etc. for the developed PCF designs are evaluated at optimum geometrical conditions. Required calculations has been carried out in COMSOL and MATLAB. The obtained results compared with recently proposed works. In addition, potential of fabricating the proposed designs is also described briefly considering the present fabrication technologies for the PCF structures introduced.

The PCF design and analysis processing steps are summarized as below:

Considering the fabrication potential and purpose of uses, different PCF geometry has been developed.

Design of PCF geometry using COMSOL Multiphysics software

Different optical properties for both waveguiding and sensing cases are measured using FEM in COMSOL Multiphysics for evaluation.

Optical properties are measured through Finite Element Method in COMSOL multiphysics

Analyzed the numerical data of the proposed PCFs by tunning the geometrical parameters.

Measured the output of different optical properties at optimum geometrical condition and compared the result with existing works. Considering the fabrication tolerance, performances of the designed PCF also evaluated by changing the geometrical parameters.

Different optical properties for both waveguiding and sensing cases are measured using Finite Element Method (FEM) in COMSOL Multiphysics by tunning the geometrical parameters. By comparing the measured results an optimum geometrical condition is identified for better attainment.

Find out the optimum geometrical conditions.

Measured & compared the numerical outcomes with existing PCF

Graphical interpretation using MATLAB software

Figure 3.1: PCF Design and analysis methodology flowchart.

3.3 Optical Properties for Waveguiding & Analyte Sensing

Several limiting factors are present in the terahertz regime that limit the transmission and efficient detection of analytes namely effective material loss (EML), confinement loss (CL), bending loss, dispersion, sensitivity, numerical aperture, effective area, etc. Finite element method (FEM) with Comsol software (v.5.3a) is employed to design, and for modeling and measuring the necessary optical properties for evaluating the performances. The necessary optical properties for waveguiding and sensing cases will be discussed in the following sections.

3.3.1 Effective Material Loss (EML)

When an optical pulse travels through the internal portion of a PCF some losses occur by a guided mode. Indeed, this loss is formed due to the use of polymer materials which has the feature of light absorption. Material absorption loss or effective material loss (EML) is the most limiting factor in THz wave transmission through a PCF.

The mathematical expression of EML can be derived using conjugate and non-conjugate reciprocity theorem of Maxell's laws [86]. Two different electromagnetic conditions are needed in this regard. As a first condition we can consider, index of refraction n, current density, J, electric and magnetic fields E and H respectively. On contrast, $\overline{n}, \overline{J}, \overline{E}$ and $\overline{H}$ can be consider as second condition. All vector components hold the time dependence, $e^{-j\omega}$, where ω is angular frequency. Index refraction profiles n and $\overline{n}$ determined spatial variables.

The vector function $\boldsymbol{F_c}$ can be defined by following expression in conjugate form,

$$F_c = E \times \overline{H}^* + \overline{E}^* \times H \tag{3.1}$$

Here, * indicate the complex conjugate. The EM fields satisfy conjugate form of Maxwell's equations [86]

$$\nabla \times \overline{E}^* = -i \left(\frac{\mu_0}{\varepsilon_0} \right)^{\frac{1}{2}} k \overline{H}^*$$

$$\nabla \times \overline{H}^* = \overline{J} + i\left(\frac{\mu_0}{\varepsilon_0}\right)^{\frac{1}{2}} k\left(\overline{n}^*\right)^2 \overline{E}^* \tag{3.2}$$

Where, μ_0, ε_0 and k are real.

To express equation (3.2) the following vector identity can be followed

$$\nabla_t (A \times B) = B(\nabla_t \times A) - A(\nabla_t \times B)$$

Now, equation (3.2) can be written as,

$$\nabla \cdot F_c = -i\left(\frac{\mu_0}{\varepsilon_0}\right)^{\frac{1}{2}} k\left\{\left(\overline{n}^*\right)^2 - n^2\right\} E \cdot \overline{E}^* - \left(\overline{E}^* \cdot J + \overline{J}^* \cdot E\right) \tag{3.3}$$

Applying divergence theorem, Fc can be written as

$$\int_A \nabla \cdot F_c dA = \frac{\partial}{\partial z}\int_A F_c \cdot \overline{z}dA + \int_l F_c \cdot \overline{n}dl \tag{3.4}$$

[The divergence theorem, $\int_S \nabla \cdot A ds = \frac{\partial}{\partial z}\int_S A \cdot \overline{z}ds + \int_l A \cdot \overline{n}dl$]

Here, A represents the arbitrary cross-sectional area, unit vector parallel to the z-axis represent by $\overline{z}$, For optical waveguide, the line integral over the circle $r = \infty$, where r is the cylindrical radius. That indicates Fc vanishes as $r \to \infty$, since the bound node amplitude falls exponentially. As per discussion we obtain the reciprocity theorem from (3.4) by dropping the line integration part,

Now,

$$\frac{\partial}{\partial z}\int_{A\infty} F_c \cdot \overline{z}dA = \int_{A\infty} \nabla \cdot F_c dA \tag{3.5}$$

This expression is applicable for uniformed refractive index profile, including material absorption, When, n has imaginary part.

For deriving the attenuation constant, we replace F_c by G_c in (3.1)

$$G_c = E \times \overline{H}^* \tag{3.6}$$

The magnetic permeability μ has very close value to free space value of μ_0.

$$\nabla \times E = i\left(\frac{\mu_0}{\varepsilon_0}\right)^{\frac{1}{2}} kH$$

$$\nabla \times H = J - i\left(\frac{\mu_0}{\varepsilon_0}\right)^{\frac{1}{2}} kn^2 E \tag{3.7}$$

$$\nabla \cdot \left(n^2 E\right) = \frac{\sigma}{\varepsilon_0}$$

$$\nabla \cdot H = 0$$

Consider that, $n = \overline{n},\ J = \overline{J} = 0$. Using (3.6), the vector identity can be deduced as,

$$\nabla \cdot F_c = ik\left\{\left(\frac{\mu_0}{\varepsilon_0}\right)^{\frac{1}{2}} kH \cdot \overline{H}^* - \left(\frac{\mu_0}{\varepsilon_0}\right)^{\frac{1}{2}} \left(n^2\right)^* E \cdot \overline{E}^*\right\} \tag{3.8}$$

Replacing *Fc* by *Gc* in (3.5),

$$\frac{\partial}{\partial z}\int_{A\infty} E \times \overline{H}^* \cdot \overline{z}dA = \int_{A\infty}\left\{\left(\frac{\mu_0}{\varepsilon_0}\right)^{\frac{1}{2}} kH \cdot \overline{H}^* - \left(\frac{\mu_0}{\varepsilon_0}\right)^{\frac{1}{2}} \left(n^2\right)^* E \cdot \overline{E}^*\right\}dA \tag{3.9}$$

The EM fields in forward and backward propagation mode in terms of propagation constant βj,

$$E = e_j e^{i\beta jz}$$

$$H = h_j e^{i\beta jz} \tag{3.10}$$

$$\overline{E} = e_{-j} e^{-i\beta jz}$$

$$\overline{H} = h_{-j} e^{-i\beta jz}$$

From (3.9) and (3.10) we can write,

$$\beta_j = \frac{\dfrac{k}{2}\int_{A\infty}\left\{\left(\dfrac{\mu_0}{\varepsilon_0}\right)^{\frac{1}{2}} h_j - \left(\dfrac{\mu_0}{\varepsilon_0}\right)^{\frac{1}{2}} \left(n^2\right)^* \left|e_j\right|^2\right\}dA}{\int_{A\infty} e_j \times h_j \cdot \overline{z}dA} \tag{3.11}$$

This solution only applicable for absorbing waveguide. For non-absorbing waveguide (3.11) can be written as

$$\beta_j = \frac{k\left(\dfrac{\mu_0}{\varepsilon_0}\right)^{\frac{1}{2}}\int_{A\infty}\left\{n^2 e_j \times h_j^*\right\}dA}{\int_{A\infty} n^2 \left|e_j\right|^2 dA} \tag{3.12}$$

In terms of attenuation, (3.12) can be expressed as

$$\gamma_j = \frac{2k\left(\dfrac{\mu_0}{\varepsilon_0}\right)^{\frac{1}{2}} \displaystyle\int_{Ax} n^r n^i \left|e_j\right|^2 dA}{\mathrm{Re}\left\{\displaystyle\int_{All} e_j \times h_j^* \cdot \bar{z} dA\right\}} \tag{3.13}$$

where, γ_j is the power attenuation constant, which can be further simplified as

$$\alpha_{eff} = \left(\frac{\mu_0}{\varepsilon_0}\right)^{\frac{1}{2}} \frac{\displaystyle\int_{A_{mat}} n\alpha_{mat} \left|E\right|^2 dA}{\mathrm{Re}\left\{\displaystyle\int_{All} E \times H^* \cdot \bar{z} dA\right\}} \tag{3.14}$$

Here, ϵ_0 and μ_0 denote the relative permittivity and relative permeability into the free space, respectively, n and α_{mat} the refractive index and absorption by Topas, $\bar{z}$ represents the z-component of the Poynting vector, and the electric field component is denoted by E.

3.3.2 Confinement Loss (CL)

Confinement loss is considered as another crucial factor because the length of propagation of the transmitted signal is limited by the confinement loss in the THz waveguide. It maintains a direct relationship with the number of holes in the cladding, shape of air holes and strut of air holes. If the cladding consists of an infinite number of air holes, it will lead to zero confinement loss. In practice, for design simplicity finite numbers of air holes are used in the cladding region. The loss is expressed as [20]

$$L_c = \left(\frac{4\pi f}{c}\right) Im(n_{eff}), cm^{-1} \tag{3.15}$$

where c and f indicate the speed of light and working frequency, respectively. The imaginary part of the complex refractive index is denoted by $I_m(n_{eff})$.

3.3.3 Core Power Fraction (CPF)

The mode power is propagated through the different region of the PCF including core air holes, core material and cladding area. The amount of mode power propagation

through any region can be calculated by (3.16), which is called power fraction [5-6]. Core power fraction (CPF) is defined as the volume of power which will propagate through the area of the core. CPF is given by

$$Core\ power\ fraction = \frac{\int_X S_z dA}{\int_{All} S_z dA}$$

(3.16)

The denominator part of the above equation is integrated for the total fiber region and the numerator part is for the core region.

3.3.4 Effective Area (EA)

Another important property of PCF is effective area, which is defined as the interaction area of light with matters within the PCF. Large value of effective area is very important for communications devices, because large effective mode area minimizes the impairments arising by the different nonlinear effects. Large effective area can be achieved by using small air holes and increasing the distance between the air holes in the cladding section. The effective area can be characterized by following relationship [18-19]

$$A_{eff} = \frac{[\int I(r) r dr]^2}{[\int I^2(r) dr]^2}$$

(3.17)

Here, electric field distribution over the cross-section of fiber is denoted by $I(r)$, where $I(r) = |E_t|^2$.

3.3.5 Dispersion

A significant factor that limits the signal transmission quality is dispersion. Lower and broader range flattened dispersion helps to improve the ability of a PCF based THz sensor for multichannel sensing operations [22]. Flattened dispersion of PCF indicates that the capability of traveling multiple signals simultaneously. There are two types of dispersions in a single mode fiber, waveguide dispersion and material dispersion. In our all-proposed designs, Topas has been used as background material due to well suited properties including negligible material dispersion [87-88]. Thus, material dispersion can be ignored. Waveguide dispersion is mainly dependable on the variations of

effective refractive index in core and cladding. Highly porous cladding and air core selection are other key reasons to mitigate waveguide dispersion fluctuation. If the range of dispersion is high, then the adjacent bits will overlap with each other which situation will create the problem of bit error. The dispersion can be described as [22]

$$\beta_2 = \frac{2}{c}\frac{dn_{eff}}{d\omega} + \frac{\omega}{c}\frac{d^2n_{eff}}{d\omega^2} \tag{3.18}$$

where velocity of light into free space is c, angular frequency ω and η_{eff} the effective refractive index of the material.

3.3.6 V-parameter

For long range, THz transmission light pulse will have to propagate in a single mode environment, which is quantified by the following [89]

$$V = \frac{2\pi r f}{c}\sqrt{n_1^2 - n_2^2} \tag{3.19}$$

where V represents the modeness of the fiber. If V crosses the value of 2.405, it behaves as multimode fiber otherwise it will operate as single mode fiber. Here, velocity of light is represented by c, r is the fiber core radius, the refractive index of core and cladding are denoted by n_1 and n_2 respectively.

The above equation is suitable for classical waveguide [90]. For porous core with symmetrical air holes PCF the classical equation of V- parameter can be modified for single mode condition is given below as V_{CPF} [89],

$$V_{PCF} = \frac{2\pi}{\lambda}\Lambda\sqrt{n_{eff}^2 - n_2^2} < \pi \tag{3.20}$$

where Λ is the air-hole pitch. n_{eff} and n_2 are effective mode index and cladding refractive index respectively.

3.3.7 Birefringence

For functioning as a polarization-maintaining fiber, a notable refractive index difference is required in *x*-polarization and *y*-polarization modes. This is known as

birefringence and expressed as [91]

$$B = \left| n_x - n_y \right|$$

(3.21)

where n_x and n_y represent the refractive index of x and y polarization modes, respectively.

3.3.8 Polarization Mode Dispersion (PMD)

In a polarization maintaining waveguide, normally the light is travel at the same speed. Due to random imperfections and asymmetries the two polarization modes propagate with different group velocities, that results in group delay between two polarization modes, causing random spreading which limits the performance of the fiber. Here PMD is considered in terms differential group delay $\Delta\tau$, which can be calculated by [91],

$$\Delta\tau = \frac{B_g}{c}$$

(3.22)

where B_g represents the group birefringence and B_g can be calculated in terms of phase birefringence, B is as follows,

$$B_g = B - \lambda \frac{dB}{d\lambda}$$

(3.23)

3.3.9 Sensitivity

The relative sensitivity is one of the prime properties of a sensor to assess the sensing response. It can be calculated by the intensity of light-substance interaction. The amount of interaction is measured using the absorption coefficient at a certain frequency according to the Beer-Lambert law [21] as,

$$I(f) = I_0(f)\exp[-r\alpha_m l_c]$$

(3.24)

where $I(f)$ and $I_0(f)$ denote intensity of light after placing the analytes in the designated place and intensity of light before placing the analytes in the designated place, respectively, α_m is called absorption coefficient, length of the channel is l_c, which is inversely related to the α_m, while f is the working frequency and r the sensitivity.

The absorbance of the evanescent or liquid concentration can be calculated as [21]

26

$$A = \log \left[\frac{I(f)}{I_0(f)} \right] = -r\alpha_m l_c \tag{3.25}$$

The sensitivity of designed PCF is measured as [22]

$$r = \frac{n_r}{n_{eff}} \times F \tag{3.26}$$

where n_r describes the refractive index of targeted samples, n_{eff} the effective refractive index of guided mode and F is the rate of interaction between light intensity and targeted analytes that can be expressed as [21]

$$F = \frac{\int_{sample} R_e(E_x H_y - E_y H_x) dxdy}{\int_{total} R_e(E_x H_y - E_y H_x) dxdy} \times 100 \tag{3.27}$$

where E_x and E_y, and H_x and H_y are the electric field and magnetic field components in x and y modes, respectively.

3.3.10 Numerical Aperture

The light compile ability of a PCF device is defined as a numerical aperture (NA). The value of NA depends on the RI difference of core and cladding. For broad sensing applications, a higher value of NA is expected which can be assured by large refractive index difference between core and cladding. NA can be measured as [22]

$$NA = \frac{1}{\sqrt{(1 + \frac{\pi A_{eff} f^2}{c^2})}} \tag{3.28}$$

where A_{eff} is the effective area, while f and c are the operating frequency and speed of light respectively.

3.4 Electromagnetism and Wave Equation

The behaviour the electromagnetic signal needs to elucidate as the pulse is an electromagnetic radiation. Wave equation also needs to be solved from Maxwell's equation to reveal the propagation characteristics and for finding the modal solution of the waveguide.

The Maxwell's equations are listed below in differential form [92]. These equations represent the situation of magnetic field and electric field when both travels together in a medium.

$$\nabla \times E = -\frac{\partial B}{\partial t} \tag{3.29}$$

$$\nabla \times H = \frac{\partial D}{\partial t} + J \tag{3.30}$$

$$\nabla . D = \rho \tag{3.31}$$

$$\nabla . B = 0 \tag{3.32}$$

where, E indicate that the electric filed intensity, B represent magnetic flux density, H is the magnetic field intensity, D is the electric flux density, J denotes the electric current density, and ρ stands for electric charge density.

The fundamental relation between E and D considering the permeability of a medium μ is shown in (3.33), and the relation between H and B in terms of μ in 3.34 [92, 93],

$$B = \mu H = \mu_0 \mu_T H \tag{3.33}$$

$$D = \varepsilon E = \varepsilon_0 \varepsilon_T E \tag{3.34}$$

where, μ_0 and ε_0 are the permeability and permittivity of the vacuum. μ_T and ε_T are the relative permittivity and permeability respectively.

To derive the wave equation, four Maxwell's equation needs to combines for a solution. The combines signal will produce a second differential equations that can be solved for the solution. From equations (3.33) and (3.29) it can be written as [92],

$$\nabla \times E = -\mu \frac{\partial}{\partial t} H \tag{3.35}$$

Applying curl both sides and written as,

28

$$\nabla \times (\nabla \times E) = -\mu \frac{\partial}{\partial t}(\nabla \times H) \tag{3.36}$$

substitute (3.30) and (3.34)

$$\nabla \times (\nabla \times E) = -\varepsilon\mu \frac{\partial^2}{\partial t^2} E \tag{3.37}$$

Electric field component can be expressed in frequency domain considering the angular frequency ω in polar form as [94],

$$E(x, y, z, t) = E(x, y, z)e^{j\omega t} \tag{3.38}$$

In phasor form we can also replace the time derivative with jω and can be expressed as [93],

$$\frac{\partial e^{j\omega t}}{\partial t} = j\omega e^{j\omega t} \tag{3.39}$$

$$\frac{\partial}{\partial t} = \partial\omega \tag{3.40}$$

From (3.32) and (3.37) one can write

$$\nabla \times (\nabla \times E) = \omega^2 \varepsilon\mu E \tag{3.41}$$

Similarly, we can express the magnetic field (H) as

$$\nabla \times \frac{1}{\varepsilon}(\nabla \times H) = \omega^2 \varepsilon\mu H \tag{3.42}$$

As per the vector calculus relation we can write, $\nabla \times (\nabla \times E) = \nabla(\nabla.E) - \nabla^2 E$. It can be rewrite as, $\nabla(\nabla.E) = -\nabla(\ln \varepsilon)E$.

Now, putting this value in equation (3.41) we can get the electric field vector wave equation. After rearranging, we can write as,

$$\nabla^2 E + \omega^2 \varepsilon\mu E = -\nabla(\ln \varepsilon).E \tag{3.43}$$

Similarly, the magnetic field vector wave equation can be expressed as,

$$\nabla^2 H + \omega^2 \varepsilon\mu H = -\nabla(\ln \varepsilon) \times \nabla \times H \tag{3.44}$$

Equations (3.43) and (3.44) can be represented in scalar form as,

$$\nabla^2 E = \omega^2 \varepsilon \mu E \qquad (3.45)$$

$$\nabla^2 H = \omega^2 \varepsilon \mu H \qquad (3.46)$$

These equations need to solve for knowing the modes of a waveguide. Various methods can be used to analyze the optical optical properties. FEM has been used in this thesis as the computational method. FEM and its characteristics will be discussed in the next sessions.

3.5   Methods of Analysis

Wave propagation and sensing in the optical platform both analysis is a complex mathematical process. Accurate analytical solution requires huge time for processing. A proper computational technique can minimize the time significantly. Additionally, it opens the door to examine the results by numerical analysis. Current several computational methods and algorithms are allowing to investigate the optical characteristics of PCF devices [95]. Methods of Moments (MOM), Method of Lines (MOL), Finite Difference Method (FDM), Finite-Time Finite-Domain method (FDTD), Finite Element Method (FEM), etc. are the well-developed optical device numerical analysis techniques. In our case we have been utilized the FEM for numerical analysis by considering several unparallel features. The investigation process in the FEM is discussed in the following sections.

3.6   Finite Element Method (FEM)

In 1940, first the proposal of FEM was revealed and its applications in the area of science and engineering were developed in 1960 [96]. From then on FEM is being used for solving different complex geometrical structure as well as for more advanced like PCF structure. COMSOL Multiphysics with FEM is now strongest computational technique for optical or others complex device's structure analysis [96]. The main idea of FEM is that the subdomain/element are constructed from the domain. Each element is estimated the solution using basis function usually polynomials. In general, the

polynomials have a non-zero value for the elements but in other case it put zero. The solution can be enumerated at any point of the element because inside the sub-domain, basis function makes effective use of interpolation function which is continuous. If Ψ is considered as interpolation function for the unknown field of each element, and e is considered as field element, then we can write [96]

$$\psi^e = \sum_{i=1}^{m} N_i \psi_i \tag{3.47}$$

where, m is denoted as the number of nodes in the element, N_i and Ψ_i are the interpolation function and field value at node i respectively.

FEM is capable to handle boundary value problem in both domain frequency or and time by setting either variational approach (Rayleigh-Ritz method) or weighted residuals (Galerkin method). By using both approaches FEM can reduce the boundary value problem and their solution into eigenvalue matrix equations [97].

Using the Rayleigh-Ritz method the magnetic field **H** formula can be derived by the followings,

The wave equation can be represented interms of eigenvalue equation as

$$LH - \lambda MH = 0 \tag{3.48}$$

where, M is the operators and $M = \mu$, L is the self-joining operator and $L = \nabla \times \varepsilon^{-1} \nabla$, and λ is the eigenvalue and $\lambda = \omega^2$.

In case of self-joining operator, $(\langle L\varphi, \psi \rangle = \langle \varphi, L\psi \rangle)$, so, functional provides:

$$F(H) = \frac{1}{2}\left\langle L\overline{H}, \overline{H} \right\rangle - \frac{\lambda}{2}\left\langle M\overline{H}, \overline{H} \right\rangle \tag{3.49}$$

Here, the symbol $\langle \rangle$ indicate as inner product and $*$ stands for conjugate,

$$\langle f, g \rangle = \int g^* \cdot f dV \tag{3.50}$$

At F($\overline{H}$) = 0, the stationary value of the functional is

$$\lambda = S.V. \frac{\langle LH, H \rangle}{\langle MH, H \rangle} \tag{3.51}$$

Here, $S.V$ represent hat the stationary value. As per Rayleigh-Ritz method full vectoral **H** field component [98]:

$$\omega^2 = S.V. \frac{\iint (\nabla \times H)^* \cdot \varepsilon^{-1} (\nabla \times H) dV}{\iint H^* \cdot \mu H dV} \tag{3.52}$$

The limiting technique constructed as an eigenvalue problem

$$[A]x = \lambda [B]x \tag{3.53}$$

where, A indicate the mass matrix, B represent the stiffness matrix, x and λ stands for eigenvector and eigenvlue accordingly. Becuase of this matrix formation its minimizes the computational time.

In weighted residuals method no need to include information regarding functional. It can be presented as following interms of operator

$$Lu = v \tag{3.54}$$

Here, differential Laplace operator is represented by L, v indicate the excitation of source, and undefined quantity is denoted by u. Using some identified basis functions and unidentified coefficients, unidentified function can be contrstructed. The unidentified coefficient is chosen as to minimize the residual error. From (3.54) it can be written as [92].

$$R(s) = Lu - v \tag{3.55}$$

(3.53) can be represented in matrix form as

$$[L][u] = [v] \tag{3.56}$$

According to the electromagnetic theorem, here unknown quality u represents the magnetic field and the L is the operator where $L = \nabla \times \varepsilon^{-1} \nabla \times (-\omega^2 \mu)$ and v the source where, $[v] = 0$.

Both of the above mentioned approaches can be applicable to set up the FEM, although in weighted residuals, the natural boundary conditions need extra attention [96]. In this

thesis work Rayleigh-Ritz method has been utilized for necessary evaluation. The vector formation as well as scalar fomation process in FEM have discussed in the following Sections.

3.6.1. Scalar Formation

The FEM can handle efficiently both vector and scalar wave equations. If the cahnges of refractive index is not significant then the right hand side of the vector equation can be ignored. In that case scalar wave equation can be used which will also minimize the complexity. The optical waveguide the confined field not behaves as like transverse electric not as like transverse magnetic, it acts as actually quasi- transverse electric (TE) or quasi-transverse magnetic (TM). Electric field (*Ex*) is dominat in TE mode and magnetic field (*Hx*) is dominant in TM mode and their respective eqautions are presented in (3.57) and (3.58) [92],

$$L = \iint_{\Omega} \left[\left(\frac{\partial E_x}{\partial x} \right)^2 + \left(\frac{\partial E_x}{dy} \right)^2 - k_0 n^2 E_x^2 + \beta^2 E_x^2 \right] d\Omega \qquad (3.57)$$

$$L = \iint_{\Omega} \left[\frac{1}{n^2} \left(\frac{\partial E_x}{\partial x} \right)^2 + \frac{1}{n^2} \left(\frac{\partial E_x}{dy} \right)^2 - k_0 n^2 H_x^2 + \frac{1}{n^2} \beta^2 E_x^2 \right] d\Omega \qquad (3.58)$$

Here, Ω is termed as cross section area of waveguide and the Laplacian operator is represented by *L*. β^2 would be the eigenvalue for k_o and $k_o{}^2$ would be the eigen vlaue for β .

Equations (3.57) and (3.58) have continuity of $\frac{\partial E_x}{\partial n}$ and $\left(\frac{1}{n^2} \right) \left(\frac{\partial H_x}{\partial n} \right)$ for the natural boundary condition accordingly. Now sub-domain creation process from the domain usinng FEM will be discussed in the next Section.

3.6.2. Elements Formation in Finite Elelment Method

Meshing is the most crucial stage of FEM, beacuse the computational processing time

and storage requirments depends on it. Acuracy of the results also has a dependency on meshing. Meshing basically a step of solving complex structure and this stgae the domain is subdivided by considering without overlapping and no space between two adjacent elements. Meshing condition of a proposed PCF (zoomed view) is shown in Figure 3.2. In the FEM the subdivided elements can be one dimentional line element, or two dimentional triangular, square, or third dimentional triangular prism, rectangular brick or to more complex. The fundamental elements for 1D, 2D, 3D are diaplayed in Figure 3.3 [96].

One diementional line element consists of two nodal points. In the two dimentional case the element can be either triangular or square. For triangular shaped element have three nodal points, similarly square shaped element have four nodal points. It will be mentioned that higher numbers of nodal points provide the better accuracy in results though higher nodal points solutions will be more compleated. In 2D, triangular elements covers the boundaries more accurately than the rectangular or square shapes element which is graphically displayed in Figure 3.4 [96]. Due to this reason in our case we have utilized triangular elements in the meshing stage.

Number of nodal points can be estimated by the interpolation function. The polynomial should contain all possible terms to be complete. That indicates that every polynomial should be unique and has no effect on the shape function. Number of terms of the polynomial must be equivalent of the nodal pints to be unique. Required number of terms of a polynomial can be termed as Pascal triangle. The Pascal triangle for a complete polynomial is shown in Figure 3.5.
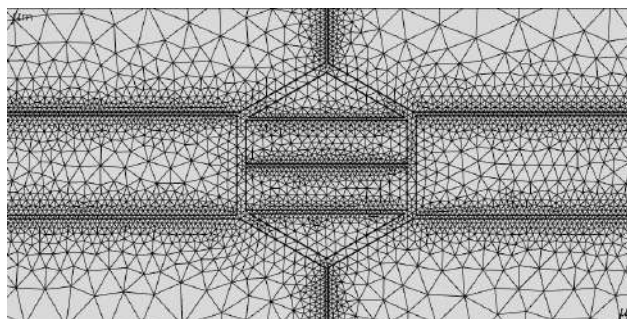
Figure 3.2: Meshing Condition
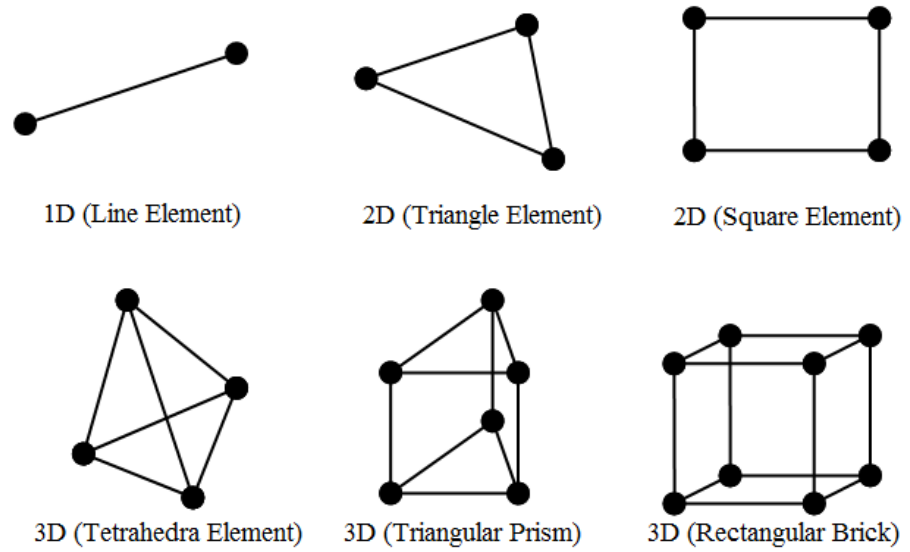
Figure 3.3: Basic finite elements 1D, 2D and 3D [96].
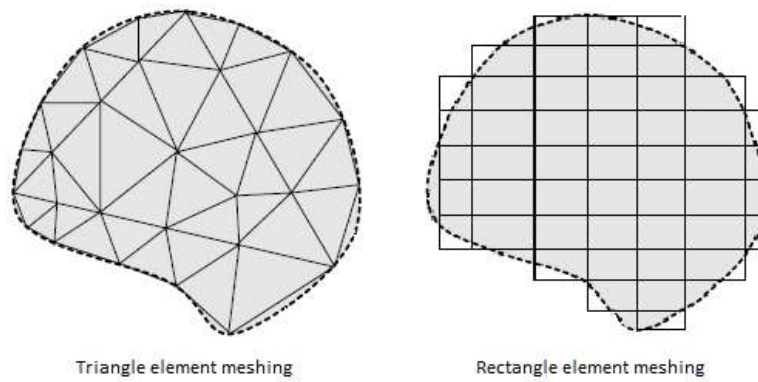
Figure 3.4: Mesh comparison of triangular (left) and rectangular (right) elements [96]
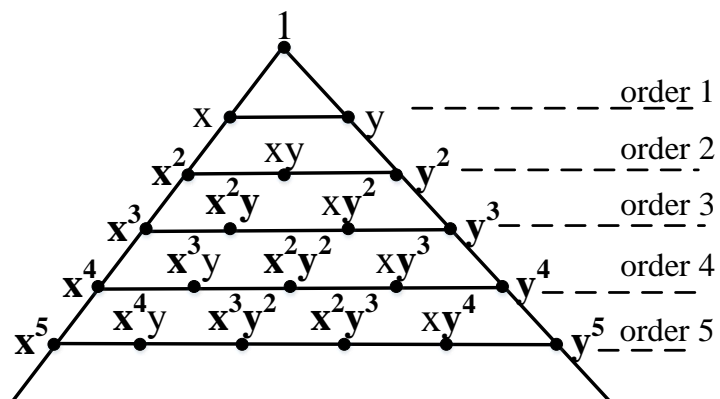
Figure 3.5: Complete polynomials of pascal triangle [96].

For the first order triangle mesh, the polynomial can be expressed as (a + bx + cy) [96].

The field(ϕ_e) of each elements can be represented by,

$$\phi_e(x, y) = a + bx + cy \tag{3.59}$$

Here, a,b, c represented as constants,

The field at node can written as,

$$\phi_e + (x_i, y_i) = \phi_i; i = 1, 2, 3 \tag{3.60}$$

The field for three node points it can be expressed as,

$$\begin{aligned}
\phi_1 &\equiv \phi_e(x_1, y_1) = a + bx_1 + cy_1 \\
\phi_2 &\equiv \phi_e(x_2, y_2) = a + bx_2 + cy_2 \\
\phi_3 &\equiv \phi_e(x_3, y_3) = a + bx_3 + cy_3
\end{aligned} \tag{3.61}$$

(3.61) can be represented in matrix form as,

$$\begin{Bmatrix} \phi_1 \\ \phi_2 \\ \phi_3 \end{Bmatrix} = \begin{bmatrix} 1 & x_1 & y_1 \\ 1 & x_2 & y_2 \\ 1 & x_3 & y_3 \end{bmatrix} \begin{bmatrix} a \\ b \\ c \end{bmatrix} \tag{3.62}$$

where,

$$\begin{aligned}
a &= \frac{1}{2A_e}\left[\phi_1(x_2 y_3 - x_3 y_2) + \phi_2(x_3 y_1 - x_1 y_3) + \phi_3(x_1 y_2 - x_2 y_1)\right] \\
b &= \frac{1}{2A_e}\left[\phi_1(y_2 - y_3) + \phi_2(y_3 - y_1) + \phi_3(y_1 - y_2)\right] \\
c &= \frac{1}{2A_e}\left[\phi_1(x_3 - x_2) + \phi_2(x_1 - x_3) + \phi_3(x_2 - x_3)\right]
\end{aligned} \tag{3.63}$$

Here, A_e indicates the area of a triangular element and it can be given by [96],

$$A_e = \frac{1}{2}\begin{vmatrix} 1 & x_1 & y_1 \\ 1 & x_2 & y_2 \\ 1 & x_3 & y_3 \end{vmatrix} = \frac{1}{2}\left[(x_2 y_3 - x_3 y_2) + (x_3 y_1 - x_1 y_3) + (x_1 y_2 - x_2 y_1)\right] \tag{3.64}$$

Solving (3.41) using (3.63), we obtain

$$\phi_e(x, y) \equiv N_1(x, y) \cdot \phi_1 + N_2(x, y) \cdot \phi_2 + N_3(x, y) \cdot \phi_3 \tag{3.65}$$

$$\phi_e(x, y) \equiv [N]\{\phi_e\}$$

Here, N_i indicate the shape functions and is expressed as

$$\{N\}^T = \begin{bmatrix} N_1 \\ N_2 \\ N_3 \end{bmatrix} = \frac{1}{2A_e} \begin{bmatrix} x_2 y_3 - x_3 y_2 & y_2 - y_3 & x_3 - x_2 \\ x_3 y_1 - x_1 y_3 & y_3 - y_1 & x_1 - x_3 \\ x_1 y_2 - x_2 y_1 & y_1 - y_2 & x_2 - x_1 \end{bmatrix} \begin{bmatrix} 1 \\ x \\ y \end{bmatrix} \qquad (3.66)$$

Or, $$\{N\}^T = \begin{bmatrix} N_1 \\ N_2 \\ N_3 \end{bmatrix} = \frac{1}{2A_e} \begin{bmatrix} a_1 + b_1 x + c_1 y \\ a_2 + b_2 x + c_2 y \\ a_3 + b_3 x + c_3 y \end{bmatrix} \qquad (3.67)$$

a_i, b_i, c_i and $i = 1, 2, 3$ are found as,

$$a_1 = x_2 y_3 - x_3 y_2$$
$$b_1 = y_2 - y_3$$
$$c_1 = x_3 - x_2 \qquad (3.68)$$

Similarly, a_2, b_2, c_2, a_3, b_3 and c_3 can be easily calculated just by simple cyclical exchange of $1 \rightarrow 2 \rightarrow 3$ in (3.68).

3.6.3. Global Metric Formtion

Formation of global and element matrix from wave equation will be discussed in this Section. The field components in all three H_x, H_y and H_z can be represented as [96]

$$\{H\}_e = \begin{bmatrix} \{H_x\}_e & \{H_y\}_e & \{H_z\}_e \end{bmatrix}^T \qquad (3.69)$$

and,

$$\{N\}^T = \begin{bmatrix} \{N\} & \{0\} & \{0\} \\ \{0\} & \{N\} & \{0\} \\ \{0\} & \{0\} & j\{N\} \end{bmatrix} \qquad (3.70)$$

Here, $\{N\} = [N_1 N_2 N_3]^T$ and $\{0\}$ is null vector.

From (3.59) and (3.70), we obtain

$$\{H\}_e = \begin{bmatrix} N_1 & N_2 & N_3 & 0 & 0 & 0 & 0 & 0 & 0 \\ 0 & 0 & 0 & N_1 & N_2 & N_3 & 0 & 0 & 0 \\ 0 & 0 & 0 & 0 & 0 & 0 & jN_1 & jN_2 & jN_3 \end{bmatrix} \begin{bmatrix} H_{x1} \\ H_{x2} \\ H_{x3} \\ H_{y1} \\ H_{y2} \\ H_{y3} \\ H_{z1} \\ H_{z2} \\ H_{z3} \end{bmatrix} \qquad (3.71)$$

The global matrices [A] and [B] can be expressed as [96]:

$$(\nabla \times H)_e = [\nabla][N]^T \{H\}_e = \begin{bmatrix} 0 & -\frac{\partial}{\partial z} & \frac{\partial}{\partial y} \\ \frac{\partial}{\partial z} & 0 & \frac{\partial}{\partial x} \\ \frac{\partial}{\partial y} & \frac{\partial}{\partial x} & 0 \end{bmatrix} \tag{3.72}$$

(3.62) can be simplified as

$$(\nabla \times H)_e = [Q]^T \{H\}_e \tag{3.73}$$

Here [Q] is,

$$[Q] = \begin{bmatrix} \{0\} & j\beta\{N\} & \frac{\partial\{N\}}{\partial y} \\ -j\beta\{N\} & \{0\} & \frac{\partial\{N\}}{\partial x} \\ -\frac{\partial\{N\}}{\partial y} & \frac{\partial\{N\}}{\partial x} & \{0\} \end{bmatrix} \tag{3.74}$$

Then, mass matrix, A is written as,

$$A = \sum_e [A]_e = \sum_e \iint_e \frac{1}{\varepsilon_e} [Q]^* [Q]^T \, dxdy \tag{3.75}$$

$$A = \begin{bmatrix} A_{xx} & A_{xy} & A_{xz} \\ A_{yx} & A_{yy} & A_{yz} \\ A_{zx} & A_{zy} & A_{zz} \end{bmatrix} \tag{3.76}$$

and,

$$[A_{xx}] = \iint_e \left[\beta^2 \{N\}\{N\}^T + \frac{\partial\{N\}}{\partial y}\frac{\partial\{N\}^T}{\partial y} \right] dxdy \tag{3.77}$$

$$[A_{xy}] = \iint_e -\frac{\partial\{N\}}{\partial y}\frac{\partial\{N\}^T}{\partial x} dxdy \tag{3.78}$$

$$[A_{xz}] = \iint_e \beta\{N\}\frac{\partial\{N\}^T}{\partial x} dxdy \tag{3.79}$$

$$[A_{yy}] = \iint_e \left[\beta^2 \{N\}\{N\}^T + \frac{\partial\{N\}}{\partial x}\frac{\partial\{N\}^T}{\partial x} \right] dxdy \tag{3.80}$$

38

$$\left[A_{yz} \right] = \iint_e \beta \{N\} \frac{\partial \{N\}^T}{\partial x} dxdy \tag{3.81}$$

$$\left[A_{zz} \right] = \iint_e \left[\frac{\partial \{N\}}{\partial y} \frac{\partial \{N\}^T}{\partial y} + \frac{\partial \{N\}}{\partial x} \frac{\partial \{N\}^T}{\partial x} \right] dxdy \tag{3.82}$$

Stiffness matrix, B as [96],

$$B = \sum_e \iint_e [N]^* [N]^T dxdy \tag{3.83}$$

$$B = \begin{bmatrix} [B_{xx}] & [0] & [0] \\ [0] & [B_{yy}] & [0] \\ [0] & [0] & [B_{zz}] \end{bmatrix} \tag{3.84}$$

$$\left[B_{xx} \right] = \left[B_{yy} \right] = \left[B_{zz} \right] = \sum_e \iint_e [N]^* [N]^T dxdy \tag{3.85}$$

The presented form of stiffness matrix and mass matrix B are in universal global matrix form for a two-dimensional problem. A triangular shape element and first order node is considered to construct matrix. The matrix size is 9×9. The matrix parameters are calculated as follows:

$$\int_e N_1^2 dxdy = \int_e N_2^2 dxdy = \int_e N_3^2 dxdy = \frac{A_e}{6} \tag{3.86}$$

$$\int_e N_1 N_2 d\Omega = \int_e N_2 N_3 d\Omega = \int_e N_1 N_3 d\Omega = \frac{A_e}{12} \tag{3.87}$$

$$\iint_e \{N\}\{N\}^T dxdy = \frac{A_e}{12} \begin{bmatrix} 2 & 1 & 1 \\ 1 & 2 & 1 \\ 1 & 1 & 2 \end{bmatrix} \tag{3.88}$$

$$\frac{\partial \{N\}}{\partial x} = \frac{1}{2A_e} \begin{bmatrix} b_1 \\ b_2 \\ b_3 \end{bmatrix} \tag{3.89}$$

$$\frac{\partial \{N\}}{\partial y} = \frac{1}{2A_e} \begin{bmatrix} c_1 \\ c_2 \\ c_3 \end{bmatrix} \tag{3.90}$$

39

$$\left[\iint_e \frac{\partial \{N\}}{\partial p} \frac{\partial \{N\}^T}{\partial q} \, dxdy \right]_{ij} = A_e C_{pi} C_{qj} \tag{3.91}$$

$$\left[\iint_e \frac{\partial \{N\}}{\partial p} \{N\}^T \, dxdy \right]_{ij} = \frac{A_e}{3} C_{pi} \tag{3.92}$$

$$[A]_{e(1,1)} = \frac{1}{\varepsilon} \int_e -\beta^2 N_1^2 + \left(\frac{\partial N_1}{\partial y} \right)^2 dxdy = \frac{1}{\varepsilon} \left[\frac{-\beta^2 A_e}{6} + c_1^2 A_e \right] \tag{3.93}$$

$$[A]_{e(1,4)} = \frac{1}{\varepsilon} \int_e \frac{-\partial N_1}{dy} \frac{\partial N_1}{dx} d\Omega = -\frac{1}{\varepsilon} c_1 b_1 A_e \tag{3.94}$$

$$[B]_{e(1,1)} = \mu \int_\Delta N_1^2 d\Omega = \mu \frac{A_e}{6} \tag{3.95}$$

$$[B]_{e(1,4)} = 0 \tag{3.96}$$

B_e is given by

$$B_e = \begin{bmatrix}
\frac{A}{6} & 0 & 0 & \frac{A}{12} & 0 & 0 & \frac{A}{12} & 0 & 0 \\
0 & \frac{A}{6} & 0 & 0 & \frac{A}{12} & 0 & 0 & \frac{A}{12} & 0 \\
0 & 0 & \frac{A}{6} & 0 & 0 & \frac{A}{12} & 0 & 0 & \frac{A}{12} \\
\frac{A}{12} & 0 & 0 & \frac{A}{6} & 0 & 0 & \frac{A}{12} & 0 & 0 \\
0 & \frac{A}{12} & 0 & 0 & \frac{A}{6} & 0 & 0 & \frac{A}{12} & 0 \\
0 & 0 & \frac{A}{12} & 0 & 0 & \frac{A}{6} & 0 & 0 & \frac{A}{12} \\
\frac{A}{12} & 0 & 0 & \frac{A}{12} & 0 & 0 & \frac{A}{6} & 0 & 0 \\
0 & \frac{A}{12} & 0 & 0 & \frac{A}{12} & 0 & 0 & \frac{A}{6} & 0 \\
0 & 0 & \frac{A}{12} & 0 & 0 & \frac{A}{12} & 0 & 0 & \frac{A}{6}
\end{bmatrix} \tag{3.97}$$

FEM solves these matrices for solving a mode in COMSOL.

3.7. Perfectly Matched Layer (PML)

The physical dimention of a problem should be finite due to the limitation of computational resources. A boundary should be introduced to truncate the domain. The boundary can reflect the incident wave that may cause unwanted radiation in the structure. For protecting the unwanted reflected wave two methods were proposed. The first technique is called local mathematical technique, which is purely a mathemedical model, but this boundary connot be placed near the source [99]. The second method is called Perfectly Mached Layer (PML) which is basically a physical layer insertion as artificial medium. This concept was first introduced by Berenger [100]. Since it has been used as a boundary in FDTD and FEM. The idea PML is to place an boundary with the same material with the main domain. This is a non reflecting medium that can absorb all the incident wave with any angles and frequencies [99].

In this research work, all the proposed PCFs are evaluated with a cylindrical PML in the outer shell of the PCF's structure due to the use of FEM as a computaional method. Throughout the evaluation process (7-8) % of the total diameter of the PCF has been considered, respectively.

The PML is implemented as stretching of the complex coordinate in FEM [96, 99].

$$x \rightarrow \overline{x} = \int_{0}^{x} S_x(x')dx' \qquad (3.98)$$

$S_x(x')$ is termed as complex stretching variable.

This stretching function offers a change in the nabla operator, which is denoted by ∇, and expressed as

$$\nabla \rightarrow \overline{\overline{\nabla}} = \overline{x}\frac{\partial}{\partial \overline{\overline{x}}} + \overline{y}\frac{\partial}{\partial \overline{\overline{y}}} + \overline{z}\frac{\partial}{\partial \overline{\overline{z}}} = \overline{x}\frac{1}{S_x}\frac{\partial}{\partial x} + \overline{y}\frac{1}{S_y}\frac{\partial}{\partial y} + \overline{z}\frac{1}{S_z}\frac{\partial}{\partial z} \qquad (3.99)$$

This lead to a modification in the Maxwell's equations. The modified maxwell's equations can be written as by replacing ∇ by $\overline{\nabla}$ and $\partial/\partial t$ is replaced with jω,

$$\nabla \times E = -j\omega\beta$$
$$\nabla \times H = j\omega D$$
$$\nabla \cdot D = \rho \qquad (3.100)$$
$$\nabla \cdot D = 0$$

This results also lead to a changes in (3.40),

$$\nabla \times \left([p]\nabla \times H\right) - k_0^2 [q] H = 0 \qquad (3.101)$$

wrere, $k_0^2 = \dfrac{\omega^2}{c^2} = \omega^2 \mu E$, and

$$[p] = \begin{bmatrix} \dfrac{s_y s_z}{s_x}\varepsilon_{xx} & s_z\varepsilon_{xy} & s_y\varepsilon_{xz} \\[2ex] s_z\varepsilon_{yx} & \dfrac{s_z s_x}{s_y}\varepsilon_{yy} & s_x\varepsilon_{yz} \\[2ex] s_y\varepsilon_{zx} & s_x\varepsilon_{zy} & \dfrac{s_x s_y}{s_z}\varepsilon_{zz} \end{bmatrix}^{-1} \qquad (3.102)$$

$$[q] = \begin{bmatrix} \dfrac{s_y s_z}{s_x} & 0 & 0 \\[2ex] 0 & \dfrac{s_z s_x}{s_y} & 0 \\[2ex] 0 & 0 & \dfrac{s_x s_y}{s_z} \end{bmatrix} \qquad (3.103)$$

Besides unwanted radiation absorbance, PML also helps to measure the confinement loss and bending loss.

3.8 Summary

All the necessary optical properties for both THz wave guidance and analyte sensing are discussed in this Chapter. It can be stated that EML is the most limiting factor for efficient waveguiding and sensitivity is the main parameter for evaluating a sensing device. Confinement loss is the most challenging factor for both cases. FEM is the most efficient and strongest computational methods now for solving complex structure as well as matrix solution. In PCF all the optical properties can be controlled by the

geometrical specifications. Thus, proper geometry development and parameters optimization are the main challenges for PCF development. Design of the proposed PCFs and their performances for waveguiding and sensing applications will be discussed in Chapters 5, 6 and 7.

Chapter 4

PCF for THz waveguiding: Design & Analysis

4.1 Introduction

An unguided air medium for THz transmission established a number of problems such as unpredictable absorption loss caused by the atmospheric situation, alignment complexity between transmitter and receiver etc. Various types of guided media are proposed, most of these demonstrated high absorption, high weight, and ohmic loss in THz wave propagation [11-15]. The photonic crystal fiber (PCF) provides a highly promising solution due to its remarkable wave guiding capability with reduced absorption loss, near-zero flattened dispersion and lower confinement loss [16, 18]. Excepts lower absorption loss, high core power fraction, low confinement loss, high effective area, low dispersion property, the geometries' parameters such as pitch size, air hole radius, strut size and core radius can be readily selected. Therefore, for proper utilization of PCF's remarkable properties as a THz waveguide with desired outcomes, geometry selection and parameters value optimization are the main challenges. Taking these challenges, we have modelled several PCF structures and optical properties are evaluated and optimized the geometrical specifications for better attainment. In this Chapter we have presented our proposed PCF structures and discussed their performances. The design procedures, reasons for such types of structures development and the performance comparisons with the existing works also discussed in this Chapter in details.

4.2 Proposed PCFs for THz waveguiding

Considering the performances and simplicity of the design, square and circular shaped porous core PCFs geometry has been constructed for THz wave guidance. Highly porous geometry in cladding also considered for better attainment. All the necessary optical properties are evaluated and compared the result with existing works. The

design process of proposed PCFs and their performances will be discussed in the following sections.

4.2.1 Square shaped core-cladding structured PCF

PCF is a consummate medium for guiding THz wave because the PCF's has surprising light guiding properties with low material loss characteristics but proper design of PCF is the main issue to achieve minimum material loss. In this work, we have proposed a PCF structure with 45^0 rotation air holes in both core and cladding for minimizing the fabrication complexity and improving the performances for THz wave guidance with extremely low EML. Additionally, it renders an average core power fraction near about 40% at core porosity of 81%.

4.2.1.1 Design Methodology of Proposed PCF

Here, we have proposed a new PCF design which is structured by finite numbers of 45-degree rotational square air holes in the cladding region and the core consists of 4 (four) 45-degree rotational square air holes. To design the PCF geometry and evaluate the guiding performances of suggested PCF FEM-based software COMSOL Multiphysics (version 5.3a) has been used. The presented PCF structure is selected because its exhibit extremely low loss when it operates as a guided vehicle. In this structure, because of low bulk absorption loss, TOPAS is used as background material.

The geometry of proposed PCF with enlarge version of core is shown in Figure 4.1. The proposed PCF's core consists of four 45^0 rotational square lattice air holes to reduce the material loss. In Figure 4.1, D_{core} denotes the side length of core which is selected as optimum of 300 µm and side length of one square lattice of core is 121.5µm. The pitch of the core (A1) is the distance between two centers of adjacent square lattices, which is represents by $A1 = 0.43D_{core}$ and the distance between two center of opposite square lattices is $0.61D_{core}$. The side length of the air holes in the core region is denoted by D1, the value of D1 depends on the porosity of the core. The core porosity is defined by the ratio of total area covert by the air holes in the core section and total area of the core. We have varied the porosity from 71% to 81% at wide range of operating

frequency from 0.6 to 1.8 THz to observe the effect on EML as well as core power fraction and effective area. We took this range of porosity because higher value of porosity may causes overlapping the air holes during fabrication, on other hand lower value of porosity causes higher losses.
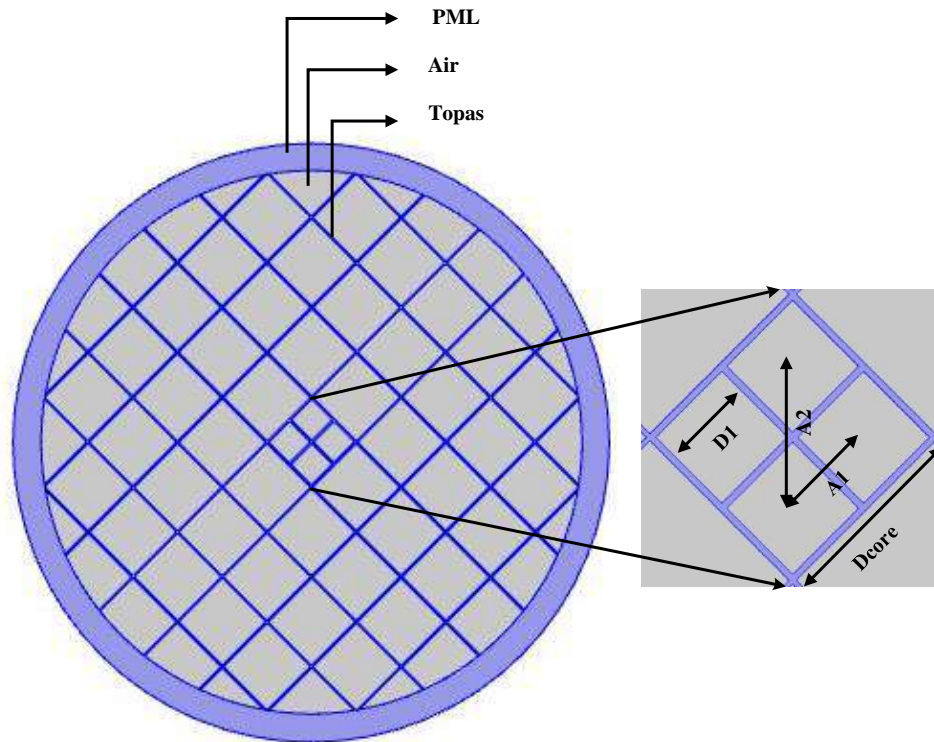
Figure 4.1: Geometry of proposed square shaped core-cladding structured PCF.

4.2.1.2 Simulations and Results

A circular Perfectly Matched Layer (PML) has been used in the outer region of the PCF and the presented PCF structure tested by Comsol software (V.5.3a) software. The thickness of PML is selected 10% of the total fiber, it is important the size of PML because it has a large impact on numerical. For selecting optimum geometrical specifications, we have synthesized the geometrical parameters in several points by several subsequent simulations. Finally, we find out the optimum geometrical conditions and listed in the Table 4.1. For attaining better accuracy fine element size is maintained in the simulation process. Complete mesh consists of 288 vertex elements, 7376 number of boundary elements and total 54060 number of elements.

Table 4.1: Optimum Design Parameters

Parameters	Value
Core Length (D_{core})	300 µm
D1	121.5 µm
Al	129 µm
A2	183 µm
Porosity	(71 - 81) %
Frequency	(0.6 - 1.8) THz

(a)   (b)   (c)
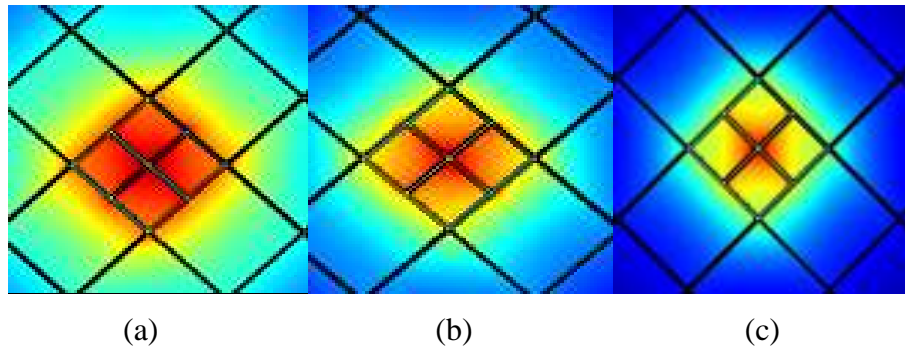
Figure 4.2: Interaction of light of suggested structure for different frequencies at Porosity = 81% (a) Frequency = 0.8THz (b) Frequency = 1THz and (c) Frequency = 1.2THz

Electromagnetic field distribution within the fiber is shown in Figure 4.2 where tight confinement occurs in the core area for different terahertz frequencies this indicates that this proposed PCF can perform as long-distance THz waveguide with low losses.

In our proposed PCF, behaviour of EML with respect to frequency is shown in Figure 4.3. This figure depicts that the increment of frequency boosts up the EML which satisfie the EML calculation using empirical relation. Figure 4.3 also shows that when porosity increases, the EML decreases. Because when porosity increases the area of background material inside the core section decreases, which absorb less light as a result EML reduction. At optimum value of core size 300µm and porosity 81% the presented PCF depicts EML of 0.016 cm^{-1} in the frequency 1 THz and this outcome is comparable with that of previously presented PCF structures [101-104].
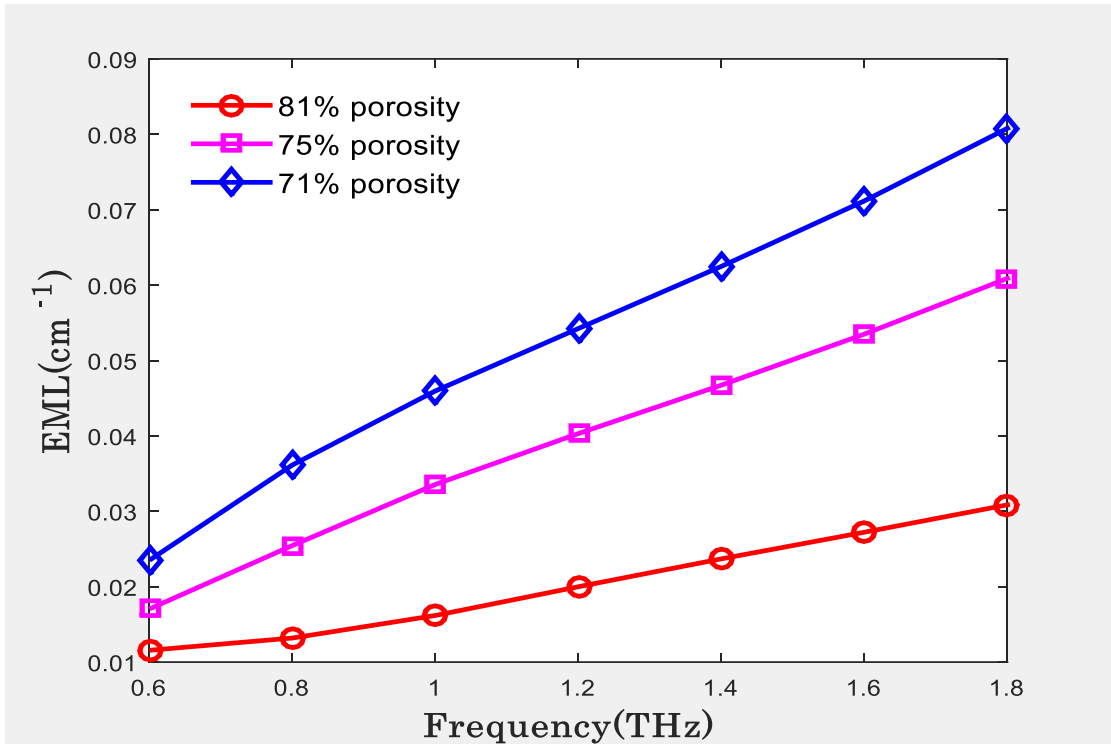
Figure 4.3: Behaviour of EML as a function of frequency at different porosity.
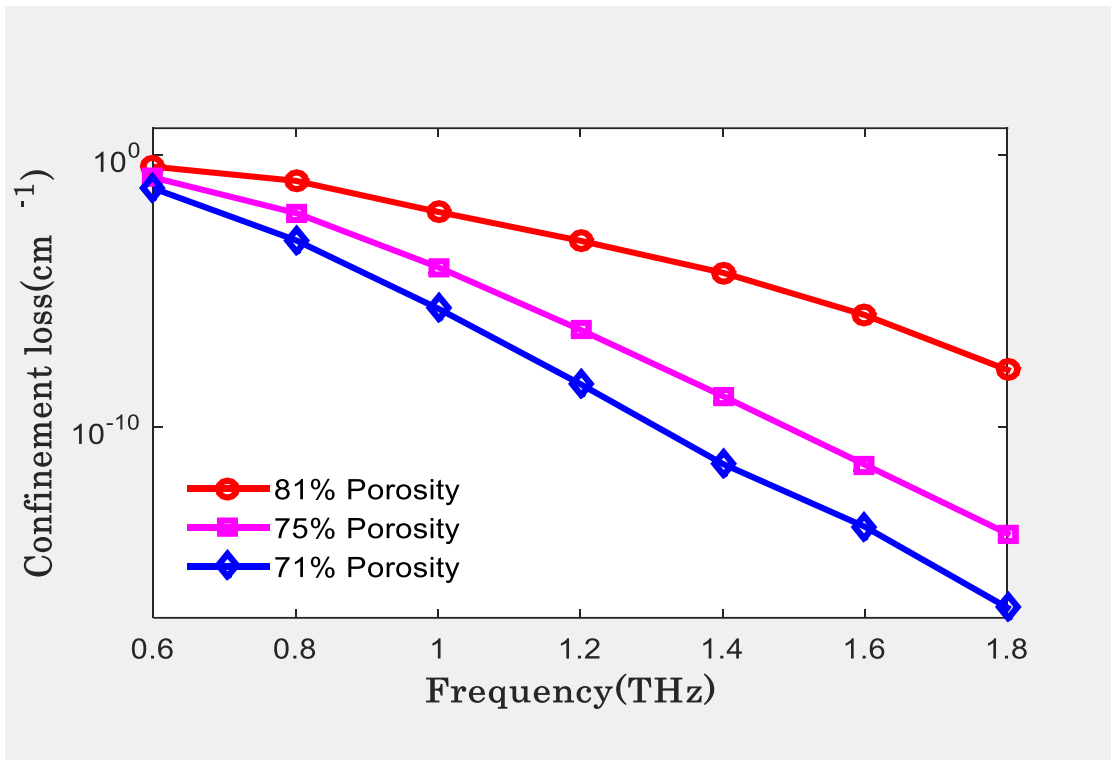
Figure 4.4: Behaviour of Confinement loss as a function of frequency at different porosity.
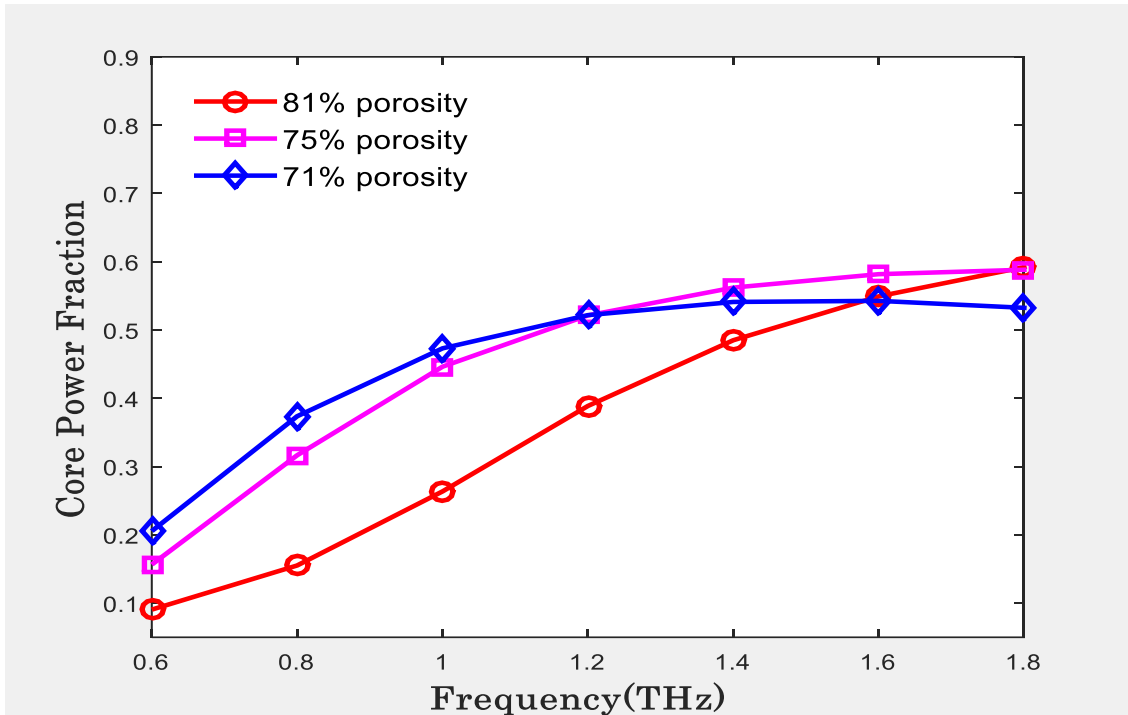
Figure 4.5: Behaviour of core power fraction with respect to frequency at different porosity.
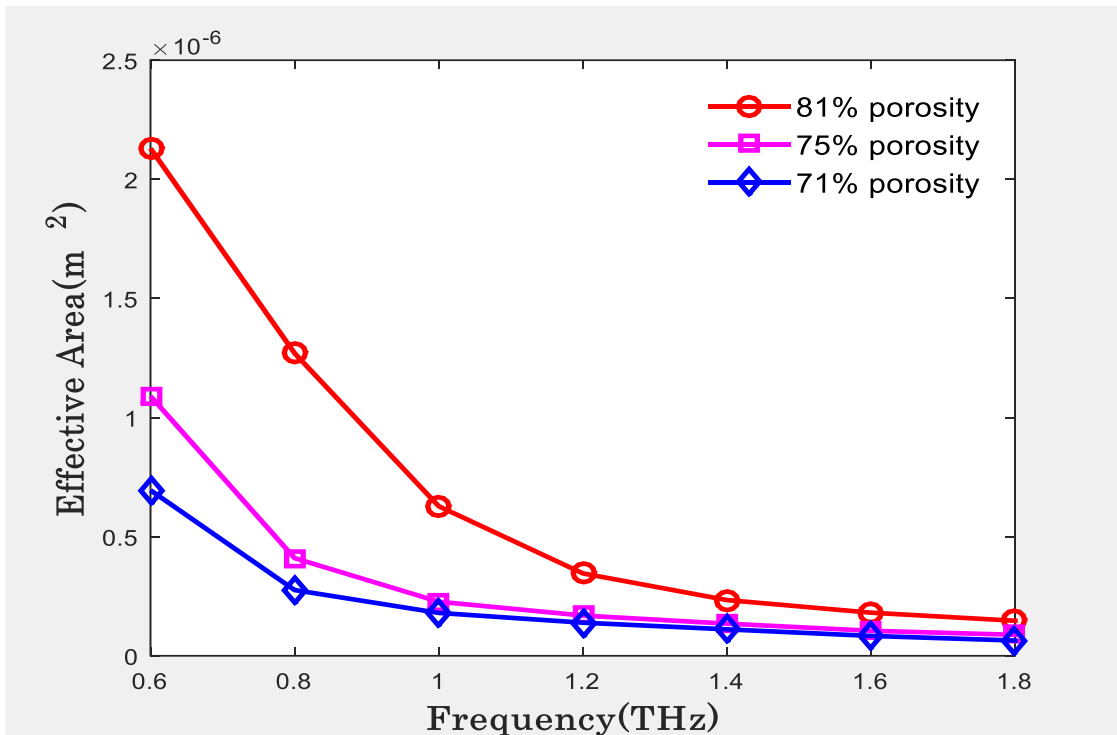
Figure 4.6: Response of effective area with respect to frequency at different porosity.

Confinement loss is shown in Figure 4.4 as a function of frequency. It is found that the confinement loss of the proposed PCF is 0.008 cm^{-1} at optimum 1 THz, 300µm core size, low compared to the EML and this value is comparable with that of the previously reported PCF [101-104].

Power fraction in the core section of the proposed fiber as a function of frequency at different porosity is illustrated in Figure 4.5. We observe that the core power fraction increases when frequency increases. Because more mode power propagates through the core area with increment of frequency while the core power fraction is inversely proportional to the porosity. When we decrease the porosity from 81% to 71% we see the maximum core power fraction reduces to 50.47% at 1THz frequency.

The response of effective area for increment of frequency for 71%, 75% and 81 % core porosity at optimum core length of 300µm is illustrated in Figure 4.6. We observe at optimum core side length of 300µm the effective area decreases with the increment of frequency. If the core porosity decreases the effective area also decreases. The reason behind this is the lower value of core porosity restricts the mode power propagation, consequently effective area decreases. At optimum core side length of 300µm, 81% of core porosity and 1THz of frequency the PCF exhibits large effective area of 6.28×10^{-7} m^2.

EML of the presented design with respect to porosity for different frequency is shown in Figure 4.7. It is evident that when we increase the porosity the EML decreases but when frequency increases the EML behaves in the opposite manner. We evaluate here the EML for a porosity range from 71% to 81%. For porosity as low as 71%, the EML is maximized. The reason is that when porosity increases, it reduces the volume of background material in the core. On the other hand, the relation between the absorption loss by the material (EML) and frequency is directly proportional at a specific porosity.
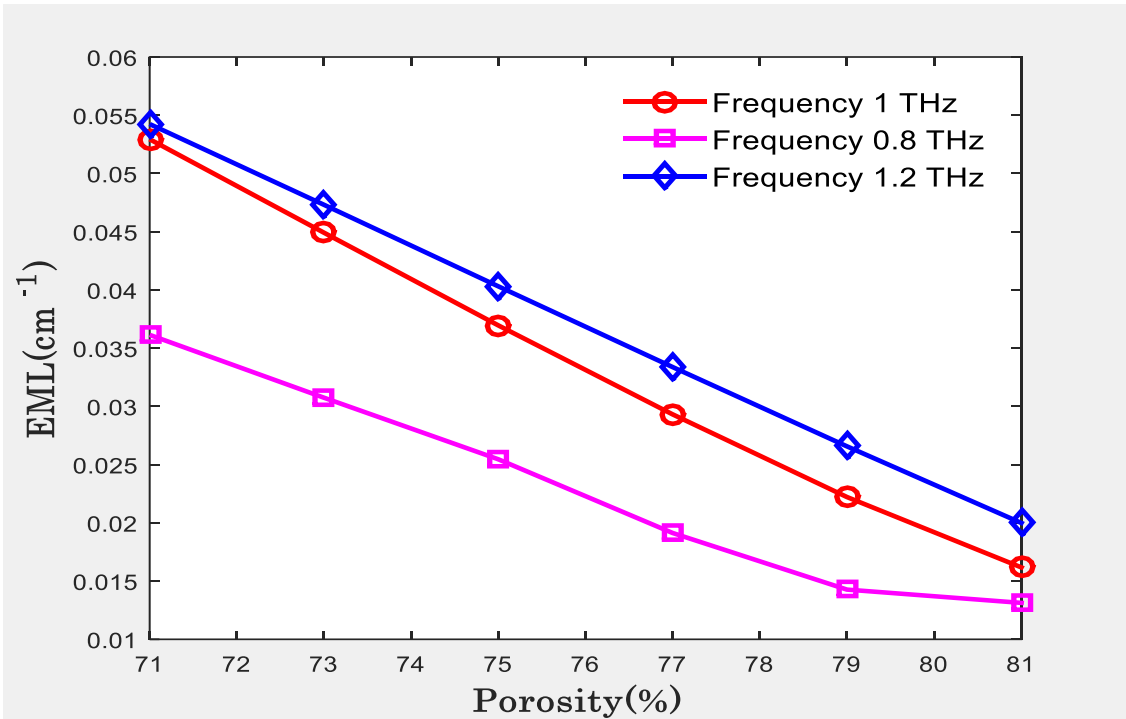
Figure 4.7: EML behavior with respect to porosity at three different frequencies.
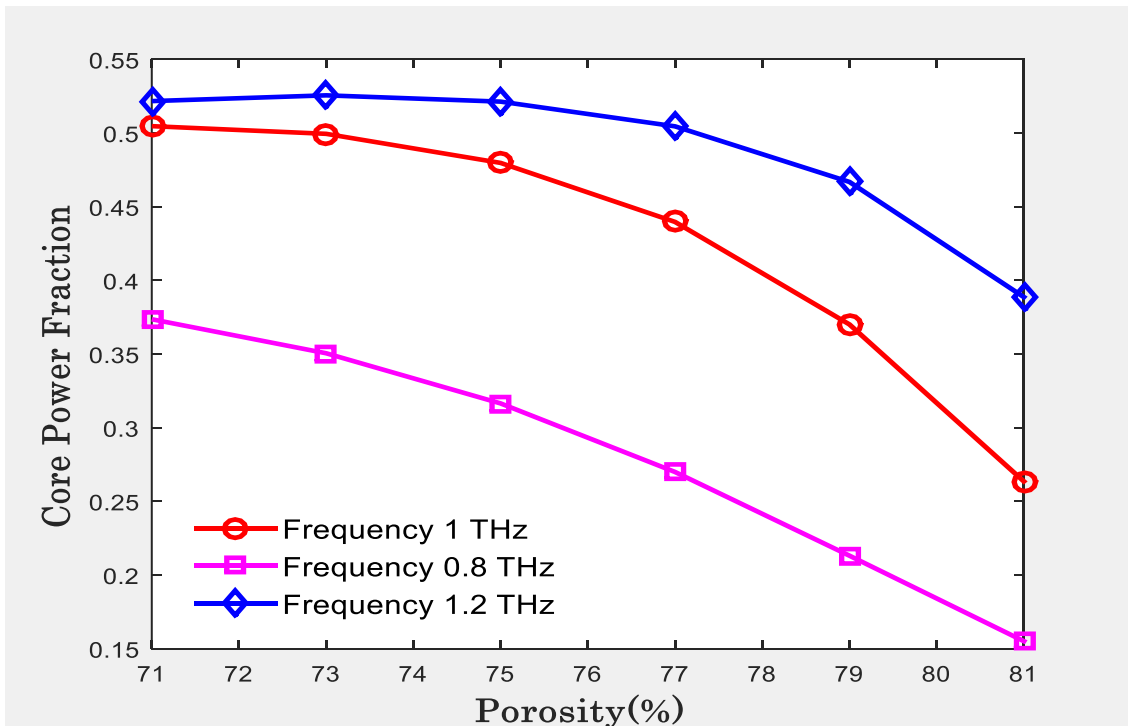
Figure 4.8: Power fraction in core section with respect to porosity at different frequencies.
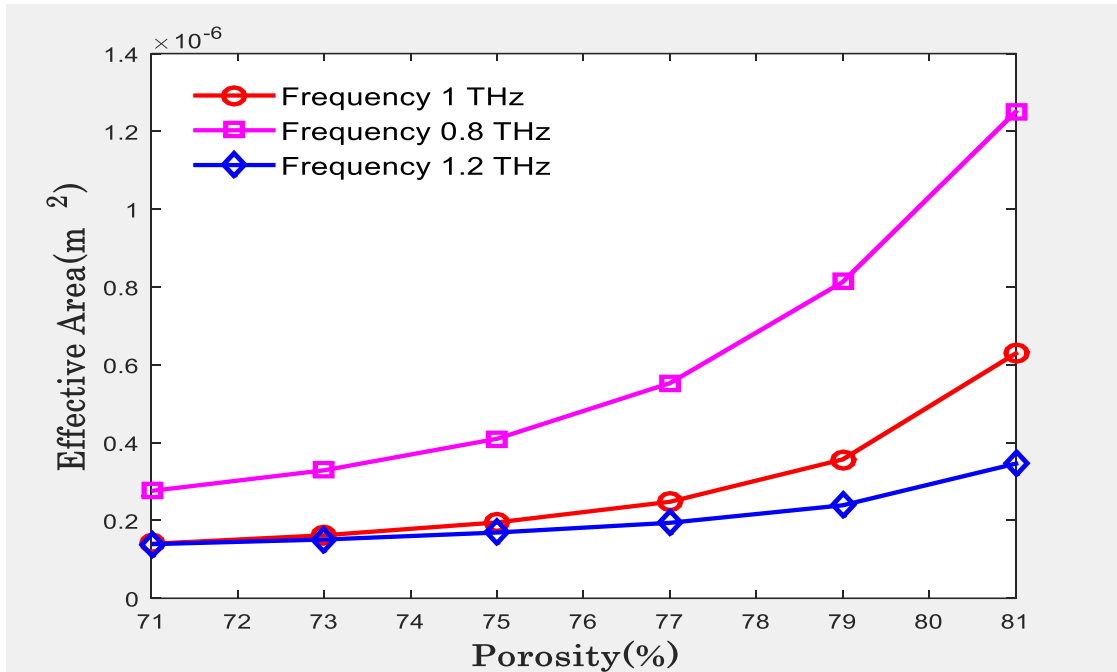
Figure 4.9: Behavior of Effective Area with respect to porosity at three different frequencies.

Performance of core power fraction is another parameter to define an efficient PCF design for THz waveguide. Higher core power fraction is desirable for any PCF design but when porosity decreases the background materials area of core increases, as a result the core power fraction increases. Because of large background area of porous core, the EML is increased. In our design for different porosities core power fraction at different frequency and shown in Figure 4.8. We consider the different frequencies to identify the effects of frequencies on the core power fraction. It is seen that the porosity and core power fraction inversely proportional and the core power fraction is directly proportional to porosity.

How much energy a core can carry indicates the effective area of a PCF without any nonlinear effect. Changing the size of background material, we observe the effect on effective area at 0.8THz, 1 THz and 1.2 THz for different porosities. When we change the frequency, we can see that from Figure 4.9 when frequency increases with respect to porosity the effective area decreases. The lowest frequency gives the better values of effective area for different porosities.

A simple air core based 45^0 rotational square lattice PCF design with extremely low effective material loss 0.016 cm^{-1} at 1THz operating frequency is presented in this work. Moreover, around 40% average core power fractions is achieved in the range of frequency (0.6 to 1.8) THz with a core power fraction of 58.88%. In addition, for different porosities we observed the effect on EML, core power fraction and effective area. The proposed PCF design is feasible for practical implementation using existing developed fabrication technology (Discussed in Chapter 7). It is expected that the presented novel PCF geometry will be suitable for efficient THz wave guidance considering effective material loss, as well as other parameters.

4.2.2 Square shaped suspended core-cladding structured PCF

Porous core terahertz (THz) waveguide consists of sectored cladding and square core photonic crystal fiber (PCF) is designed with low losses and flattened dispersion. The mode test and others wave guiding properties are evaluated by using finite element method (FEM) and a perfectly matched layer (PML) as a boundary condition. The mode test result of proposed PCF structure shows single mode characteristics. Besides it renders extremely low effective material loss of 0.0257 cm^{-1} and confinement loss of 0.0001 cm^{-1} at 1 THz operating frequency. Additionally, a very flat dispersion is achieved from this proposed PCF structure. The effective area and core power fraction are also studied for efficient THz wave guidance.

4.2.2.1 Geometry Design Guidelines of Proposed PCF

To reduce the EML we designed a PC-PCF which reduces the light interaction with the background material. A sectored cladding design is presented here, which exhibits the large air area in the cladding section. In the core region a square core with four square shape air fragments is used, which ensure the less light absorption by the background material in the core section. The guided dry air can be considered as a lossless medium. That's why more air area in the PCF improve the efficiency of the fiber. Comsol V5.3a has been used to design our proposed waveguide. Schematic cross-sectional view of proposed design is shown in Figure 4.10. In the cladding section, the whole circular cladding is sectored by four (4) rectangles and in the core section the square core is

filled by four square air lattices. Losses are mainly depending on the geometry of PCF and optimum value selection of different parameters such as air hole size, core size, strut size, porosity of the core etc. For optimization the length of the core is selected, $L_{core} = 300\mu m$ and the length of the core air holes (L_1) depend on the core porosity. Core porosity is defined as the ratio of air area in the core region and total core area. Length of air lattice in cladding is denoted by L_2, whose length is 1156μm.
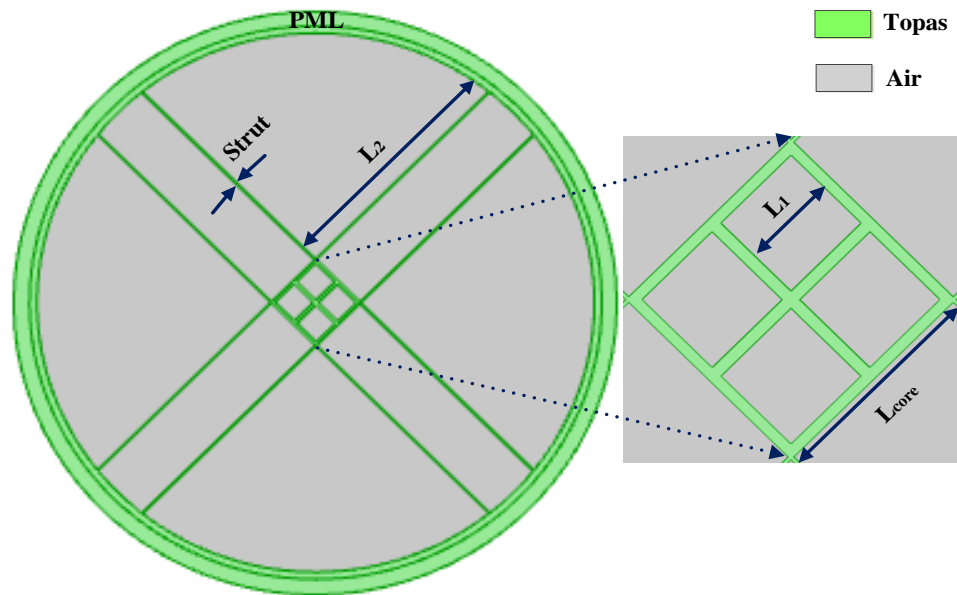
Figure 4.10: Cross section view of proposed PC-PCF with amplified core.

The strut size of the cladding, Strut = 5 µm, lower value of strut may causes overlapping between the cladding air lattices during fabrication. Due to some salient transmission features of Topas, it is considered as a background material in the proposed PCF. A perfectly matched layer (PML) is used in the outer region of the fiber as an antireflecting layer and the size of PML is selected as 10% of the total fiber.

4.2.2.2 Numerical Analysis

To investigate the key properties of presented PCF a commercially available FEM

<div align="center">(a)   (b)   (c)</div>
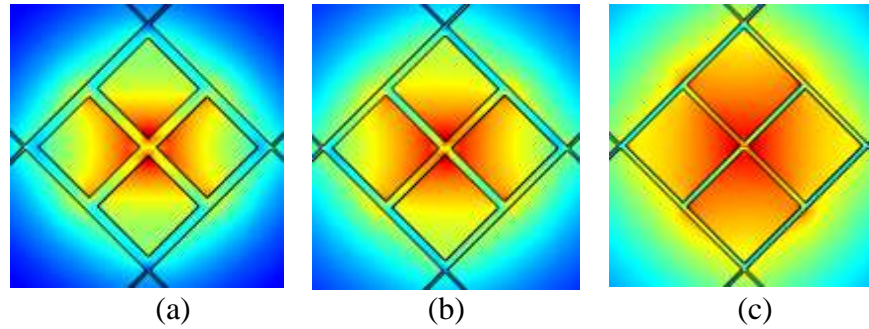
Figure 4.11: Elelctric filed distribution of proposed PCF at 1 THz operating frequency for different porosities (a) 80% porosity (b) 85% porosity (c) 90% porosity.

-based software Comsol vesion 5.3a is used. The main motive of this PCF design is to reduce the losses and achieve flat dispersion. Ensure the accuracy of the PCF fine element size is selected throughout whole simulation. The complete structure consists of 31594 domain elements and 3584 boundary elements. The electromagnetic field distribution of designed PCF is shown in Figure 4.11. This figure confirms that the light is tightly confined and well guided in the core region.

The response of V-parameter of proposed PCF with respect to frequency at optimum design parameters ($L_{core} = 300\mu m$, porosity = 85%) is shown in Figure 4.12. Numerical value of V-parameter ensures that the presented PCF carries single mode fiber characteristics within a large THz frequency range of (0.5-1.8) THz. The maximum value of V-parameter is shown 2.35 at 1.8 THz frequency.

The behaviour of EML and confinement loss as a function frequency for different core length (L_{core}) and different porosity are represented in Figure 4.13(a) and 4.13(b), respectively. It is seen that the EML responses upwardly and the confinement loss behave oppositely with the increment of frequency. This is because, with the increment of frequency the light is tightly confined in the core area which increases the interaction of light with the material that boost up the absorption loss. On the contrary, because of tightened confinement, accuracy of the light improves in the core region which reduces the confinement loss. When the area of background material increases, because of core size increment or porosity decrement
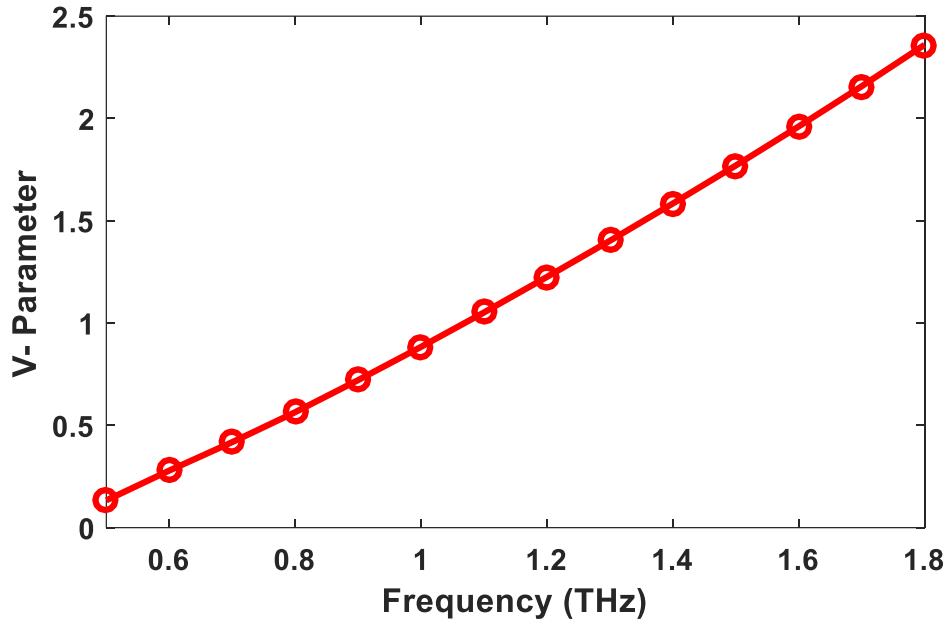
Figure 4.12: Response of V-parameter with respect to frequency at optimum design parameters.
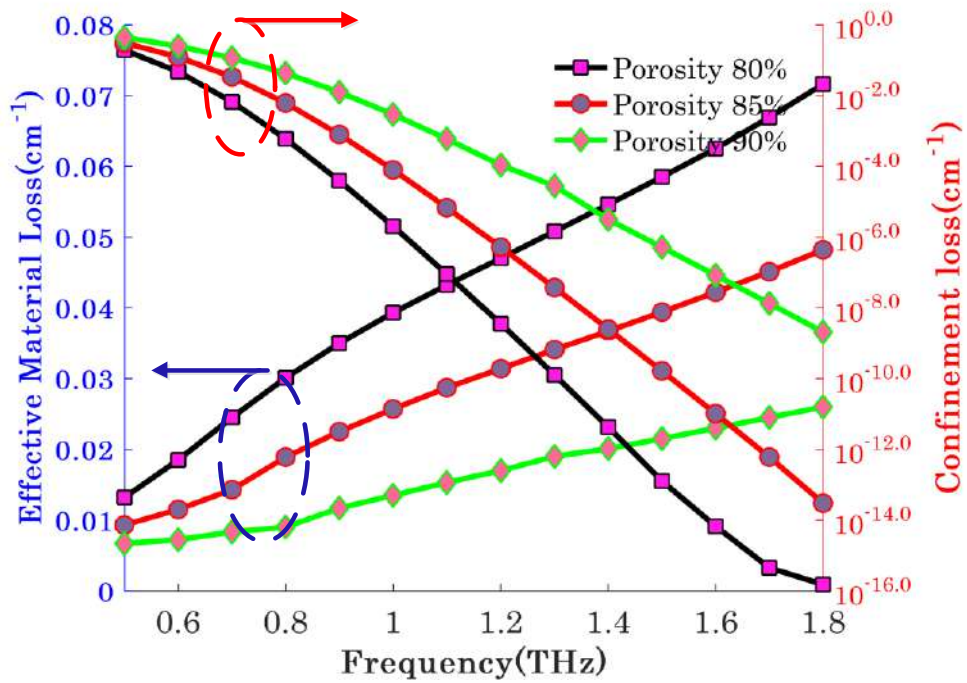
(a)
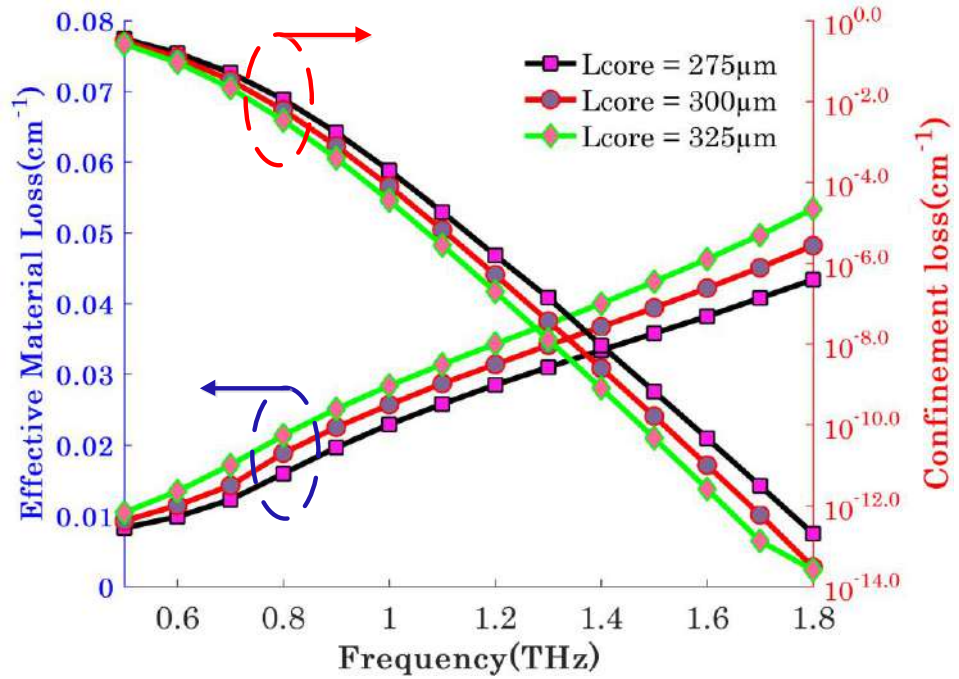
(b)
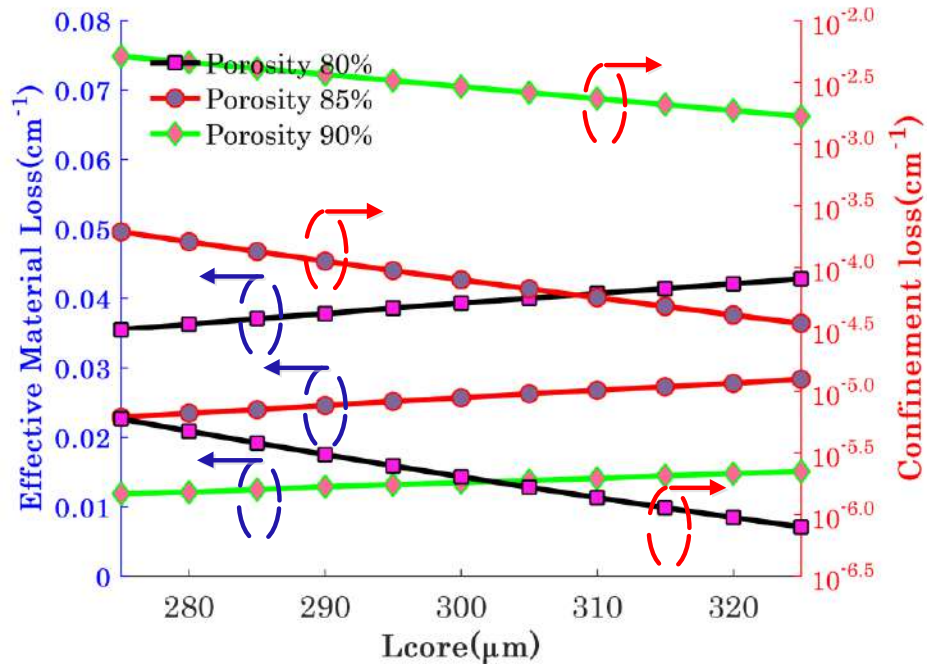
(c)

Figure 4.13: Behaviors of EML and Confinement loss at (a) different core sizes (b) different porosities with respect to frequency, and (c) different porosities with respect to core size.

the EML also increases, since it increases the interaction area of light with the material, reduces confinement loss more, also depicted in Figures 4.13(a) and 4.13(b). At optimum design parameters this presented PCF exhibits a very low EML of 0.0257cm^{-1} and confinement loss of 10^{-4} cm^{-1} at 1THz. The response of EML and confinement loss with frequency for different porosity is also represented in Figure 4.13 (c).

Total loss (EML and confinement loss) of the PCF is shown in Figure 4.14 for different porosity with the increment of frequency. Total loss at optimum value of 0.0258cm^{-1} is noticed in Figure 4.14 and this loss is considerable for a THz wave guide.

For efficient THz wave transmission waveguide dispersion should be minimum as much as possible because higher value of dispersion limits the data rate. Large fluctuations of waveguide dispersion indicate high bit error. The behavior of waveguide dispersion of proposed PCF as a function frequency is delineated in Figure
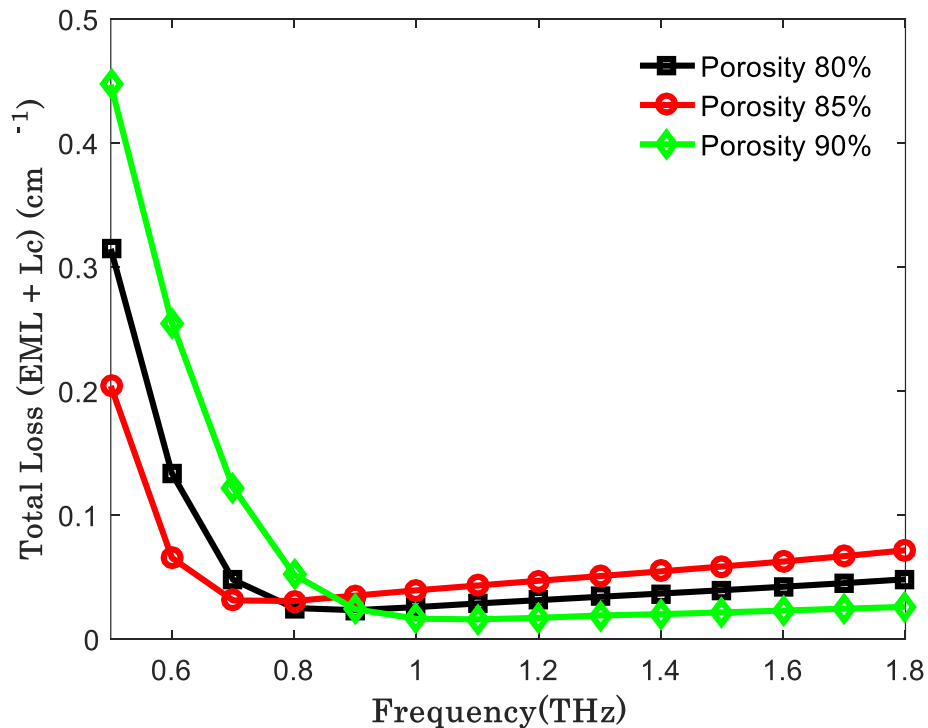
Figure 4.14: Total loss versus frequency at different porosities.
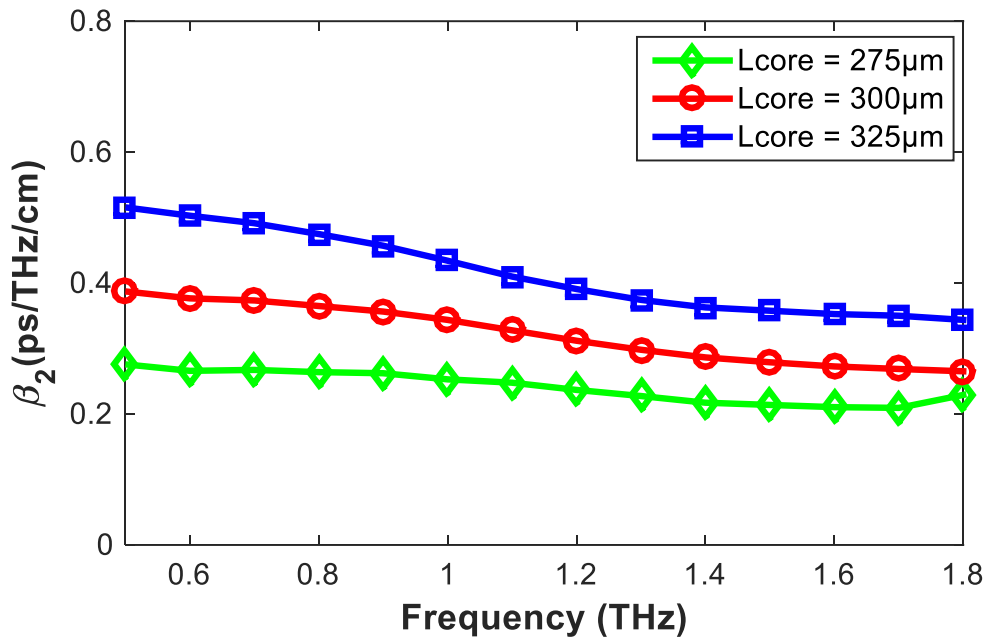
Figure 4.15: Behavior of waveguide dispersion as a function of frequency at different core sizes.
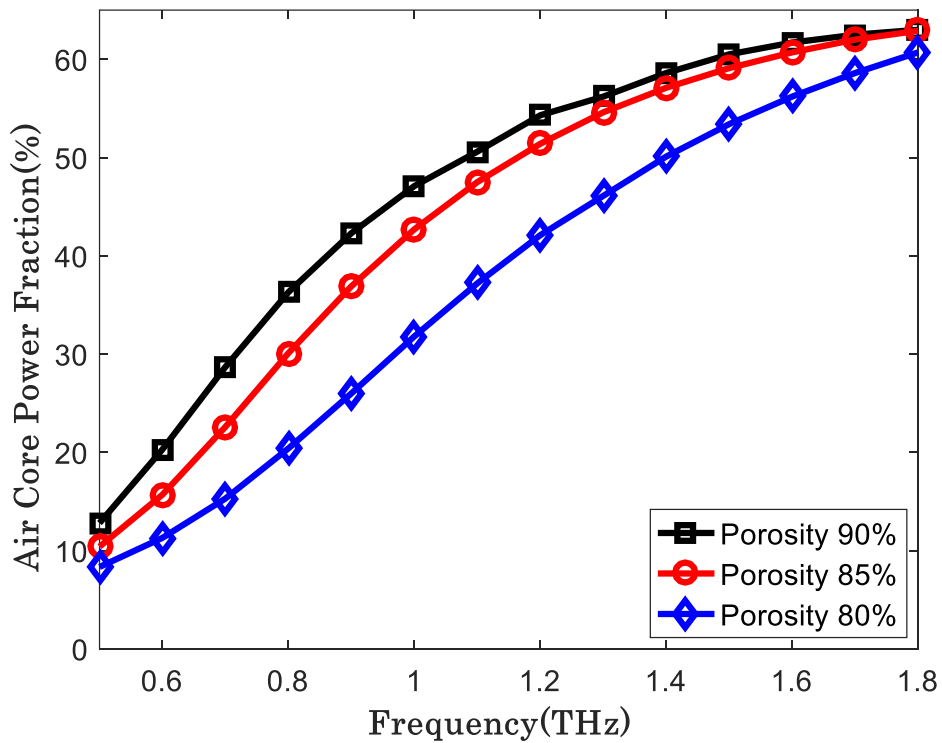
(a)
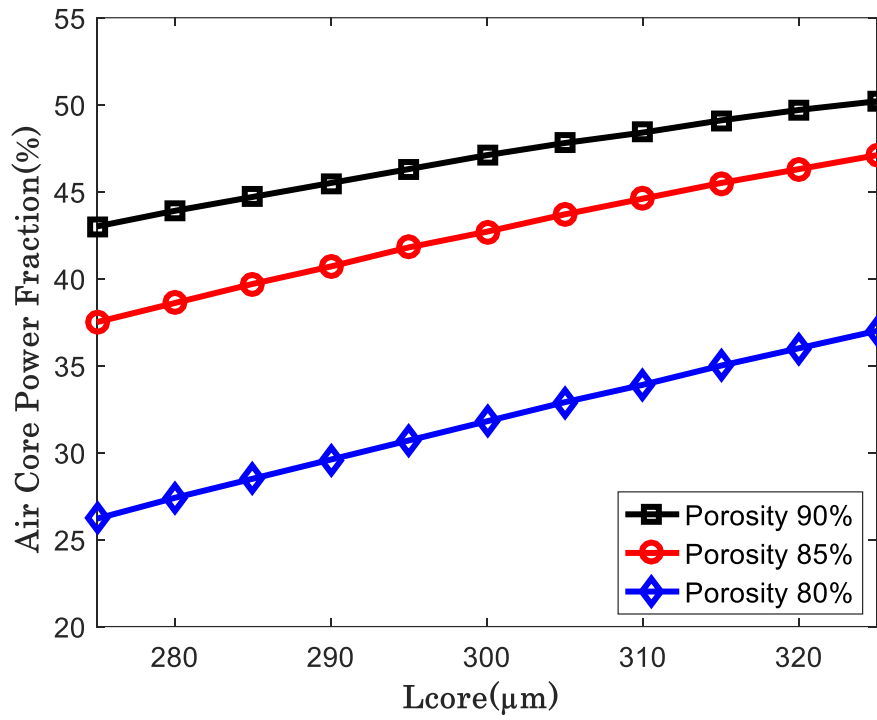
(b)

Figure 4.16: Responses of air core power fraction at different core porosities (a) with respect to frequency, and (b) with respect to core length
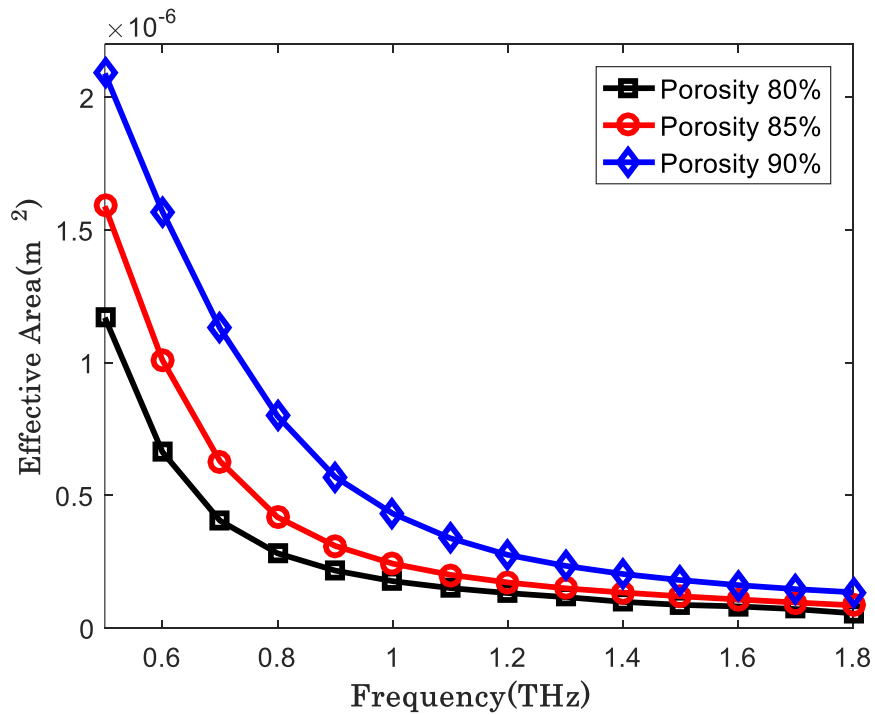
Figure 4.17: Effective area as a function of frequency at different porosities.

4.15. Note that the waveguide dispersion of suggested PCF is under 0.4 (ps/THz/cm) in the frequency (0.6-1.8) THz and the fluctuation of waveguide dispersion is ±0.05, which is better than the previously accepted design in renowned journals [105, 26] .

The responses of air core power fraction with respect to frequency and core length for different core porosity are shown in Figures 4.16(a) and 4.16(b) respectively. Air core power fraction is an incremental fraction with the increment of frequency, the reason behind that higher value of frequency tightened the confinement, as a result more power propagates through the air lattices of the core. When air lattices size is increased because of core length increment or porosity increment, the absorption of mode power by the air core also increases which boost up the air core power fraction, as shown in Figure 4.16(a) and 4.16(b). It is seen that from the proposed PCF can carry 63.6% of total power by the air core only.

The modal effective area as a function of frequency at different porosity is depicted in Figure 4.17. This figure represents that higher value of frequency scales down the effective area. This is because when frequency increases the light is closely confined in the core thus reducing the effective area. When porosity increases the light tends to penetrate in the cladding region that enlarges the effective area (see Figure 4.17). At optimum design parameters the effective area of 2.43×10^{-7} m^2 is achieved.

Besides the wave guiding properties, fabrication of PC-PCF is a difficult task. Presently lots of fabrication techniques are available such as capillary stacking, stack and draw [108], sol-gel [109], extrusion etc. for different shaped PCF fabrication. Recently,

Table 4.2: Comparison with previously published PC-PCF and this proposed PCF

References	f (THz)	EML (cm^{-1})	L$_c$ (cm^{-1})	β_2 (ps/THz/cm)
[26] 2019	1	0.056	0.0023	± 0.10
[39] 2018	1	0.047	9.4×10^{-3}	± 0.35
[105] 2017	1	0.049	-	-
[106] 2017	1	0.040	1.3×10^{-4}	-
[107] 2018	1	0.030	20×10^{-2}	-
This PCF	1	**0.0257**	**10^{-4}**	**± 0.05**

developed 3D printing fabrication technique are able to fabricate any shaped structured PCF [110]. Thus, using existing fabrication techniques our proposed PCF is very much feasible for fabrication.

Table 4.2 shows that, this proposed PC-PCF is comparable with the recently accepted PCF geometry. This table also reveals that this PCF structure achieves tremendous improvement in EML reduction, as well as confinement loss minimization. Moreover, waveguide dispersion fluctuates very shortly.

The key attention of this work is to design and analysis of a well guided single mode THz waveguide with extremely low losses and flat waveguide dispersion. This designed PC-PCF delineated extremely low EML of 0.0257cm^{-1} and confinement loss of 10^{-4} cm^{-1} with a very flat dispersion of ± 0.05 (ps/THz/cm) at 1THz. Moreover, maximum air core power fraction of 63.6%, large effective modal area of 2.43×10^{-7} m^2 and design make the presented PC-PCF suitable for efficient THz wave guidance in the large THz frequency range.

4.2.3 Circular shaped suspended core-cladding structured PCF

A circular sectored core cladding structured photonic crystal fiber (PCF) is presented here, where core and cladding are sectored by few numbers of rectangles. The air fragments of core and cladding are constructed with circular manner that can facilitate the fabrication process. To design the porous core PCF and characterize the properties for THz wave propagation, finite element method based Comsol Multiphysics software version 5.3a is employed. It is shown that the presented design yields an ultra-low effective material loss (EML) of 0.0153cm^{-1} with very flat dispersion of ± 0.010 (ps/THz/cm) at optimum operating frequency of 1THz, outperforming a number of recently reported designs in the literature. Additionally, it renders comparable low confinement loss, higher core power fraction, large effective area and exhibits single-mode fiber (SMF) characteristics.

4.2.3.1 Design Methodology

Figure 4.18 delineates the widened end face view of the PCF with the magnification of the core region. The geometrical structure of the PCF is also distinctly depicted in this figure. The outer region of PCF is called cladding which contains four air fragments. Considering the fabrication simplicity, flattened dispersion and low losses, the four air fragments were kept same geometry, where the radius of each fragment is denoted by R_{clad} (1325 µm) and the two fragments of cladding are separated by S_{clad} which is called strut of cladding with a numerical value of 5 µm. The core region is divided into four equal sectors in a circular manner by two rectangles. Diameter of core is denoted by D_{core} which is selected as optimum of 300µm. The separation between two air fragments of core is denoted by $S_{core,}$ which is 5µm. The size of air lattice in the core depends on the porosity of the core. Porosity is defined as the ratio of the air holes area in the core region and the total core area. Higher value of porosity helps to minimize the losses as well as it minimizes the bulk material
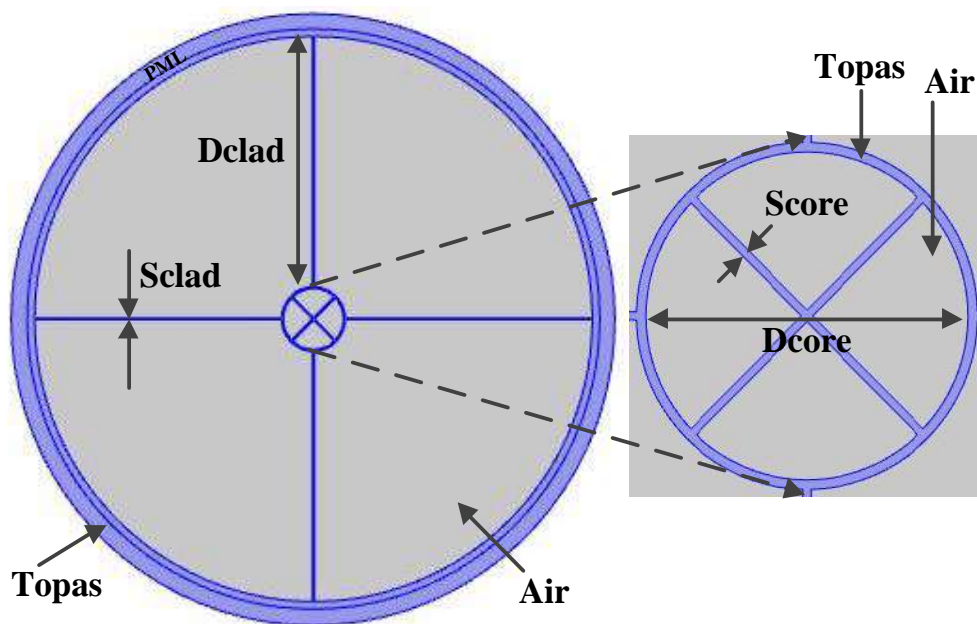
Figure 4.18. Ends face view of proposed PCF with magnification of core.

requirements. However, to maintain the fabrication tolerance, porosity should be kept at an optimum level which helps to avoid overlapping between two adjacent air holes during fabrication. Existing sol-gel technique is very much feasible to fabricate circular structure PCF fabrication and this process is capable to fabricate with 87% porosity [110]. In our proposed PCF design we selected strut (S_{core} & S_{clad}) size 5µm and porosity 85% as optimum. In the outer shell a Perfectly Matched Layer (PML) is used as a boundary condition to protect the fiber from unwanted disturbance by the environment. TOPAS is used as a background material since the Topas contains very low material absorption loss with a constant refractive index within a wide range of frequency.

4.2.3.2 Simulation Results and Discussion

For numerical analysis and modelling of electromagnetic wave propagation of proposed THz waveguide a FEM (Finite Element Method) based Comsol software version 5.3a has been used. To ensure the accuracy of the proposed PCF a *fine* element size is maintained throughout the whole simulation. Complete mesh of the PCF structure consists of 24,386 domain elements and 2176 boundary elements with minimum element quality of 52.58%. The light propagation inside the core for different frequency with the variations of core size, as well as for different porosities presented in Figure 4.19. It is seen that the light is well guided inside the core region with tight confinement and the interaction of light in the cladding region is very low.

The response of effective material loss and confinement loss with the increment of frequency for different core diameters and porosities are depicted in Figure 4.20(a) and 4.20(b) accordingly. Figures 4.20 (a) and 4.20 (b) reveals that the EML behaves linearly upward manner with increasing frequency, It is also obvious from the the empirical equation of calculating material absorption loss in terms of operating frequency can be expressed by $\alpha(f) = f^2 + 0.63f - 0.13$ [dB/cm], where, f is the operating frequency.

Figure 4.20(a) and 4.20(b) also exhibit that when diameter of core increases the EML also increases, since with the increase of core diameter the area of background material also increases. As a result the interaction of light with the material inside the core
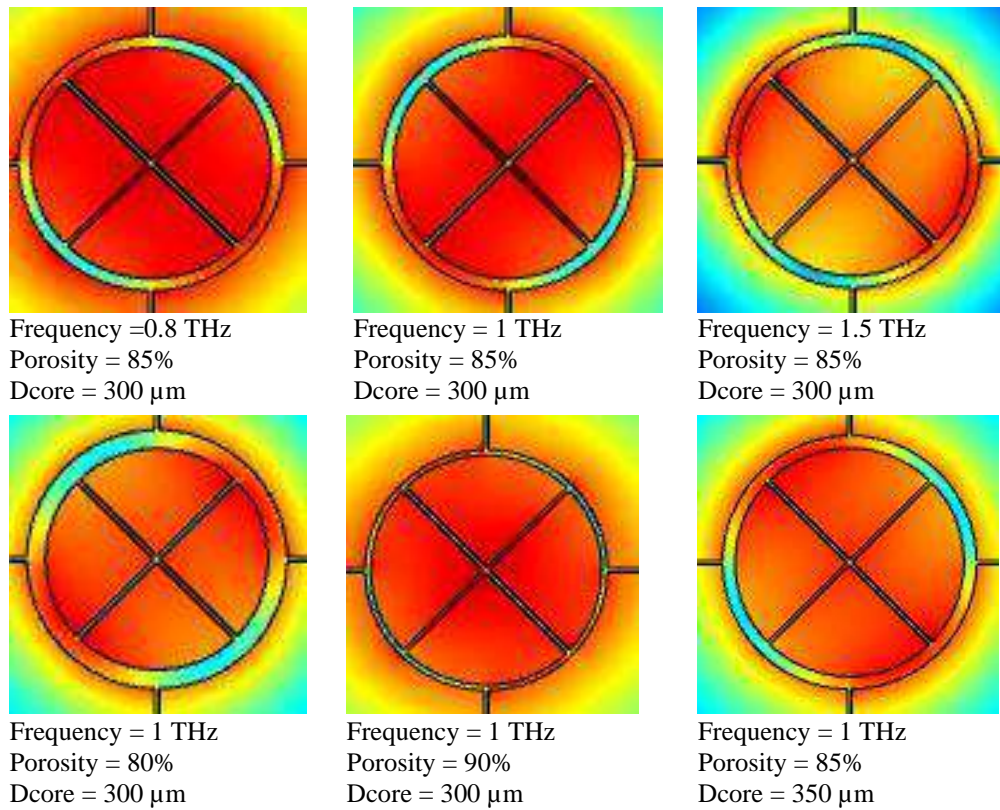
Figure 4.19. Electric field distribution of proposed PCF for different frequency with the variations of porosity and core size.

increases which boost up the EML. Same thing happens when the core porosity changes at downward manner. At optimum parameters, D_{core} = 300μm, Porosity = 85%, frequency = 1 THz, the numerical outcomes of this PC-PCF structure exhibit that EML of 0.0153 cm^{-1} which is very low compared to recently published renowned articles [35-42].

Confinement loss behaves as a decremental function with increment of frequency as seen in Figures 4.20 (a) and 4.20 (b). When frequency increases more light begins towards tightened confinement inside the core; consequently, of confinement loss decreases. If the area of background materials inside the core region increases because of porosity decrement or increment of core diameter, more light initiate to pass through the core region with more tightened confinement, which minimizes the confinement loss. The numerical analysis of reported PCF shows the confinement loss of 0.0014 cm^{-1} at D_{core} = 300μm, Porosity = 85% and frequency = 1 THz, which is comparable with

(a)

(b)

(c)
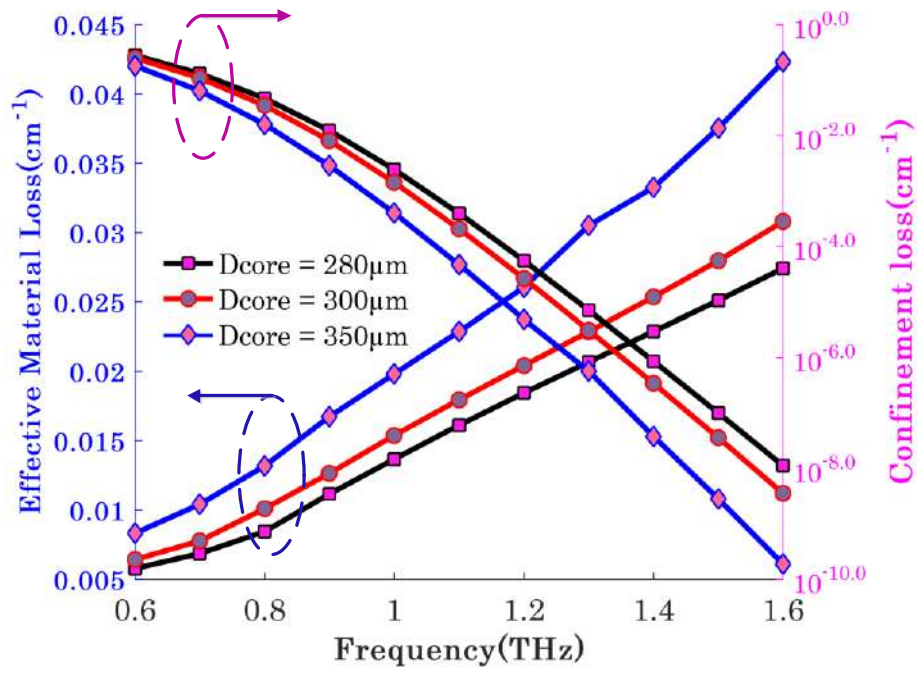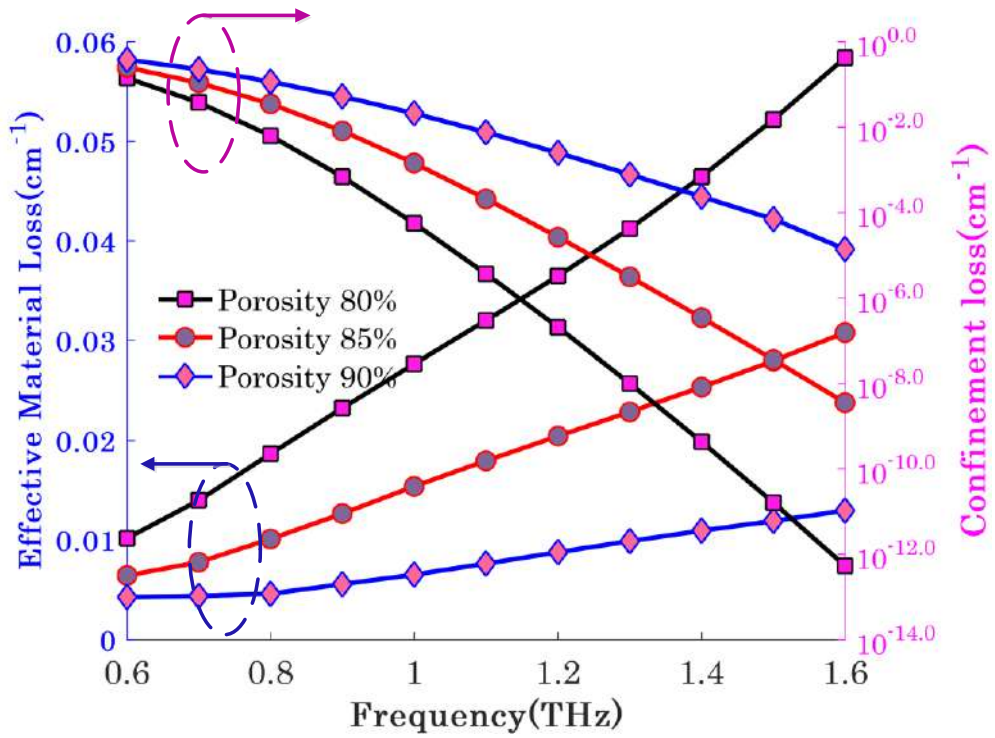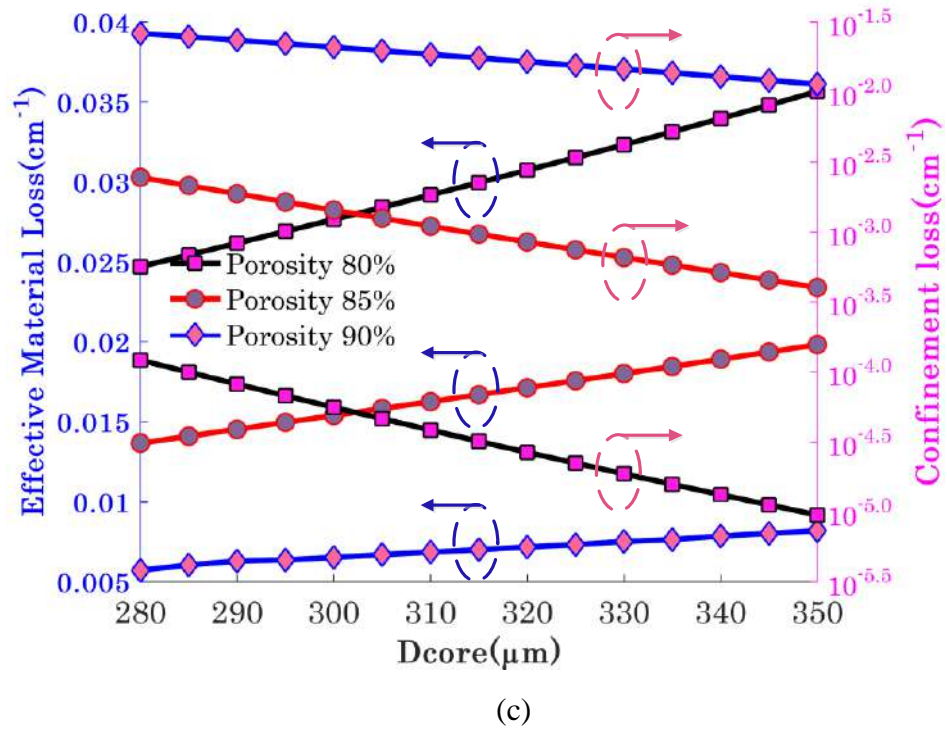
Figure 4.20. Responses of EML and confinement loss as function of (a) frequency at different core size (b) frequency at different porosity and (c) core diameter at different porosity.
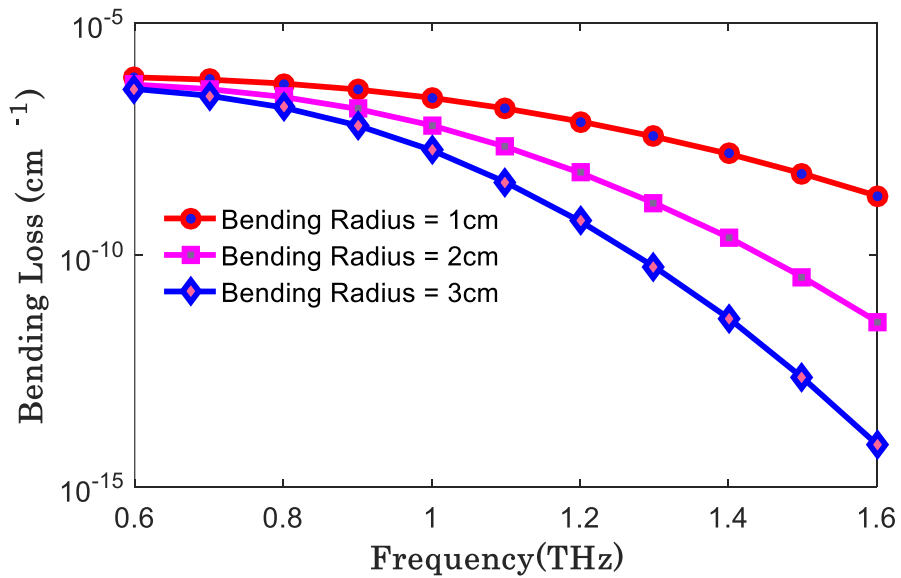
Figure 4.21. Bending loss as function of frequency at optimum design parameters for bending radius = 1cm, 2cm & 3cm.
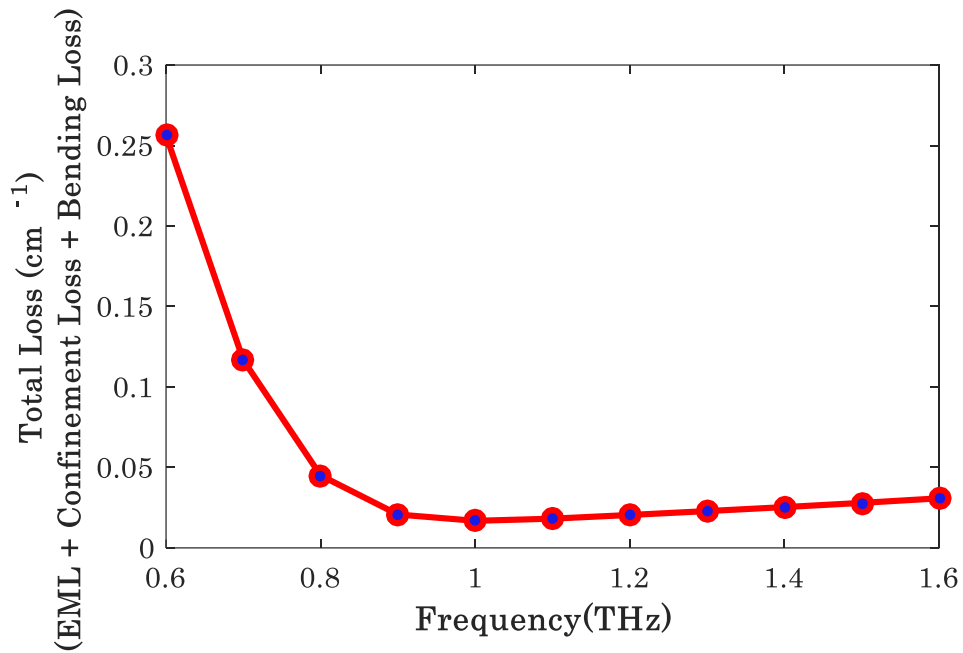
Figure 4.22. Frequency versus total loss at optimum design parameters & R_b = 2cm.

[35-36, 40] wave guiding PCF structure. The repercussion of EML and confinement loss for core diameter variations is depicted in Figure 4.20 (c) considering three types of core porosity.

The scenario of bending loss per centimeter fiber length as a function of frequency is shown in Figure 4.21 for bending radius of R_b = 1cm, 2cm and for 3cm at optimum design parameters. It is observed that the bending loss is very negligible and its responses as downward manner with the increment of frequency. At optimum design parameters this designed PC-PCF exhibits bending loss of 2.5×10^{-7} cm^{-1} at R_b = 1cm, 1.4×10^{-7} cm^{-1} at R_b = 2cm, and 6.2×10^{-8} cm^{-1} at R_b = 3cm, which is very negligible compare to EML.

For total loss calculation we combine three losses (EML, confinement loss and bending loss) at optimum design parameters and its graphically presented in Figure 4.22. These three losses are the main obstacles for practical THz wave transmission. This figure describes that the total loss is less than 0.05cm^{-1} in the range of frequency 0.8 to 1.6

THz and at optimum total loss is only 0.0168cm^{-1} at 1 THz, which is outperforming than the recently published literature [35-42].

The mode power propagation by the air core with respect to frequency for different core diameter is illustrated in right y axis of Figure 4.23. This figure shows that the air core power fraction is an increasing function with increment of frequency. Increment of frequency facilitated tightened confinement which increases the mode power absorption inside the core region by the air holes. Once can also see that core diameter is an incremental function with air core power fraction. When core diameter increases the size of air holes also increases, thus helping to to propagate more power through the air holes that increases the air core power fraction. The same behavior happens when we increase the porosity which is illustrated in Figure 4.24. This proposed design structure is able to propagates maximum 46.42% of mode power by the core air holes within the frequency range of (0.6-1.6) THz.

The behavior of effective area with the increasing frequency is presented in Figure 4.23. It is clear that the effective area is a decreasing function with the incremental changes of frequency because with the increment of frequency the mode power closely confined in the core section which reduce the effective area. The effective area of proposed PCF at 1 THz frequency is $3.5 \times 10^{-7} \, \text{m}^2$, which is comparable with earlier published articles [35]. The behavior of effective area with the enhancement of core diameter is delineated in Figure 4.25. The scenario of this figure describes that, augmentation of porosity increases the effective mode area. This is because when porosity increases the mode power starts to penetrates towards the cladding, as a consequence effective mode power area increases.

Behaviour of waveghuide dispersion of proposed PCF as a function of frequency for different core size is presented in Figure 4.26. It can be seen that at optimum design parameters the wave guide dispersion is impressively flatter within the a large THz ranges (0.6 – 1.6)THz. Tthe reason behind this, the waveguide dispersion depends on the refractive index of core and cladding. Different refractive indexes of core and
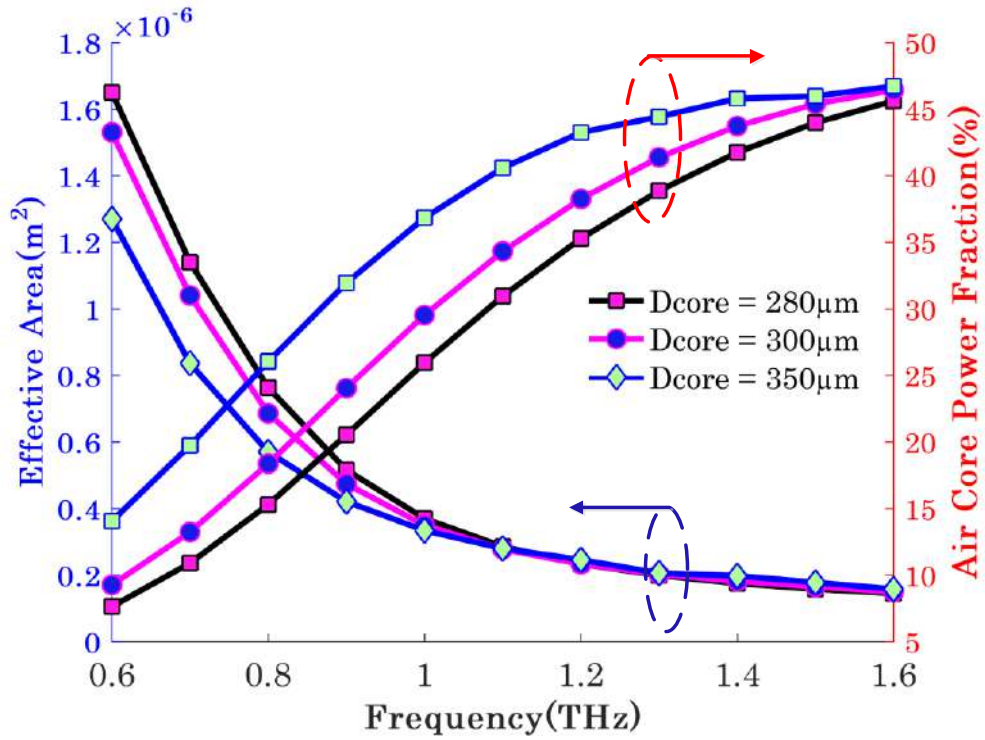
Figure 4.23. Responses of effective area and core power fraction with respect to frequency at different core diameter.
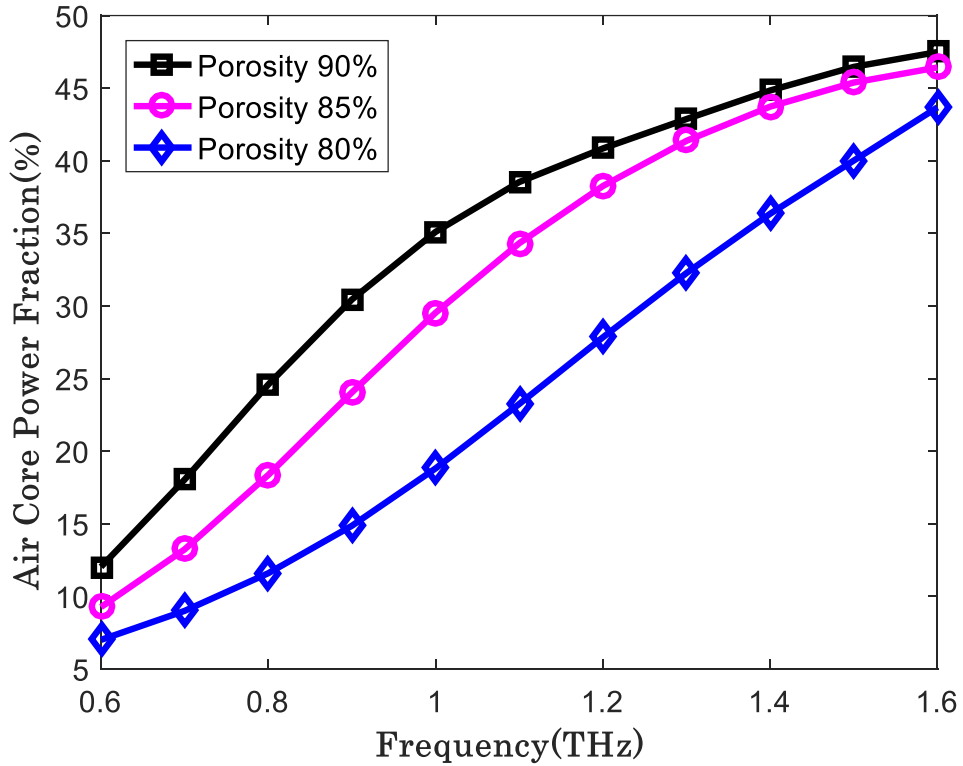
Figure 4.24. Core power fraction versus frequency at different porosity
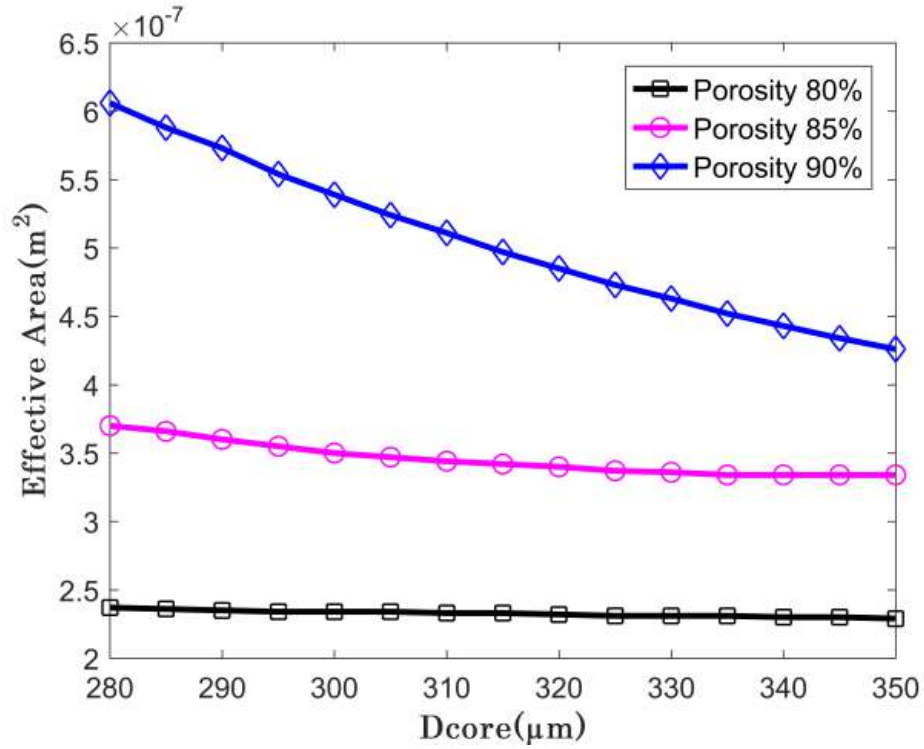
Figure 4.25. Response of effective area with respect to core diameter at different porosity.
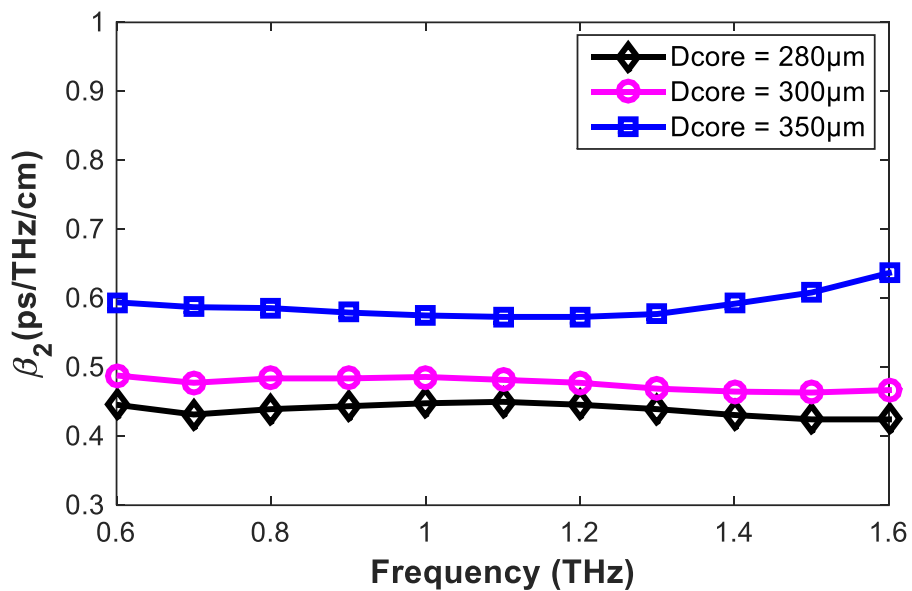
Figure 4.26. Waveguide dispersion of proposed PCF with respect to frequency at different core size.
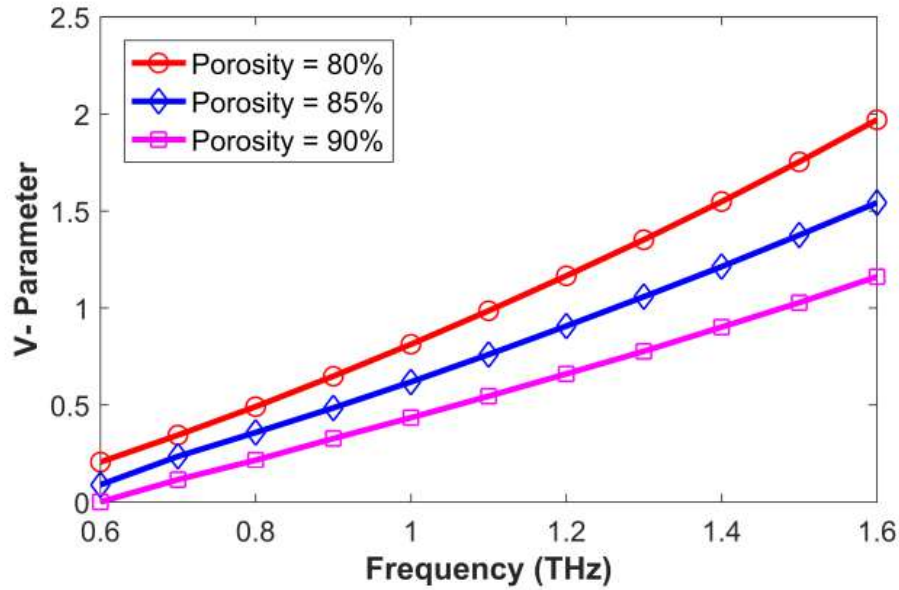
Figure 4.27. Mode test results with respect to frequency at different porosity.

Table 4.3. Comparison with previously published design and this proposed design

Ref.	f (THz)	α_{eff} (cm^{-1})	β_2 (ps/THz/cm)	Desgin Structure	
				Core	Cladding
[35]	1	0.04	-	Circular	Circular
[36]	1	0.035	± 0.6	Rombus	Hexagonal
[37]	1	0.06	± 0.02	Elliptical	Rectangular
[38]	1	0.065	± 0.03	Elliptical	Hexagonal
[39]	1	0.047	± 0.35	Elliptical	Sectored
[40]	1.3	0.029	± 0.06	Hexagonal	Kagome
[41]	1	0.056	-	Elliptical	Kagome
[42]	1	0.0167	-	Decagonal	Spiral
This Article	**1**	**0.0153**	**± 0.01**	**Circular (Sectored)**	**Sectored (Circular Manner)**

cladding enhance the dispersion. In this proposed PCF, air is used in both core and cladding which assisit to flat the dispersion. Moreover, air hole size and distance between the air holes are related to dispersion fluctuations, this was our another key concern of selecting this type of PCF geometry. The numerical value of waveguide

dispersion is very near to zero with a neglegible variations ±0.010 (ps/THz/cm) achieved in this PCF structure, highly compareble with priviously proposed PCFs [35-42].

The mode test result of proposed PCF is shown in Figure 4.27 with respect to frequency. This figure exhibits that within the wide frequency range (0.6 – 1.6)THz the value of V is less than 2.405 for different porosities. Thus this PCF is able to perform as a SMF within the THz range, which is very importnat for long haul THz communication.

Table 4.3 provides a comparison between our proposed PCF structure and previously proposed different PCF structure considering effective material loss, dispersion fluctuations and design structure. Notice that our proposed design achieves significant EML reduction and flat dispersion as compared to previously proposed terahertz waveguides.

The principle aim of this work is to design a porous core photonic crystal fiber with ultra-low EML and near zero flattened dispersion for THz wave propagation, which can be easily fabricable using existing fabrication techniques. In this context we presented here a simple circular structure sectored core cladding geometry and characterized different THz wave guiding properties. Extensive simulation reveals impressive results in effective material loss of 0.0153 cm^{-1} with a very low confinement loss of 0.0014 cm^{-1} at 1 THz frequency. The other properties of the suggested PCF including waveguide dispersion shows an ultra-flattened dispersion variation of ±0.01 (ps/THz/cm). The core power fraction reveals that more than 46% of mode power can propagate through the air core only with very large effective area.

4.3 Summary

For efficient THz waveguiding three (03) unique PCF geometries have been proposed here. At first a PCF structure constructed with 45^{0} rotational square holes in the core and cladding section. This developed PCF rendered better performances than the many of existing works. Still, it seems fabrication of this geometry would be quite complex due to 65 holes needs to implement in the cladding region. Considering the fabrication

complexity, modified the first design and designed a new geometry with suspended cladding structure. This new geometry revealed comparatively better results than the first one. Some additional optical properties namely waveguide dispersion and mode profile are also investigated in these cases and achieved superior performances. For practical implementation circular shaped air holes development is comparatively less complex with current fabrication techniques as well as circular shaped core show better performances than other shapes. Considering the mentioned factors, a circular shaped core with suspended cladding structured PCF has been proposed. This designed PCF shows a noticeable improvement in performances than the previous proposed two designs as well as many of existing works. Considering the practical use of this proposed PCF some additional properties namely bending loss, loss profile with fabrication tolerance have also been evaluated. Overall, all the proposed PCF structures not only provide a comparatively superior performance for THz wave guiding as compared to existing works, but also gives highly satisfactory optical properties in the THz domain.

Besides efficient THz wave guidance, PCF has great potential for sensing applications. Considering this we have also investigated the PCF in sensing application for different analyte sensing cases. Proposed PCFs design and analysis will be discussed in Chapter 5.

Chapter 5

PCF for Analytes Sensing: Design & Analysis

5.1 Introduction

Considering the potential of PCF devices in sensing cases and the scopes of improving performance, PCFs geometry have been proposed and further studied for sensing a number of harmful liquid analytes (cholesterol, methanol, ethanol and benzene), well-known air pollutants (dioxin, sodium cyanide, nitrogen dioxide and hydrogen sulfide), important blood components (RBC, hemoglobin, WBC, plasma, and water), and Albumin in Urine. Considering the several lacks in existing works and scopes of performance improvement by the proper geometry development, different PCF geometries are proposed for necessary analyte detection and the performance of the proposed PCFs are discussed in this Chapter. The design guideline of the proposed PCFs and the performance comparison with the existing works are also discussed in this Chapter.

5.2 Proposed PCFs for Analytes Identification

Considering the fabrication complexity and performances several PCF structures have been designed. Different harmful liquid, toxic gases and biological components have been considered to investigate the performances of the proposed PCF structures. Considering the harmfulness of different liquid analytes such as methanol, ethanol, benzene, etc., well-known air pollutants, for example, dioxin, sodium cyanide, nitrogen dioxide, hydrogen sulfide, etc. and for the necessity of detecting different biological components in blood or urine for the diagnosis of hematologic diseases like blood cholesterol, blood protein, blood components, etc. have considered as targeted analytes in this research. Methanol, ethanol, and benzene are highly pernicious for human health and these toxics are mixed with various liquid foodstuffs and beverages. For example, after consuming methanol, the body breaks it and produces formic acid and formaldehyde. Formic acid can cause serious damage to the central nervous system

resulting in sleepiness, confusion, difficulty in breathing, seizures, or coma. Benzene directly impacts the human body especially the bone marrow for it reduces the healthy blood cells, causing anemia. It is also reported for excessive bleeding and is a risk to the immune system. The presence of low-density lipoprotein (LDL) cholesterol in human blood is risky for brain stroke and heart diseases, as well as food cholesterol has a massive impact on normal health conditions. The importance of detecting the constituents of blood is thus extremely important and often used in diagnosing a variety of diseases and body conditions as well as for their prognosis. Maintaining kidney health is very significant because its performance disturbance creates an overall health disorder and even may lead to death. Regular monitoring of the kidney's functionality is very urgent because there have no visible symptoms of kidney disorders until it is damaged. The presence of albumin is found in the urine, definitely, it is an initial sign of a kidney abnormality that is called albuminuria or proteinuria. So, albumin identification in the urine can be an effective way to trace early kidney infections. Air pollution is another risk factor for human health since it may increase the risk of heart problems, respiratory disorders, allergies, mental disorders, asthma, and other lung complications, among others [111-112]. Efficient sensing mechanisms for detecting harmful/necessary substances in liquid as well as in the environment can be extremely useful to minimize human health risks.

Circular, square, and octagonal shaped hollow core with suspended cladding structure have been considered for PCF development. All the necessary optical properties are evaluated and compared the result with existing works. The design process of proposed PCFs and their performances will be discussed in the following sections.

5.2.1 Square Shaped Hollow Core PCF for Alcohol Detection

Alcoholic agent is excessively harmful for humans. Considering the level of harmfulness, an efficient and flexible alcohol detection method is very essential. In this context, a hollow core photonic crystal fiber (HC-PCF) based optical sensor is designed for detecting alcohol in beverages as well as in any liquid samples, which is constructed with slotted air holes in the cladding section and a square hollow core. The presented PCF structure yields an extremely high sensitivity of 89.85% with ultra-low

confinement loss of 10^{-14} cm^{-1} in THz frequency range of 0.4 to 1.2.

5.2.1.1 Design Methodology of Proposed Sensor

The cross-section view of the designed sensor and the magnification of core region are displayed in Figure 5.1. The proposed PCF geometry contains 20 numbers of slotted air holes in cladding section where hollow core is formed by a square cavity with a length of x μm. The length of 'x' is selected 255 μm as optimum and the 'x' is filled by liquid samples. Distance between two opposite slotted air hole besides the core area is denoted by 'y' and it is chosen 300 µm. The width of the slotted air hole w is 300 µm. The two adjacent air holes are separated by s = 5 µm thickness to maintain the fabrication tolerance. To protect the atmospheric a perfectly matched layer (PML) has been used which is 10% of the total fiber. In our proposed design, we selected topas as a background material because of its lower material absorption loss, constant refractive index in wide range of frequency etc. [113].
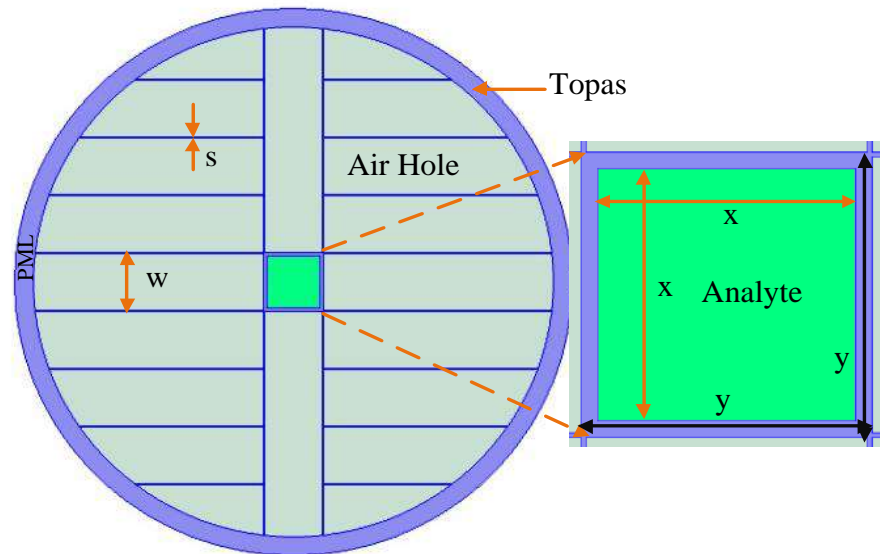
Figure 5.1: Cross section view of proposed of HC-PCF based THz sensor with amplified core.

5.2.1.2 Numerical Analysis

The distribution of electromagnetic field inside the core is presented in Figure 5.2. This
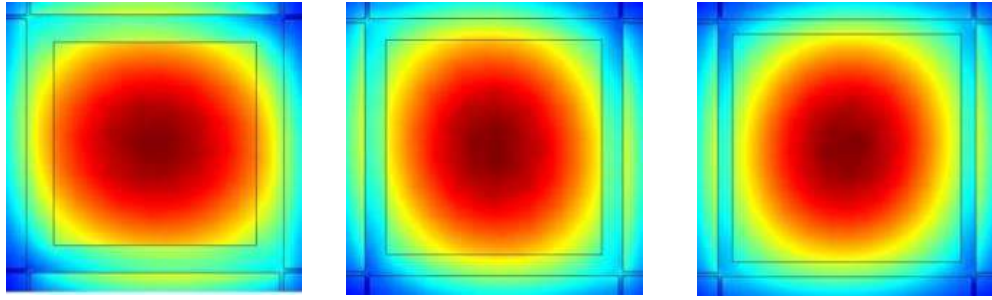
Figure 5.2: Elelctric filed distribution of proposed sensor at 1 THz for different geometrical conditions (a) $x = 0.8 \times y$, $y = 300$ µm, (b) $x = 0.85 \times y$, $y = 300$ µm, (c) $x = 0.9 \times y$, $y = 300$ µm

figure depicted that the electric field distribution is closely and tightly confined inside the core area, on the contrary negligible interaction in cladding section.

Figure 5.3 shows the sensitivity of presented PCF based THz sensor with the increment of frequency for different x and constant y. This figure exhibits that the sensitivity increases with the increment of frequency, the reason behind that when frequency increases the light is tightly confined in the core section consequently interaction of light with the matter also increases as a result the sensitivity raise gradually. The figure also shows that increment of 'x' enhances the sensitivity, the reason is that the expansion of 'x' augments the volume of analytes which increases the light interaction with the matter.

Operating frequency 1.2 THz has been considered optimum because at this frequency ethanol has a great absorbance potential [114]. At this frequency the proposed PCF shows 89.85% sensitivity in alcohol detection which better than the previously proposed PCF based alcohol sensor [52, 115-118]. The scenario of sensitivity as a function of frequency at variable x and y is depicted in Figure 5.4. At lower x, y the light tends to penetrates in the cladding region, as a consequence of sensitivity decline.

The behaviours of EML and confinement loss are displayed in figures 5.5, 5.6 and 5.7. It is clearly seen that from these figures the EML and confinement loss both going down for increment of frequency, the reason of such behaviour is that the light is more tightly
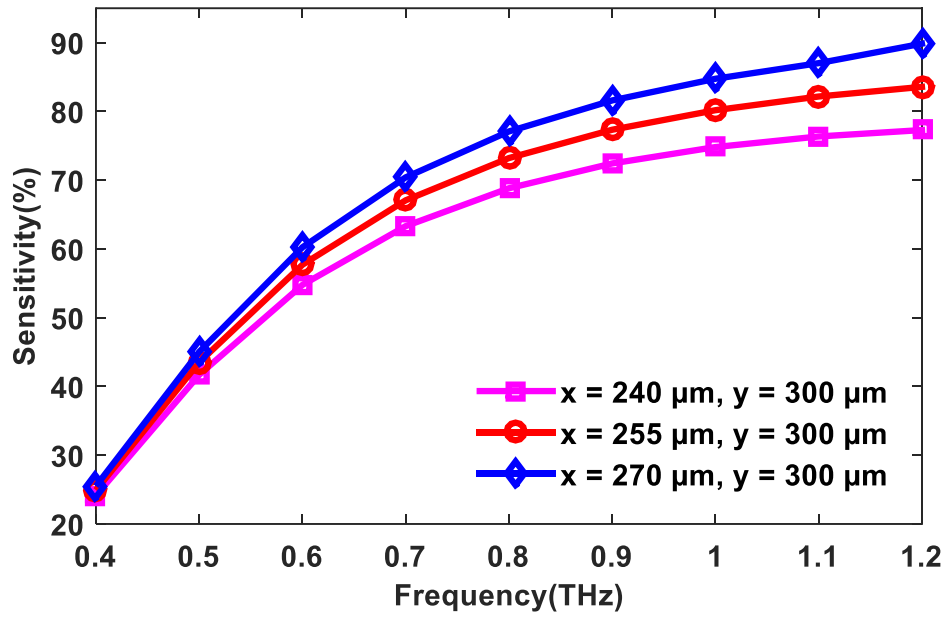
Figure 5.3: Sensitivity of alcohol with respect to frequency at variable x and constant y.
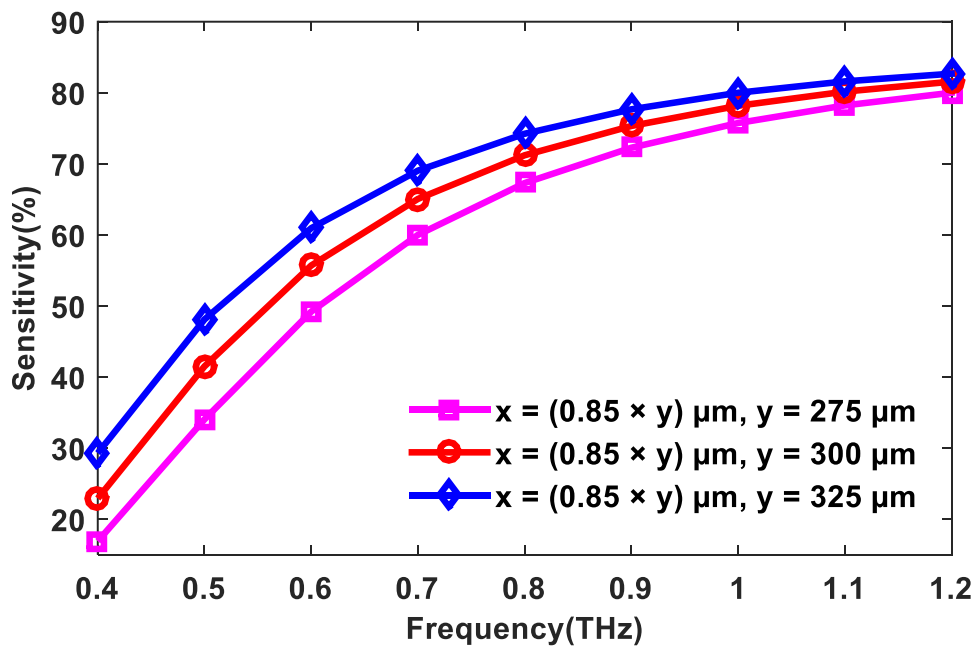
Figure 5.4: Sensitivity as a function of frequency at variable x and y.

79
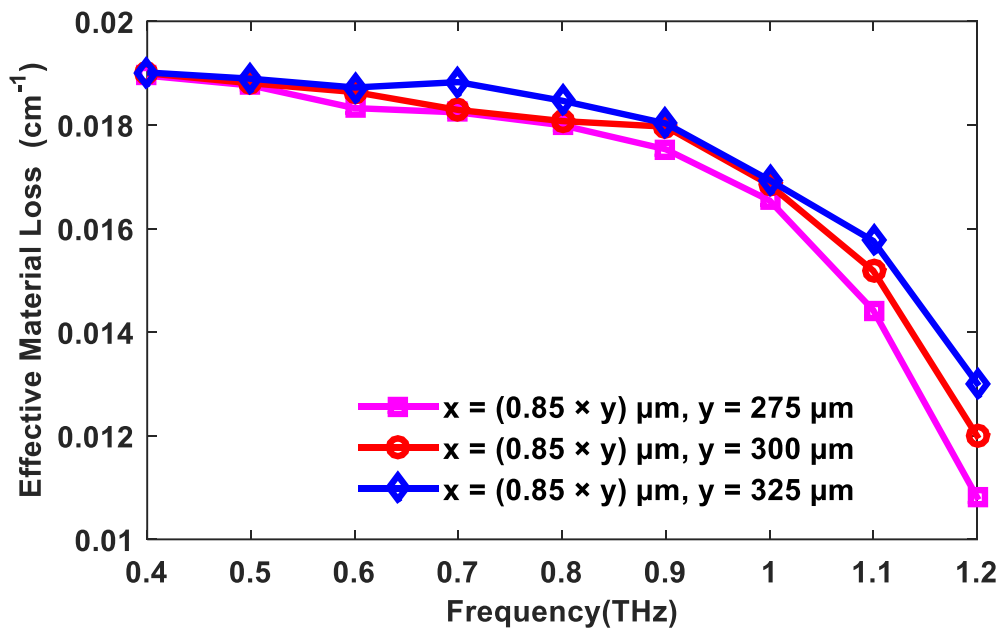
Figure 5.5: Effective material loss vs frequency at variable x and y.
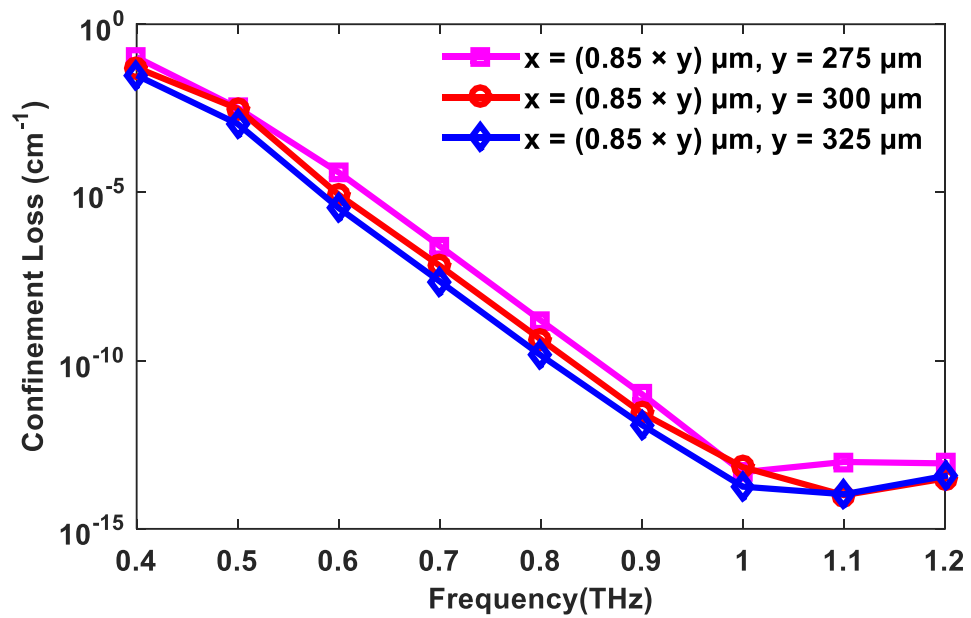
Figure 5.6: Confinement loss vs frequency at variable x and y.
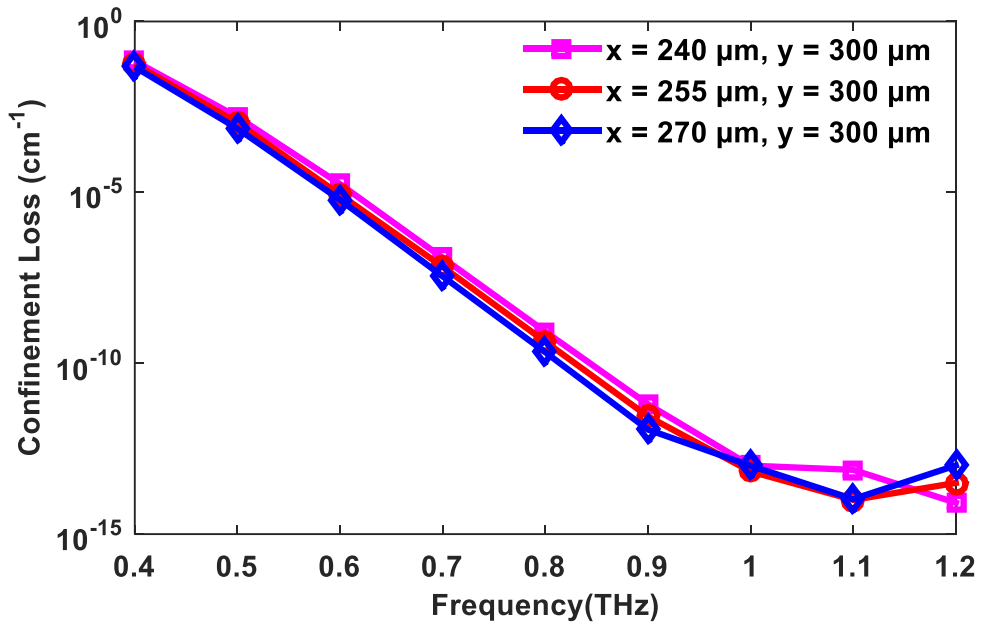
Figure 5.7: Confinement loss vs frequency at variable x and constant y.
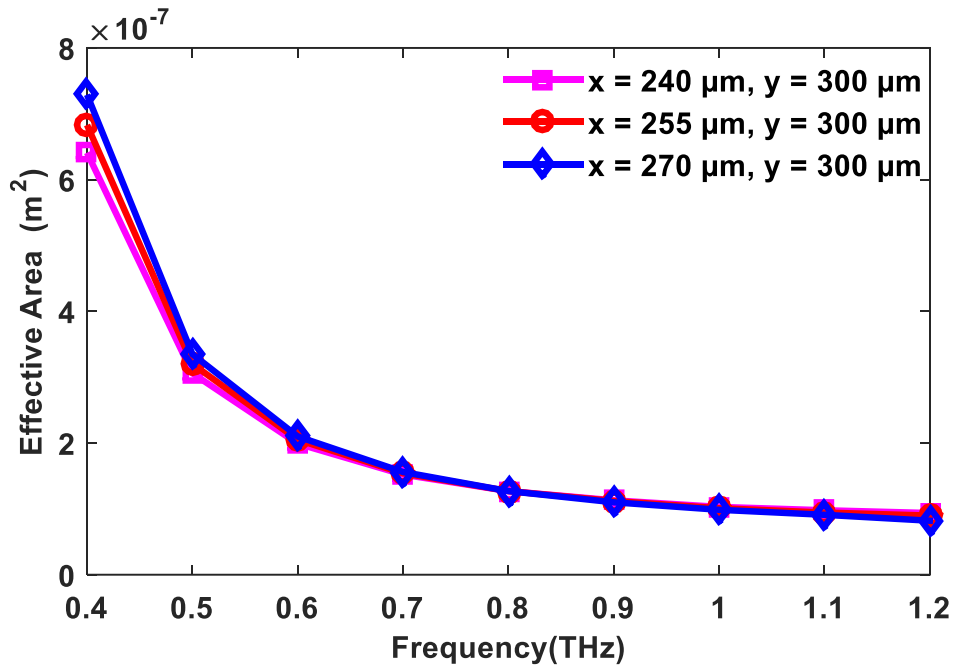
Figure 5.8: Effective Area vs frequency at variable x and constant y.

confined within the core area with the incremental frequency. After a certain frequency the light-matter interaction reaches its maximum, after that the light tends to penetrates to the cladding that increases the confinement loss. At optimum design parameters, f = 1 THz, x = 255 µm and y = 300 µm these figures exhibit EML and confinement loss 0.015 cm^{-1} and 10^{-14} cm^{-1} accordingly.

Effective area is going downward with the incremental changes of frequency, which is depicted in figure 8. The technical reason is that the light is closely confined with higher frequency as results lower effective area at higher frequency. At lower frequency of 0.4 THz the figure shows effective area of $5.9×10^{-7}$ m^2, on the other hand at 1.2 THz frequency shows effective area of $1.01×10^{-7}$ m^2 at x = 255 µm and y = 300 µm.

Table 5.1 describes that, this proposed PCF based THz alcohol detector is comparable with the recently accepted alcohol sensor. This table also reveals that this PCF structure achieved tremendous improvement in alcohol detection, as well as confinement loss minimization.

The main objective of this work is to design and characterize the different properties of PCF based THz sensor for detecting alcohol in beverages as well as in any liquid. In this context, a square hollow core and slotted cladding PCF geometry is designed which exhibit high sensitivity of 89.85% at 1.2 THz. Additionally, its renders ultra-low confinement loss of 10^{-14} cm^{-1} and low effective material loss of 0.008 cm^{-1} whose are comparable with existing PCF based alcohol detection sensor.

Table 5.1: Comparison with previously published PCF based alcohol sensor and this proposed sensor

References	Sensitivity (%)	L_c (cm^{-1})
[52]	68.87	$7.79×10^{-12}$
[115]	49.17	-
[116]	59	-
[117]	64.19	$4×10^{-6}$
[118]	26	-
Proposed Sensor	**89.85**	**10^{-14}**

5.2.2 Octagonal Hollow Core PCF for Cholesterol Detection

Low density lipoprotein (LDL) cholesterol is the leading cause of heart diseases, peripheral artery diseases, and stroke. An accurate, flexible, and efficient detection process is very urgent for identifying the cholesterol. In this context, an octagonal shaped hollow core with eight head star cladding structured photonic crystal fiber (PCF) has been proposed in this paper for cholesterol sensing in liquid analytes (human blood, cocking oil, liquid foods, etc.). The sensing performances of proposed PCF are evaluated through the COMSOL multiphysics software where the finite element method (FEM) has been used as a solver. The numerical investigation of the presented PCF structure exhibits highly sensitive characteristics for cholesterol detection in liquid samples and the proportion is 98.75% at 2.2 THz frequency. It also reveals negligible confinement loss of 3.14×10^{-20} cm^{-1} and low effective material loss of 0.0008 cm^{-1} at the same operating point. Furthermore, other crucial optical properties such as effective area, dispersion, numerical aperture are also discussed in detail.

5.2.2.1 Structural Guidelines of Proposed PCF

For enhancing the sensing capabilities, a hollow core PCF is developed because it contains the greater analyte volume inside the core area compared to a porous core. Alongside, this, hollow core PCF minimizes the requirements of bulk material that helps to reduce the material absorption loss. Geometry design and numerical analysis have been carried out through FEM (finite element method) based COMSOL multiphysics software v. 5.3a. FEM is a very efficient method for measuring electromagnetic field distribution and properties characterization. The completion of the entire process follows several steps namely geometric domain selection, physical properties assignment, boundary and initial conditions setup, mesh, and PDEs solutions for modelling of electromagnetic field distribution and interaction with surrounding components.

The cross-sectional view of proposed PCF geometry and an amplified view of the core are shown in Figure 5.9. The cladding of the proposed PCF is constructed with eight

symmetrical air holes and the core is considered with an octagonal shaped hollow core which is filled by the targeted liquid samples. Topas is selected as background material because of minimum absorption loss and almost fixed refractive index in a large frequency range [118]. Additionally, it has a higher glass temperature transition and it impermeable against environmental effects with inactive behaviour in chemical [88, 87]. The incircle diameter of the core hole is denoted by *y* and the diameter of the core is indicated by *x*. The material width around the core is denoted by *S1*, and the two air lattices in the cladding region are separated by *S2* whose are termed by *strut*. An optimum thickness of *strut* is maintained to avoid fabrication complexity throughout the entire process. An optimum value of *strut* width 7.5 µm is considered for avoiding fabrication complexity, though 6.5 µm *strut* width is tolerable in existing fabrication techniques [121]. The total diameter of the proposed PCF is optimized at 3 mm after the investigation of the prior proposed geometrical measurements.

To analyze the different sensing properties of the presented PCF in a cholesterol sensing application, geometrical parameters are varied in many ways to optimize design conditions. A perfectly matched layer (PML) has been used in the outer region to eliminate environmental effects or radiation introduced by light pulse.
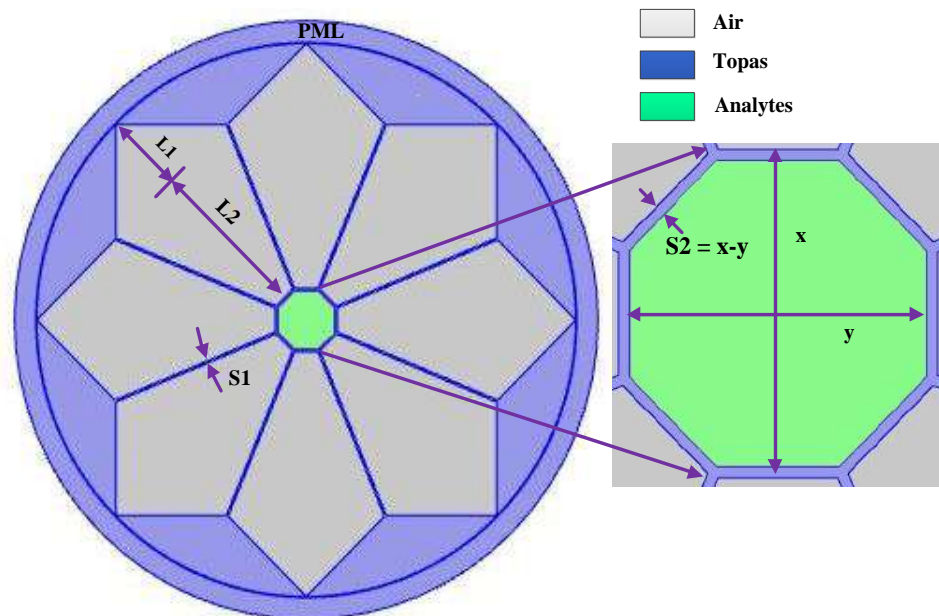
Figure 5.9: End face view of proposed PCF with amplified view of the core.

5.2.2.2 Results and Discussion

For ensuring the highest accuracy, a *fine* element size is maintained in the whole simulation process. Total 65592 domain elements are in the mesh with 5609 boundary elements. The electromagnetic field distribution within the PCF is shown in Figure 5.10 at optimum design conditions for x-polarization mode with an intensity scale. Alongside the interactive condition between the light intensity and the targeted
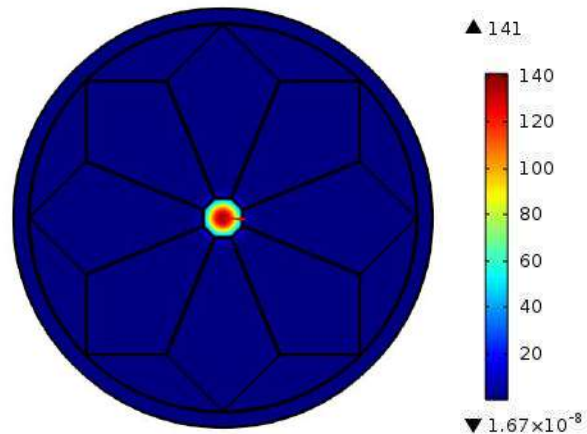
Figure 5.10: Elelctric filed distribution within the PCF at optimum design conditions in x-polarization mode with intensity scale.
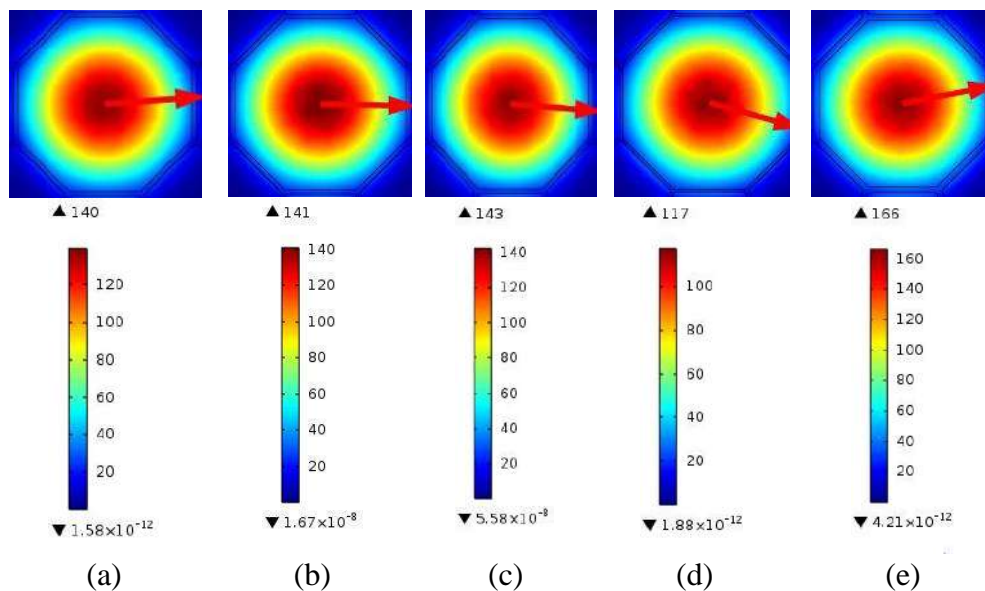
Figure 5.11: Elelctric filed distribution within the core of proposed PCF for different geometrical conditions at 2.2 THz frequency in x-polarization mode with intensity scale (a) x = 280 µm, S1= S2 = 7.5 µm, (b) x = 300 µm, S1= S2= 7.5 µm, (c) x = 320 µm, S1= S2= 7.5 µm, (d) x = 300 µm, S1 = S2 = 5 µm, and (e) x = 300 µm, S1 = S2 = 10

85

analyte in the core region is presented in Figure 5.11 for different geometrical conditions at 2.2 THz frequency. These figures exhibit that the electric field is closely confined in the core area and strongly interacts with the applied analytes, on the contrary, avoidable interaction in the cladding area is noticed. It will be mentioned that at this specific operating frequency of 2.2THz the applied analyte has a strong absorbance potential [121].

Figures 5.12 and 5.13 reveal the sensitivity of the cholesterol identification by the developed THz sensor with the incremental changes of frequency for different geometrical parameters. The scenario of these figures indicates that the sensitivity is increased with the frequency, the reason for such kind of behavior is that when the frequency is increased then light is closely confined inside the core area whereas frequency is directly related to the effective refractive index which helps to enrich the interaction of light and targeted analyte, as a result, sensitivity enhance gradually. Figure 5.12 also indicates that the increment of core size also facilitates to raise sensitivity because the expansion of core size enhances the light-matter interaction area. At optimum design conditions and 2.2 THz operating frequency, this presented PCF exhibits 98.75 % sensitivity in case of cholesterol detection in the liquid sample, which is very much comparable with existing PCF based THz sensors for similar application [20-22, 48-53].

Figure 5.13 exhibits the proportion of sensitivity with respect to frequency for different *strut* widths. This figure represents that large *strut* size slightly decreases the sensitivity, the reason is that higher *strut* size increases the light absorption possibilities by the background material consequently reduces the sensitivity. At the range of *strut* size (5 to 10) µm, this proposed PCF sensor depicts 98.4% to 99% sensitivity at 2.2 THz. It will be noticed that there is no significant effect on sensitivity for changing *strut* size of 2.5 µm than the optimum condition for this hollow core PCF, so for maintaining fabrication tolerance, it is adjustable at any *strut* size within this range.

The behavior of confinement loss is displayed in Figures 5.14 and 5.15 concerning frequency for several design conditions. Both figures exhibit that the confinement loss behaves in a downward manner for incremental changes of frequency. The main reason
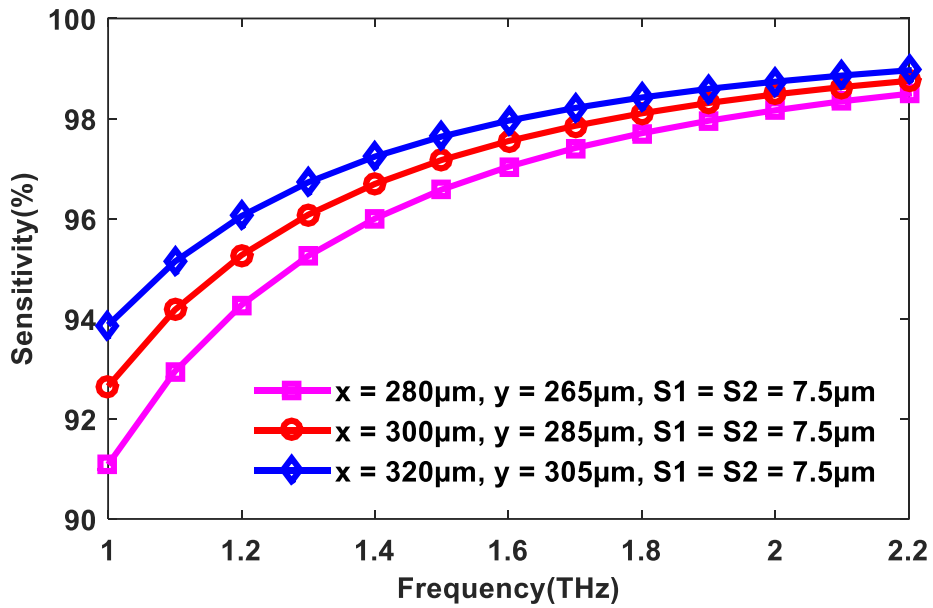
Figure 5.12: Sensitivity with respect to frequency at variable *x* and **y** with fixed *strut.*
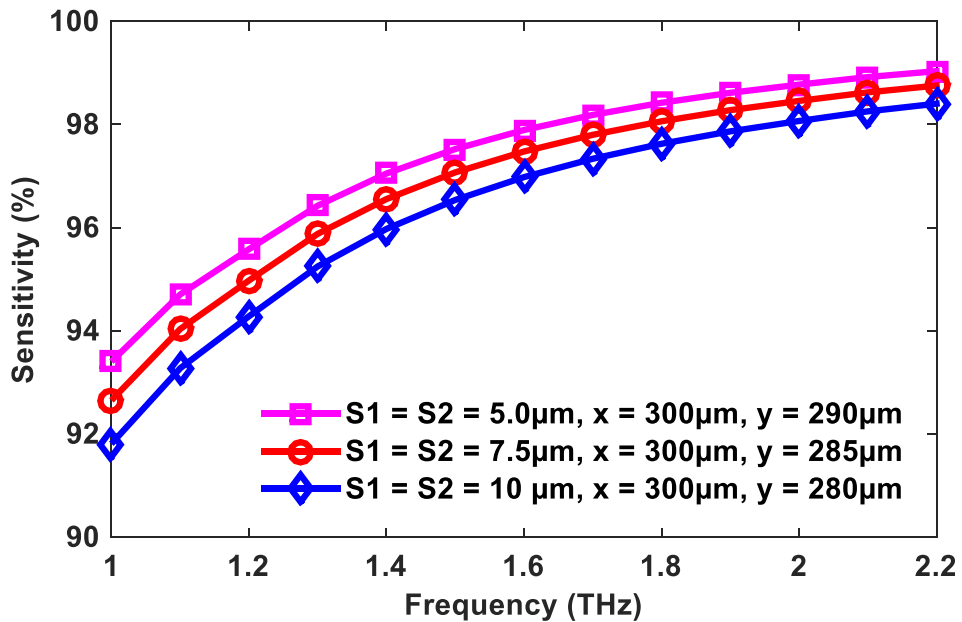
Figure 5.13: Sensitivity as a function of frequency at variable *strut* widths with fixed *x.*

for such type of behavior is that, at a higher frequency, light propagates with more tightened confinement in the core region. Because of the strong interaction experience of presented PCF structure at a higher frequency, confinement loss decreases gradually. Larger core size makes it easier to pass more light through the core which also helps to enhance the interaction area between light and targeted analyte, as a result, confinement loss is minimized more which is also clearly visualized in Figure 5.14. *Strut* size also has an impact on the confinement loss which is presented in Figure 5.15. At a fixed core size, lower *strut* size also helps for the better possible interactive areas between light and applied analytes that minimize the leakage loss. Considering the optimum design situations at 2.2 THz operating points this designed PCF exhibits negligible confinement loss 3.14×10^{-20} cm^{-1} for cholesterol sensing cases, as far as our knowledge which is lower than ever published any PCF based THz sensor for similar applications.

The response of EML is demonstrated in Figures 5.16 and 5.17 as a function of frequency for different geometrical situations. Both figures exhibit that the EML behaves in a downward manner for the augmentation of operating frequency. At higher frequency, the electromagnetic wave travels with higher intensity and compactly confined in the core region which reduces the probability of light material interaction for a hollow core PCF structure, consequently, EML is reduced. Impacts on absorption property by the core size and *strut* size are also visualized in Figures 5.16 and 5.17. At optimal design conditions, this presented PCF geometry reveals very low EML of 8.81 $\times$ 10^{-4} cm^{-1} that is lower than recently published PCF based chemical sensor [49, 52, 20, 22].

Figures 5.18 and 5.19 show the behaviour of the effective mode area of proposed geometry with respect to frequency. The visual representations of these figures indicate that higher frequency reduces the effective area. At higher frequencies, the mode field is strongly localized within the core section, as a result, the effective area decreases. The designed PCF has provided a moderate value of the effective area of 4×10^{-8} m^2 at optimum design condition. The changes of effective area for different geometric situations are also displayed in these figures.
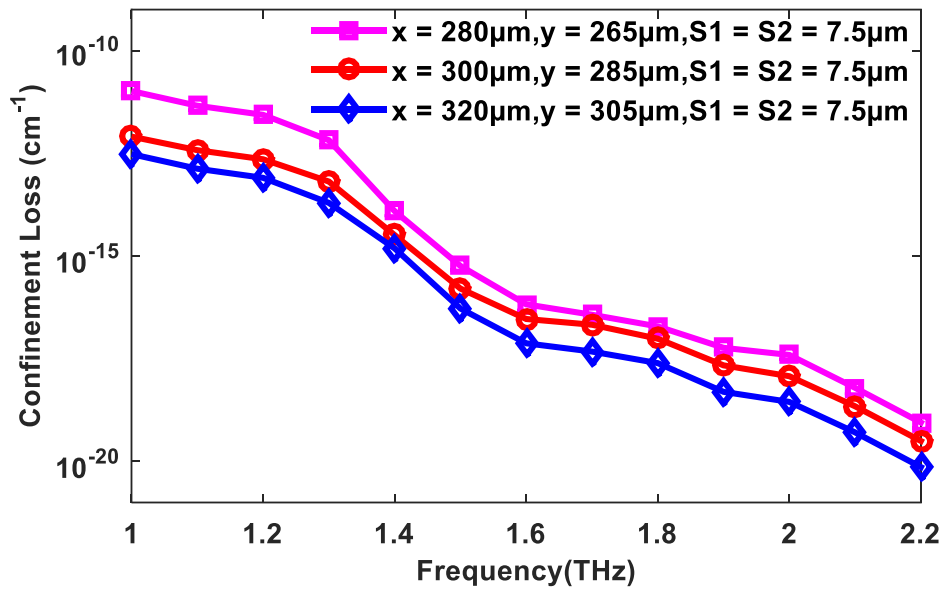
Figure 5.14: Confinement loss versus frequency at variable *x* and *y* with fixed *strut*.
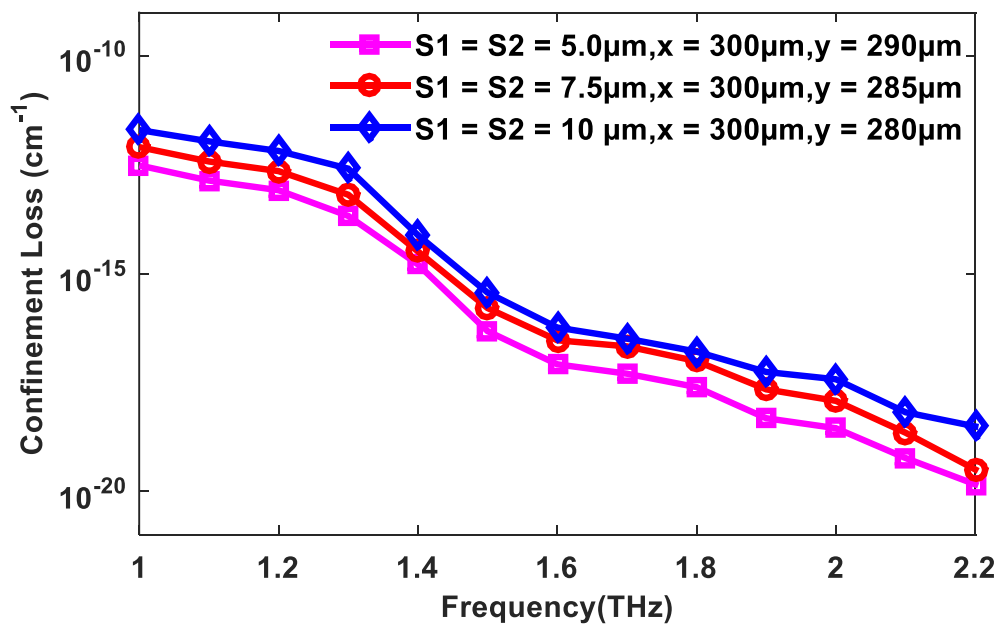
Figure 5.15: Confinement loss versus frequency at variable *strut* widths with fixed *x*.
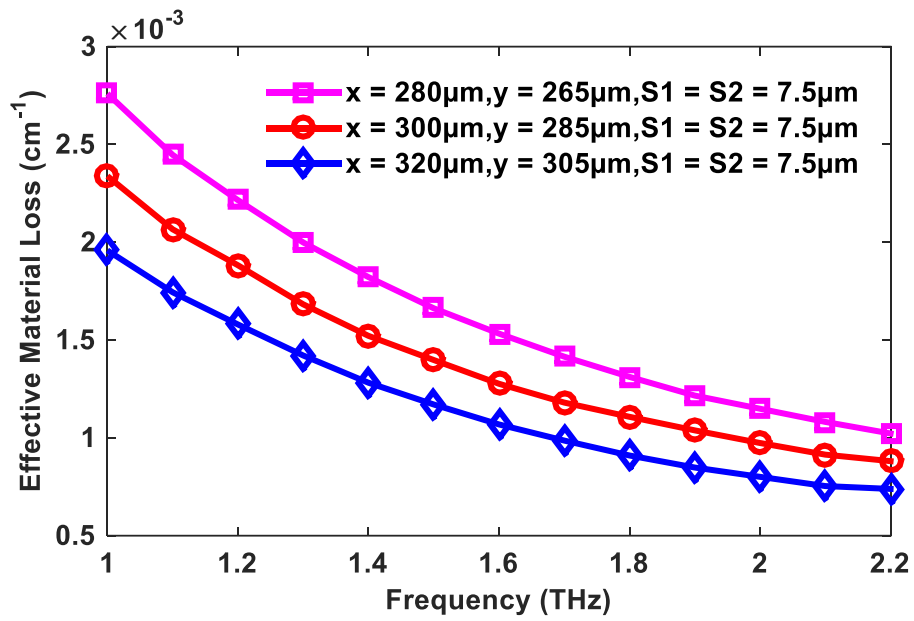
Figure 5.16: Behaviour of EML as a function of frequency at variable *x* and *y* with fixed *strut*.
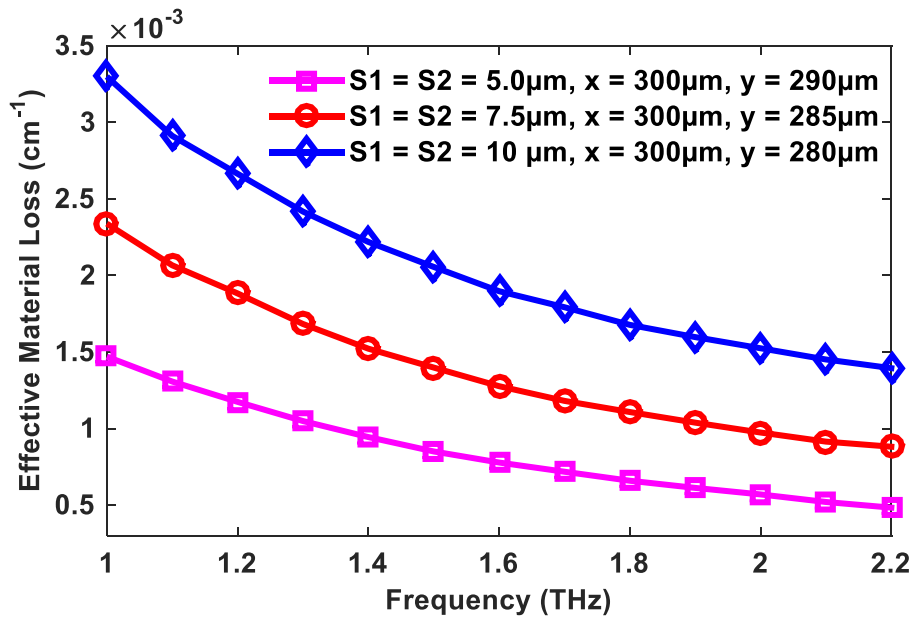
Figure 5.17: Behaviour of EML as a function of frequency at variable *strut* widths with fixed *x*.
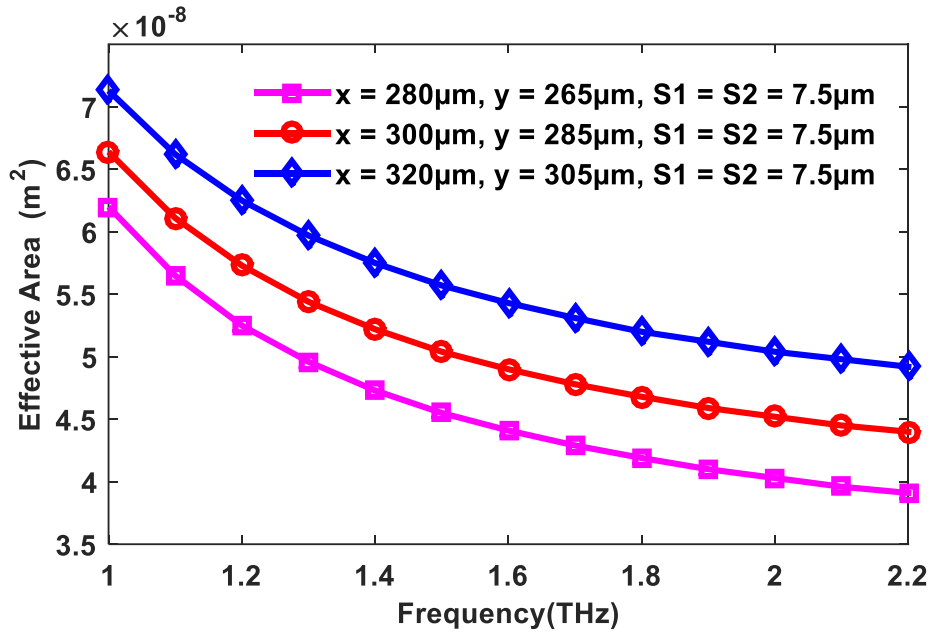
Figure 5.18: Effective area as a function of frequency at variable *x* and *y* with fixed *strut*.
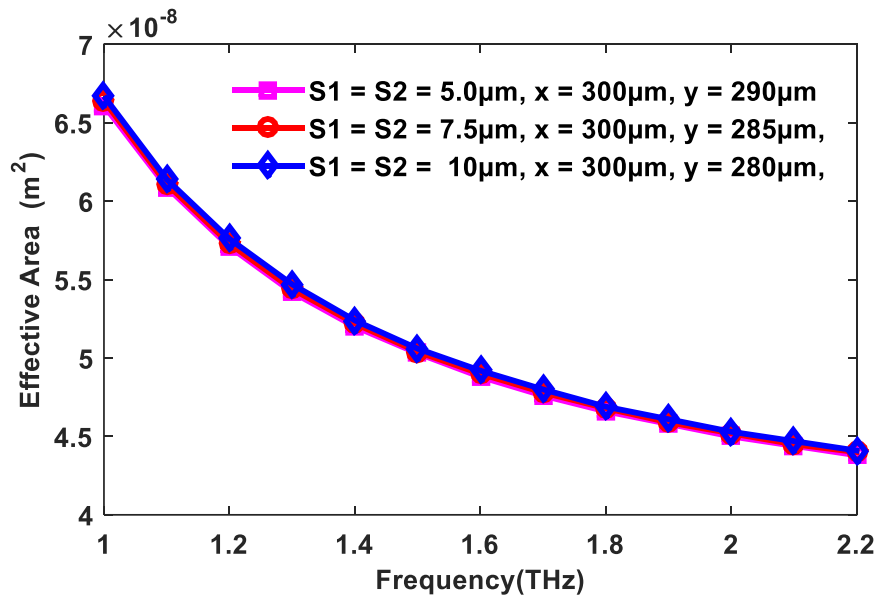
Figure 5.19: Effective area as a function of frequency at variable *strut* widths with fixed *x*.
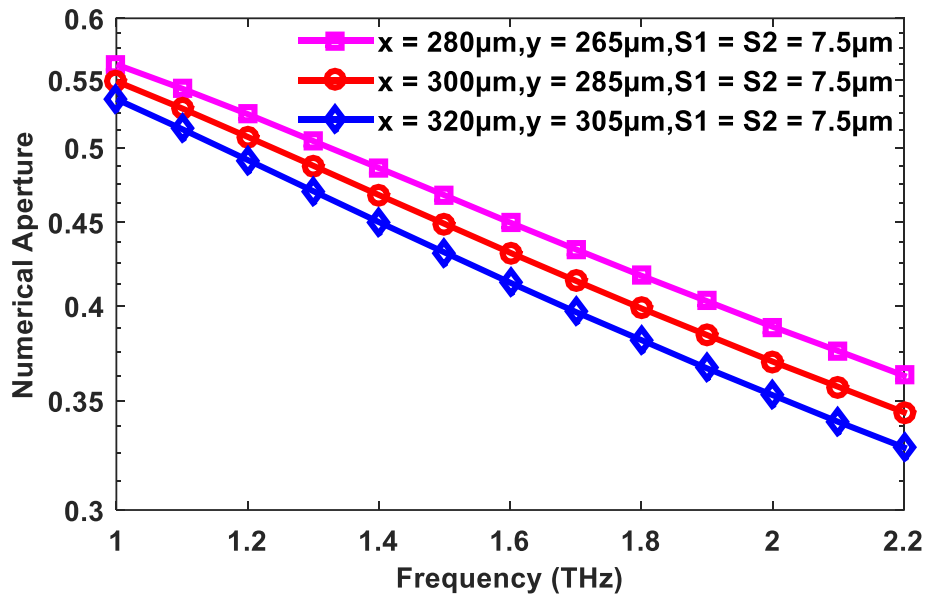
Figure 5.20: Response of numerical aperture with respect to frequency at variable *x* and *y* with fixed *strut*.
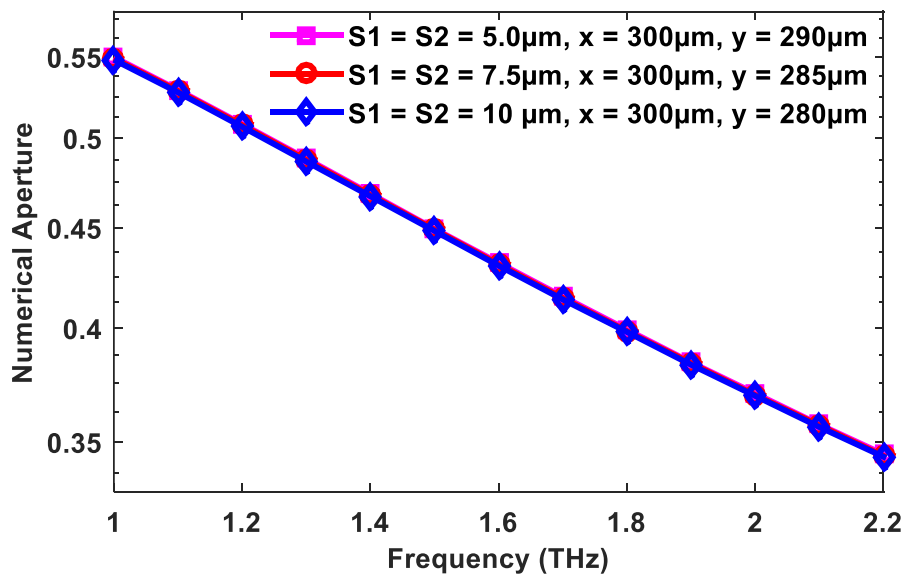
Figure 5.21: Response of numerical aperture with respect to frequency at variable *struts* with fixed *x*.
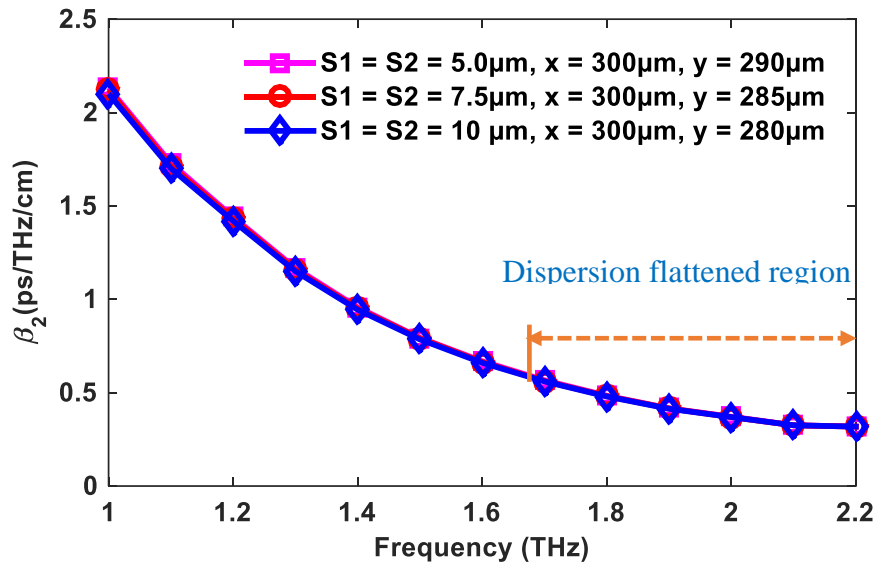
Figure 5.22: Nature of dispersion with respect to frequency at variable *struts* with fixed *x*.
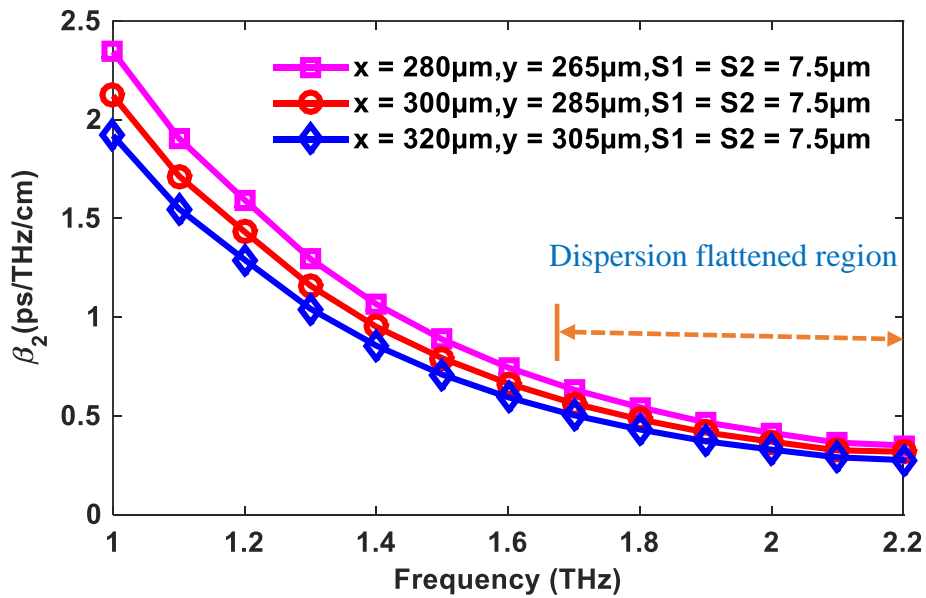
Figure 5.23: Nature of dispersion with respect to frequency at variable *x* and *y* with fixed s*trut*.

Table 5.2: Response of different optical properties for the tested sample at ± 2 % and ± 5 % geometric parameters deviation with optimum design condition.

Geometrical Parameters	Sensitivity (%)	EML (cm^{-1})	Effective Area (m^2)
+5%	98.871	0.00083748	4.79×10^{-08}
+2%	98.803	0.00086635	4.55×10^{-08}
Optimum	**98.754**	**0.00088**	**4.40×10^{-08}**
-2%	98.702	0.00090684	4.25×10^{-08}
-5%	98.616	0.00093233	4.02×10^{-08}

Table 5.3: Comparison with previously published PCF based chemical sensor and this proposed work.

References	Sensitivity (%)	L_c	Dispersion (ps/THz/cm)	EML (cm^{-1})	NA
[20]	96.80	6.95×10^{-14} cm^{-1}	-	0.0035	-
[21]	80.93	1.23×10^{-11} dB/m	± 2	-	-
[22]	86.00	1.70×10^{-9} cm^{-1}	±0.265	0.005	0.37
[48]	93.5	3.11×10^{-14} cm^{-1}	-	-	-
[49]	94.4	1.71×10^{-14} cm^{-1}	-	0.00859	-
[50]	63.24	10^{-11} cm^{-1}	-	-	
[51]	66.73	7.50×10^{-12} cm^{-1}		-	
[52]	68.87	7.79×10^{-12} cm^{-1}	±0.38	0.05	0.35
[53]	69.70	1.79×10^{-9} cm^{-1}		-	0.33
Proposed Work	**98.75**	**3.14×10^{-20} cm^{-1}**	**± 0.31**	**0.0008**	**0.35**

Figures 5.20 and 5.21 depict the scenario of the numerical aperture for the incremental function of frequency. From these figures, it is observed that NA behaves in downward manner with the incremental changes of frequency. Higher NA of 0.55 is attained at 1 THz frequency point, though we have fixed 2.2 THz as an optimum point for considering our main goal improving sensitivity where 0.34 NA is obtained which comparable with existing PCF [21, 52, 22].

The nature of dispersion of the proposed PCF with the variation of frequency for optimum and other geometrical conditions is presented in Figures 5.22 and 5.23. Considering the optimal design parameters, ± 0.31 ps/THz/cm is obtained for a wide frequency range of (1.4 – 2.2) THz which is also commensurate with prior proposed design for similar applications in same platform[21, 52].

The response of different optical properties shown in Table 5.2 by changing the geometrical parameters ± 2% and ± 5%. During the fabrication process, there is a possibility that the geometrical parameters change slightly from the optimum geometric conditions. It is seen that the proposed PCF sensor renders negligible changes with the ± 2% and ± 5% geometrical parameters changes. Only 0.051% and 0.068% sensitivity deviation are observed by changing the geometrical specifications ± 2% and ± 5% respectively. Minimal changes are observed for other optical properties with this deviation of geometrical specifications.

A comparison with previously proposed PCF based chemical sensor is presented in table 5.3. It represents that, this proposed THz sensor is significantly improved in all crucial properties for substance identification in liquid samples.

In this work, an octagonal shaped hollow core with eight head star cladding PCF is designed and investigated for different crucial optical properties of cholesterol sensing in liquid samples. The examined consequence of the proposed sensor renders a very high sensitivity profile of 98.75% at 2.2 THz. Moreover, a very negligible confinement loss of 3.14×10^{-20} cm^{-1} and very low effective material loss of 0.0008 cm^{-1} have been derived from the proposed PCF in case of cholesterol detection. Additionally, a very flat dispersion profile of ± 0.31 ps/THz/cm is also noticed from this investigation.

5.2.3 Octagonal Hollow Core PCF Bio-Sensor for Blood Components Detection

An efficient blood component detection process is essential for the diagnosis of hematologic diseases. This work presents refractive index-based terahertz (THz) sensing with photonic crystal fiber (PCF) for the identification of the various blood components. An octagonal hollow-core surrounded by symmetrical air holes structured cladding PCF is designed and the sensing performances investigated using COMSOL Multiphysics (v.5.3a) with a finite element method. The proposed PCF geometry provides a significant improvement in the identification of blood components, nearly 99% for all the tested substances (RBC, hemoglobin, WBC, plasma, and water) at THz frequency. Additionally, negligible confinement loss of $10^{-16\pm1}$ dB/cm is attained

around the same operating region. Furthermore, dispersion, effective area, effective material loss, and numerical aperture are found to be highly satisfactory and on par with published results, thus further ensuring the suitability of the use of the presented PCF in THz sensing.

5.2.3.1 Proposed PCF Geometry and Design Methodology

For modeling this PCF geometry, the COMSOL Multiphysics version 5.3a is employed. Different optical properties of PCF are analyzed through the finite element method (FEM) in the Multiphysics environment. FEM is the most comprehensive numerical technique compare to others analyzing approaches due to its convenient features such as reduction in the physical prototype, optimization of the components, and faster computation. The geometrical arrangement of the proposed PCF is demonstrated in Figure 5.24 with the magnification of the core. An octagonal structured hollow core is used in the core region to enhance the relative sensitivity compared to hexagonal, pentagonal, square, rectangular, etc. core. The optical properties of the proposed PCF with that of a circular-core as well as a decagonal-core PCF are also examined considering the same cladding structure and have found very negligible differences in performances. The reason for choosing the hollow core PCF is that it has a greater interaction area between light intensity and applied analytes that can facilitate higher sensitivity. On the other hand, it helps to minimize the light material interaction, thereby reducing EML. Blood is added in the designated place in the hollow region of the core for identifying its different components by employing the refractive index. To compete our results with existing similar works in the PCF environment we have tuned the geometrical parameters is nearly existing works and fixed the optimum design parameters. Total diameter of the PCF is fixed at 3 mm as optimal. The in-circle radius of the core *R1* is selected 150 µm as optimum where core hole radius *R2* is (*R1-strut*) µm. The circumcircle radius of core and core hole are denoted by *r1* and *r2,* respectively where $r2 = 1.0824 \times r1$. *Strut* size is the separation area between two adjacent air holes or material width between core and cladding holes. *Strut* size is found to be optimum at 7.5 µm for maintaining fabrication tolerance (the feasibility of 6.5 µm strut size already demonstrated in the existing manufacturing platform [109]). Each side length

of the octagon is indicated by L that is calculated by $L = \dfrac{R1}{2\sqrt{(4 + 2\sqrt{2})}}$. The cladding section of presented PCF is introduced with a suspended composition that lies in a circular manner. The selection of the suspended structure reduces the volume of the host material and increases the amount of air.

Topas, Zeonex, Silica, PMMA, Teflon etc. can be used as background material for PCF devices. Among these materials, Topas and Zeonex have shown lower absorption loss than others. Topas and Zeonex have almost similar glass transition temperature but the refractive index of Topas negligibly fluctuates over a wide range of THz spectrum [87]. Moreover, Topas is impervious to environmental effects and has chemical idleness with exceptional bio-sensing peculiarity [87-88]. For these reasons, Topas is chosen as background material for the proposed PCF geometry. For protecting the PCF from the incident radiation caused by environmental effects, or by light pulse an anti-reflecting layer (perfectly matched layer) is circularly bounded on the outer side of the PCF. A *fine* element size is retained for better accuracy in the meshing process. The complete mesh consists of 96150 domain elements and 6328 boundary elements with minimum element quality of 0.559.
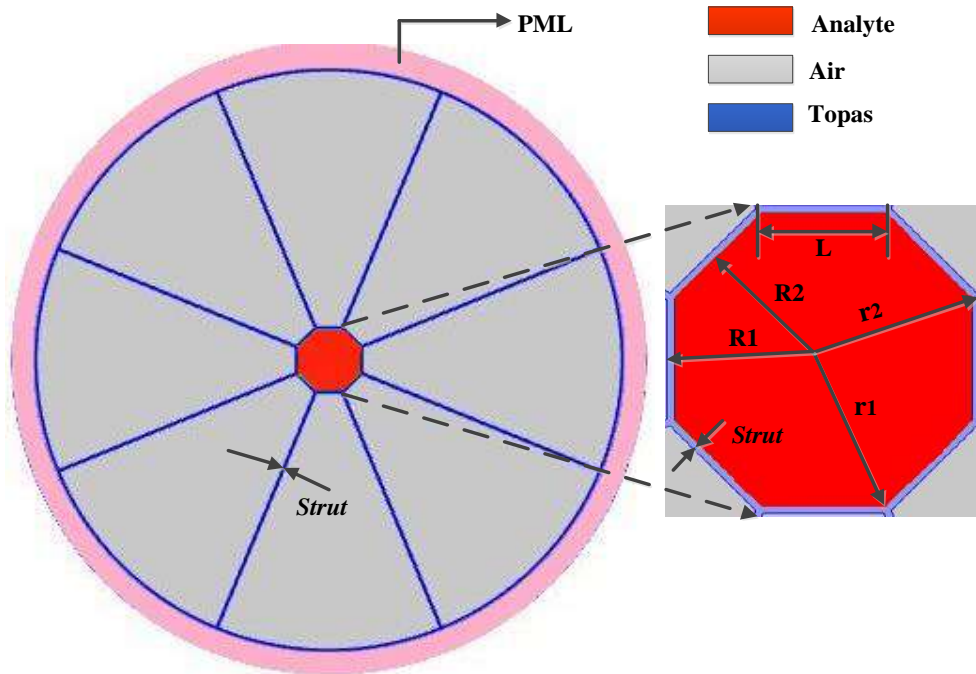
Figure 5.24: Proposed PCF geometry with the core shown in expanded form.

5.2.3.2 Results and Discussions

First, the interaction of light intensity and blood substances is illustrated in Figure 5.25 at optimum design conditions (see Section 5.2.3.1) and 4.5 THz working frequency. One can see that light intensity has strongly interacted with the blood substances and light is closely localized in the core section. On the contrary, negligible interaction is observed in the cladding region.

Commonly, in the PCF device, the effective refractive index continues to increase with the ascending frequency that enhances the optical power interaction. Such kind of superior interaction facilitates higher sensing responses. The proposed PCF also shows the same relation with frequency. This is revealed in Figure 5.26 is. Note the gradual increase in refractive index with increasing frequency for the various blood substances.

The sensing proportion of designed PCF as a function of frequency is presented in Figure 5.27 for different blood constituents at optimum geometrical conditions. To
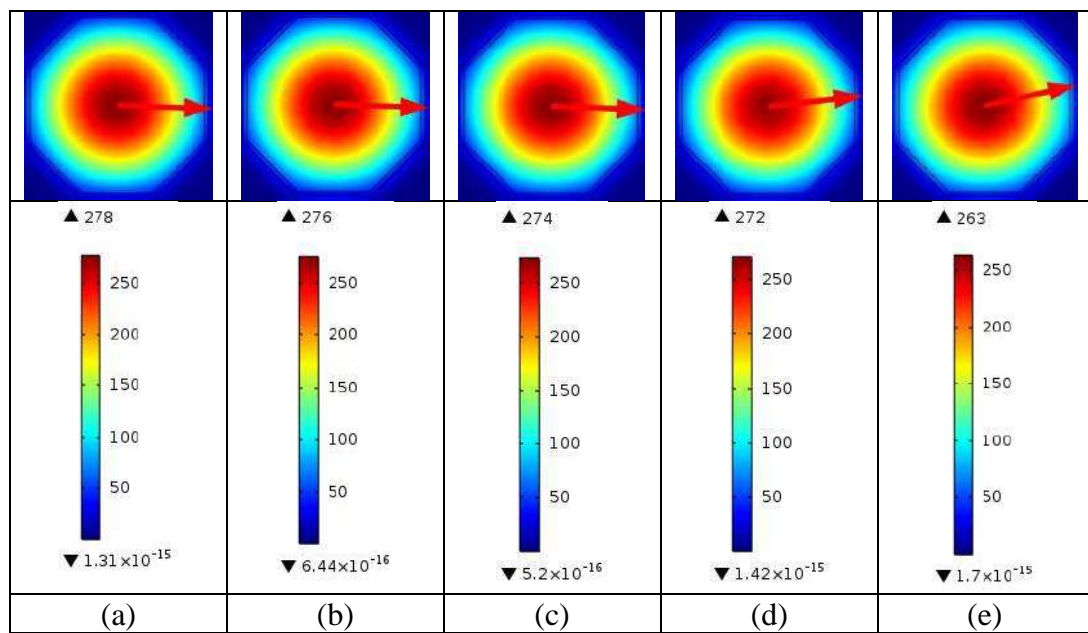
Figure 5.25: Mode power distribution of the proposed PCF for various targeted substances in x-polarization mode at 4.5 THz frequency with intensity scale (a) RBC, (b) Hemoglobin, (c) WBC, (d) Plasma, and (e) Water.
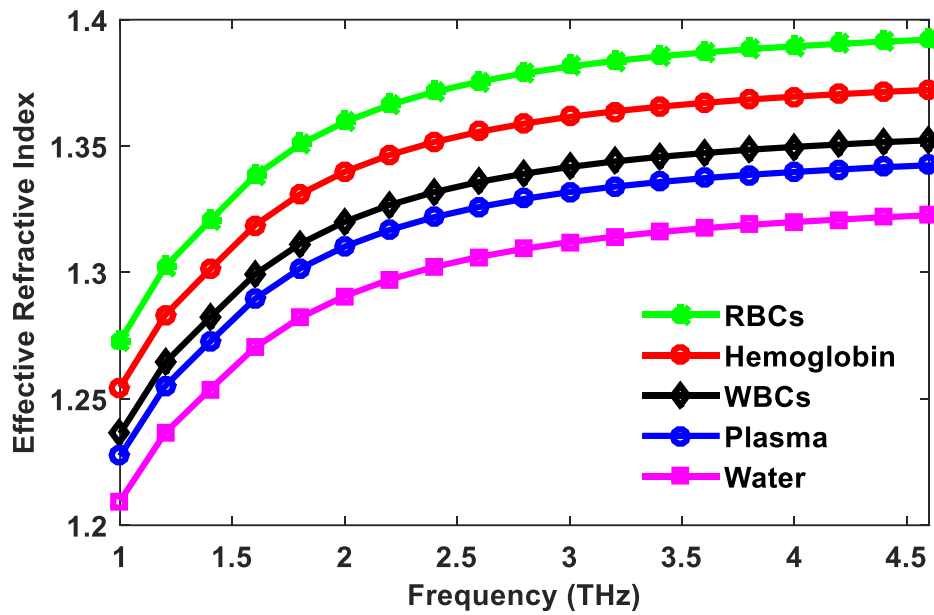
Figure 5.26: Behavior of effective refractive index of the proposed PCF for different blood components with respect to frequency.
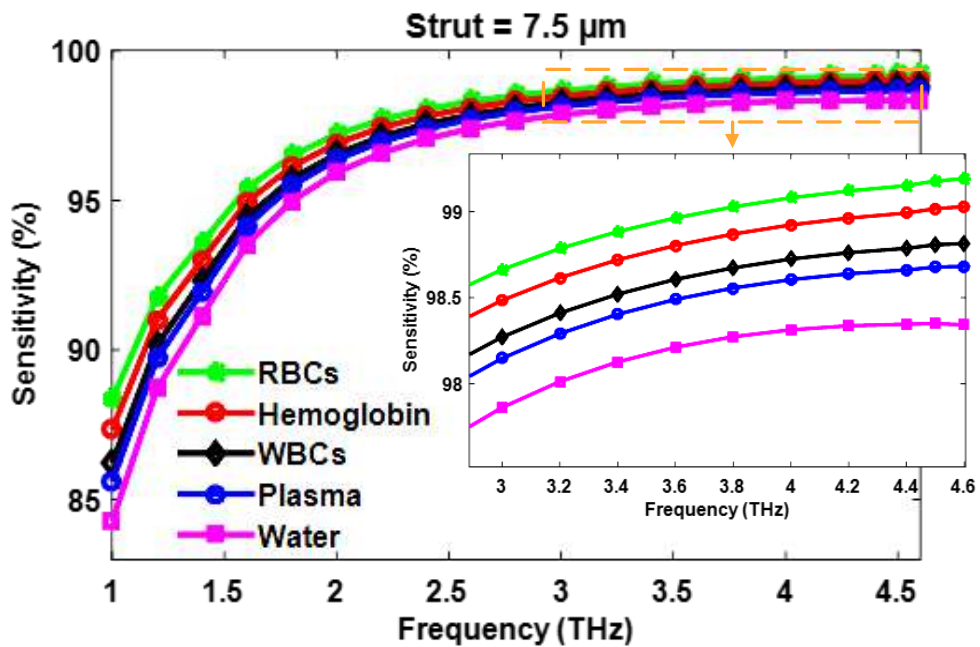
Figure 5.27: Sensitivity as a function of frequency for different blood components at optimum design conditions.
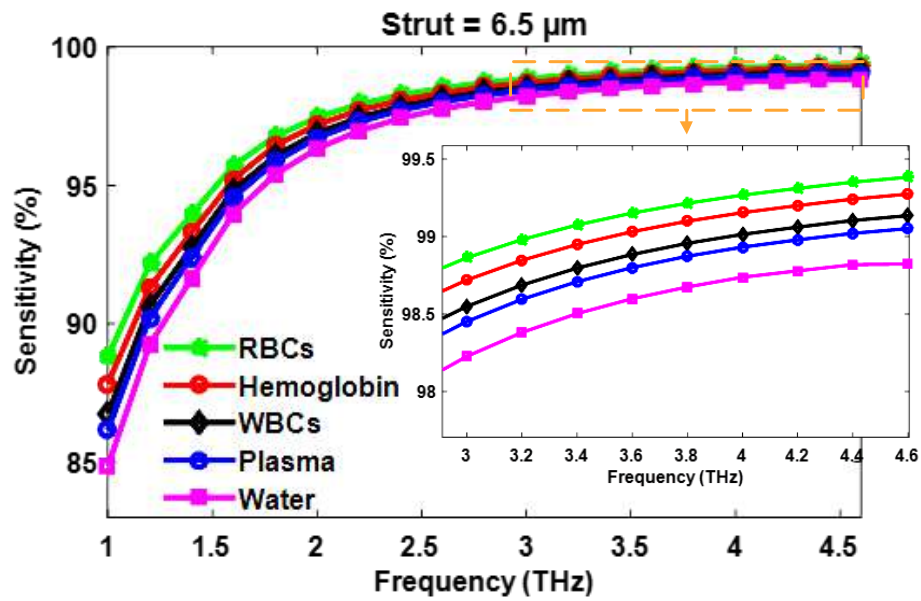
Figure 5.28: Sensitivity as a function of frequency for different blood components at 6.5 µm *strut* size.
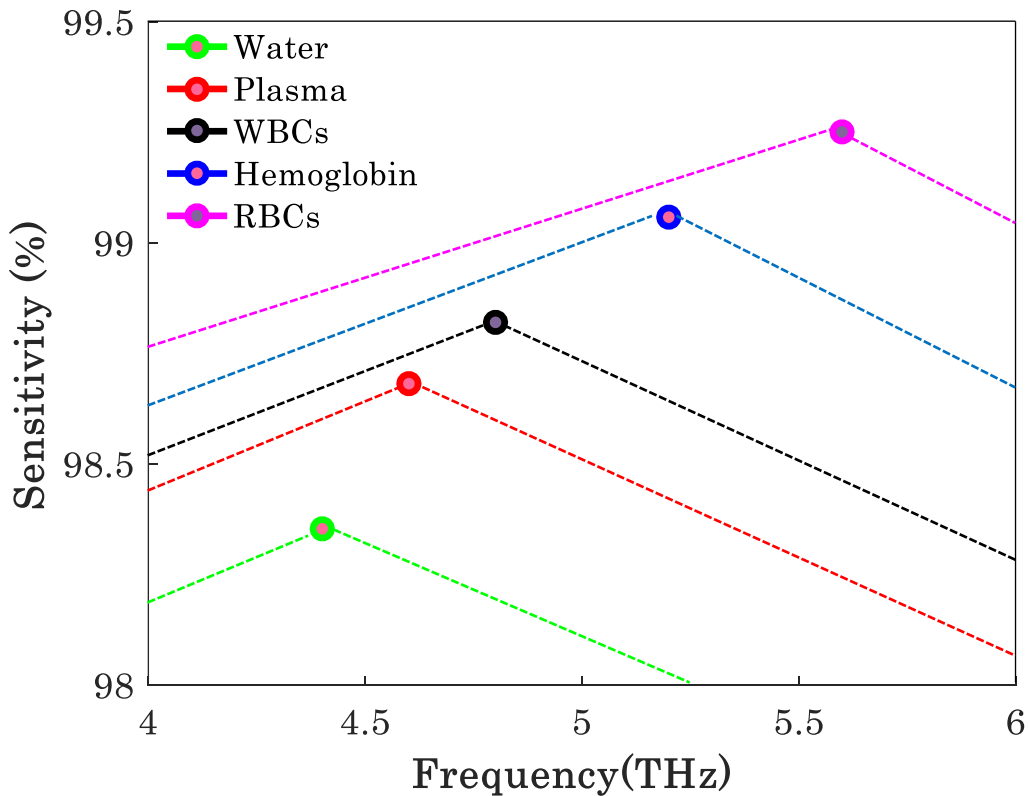
Figure 5.29: Peak sensitivity shifting with respect to frequency for different blood components.

examine the sensitivity of this PCF, several blood component cases are investigated by employing the following refractive index values: RBCs = 1.4, hemoglobin = 1.38, WBCs = 1.36, plasma = 1.35 and water = 1.33.

The refractive index of an analyte is directly related to the relative sensitivity. The RBCs exhibit highest sensitivity among the tested substances because of the refractive index of RBCs is more than the others. Higher frequency also facilitates strong interaction between light intensity and applied analytes that enhances the detection. It should be mentioned that the increasing tendency of sensitivity becomes minimal after a certain frequency and even the sensitivity starts to decline when it has experienced the maximum interaction. This certain frequency depends on the geometrical arrangements of the PCF and refractive index of the analyte. This situation is presented in Figure 5.29 for different blood components identification cases. In the proposed case, after 4.5 THz frequency, very insignificant improvement of sensitivity is seen for most of the tested blood constituents; especially, in water detection cases it starts to decline. For others blood components cases phase shifting is observed due to change of refractive index among the analytes. From the figure 5.29 it is observed that at the optimal geometrical situation, the proposed PCF renders maximum 99.25 % sensitivity for RBCs at 5.6 THz, 99.06 % for hemoglobin at 5.2 THz, 98.82 % for WBCs at 4.8 THz, 98.68 % for plasma at 4.6 THz, and 98.35 % for water at 4.5 THz frequency. It will be mentioned that at the mentioned frequency the blood components have strong absorbance potential [122-123]. This performance is superior to those of the refractive index-based PCF sensors reported before for same application [21, 46-48], as well as recently developed substances detector based on refractive index in PCF [20, 22, 45].

Because of the highly porous structure PCF, 7.5 µm *strut* width is considered to sustain manufacturing tolerance in existing fabrication platforms, note here that higher *strut* size enhances the material absorption loss. However, as reported in [109], the sol-gel technique can be used with also 6.5 µm *stru*t width, the sensitivity of presented PCF is also investigated with 6.5 µm for all the targeted analytes and the response is demonstrated in Figure 5.28. It is seen that compared to using a strut with 7.5 µm width,

the improvement achieved in sensitivity is insignificant, only 0.2 % sensitivity is enhanced with this *strut* size. Alongside it is a reality that maintaining exact optimum design parameters is somewhat difficult during fabrication. In this respect, the sensitivity of the proposed PCF is further studied for the blood constituents by changing the geometrical parameters $\pm 2\%$ and $\pm 5\%$. The results are provided in Table 5.5. Note that a meagre ± 0.015 % sensitivity change is observed with respect to the optimum values for each tested element.

Higher core size enhances the possible interactive area of light-matter inside the core that flourishing the sensing rate. The sensing proportion of different blood elements by the proposed PCF structure as a function of the core radius is presented in Figure 5.30. A gradual change of sensitivity is noticed with the increase of the core radius. About 0.25 % sensitivity is augmented for all the tested cases by increasing the core radius by 10 µm than the optimum core radius.
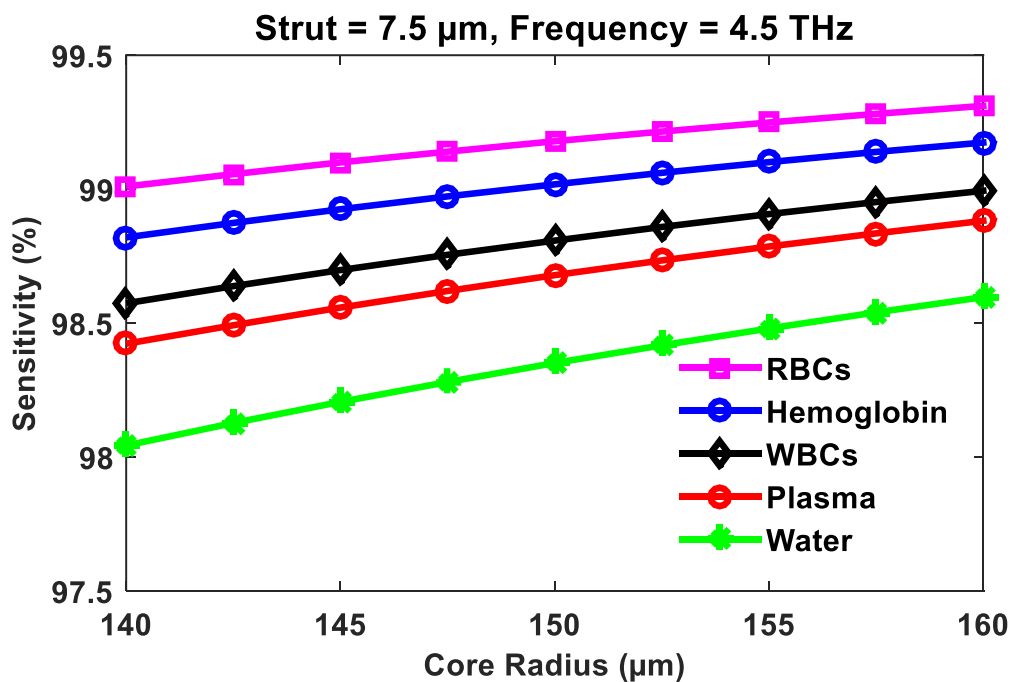
Figure 5.30: Sensitivity with respect to core radius for different blood components at the optimum operating frequency of 4.5 THz.

The sensing performance is further studied using different cores considering the same cladding structure. It is seen that the performance of proposed PCF is quite similar with that of a circular or decagonal core. For example, a very negligible difference in sensitivity is observed which is on an average value of 0.086% for different blood constituents' cases. On the other hand, the proposed PCF geometry provides an average sensitivity improvement of 0.172%, 0.325%, and 0.439% as compared to hexagonal, square, and pentagonal cores. Table 5.4 summarizes the values of the different optical properties using different cores.

The property of confinement loss with respect to frequency is shown in Figure 5.31. It is seen that confinement loss responds in a decreasing manner with the increase of frequency. Higher frequency enhances the interaction of the evanescent field with applied analytes that declines the confinement loss. The refractive index of analytes is also directly involved with this event. A higher refractive index facilitates strong interaction, as a consequence confinement loss is minimized. As seen in Figure 5.32, among the tested substances water exhibits the higher confinement loss for it has the lowest refractive index. At optimum design conditions, ultra-low confinement loss of 1.6×10^{-17} dB/cm for RBCs, 1.03×10^{-16} dB/cm for hemoglobin, 2.8×10^{-16} dB/cm for WBCs, 3.05×10^{-16} dB/cm for plasma, and 2.1×10^{-15} dB/cm for water are obtained for the presented PCF for 4.5 THz working frequency, a superior performance than the previously proposed refractometric blood components detection process using PCF [21, 46-48].

Due to the selection of hollow-core structured PCF, the requirement of Topas is minimized, as well as it reduces the possibility of light material interaction. Small scale interaction of light intensity with Topas reduces the material absorption loss (EML). The experience of light material interaction of the proposed PCF for different blood constituents' cases is shown in Figure 5.32 as a function of frequency. It is seen that EML is decreasing with increasing frequency. The light intensity is closely confined with the rising frequency that helps to minimize the EML. Considering the optimal structural conditions, the values of EML obtained are 0.0010 cm^{-1}, 0.0012 cm^{-1}, 0.0014 cm^{-1}, 0.0015 cm^{-1}, and 0.0018 cm^{-1} for RBCs, hemoglobin, WBCs, plasma, and water.
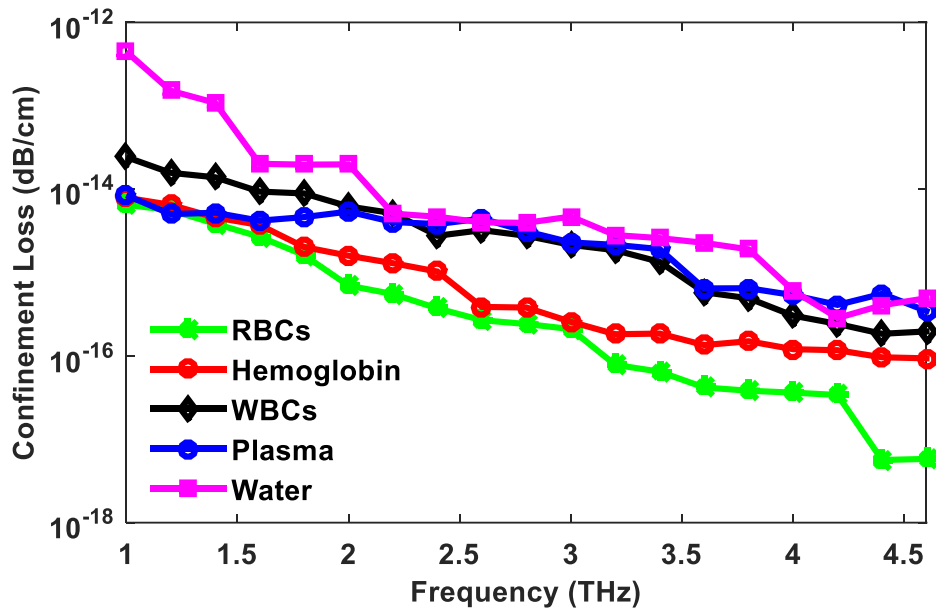
Figure 5.31: Confinement loss as a function of frequency for each blood component at optimum design conditions.
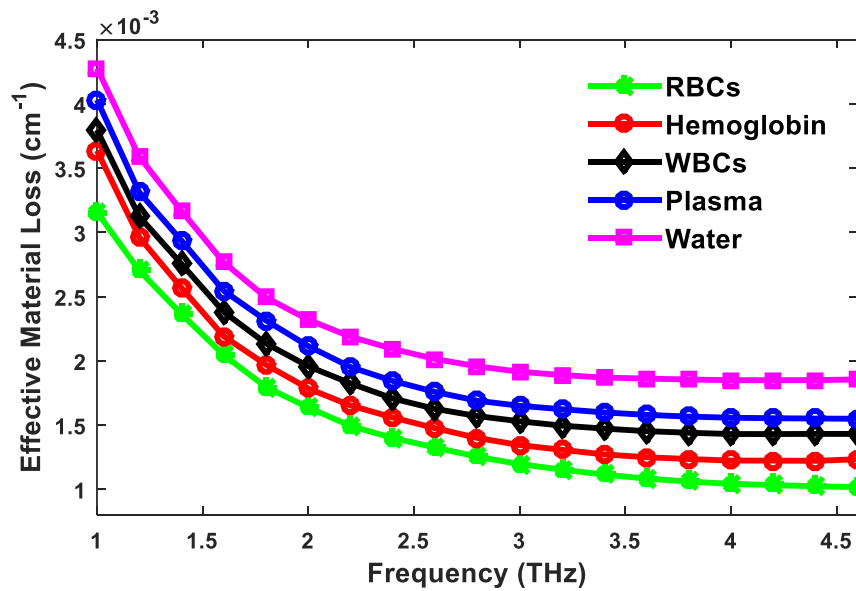
Figure 5.32: Material absorption loss as a function of frequency at optimum design condition for different blood components.
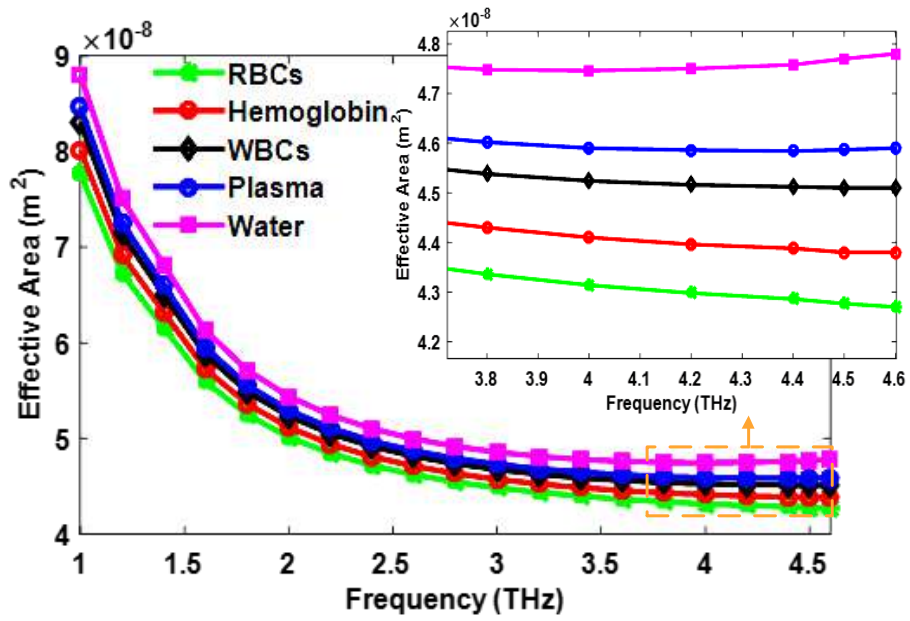
Figure 5.33: Effective area with respect to frequency for each tested analytes at optimum design condition (with zoomed-in portion)
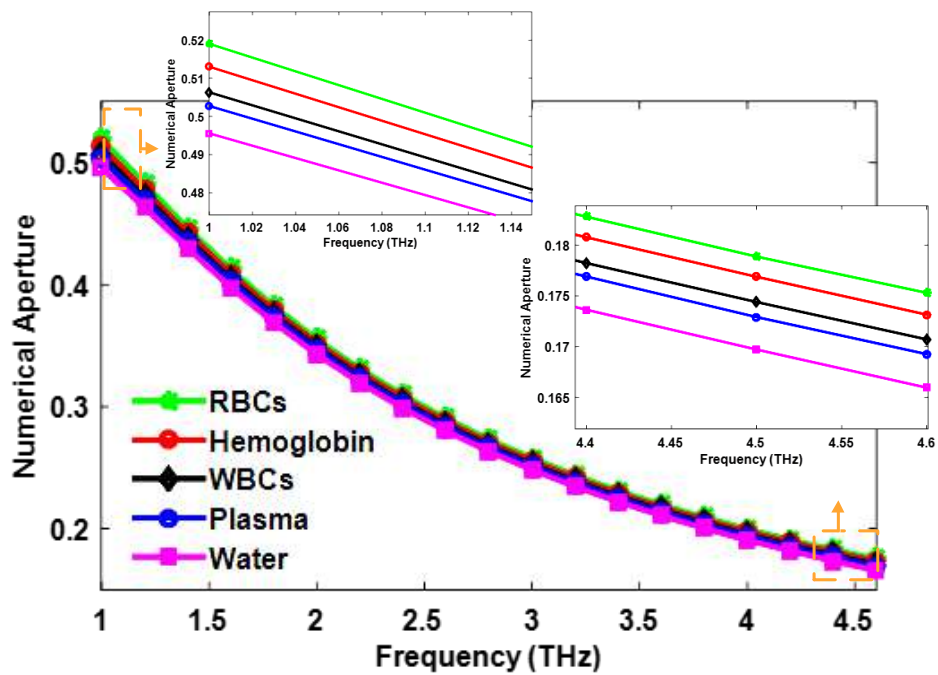
Figure 5.34: Behavior of numerical aperture (NA) with respect to frequency for each tested analyte at optimum design condition (with zoomed-in portion).

105

The behavior of the core concentrated mode power area with frequency is shown in Figure 5.33. Due to the increasing frequency, light pulses are compactly confined inside the core region. It means that when the frequency is increasing, the total guided power is concentrated towards the core area. As a result, the effective mode area decreases with higher frequency as seen in Figure 5.33. The optimal outcome of the effective area is nearly 4×10^{-8} m^2 for all the tested cases.

The response of numerical aperture (NA) as a function frequency at optimum design parameters for various blood elements is demonstrated in Figure 5.34. It is noticed that the highest values of NA achieved are 0.519, 0.513, 0.506, 0.503, and 0.496 for RBCs, hemoglobin, WBCs, plasma, and water, respectively at 1 THz frequency. However, at 4.5 THz, the chose operating frequency for the proposed PCF, the values of NA are 0.179, 0.177, 0.174, 0.173, and 0.170, respectively. It will be noticeable that all of the prior proposed PCF based blood constituents' sensors ignored presenting this characteristic [21, 46-48].

The nature of dispersion for selected blood substances at optimum design conditions in
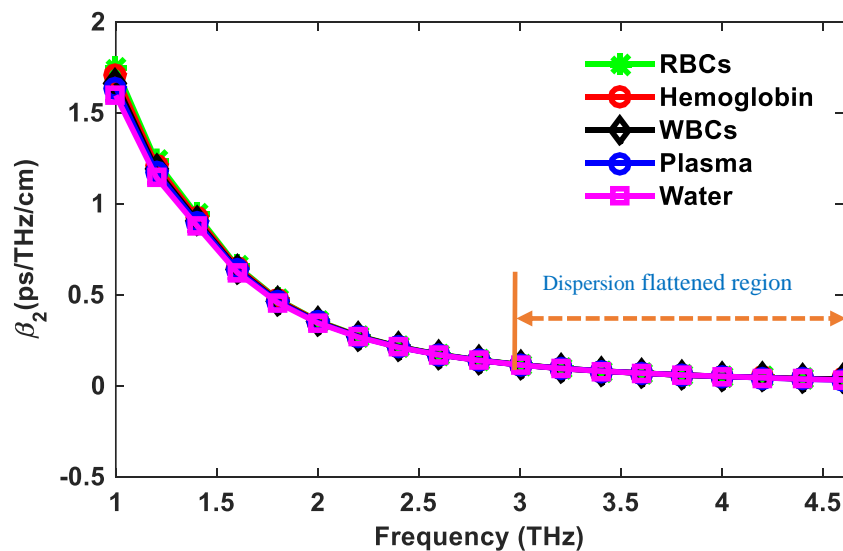
Figure 5.35: Nature of dispersion as a function of frequency for each tested analyte at optimum design conditions.

Table 5.4: Sensing performance for different cores with proposed cladding.

Analytes	Sensitivity (%)					
	Core Type					
	Octagonal	Circular	Decagonal	Hexagonal	Square	Pentagon
RBC (RI = 1.4)	99.18	99.25	99.19	99.02	98.96	98.99
Hemoglobin (RI = 1.38)	99.02	99.10	99.04	98.85	98.72	98.76
WBC (RI = 1.36)	98.81	98.90	98.83	98.63	98.38	98.42
Plasma (RI = 1.35)	98.68	98.77	98.69	98.501	98.17	98.282
Water (RI = 1.33)	98.35	98.45	98.36	98.182	97.59	97.962

Table 5.5: Sensitivity of each blood component at $\pm$ 2 % and $\pm$ 5 % geometric parameters deviation with optimum design condition for 4.5 THz frequency.

	Sensitivity (%)				
	RBCs (RI = 1.40)	Hemoglobin (RI = 1.38)	WBCs (RI = 1.36)	Plasma (RI = 1.35)	Water (RI = 1.33)
+ 5%	99.206	99.040	98.820	98.690	98.357
+ 2%	99.190	99.028	98.814	98.682	98.353
Optimum	**99.179**	**99.018**	**98.808**	**98.679**	**98.351**
- 2%	99.166	99.007	98.801	98.674	98.348
- 5%	99.145	98.987	98.785	98.662	98.344

Table 5.6: Comparison with previously proposed THz sensor in PCF platform for blood constituents sensing application.

Prior Works	Sensitivity (%)					L_c	NA	β_2 [ps/THz/cm]	EML (cm^{-1})
	RBCs RI = 1.4	Hemoglobin RI = 1.38	WBCs RI = 1.36	Plasma RI = 1.35	Water RI = 1.33				
[28]	56.05	66.47	53.72	54.05	55.09	$10^{-10 \pm 1}$ (dB/cm)	-	-	-
[29]	66.46	65.05	62.72	58.04	55.82	$10^{-14.5 \pm 1.5}$ (dB/cm)	-		-
[30]	80.93	80.56	80.13	79.91	79.39	$10^{-13.5 \pm 0.5}$ (dB/cm)	-	$\pm$ (1.81 to 2.14)	-
[31]	93.50	92.41	91.25	90.48	89.14	$10^{-13.5 \pm 0.5}$ (cm^{-1})	-	-	-
[47]	95.80	95	93.6	92.5	91.4	$10^{-10 \pm 1}$ (dB/m)	0.38	-	-
Proposed Work	**99.18**	**99.02**	**98.81**	**98.68**	**98.35**	**$10^{-16 \pm 1}$ (dB/cm)**	**0.170 to 0.179**	**$\pm$ (0.066 to 0.069)**	**0.0010 to 0.0018**

the frequency range of 1-4.6 THz is shown in Figure 5.35. It is seen that the analytes behave almost similarly with slight deviations. A higher refractive index containing analytes produces comparatively leading dispersion. The behavior of dispersion for each analyte becomes almost flattered in the wide range of frequency (2.6 – 4.6) THz, indicative of the PCFs working ability in multichannel sensing application. For example, the obtained dispersion at 4.5 THz frequency is very close to 0.036 ps/THz/cm for each component and the deviations are $\pm$ 0.067 ps/THz/cm, $\pm$ 0.067 ps/THz/cm, $\pm$ 0.066 ps/THz/cm, $\pm$ 0.069 ps/THz/cm, and $\pm$ 0.069 ps/THz/cm for RBCs, hemoglobin, WBCs, plasma, and water, respectively in the huge operating range of (2.6 – 4.6)THz. This is lower and flatter than recently reported PCF geometry for blood components identification in the THz regime [21].

Finally, a performance comparison is carried out in Table 5.6 with prior proposed blood components identification using PCF in THz domain. It is observed that the proposed PCF while giving better sensitivity, enhances the other crucial properties.

In this work, a PCF geometry has been presented for identifying different blood constituents based on the refractive index in the THz spectrum. The highest sensitivity values that have been achieved are 99.18 % for RBCs, 99.02 % for hemoglobin, 98.81 % for WBCs, 98.68 % for plasma, and 98.35 % for water at the selected operating frequency of 4.5 THz and optimum geometric conditions. Alongside, the proposed PCF exhibits negligible confinement loss of 1.6×10^{-17} dB/cm for RBCs, 1.03×10^{-16} dB/cm for hemoglobin, 2.8×10^{-16} dB/cm for WBCs, 3.05×10^{-16} dB/cm for plasma, and 2.1×10^{-15} dB/cm for water at the same operating frequency. Additionally, near-zero flattened dispersion in a wide THz range with a very low material absorption loss, and high numerical aperture individuality have been reported for the proposed PCF, making its well-suited for improved sensing.

5.2.4 Circular Hollow Core PCF Bio-Sensor for Blood Protein Detection

The presence of albumin in human urine is one of the confirmed early symptoms of

kidney dysfunction. A precise urine protein identification process is very urgent to monitor the kidney's proper functioning. In this context, a refractometric protein sensing approaches in the photonic crystal fiber (PCF) environment has been introduced here. A PCF geometry with suspended cladding and circular hollow core have been developed and investigated in the Terahertz (THz) spectrum for protein identification in the liquid samples. Three levels of albumin concentrations 7-125 mg/dl, 250-500 mg/dl, and 1000 mg/dl are considered to evaluate the sensing performances of proposed PCF. The numerical investigations are performed in the Comsol Multiphysics platform where the finite element method figure out the numerical behaviors. The performances of proposed PCF exhibit highly sensitive characteristics for albumin identification in the different albumin concentration levels of urine and the sensitivity is more than 98.5 % for all the tested concentration levels due to the strategic selection of geometrical parameters and proper optimization. Alongside negligible confinement loss of 10^{-16} cm^{-1} is attained at the same operating point of 4.3 THz.

5.2.4.1 Design methodology of proposed PCF geometry

The performances of existing PCF in sensing cases indicate that micro-structured fiber can be a potential solution for sensing applications. Sensing performances of PCF devices mostly dependent on geometrical arrangements. The geometrical arrangements of proposed PCF are displayed in Figure 5.36 with the amplified core and the 3D view of developed PCF is presented in Figure 5.37 for better visualization. A horse wheel-like, simple PCF geometry is developed for the bio-sensing applications. A most common circular shaped core is considered to form the PCF core for avoiding fabrication complexity. The hollow core with circular shaped is constructed to enhance the interactive area of targeted substance and light intensity. Alongside it also helps to minimize the background material requirement that also facilitates reduce absorption loss. Most of the prior developed PCF geometry are considered nearly 300 µm core diameters to investigate in the THz spectrum in case of sensing. For competing our investigated results with previously designed PCF, 160 µm core radius r_c is fixed as optimum after setting the design parameters at several points. The core hole radius is

indicated by r_h which fixed at 152.5 µm considering the *strut* width of 7.5 µm.

At above mentioned geometrical conditions the developed PCF exhibit improved sensing properties such as sensitivity, confinement loss, dispersion, effective material loss etc. The optimized geometrical parameters are listed in Table 5.7. Strut width can be defined here as the material width between the core hole and the cladding hole. Strut in the cladding area is indicated that the separation area between two adjacent holes is also considered the same as the core strut. A symmetrical circular manner 60^0 sectoring
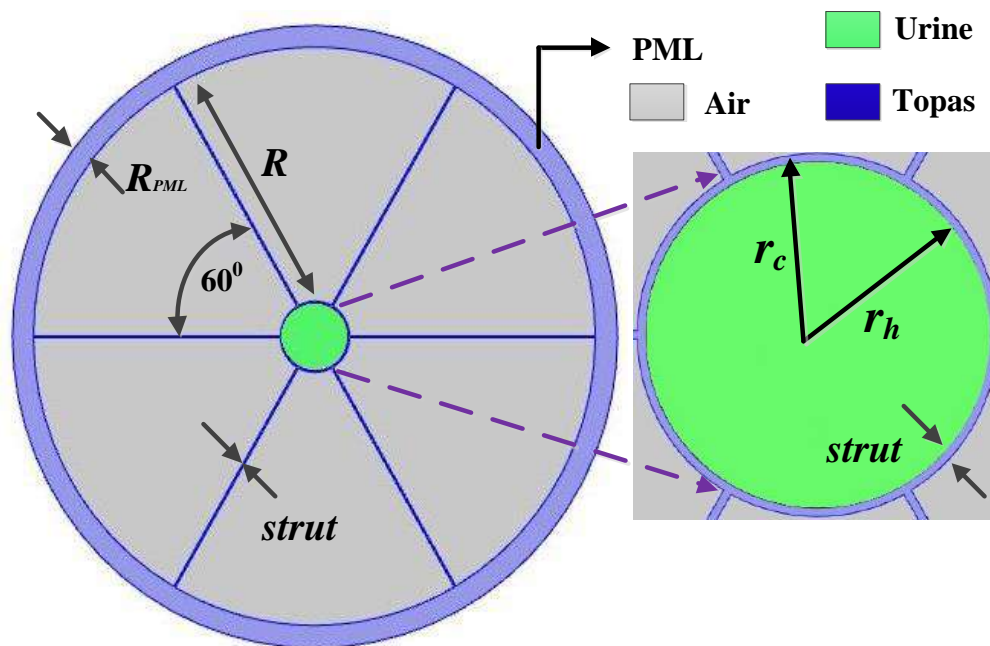
Figure 5.36: Geometrical cross-sectional view of proposed PCF with amplified core.
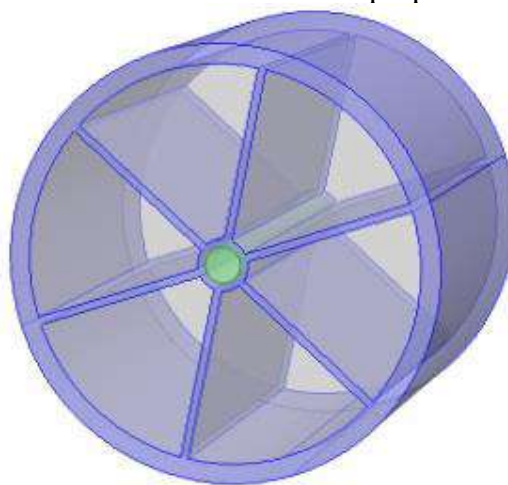
Figure 5.37: 3D view of proposed PCF Geometry.

cladding structure is designed considering the fabrication complexity. Targeted stuff concentration has been applied in the core hole and dry air is considered in the cladding holes for this investigation.

Usually, several polymer materials can be the strong candidates as a host material. Because of higher absorption loss by the PMMA, Teflon, these are not considered in this case. Zeonox and Topas are the two-dominant postulant in this area with similar absorption loss (~0.2 cm^{-1}), high glass transition point, high light transmission (91%), avoidable material dispersion, and material insensitive, etc. [118].   As per the experimental evaluation of Zeonox and Topas there are no significant differences between them in almost all the tested properties cases [118, 129]. So, any of these can be well suited for PCF devices. In this investigation, Topas was chosen as background material. For reflecting the incident radiation produced by the environmental effect, a perfectly matched layer has been used as an antireflecting layer in the outer region of the fiber.

Table 5.7: Optimized geometrical parameters

Parameters	Dimension(µm)
Core hole radius (r_h)	152.5
Core radius (r_c)	160
Cladding radius (R)	1132.5
Strut	7.5
PML radius (R_{PML})	100
Total PCF diameter	3000

5.2.4.2 Results and discussions

To design the PCF geometry and analyze the sensing properties of developed PCF, the most powerful computational technique finite element method has been utilized in the Comsol Multiphysics v. 5.3a environment. Because of less computational time and complex, PDEs solution ability made it the best than the other techniques for optoelectronics devices. The interactive situation of targeted substance and light
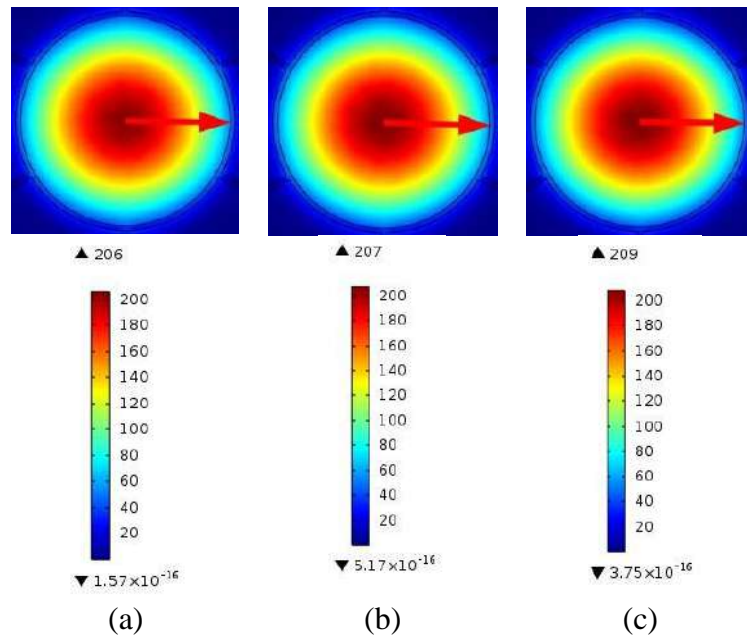
Figure 5.38: The mode field distribution with intensity scale of proposed PCF for different level of protein concentration in x-polarization mode at optimum design conditions (a) 7-125 mg/dl, (b) 250-500 mg/dl, and (c) 1000 mg/dl.

intensity are presented in Figure 5.38 with the intensity scale in x-polarization mode. Because of symmetrical arrangement in the cladding region with hollow core settlement both polarization modes render the same behavior.

From this figure, it is clearly visualized that the interactive area is closely localized in the core area and the light pulse and targeted substance have strongly interacted. Contrariwise inconsequential interaction in the cladding region is noticed.

The sensing capability of developed PCF for protein identification as a function of frequency is presented in Figure 5.39. Three concentration levels of protein in urine are considered for evaluating the sensitivity of the proposed PCF. The proportion of sensitivity mostly depended on the refractive index of targeted analytes at a fixed design parameter and a certain operating region. Changes of refractive index for different concentration levels are very tiny as a result rate of sensitivity seems the same for all the samples. But the deviations are shown in the enlarged view of the figure. With the augmentation of frequency light intensity strongly interact with the targeted analyte that enhances the sensitivity. At a certain frequency, the light-matter interaction is reached

112
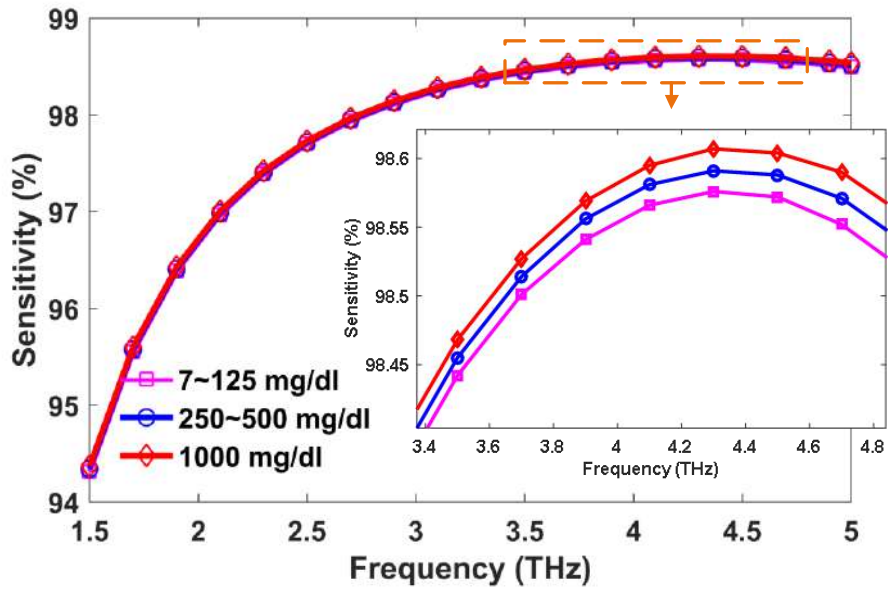
Figure 5.39: The response of sensitivity for different protein concentration of urine as a function of frequency.
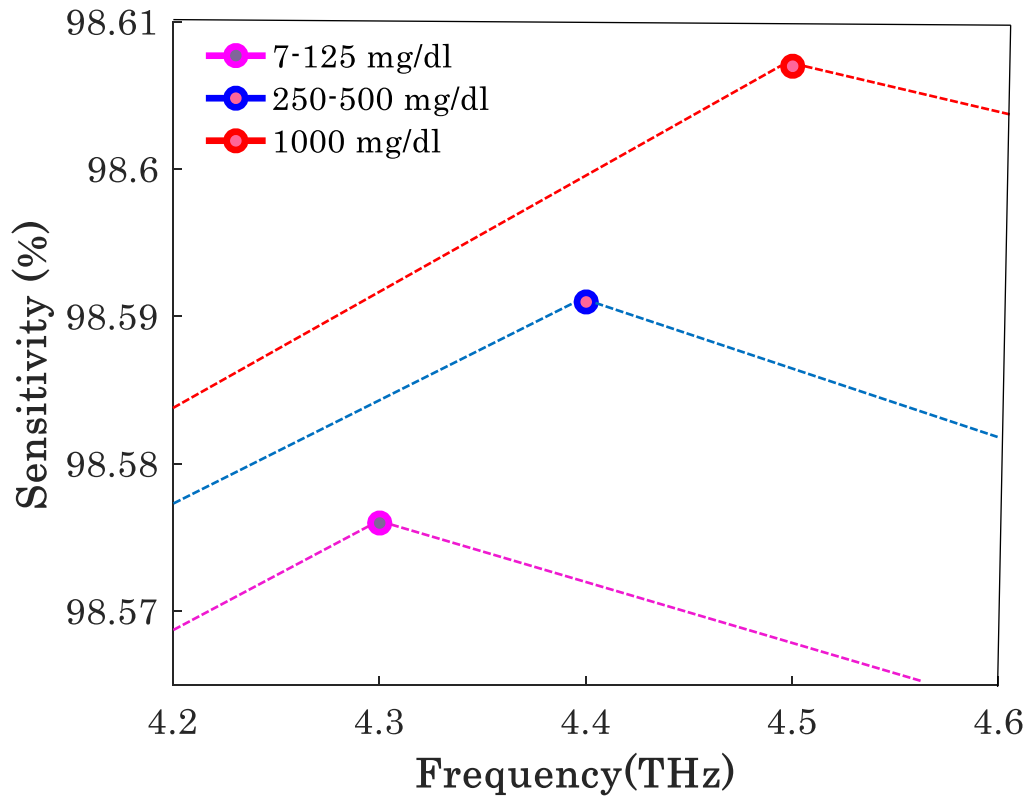
Figure 5.40: Peak sensitivity shifting for different protein concentration of urine as a function of frequency.

113
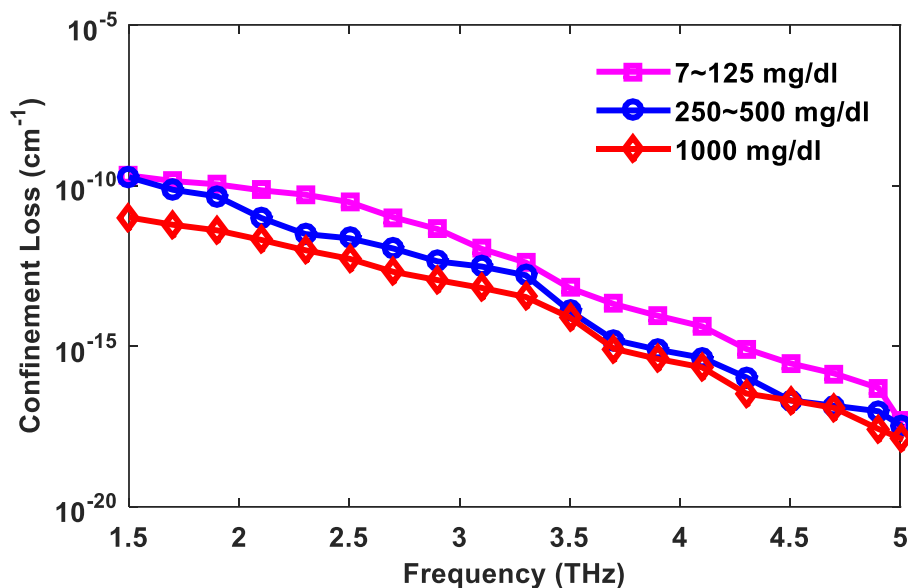
Figure 5.41: Nature of confinement loss with respect to frequency for different concentrations level of albumin in urine at optimum design conditions

at a maximum level, after that the sensitivity starts to decline which is clearly displayed in Figure 5.40. It will be mentioned that at this specific frequency the Albumin has a strong absorbance potential [130]. At 4.3 THz operating points the proposed PCF renders maximum sensitivity of 98.576 % for 7-125 mg/dl albumin concentration, a small shifting of the peak is noticed for 250-500 mg/dl, and obtained maximum sensitivity is 98.591% at 4.4 THz frequency. Similarly, maximum sensitivity of 98.607 % is observed for 1000 mg/dl concentration at 4.5 THz frequency. Due to a small change of refractive index among the different concentration levels of albumin in urine, only 0.1 THz phase shifting is observed for maximum sensitivity attainment however this shifting of frequency is acceptable for identifying the different levels of albumin in the urine.

It is to be mentioned that during fabrication exact optimum geometrical situations maintaining is a big challenge. Considering this fact sensitivity of presented PCF for

protein detection in urine concentration is listed in Table 5.8 by changing $\pm$ 2 % and $\pm$ 5 % geometrical parameters. It can be expressed that from Table 5.8, the impact on sensitivity by these geometrical variations is very insignificant. The subtlety of geometries can be varied up to 5 % without any significant consequences.

The variations of confinement loss for different concentrations of albumin have been demonstrated in Figure 5.41 with the shifting frequency. Due to the ascending manner of frequency, the propagated optical signal compactly passes inside the core region that has an impact on increasing sensitivity. It indicates that when the frequency acts in the incremental nature, the mode fields constrict more strictly towards the hollow core area, and hence, the CL curves exhibit descending nature for the high level of frequency that neatly signifies in Figure 5.41. At optimal frequency conditions, the CL is investigated 8.3×10^{-16} cm^{-1}, 1.07×10^{-16} cm^{-1}, and 3.37×10^{-17} cm^{-1} for (7-125mg/dl), (250-500mg/dl), and 1000 mg/dl concentrations of albumin accordingly which are trivial as compared to the recently proposed RI- dependent sensors for similar application in the PCF platform [2, 20-22, 43, 48-49,52, 135, 132].

A comparison with the recently developed PCF based THz sensor for chemical identification is presented in Table 5.9. It can be mentioned that from Table 5.9, this proposed work not only improved the sensitivity, besides all other necessary optical properties have improved at a significant level including confinement loss, effective area and effective material loss. Hollow core with circular shaped PCF has the greater interactive area that enhances the interaction area between applied analyte and light intensities. Besides, the highly porous structure of cladding and hollow core reduces the interactive area of the light pulse with bulk material that also helps to reduce the losses. Depending on these matters, we have chosen a hollow and circular shaped core with highly porous cladding geometry. The listed previous works in table 5.9 have not considered the above mentioned two factors together, that makes our developed structure unique with improved performances.

In this research, a RI based HC-PCF biosensor has been developed for albumin detection in urine on basis of kidney's dysfunctionality identification. To investigate

Table 5.8: Sensitivity of each tested sample at $\pm$ 2 % and $\pm$ 5 % geometric parameters deviation with optimum design condition at 4.3 THz frequency.

Geometrical Parameters	Sensitivity (%)		
	7-125 mg/dl Concentration	250-500 mg/dl Concentration	1000 mg/dl Concentration
+5%	98.581	98.596	98.612
+2%	98.577	98.592	98.608
Optimum	98.576	98.591	98.607
-2%	98.574	98.589	98.603
-5%	98.565	98.580	98.594

Table 5.9: Comparison with recent RI- dependent sensors for similar application in the PCF platform.

Ref.	Targeted Analyte/s	Refractive Index	Sensitivity (%)	Lc	β_2 [ps/THz/cm]	EML (cm^{-1})	A_{eff}
[2]	Ethanol	1.36	73.78	10^{-8} dB/m	0.4 ± 0.5	-	-
[21]	Water, Plasma, WBCs, Hemoglobin, and RBCs	1.33 – 1.4	79.39 - 80.93	$10^{-10 \pm 1}$ (dB/cm)	2.1 ± 2.02		$\approx 1 \times 10^5$ (μm^2)
[48]	Water, Plasma, WBCs, Hemoglobin, and RBCs	1.33 – 1.4	89.14 - 93.50	$10^{-13.5 \pm 0.5}$ (cm^{-1})		-	2.2×10^5 μm^2
[49]	Sarin, Soman, and Tabun	1.366 -1.44	92.84 - 94.4	1.71×10^{-14} cm^{-1}	-	0.0085-0.0094	-
[132]	Dioxin, Toluene, Hydrogen sulfide, Nitrogen dioxide, Sodium cyanide	1.36-1.65	89.6-91.5	$10^{-16 \pm 1}$ (cm^{-1})	-	0.019 ± 0.001	$(4-5) \times 10^{-8}$ m^2
Proposed Work	**Albumin**	**1.335-1.337**	**98.58 - 98.61**	**$10^{-16.5 \pm 0.5}$ (cm^{-1})**	**0.30 ± 0.33**	**≈ 0.0173**	**$\approx 5.06 \times 10^{-8}$ m^2**

the sensing performance of the presented PCF, three levels of protein concentration in urine have been considered. The investigated consequence of the proposed PCF reveals a superior response of relative sensitivity for all the tested level of concentration in the terahertz spectrum. Moreover, it renders a very trivial confinement loss and near zero dispersion flattened profile. The investigated results of proposed PCF and the practical implementation potential by the state-of-the-art fabrication technology apprise that it can be a great solution for biosensing applications.

5.3 Summary

Simple and unique hollow core photonic crystal fiber geometries has been developed for identifying different toxic analytes and biological components. At first a PCF with

square shaped hollow core with suspended have designed. Considering harmfulness of Alcohol, alcohol has been used as a targeted analyte in this case. This proposed PCF shown 89.85% sensitivity with very low confinement loss. After that an octagonal hollow core with suspended cladding PCF has been proposed for LDL cholesterol detection in liquid foodstuffs and blood. For medical diagnosis by an optical device numerical aperture profile verification is also important. An acceptable performance has been achieved for all the tested cases. Blood components detection is very important for hematological diseases. For efficient use of PCF as biosensor modified the previous design and designed a new PCF geometry for blood components detection. This proposed PCF renders superior performances than the existing PCF blood components detector in the THz platform. Lastly, another biosensor have been proposed with circular shaped core and suspended cladding PCF for blood protein detection. Three concentration level of blood protein in urine has been considered in this case. All the sample cases this proposed PCF sensor revealed almost 99% sensitivity with ultra-low confinement loss. The investigated consequences of the proposed PCFs reveals a superior response of relative sensitivity for all the tested cases. Moreover, these renders a very trivial confinement loss and near zero dispersion flattened profile. The investigated results of proposed PCFs and the practical implementation potential by the state-of-the-art fabrication technology apprise that these can be a great solution for sensing applications. We have discussed the proposed PCFs for waveguiding in Chapter 4 and proposed PCFs for sensing in Chapter 5, both cases the proposed PCFs have shown excellent characteristics for all the tested cases. Still, there is a lack of developing a single PCF for both applications. Thereafter, we have developed a PCF structure and tested for both waveguiding sensing applications. This PCF geometry and the performance are discussed in Chapter 6.

Chapter 6

PCF for Waveguiding and Analytes Sensing: Design & Analysis

6.1 Introduction

The photonic crystal fiber (PCF) provides a highly promising solution for THz wave guidance due to its remarkable wave-guiding capability with reduced absorption loss, near-zero flattened dispersion, and lower confinement loss. In addition, presently PCF has attained acceptance in sensing areas because of detecting potential, low weight, tiny size, etc. The purpose of this work is not only to provide high-quality THz transmission but also to render an ability for sensing different toxic analytes, basically several harmful and well-known liquid chemicals and air pollutants, with high sensitivity. In this context a hexagonal porous PCF has been developed for high-frequency communication but also for satisfactory sensing applications. This design procedure, novelty of design, performances, and applications of the proposed PCF structure are discussed in this Chapter.

6.2 Development of PCF for Waveguiding and Analytes Sensing

In this work, a hexagonal-shaped porous core and sectored-cladding structured photonic crystal fiber (PCF) is presented for efficient wave propagation in Terahertz (THz) domain. The full vector analysis based finite element method with Comsol software (v. 5.3a) is employed to design and optimize the PCF geometry and evaluate its optical properties. The PCF geometry demonstrates polarization maintaining attributes with a significant distinction between x and y polarization modes. The proposed PCF exhibits an ultra-low effective material loss (EML) of 0.013 cm^{-1} and 0.020 cm^{-1} in x and y polarization mode, respectively with a flattened dispersion of $\pm$ 0.020 ps/THz/cm and $\pm$ 0.065 ps/THz/cm in the respective modes at 1 THz.

Additionally, the proposed PCF structure is investigated for sensing different liquid chemicals (cholesterol, methanol, ethanol, and benzene) and air pollutants (cyanide, dioxin, nitrogen oxide, and hydrogen sulfide). It is shown that the proposed PCF can outperform a number of recently reported designs in the literature.

6.2.1 Proposed PCF Geometry Development

Several types of geometrical structure have been developed for similar applications in PCF platform such as square [132], Kagome [23, 26], slotted [20], hexagonal [52], D-shape [128], steering wheel [121], pentagonal [45], octagonal [130], spiral [127] and elliptical [31]. Some geometrical arrangements can enhance theoretical properties while it may not be possible to implement due to fabrication complexity. Considering the impacts on optical behavior by the size and shape of holes, separation area between two adjacent holes, symmetrical or asymmetrical holes setup and implementation possibilities in the existing fabrication environment, the present PCF geometry is proposed. Asymmetrical cladding structure in a circular manner and hexagonal shaped core with unsymmetrical holes are organized in order to preserve the effective polarization state. Higher birefringence is facilitated for improving sensitivity as well as efficient wave transmission in both polarizing states. Material is added inside the core in a way that makes the core robust and keeps the material at a minimum level to increase the sensitivity and minimize the material absorption loss. The cross-section of the proposed PCF geometry is shown in Figure 6.1 (the core is enlarged for better view). Different polymer materials such as TOPAS, Zeonex, Silica, PMMA Teflon etc. can be used as the background material. Refractive index of TOPAS is considerably fluctuated over a large frequency range, well suited for minimum material dispersion [118]. Bulk material loss is also lower compared to other polymers. Further it is insensitive to environmental aspects such as humidity and water vapor absorption and has chemical inertness with special bio-sensing properties [87-88]. For these reasons, Topas is chosen as a background material in this PCF structure.

In the design (see Figure 6.1), a core radius of $r = 150\mu m$ is selected as optimum, where *Dcore = 2r*. For sectoring the hexagonal core, three rectangles are used; two kinds of

holes are formed where *S1 = S2 = r/2 – (strut + strut/4)*, *strut* denoting the separation area between two adjacent holes. The strut width of the core and cladding is fixed at 7.5 µm as optimum to reduce fabrication complexity as well as minimize the scattering loss, (note R. T. Bise *et al.* fabricated a PCF with 6.5 µm strut [109]). Lower strut size also helps to decrease the absorption loss and improve the sensitivity. The host material width around the core is denoted by p and depends on the porosity of the core. Porosity is defined as the ratio of air holes area inside the core and total area of the core. It can be presented by the following equations,

$$\text{Core porosity (\%)} = \frac{\text{Total air area in the core}}{\text{Total area of the core}} \times 100$$

At 80 % core porosity, value of *p* is exactly same as the selected *strut* size and this value of '*p*' is considered optimum for all the tested cases. The optimum value for geometrical parameters is listed in the Table 6.1. Fragments inside the core are filled by air or different targeted samples depending on the purpose of uses. Analytes filling in the core can be done by using the capillary action [134]. The mechanical assistance of an optical fiber is its bottleneck, but because of weeny length of the PCF for detection it will not be a problem. It is important to ensure that the sample does not enter in the cladding section, to confirm that the sample could be slowly fed from a hypodermic syringe. A blockage layer could be applied in the cladding section for protecting the entrance of the liquid samples from the insertion side. A selective filling method for infiltration of analytes has been developed by Huwang *et al*. [135]. In this method, the holes of the fiber are injected by the polymer NOA 73 using an external pump and a syringe. After that, the polymer is UV-curved and then several steps the air holes of the cladding are capped with the cured polymer with the central point of the core open. Then the unknown analyte is applied in the core and RI will be detected.

In the cladding region, six rectangles are used to sector the whole cladding where two different shaped air fragments are constructed. Because of this highly porous structured cladding, we have fixed the total fiber diameter 3 mm for improving durability in practical. The width of the slot *S3* of cladding is also same as the radius of the core. In the outer shell, a perfectly matched layer (PML) is employed as a boundary condition to protect the unwanted destructions by the environment or by the applied light source.

Table 6.1: Optimum geometrical parameters

Geometrical Parameters	Size (µm)
Core radius (r)	150
Core Diameter (D_{core})	300
Core air slot (S1)	65.625
Core air slot (S2)	65.625
Strut	7.5
PML	110
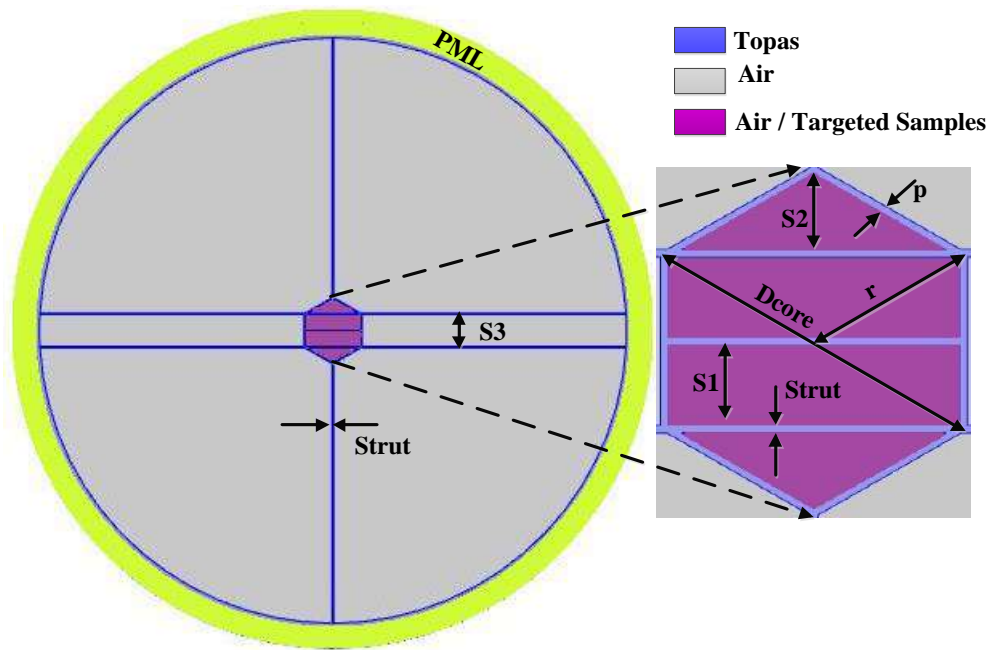
Figure 6.1: Cross section view of the proposed PCF; an enlarged view of the core is also provided.

6.2.2 Result Analysis and Discussion

Finite element method (FEM) with Comsol software (v.5.3a) is employed to design, and for modeling and measuring the interaction of electromagnetic pulses with associated components. FEM can solve for the wave propagation and estimating relevant properties including electromagnetic field distribution as a function of frequency or spatial position. Furthermore, FEM has the potential to fix the coupled physics, mechanics, chemistry and biological crux [136-138].

The use of FEM in the proposed PCF design is carried out in several steps such as model geometry selection, physical properties setting, boundary assignment and setting initial conditions, meshing, and finally partial differential equations (PDEs) for determining the electromagnetic field distribution. The complete mesh of the proposed geometry consists of 35834 domain elements and 2588 boundary elements with a maximum element size of 1801 µm, minimum element size of 17.1 µm, growth rate of 1.5, and curvature factor of 0.6. During the whole simulation, *fine* element size is maintained to improve the accuracy of the fiber.

6.2.2.1 THz Wave Transmission Properties

Tight confinement of the electromagnetic field in the core region is very important for efficient THz wave transmission. The state of the electromagnetic field in the core region is shown in Figure 6.2 for both polarizations at optimum geometrical conditions with different porosities. It is clear that the electric field distribution is narrowly confined in the core section and insignificant interaction is observed in the cladding area. At lower porosity the electromagnetic field is more closely confined in the core section due to the presence of the higher background material area in the core.
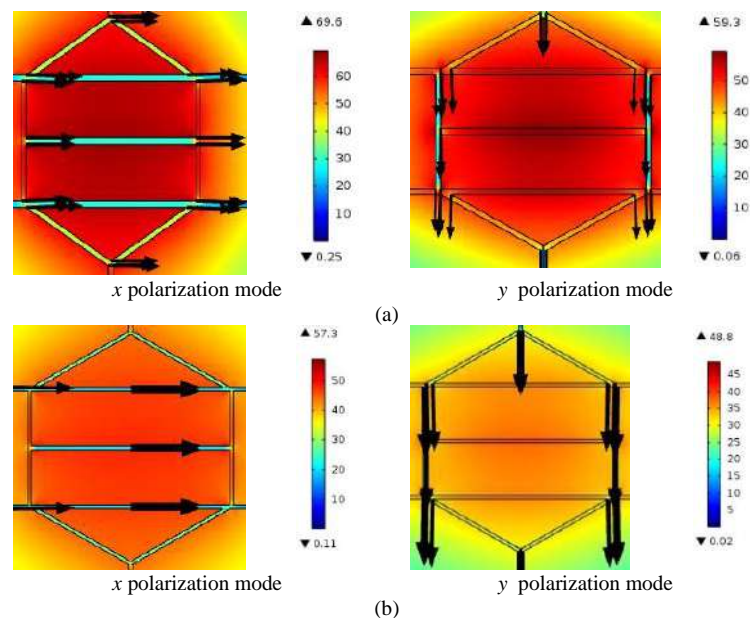
Figure 6.2: Electric Field Distribution in *x* and *y* polarization modes, (a) Dcore = 300µm, porosity = 80% frequency = 1THz, (b) Dcore = 300µm, porosity = 85% frequency = 1THz

The simulation results for confinement loss and EML with respect to frequency are depicted in Figures 6.3 (a) and (b) for *x* and *y* polarization, respectively. It is observed that EML is increasing linearly with the incremental value of frequency. This can be explained using the empirical relation $\alpha(v) = v^2 + 0.63v - 0.13$ *[dB/cm]* where *v* is the normalized frequency [26]. The incremental change of frequency helps to narrowly confine the optical pulse which rose up the EML due to intensive light matter interaction. Ultra-low EML of 0.013 cm^{-1} and 0.020 cm^{-1} is achieved for *x*-polarization and *y*-polarization modes, respectively at 1 THz for 80% core porosity. At higher frequency, the value of absorption loss coefficient increases due to the higher light intensity interacting with the material which enhances the EML. In general, the hollow core PCF shows comparatively lower EML than the porous core PCF due to the presence of the background material inside the core section for a porous core PCF.

The objective of this work is to propose a PCF structure that can be used for long-distance THz wave guidance as well as for unknown analyte identification cases. In the case of long-distance wave guidance, single-mode operation of the PCF is important

(a)

(b)
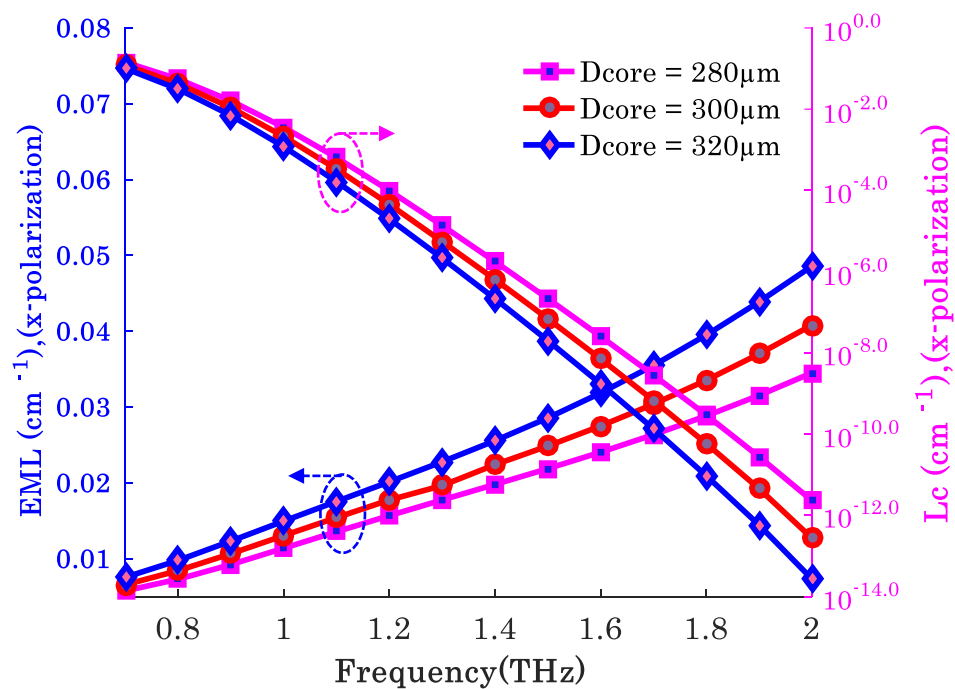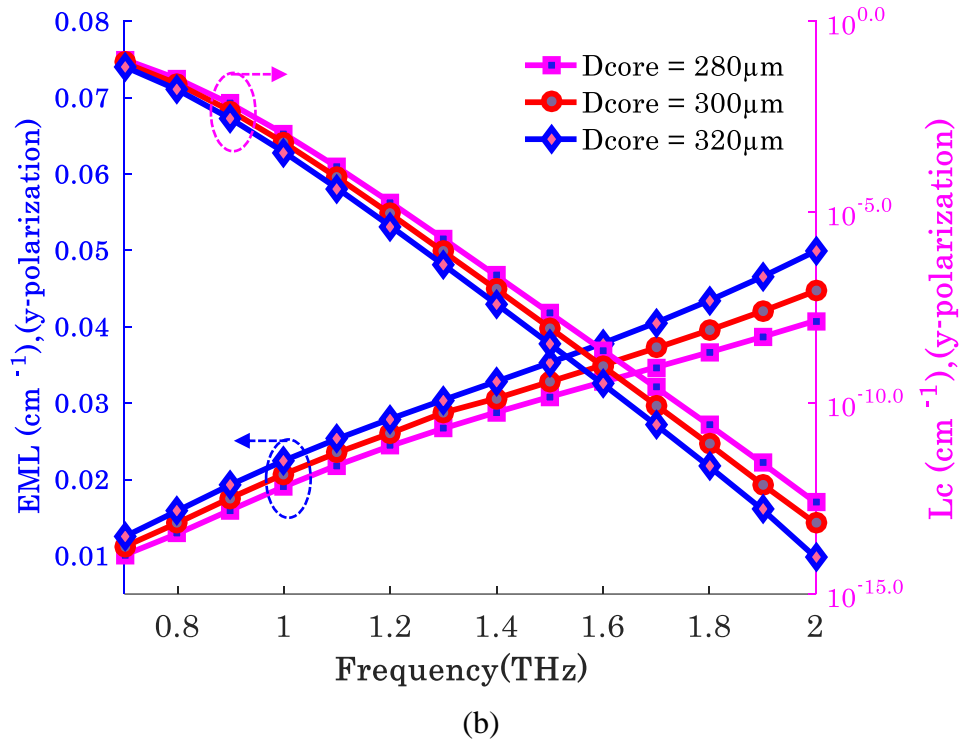
Figure 6.3: Behaviors of EML and confinement loss with respect to frequency at different core sizes (a) *x*- polarization, (b) *y*-polarization.
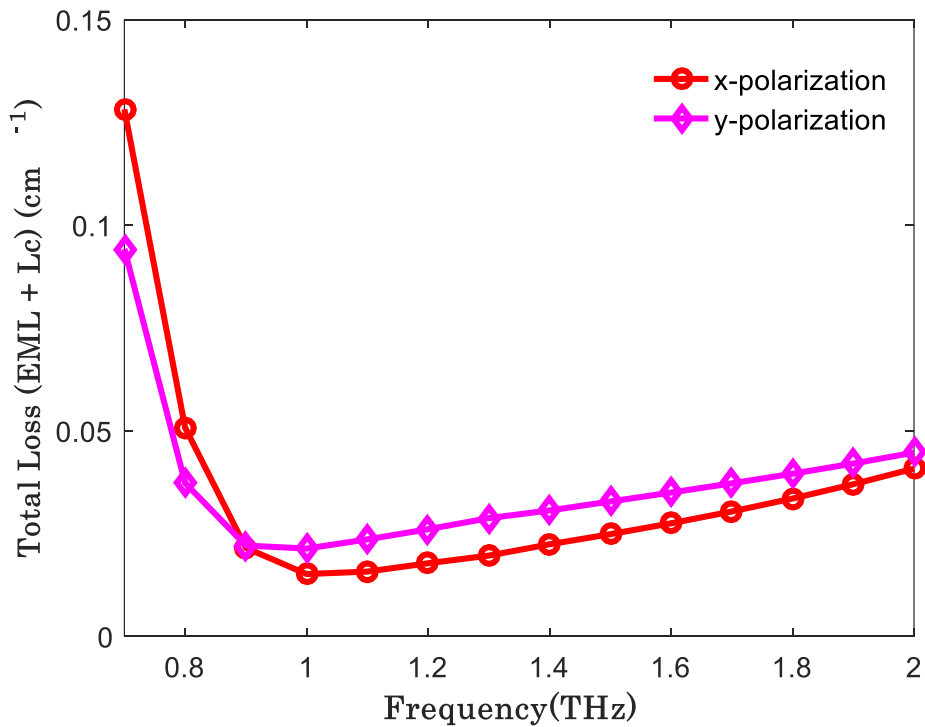
Figure 6.4: Total loss in *x* and *y* polarization mode as a funtion of frequency at optimum design conditions.

but in hollow-core structured PCF with a core radius of 150µm, it is quite impossible to operate in single mode. On the other hand, a lower core radius will reduce the sensitivity as well as core infiltration process will be more challenging. With respect to our objectives and considering the above-mentioned facts, the authors have decided to employ a porous core PCF, not only for high-frequency communication but also for satisfactory sensing application. In addition, this proposed PCF renders lower EML than the many of porous core PCF [6, 26-29].

Confinement loss as a function of working frequency is shown in the right y-axis of Figures 6.3 (a) and (b). It can be seen that with increasing frequency the confinement loss is reduced. This due to the fact that mode power starts to compress in the core region with the growth of frequency. For the proposed geometry of PCF and 1 THz operating region, the presented PCF exhibits 0.001 cm^{-1} confinement loss in x-pol mode and 0.0021 cm^{-1} in y-pol mode. Extension of core diameter increases the volume of Topas at fixed core porosity that facilitates the most interaction with the light intensity-consequently EML is augmented which can also be seen in Figures 6.3 (a) and (b). Note that a large core size helps to reduce the confinement loss because it assists to pass more light inside the core section.

Figure 6.4 depicts the scenario of total loss with respect to frequency for both x and y polarization mode. At optimum design parameters (see section 6.2) including operating frequency of 1 THz and core porosity 80%, the obtained total loss for x polarization is 0.0152 cm^{-1} and for y polarization, 0.0214 cm^{-1}. For calculating the total loss here, we considered EML and confinement loss. For a porous core fiber, bending loss is generally a negligible factor if we maintain a moderate bending radius.

From Figures 6.5 (a) and (b), it is observed that the effective area for both polarizations is decreasing with the incremental value of frequency. This can be attributed to confinement of light through the core region with increase in frequency, thus reducing the effective area of the fiber. An opposite scenario is observed when the core diameter is increased. A small core radius is used to penetrate the light pulse towards the cladding that extends the effective area. For the optimal design parameters with 80% core

porosity at 1 THz, the effective area of 3.6×10^{-7} m^2 and 2.9×10^{-7} m^2 are achieved in *x*-pol and *y*-pol, respectively.

Figures 6.5(a) and (b) also depict the core power fraction proficiency increasing in an upward manner with the change of frequency which is a desirable characteristic of an effective PCF. It is expected since higher frequency assists the light beam compression, consequently more power propagates through the core area that boosts the core power fraction. It is noticeable that x-polarized mode exhibits lower core power fraction than the y-polarized mode. It could be explained by the fact that the majority of the light is propagated through the core air holes in the y-polarized mode. These figures also demonstrate the behavior of core power fraction for various core sizes with the gradual change of frequency. It is observed that increasing core diameter improves the core power fraction, which is expected for if core diameter is increased, the light pulse will be confined nearly in the core region that helps to enhance the core power.

Figure 6.6 shows the dispersion characteristics in both polarizations with the frequency range of 0.7 THz to 2 THz. It is seen that proposed PCF geometry offers greatly flattened waveguide dispersion in the tested frequency range. For the optimal design parameters, this PCF reveals a waveguide dispersion of 0.396 ± 0.020 ps/THz/cm in *x*-polarization mode and 0.512 ± 0.065 ps/THz/cm in *y*-polarization, superior to those reported in literature [6, 26-29].

In Figure 6.7, the variation of Birefringence is demonstrated for the optimal design conditions with the change of frequency. With the incremental change of frequency, the refractive mode index changes between x and y polarized modes are increased. After a certain frequency, the refractive mode index changes responded in a decremented manner due to the tight confinement at higher frequency. It is noticed that a significant refractive index difference is attained due to asymmetric PCF structure development. A superior birefringence of 12.6×10^{-3} is gained by the proposed PCF.

It is noticed from Figure 6.8 that the value of *V* is increasing linearly with the increasing frequency. In optimum design parameter, this presented PCF structure shows the
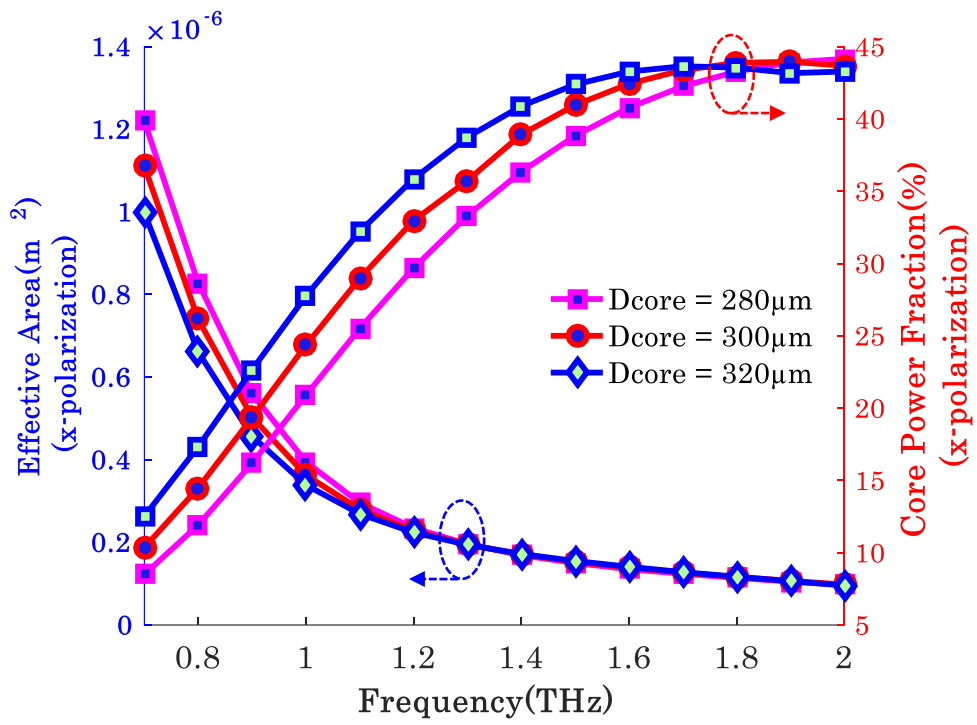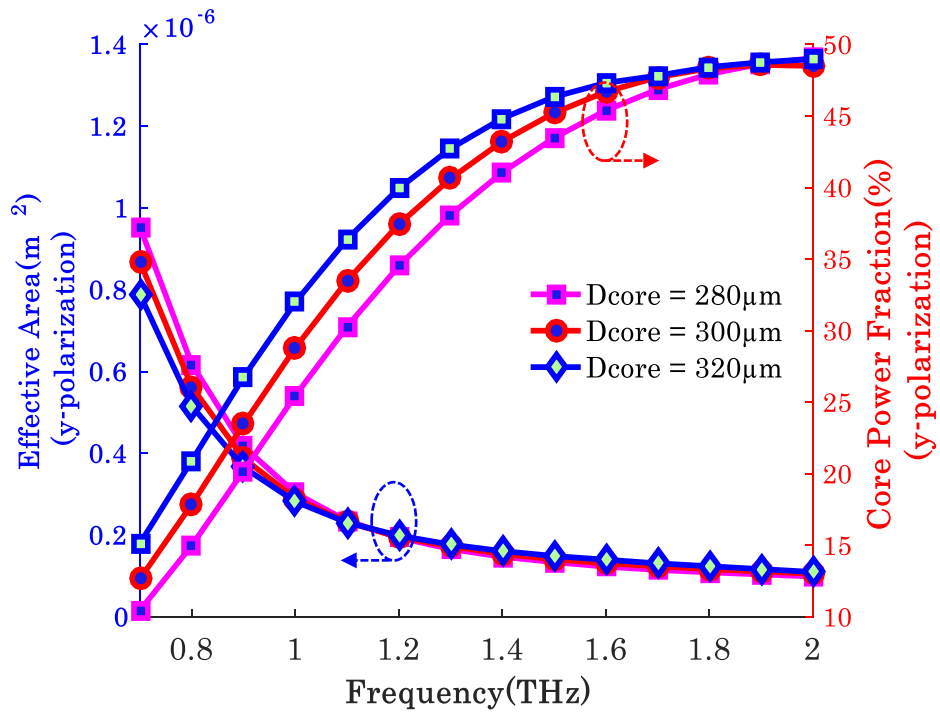
Figure 6.5: Change of effective mode area and core power fraction in *x* and *y* polarization mode with frequency at different core diameters.
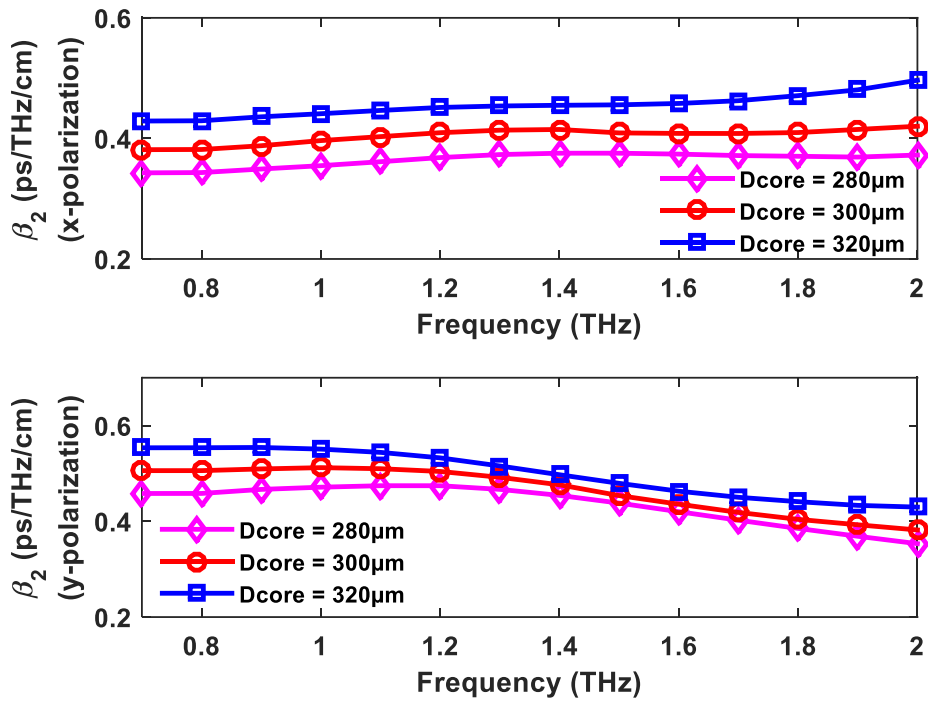
Figure 6.6: Behavior of waveguide dispersion in *x* and *y* polarization mode with respect to frequency for variouis core diameters.
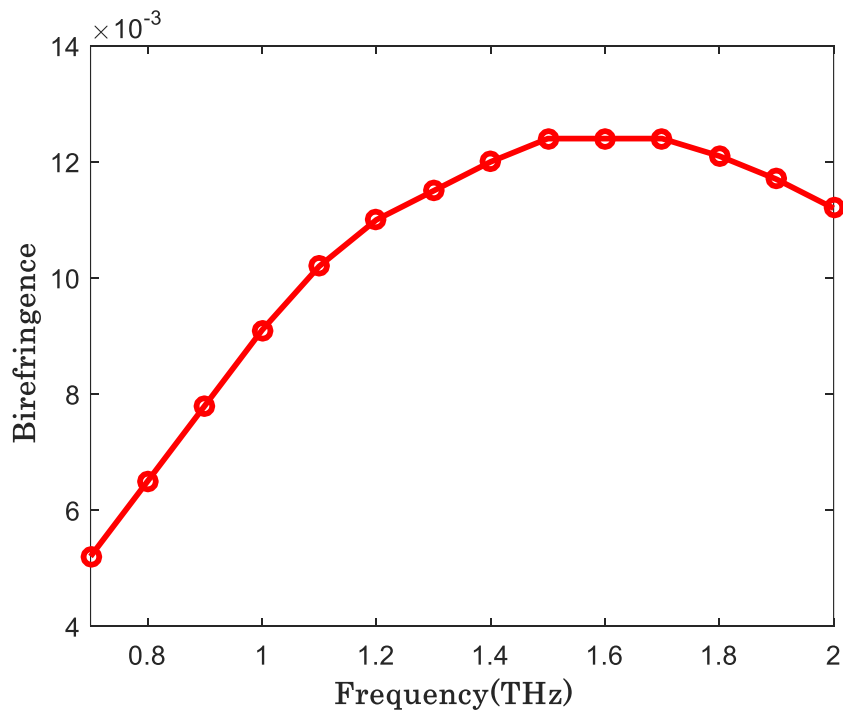
Figure 6.7: Birefringence with respect to frequency at optimum design conditions.
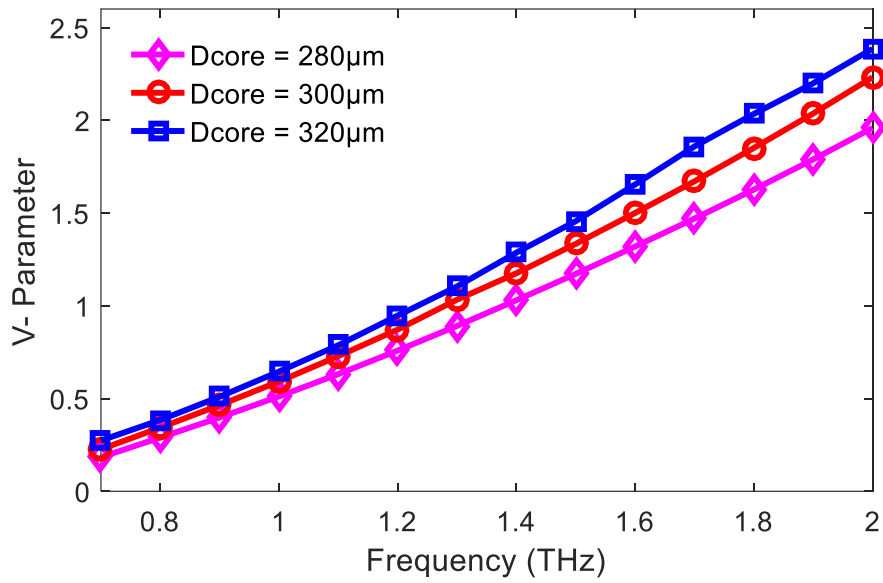
Figure 6.8: *V*-parameter as a function of frequency for different core sizes.
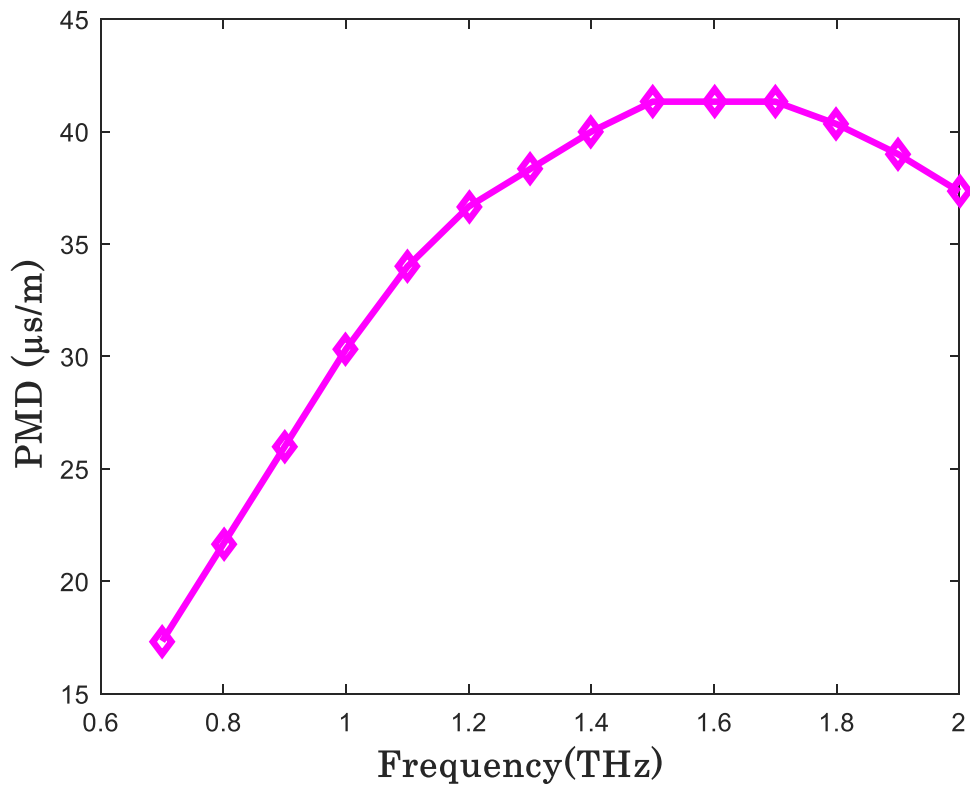
Figure 6.9: Polarization mode dispersion as a function of frequency at optimum design conditions.

maximum value of *V* is 2.23 at the highest frequency of 2 THz, which satisfies the requirements of single mode operation. From the achieved value, it is clear that our proposed waveguide is able to operate in single mode condition in the frequency range of (0.7 - 2) THz.

Higher value of delay between the velocities of light in two orthogonal modes of fiber degrades the performance of a PCF. For attainting better accuracy of a PCF, PMD should be minimum. The response of the PMD in terms of group delay for the proposed PCF is shown in Figure 4. It is noticed that the proposed PCF renders very small PMD over a wide range of frequency 0.7 to 2 THz. At optimum operating frequency of 1THz it gives very low PMD of 30.33 (µs/m).

6.2.2.2 Sensing Properties

One purpose of this paper is to present a PCF that in addition to providing effective THz wave transmission can be used to sense air pollutants and a number of damaging liquid analytes. As for the air pollutants, cyanide (RI = 1.45), dioxin (RI = 1.656), nitrogen oxide (1.449), and hydrogen sulfide (RI =1.3682) are considered. Liquid chemicals such as cholesterol (1.525), methanol (1.33), ethanol (1.36), and benzene (RI = 1.501) are studied. For this purpose, first the interaction of light intensity with the liquid analytes and evanescent samples are investigated for the proposed PCF, and shown in Figures 6.10 and 6.11 for different polarization modes. It is noted that the light intensity has strongly interacted with the analytes, while demonstrating negligible interaction of in the cladding region. The findings are indicative of improved sensitivity for the PCF.

Further, the potential of liquid chemicals detection of the proposed PCF in THz frequency range is illustrated in Figure 6.12 for *x* and *y* polarization modes. Sensitivity is directly related to the refractive index of the analytes and this is also theoretically true as per (3.26). As seen in Figure 6.12, this PCF structure provides the highest sensitivity for cholesterol and lowest for ethanol among the detected chemicals since these carry the utmost and modest refractive index respectively. Sensitivity is also

x-polarization   y-polarization   x-polarization   y-polarization

(a)   (b)

x-polarization   y-polarization   x-polarization   y-polarization

(c)   (d)
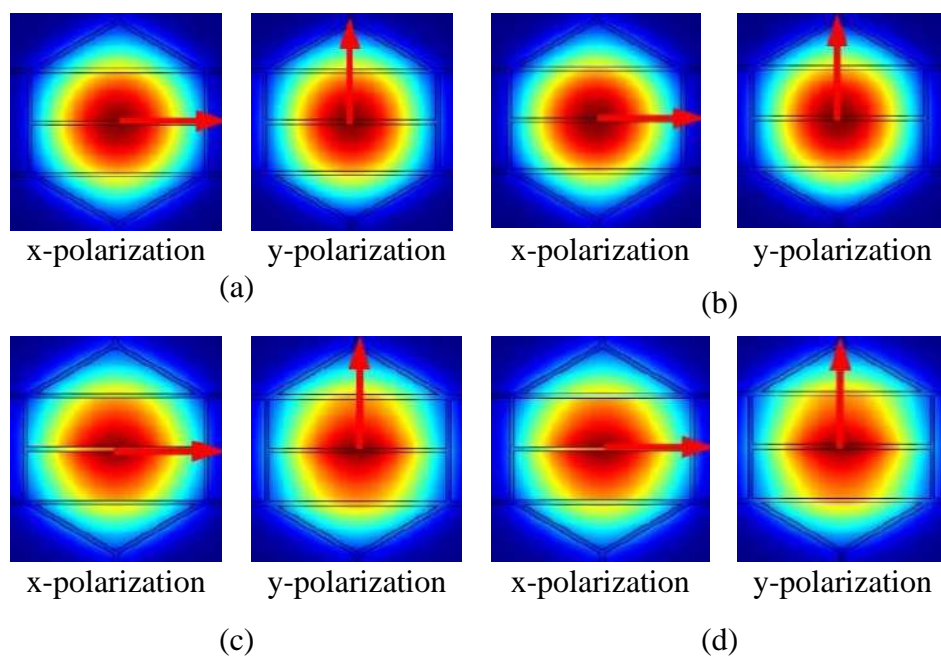
Figure 6.10: Light and liquid analytes interaction in *x* and *y* polarization modes: (a) Benzene, (b) Cholesterol, (c) Ethanol and (d) Methanol.

x-polarization   y-polarization   x-polarization   y-polarization

(a)   (b)

x-polarization   y-polarization   x-polarization   y-polarization

(c)   (d)
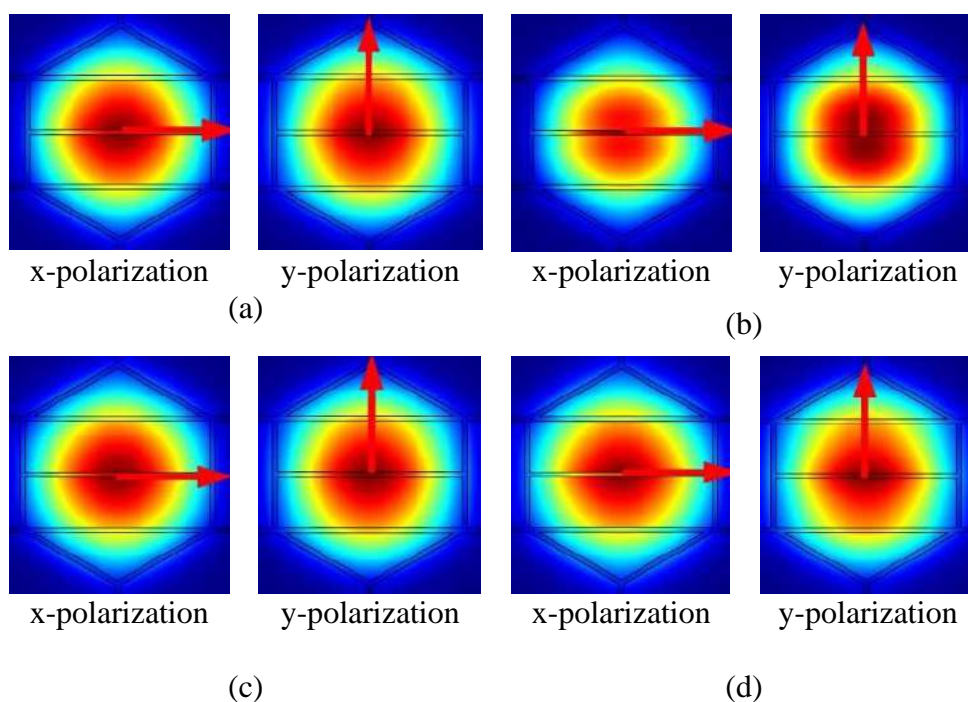
Figure 6.11: Light and air pollutants interaction in *x* and *y* polarization modes: (a) Cyanide (b) Dioxin (c) Nitrogen Dioxide and (d) Hydrogen Sulfide.

131

related to the working frequency. As the frequency is increased, light beam compression and narrowly confined within the core with a higher light intensity boosts the interaction of light and liquid sample, thus enhancing the sensitivity. With the incremental changes in frequency, the sensitivity increases till a certain frequency. Due to a higher frequency, the light pulse is more compactly confined in the core region and strongly interacted with the applied analyte that enhancing the core power fraction. Additionally, the refractive mode index also increases with the frequency as a result of sensitivity increase. For optimum design parameters, at 2.5 THz the proposed PCF gives superior performance in terms of sensitivity and losses. At this specified frequency the applied analytes have strong absorbance potential [139]. At 2.5 THz frequency the proposed PCF renders in *x*-polarization 90.4 % sensitivity for cholesterol, 90.3 % for benzene, 90.1 % for ethanol and 89.9 % for methanol and 90 % for cholesterol, 89.8 % for benzene, 88.1 % for ethanol and 87.5 % for methanol in *y*-polarization mode.

Air pollutants detection capability of the PCF is demonstrated in Figure 6.13. The highest sensitivity achieved is 91.1 % and 90 % is in *x* and *y* polarization modes for dioxin since it's refractive index is higher than the other air pollutants. Besides, this PCF is exceptionally performed in sodium cyanide, nitrogen dioxide and hydrogen sufide detection. 90.2 % in *x*-pol and 89.3 % in *y*-pol modes for Cyanide, 90.2 % in *x*-pol and 89.2 % in *y*-pol modes for Nitrogen dioxide, 90.1 % in *x*-pol and 88.2 % in *y*-pol modes for hydrogen sulfide are attained by this designed PCF structure at the optimum geometric condition.

Strut size has a crucial impact on different optical properties like sensitivity. Lower strut size assists to improve the sensitivity by reducing the light materials interaction area. On the other hand, lower strut size may cause fabrication complexity. Keeping this in mind, we have selected a moderate strut size of 7.5 µm as optimum. Since R. T. Bise et al. has already fabricated PCF with 6.5 µm strut [109], the sensitivity of this
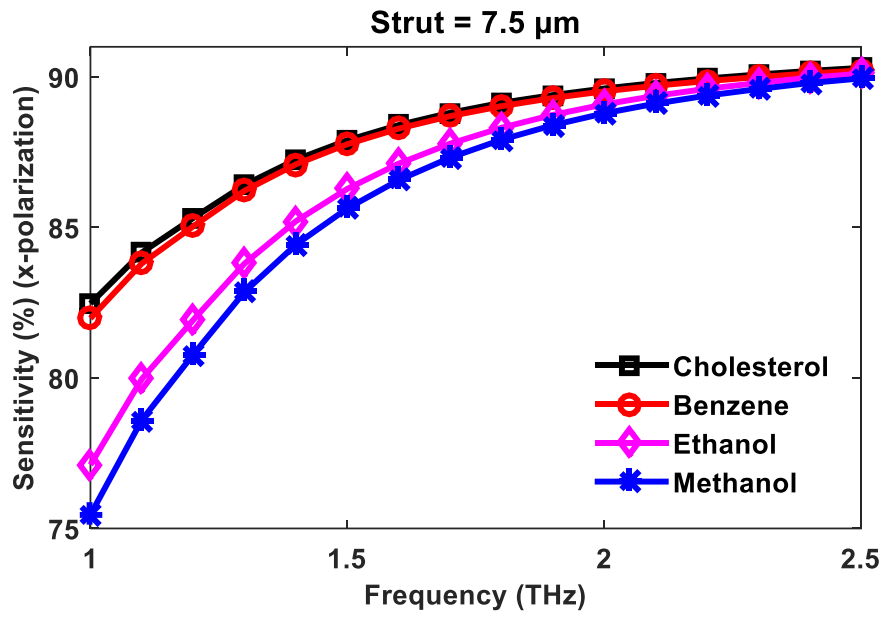
(a)
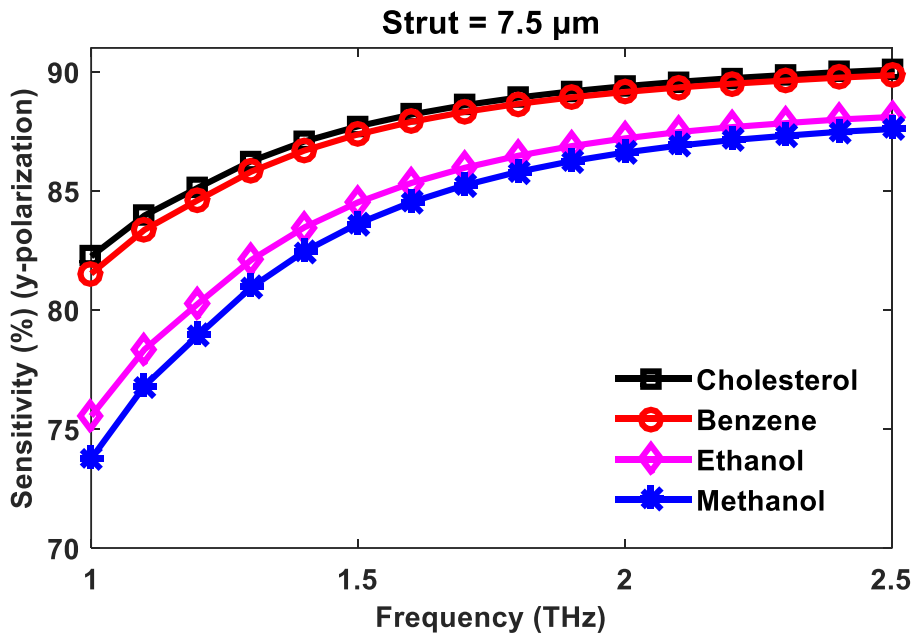
(b)

Figure 6.12: Sensitivity with respect to frequency for different liquid analytes at optimum design conditions for the proposed PCF: (a) *x*-polarization and (b) *y*-polarization.
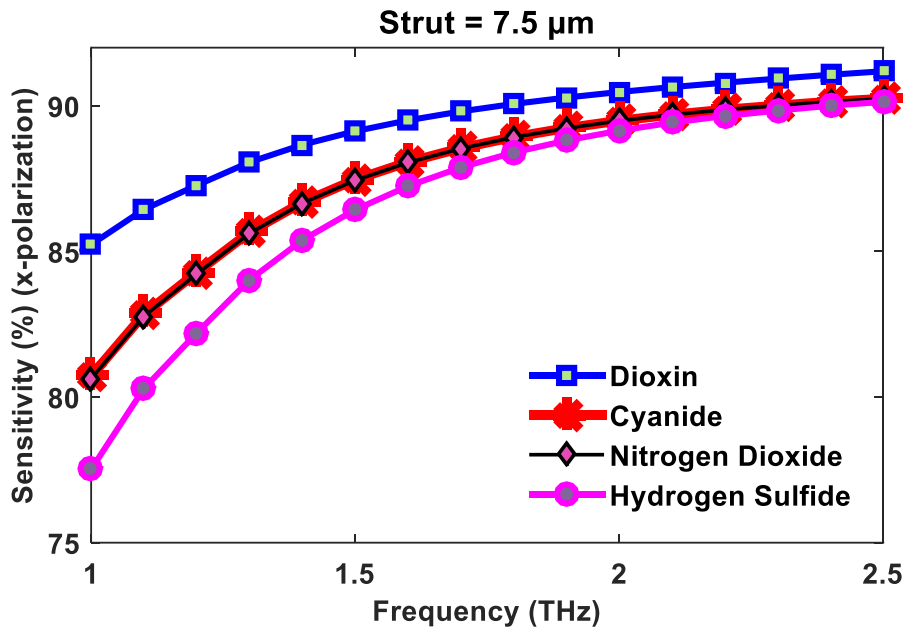
(a)
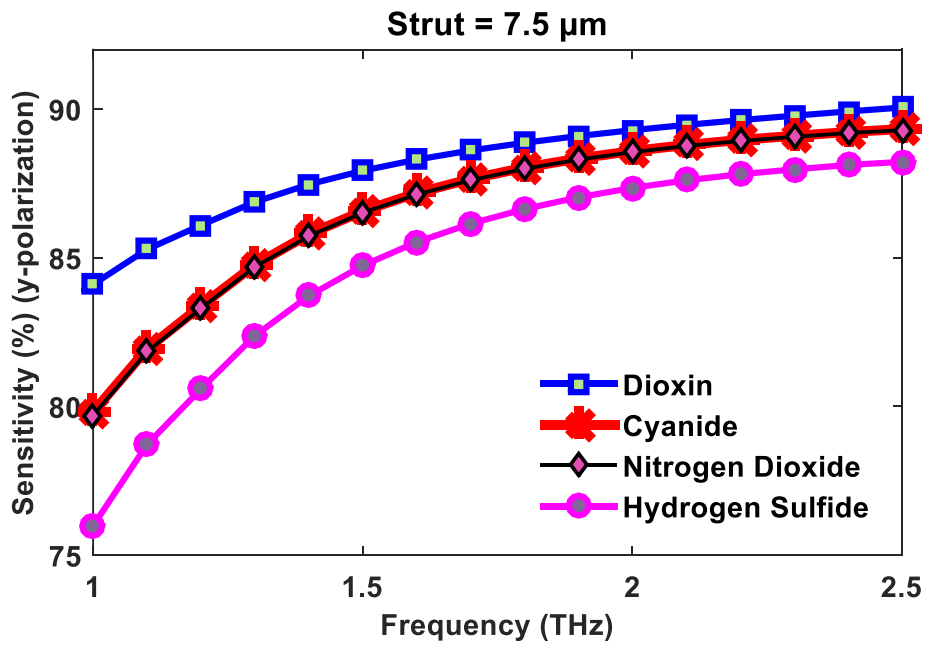
(b)

Figure 6.13: Sensitivity with respect to frequency for different air pollutants at optimum

design condition for the proposed PCF (a) *x*-polarization and (b) *y*-polarization.

presented PCF at 6.5 µm strut size for all the detection cases are presented in Figures 6.14 and 6.15 for *x*-polarization mode. These figures indicate that lower strut size improves the sensitivity, nearly 2% higher sensitivity for all cases because of 1 µm strut size reduction. If existing fabrication processes can tolerate 6.5 µm or less strut size it can be favorable for performance improvement. In [1] it is claimed that 2 µm strut size is tolerable in the existing fabrication platforms for a suspension structured PCF but avoiding scattering loss they have considered 6 µm strut throughout the investigation. For the same reason as well as considering the durability in practice we have fixed it at 7.5 µm.

Because of the strong interaction between light and analytes in the designed PCF, significant improvement is achieved to reduce the confinement loss as shown in Figures 6.16 and 6.17. Higher frequency helps to compact the electromagnetic radiation, thus, restricting light leakage beside the core, consequently, confinement loss is minimized. Notice that the confinement loss is over a wide studied frequency range of 1-2.5 THz.
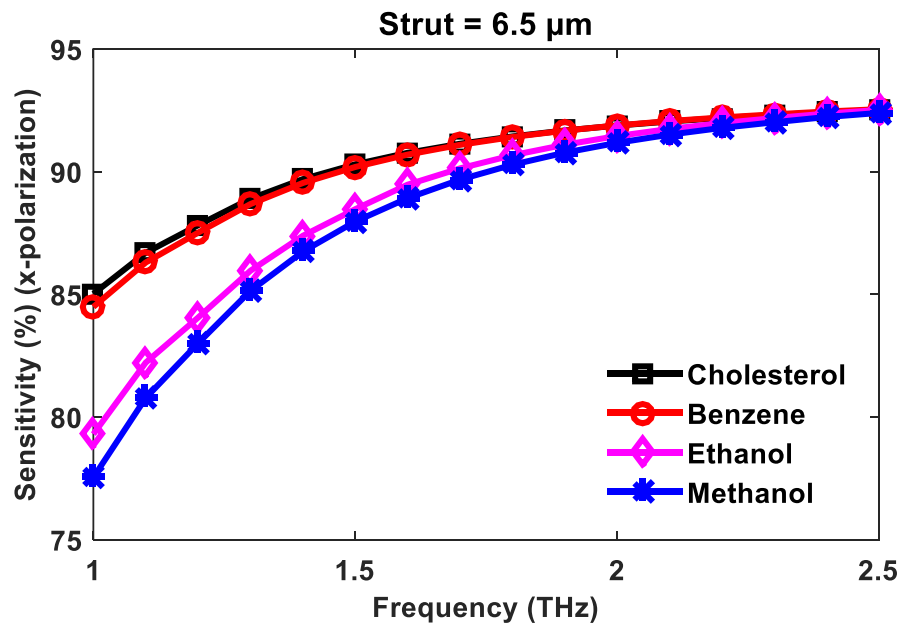
Figure 6.14: Sensitivity with respect to frequency for different liquid analtyes for strut size of 6.5 µm in *x*-polarization.
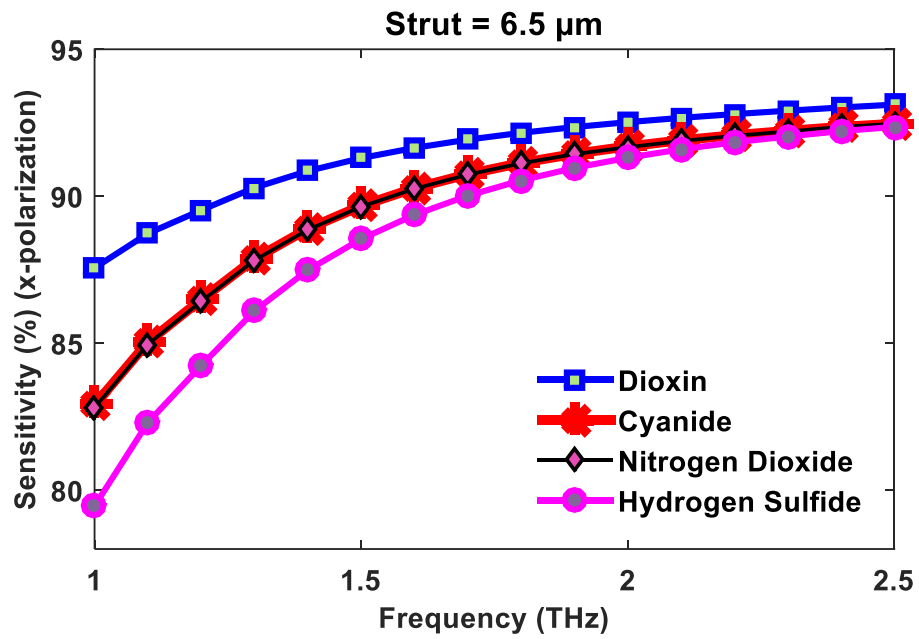
Figure 6.15: Sensitivity with respect to frequency for different air pollutants for strut size of 6.5 µm in *x*-polarization.
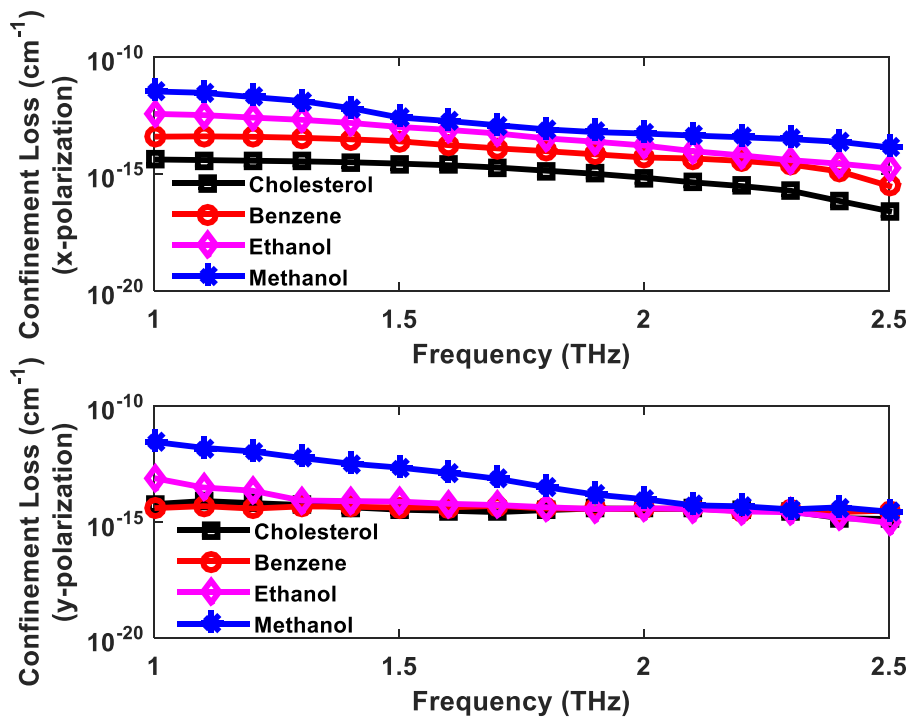
Figure 6.16: Variation of confinement loss with frequency for different liquid analytes at optimum design conditions in *x*-polarization and *y*-polarization.
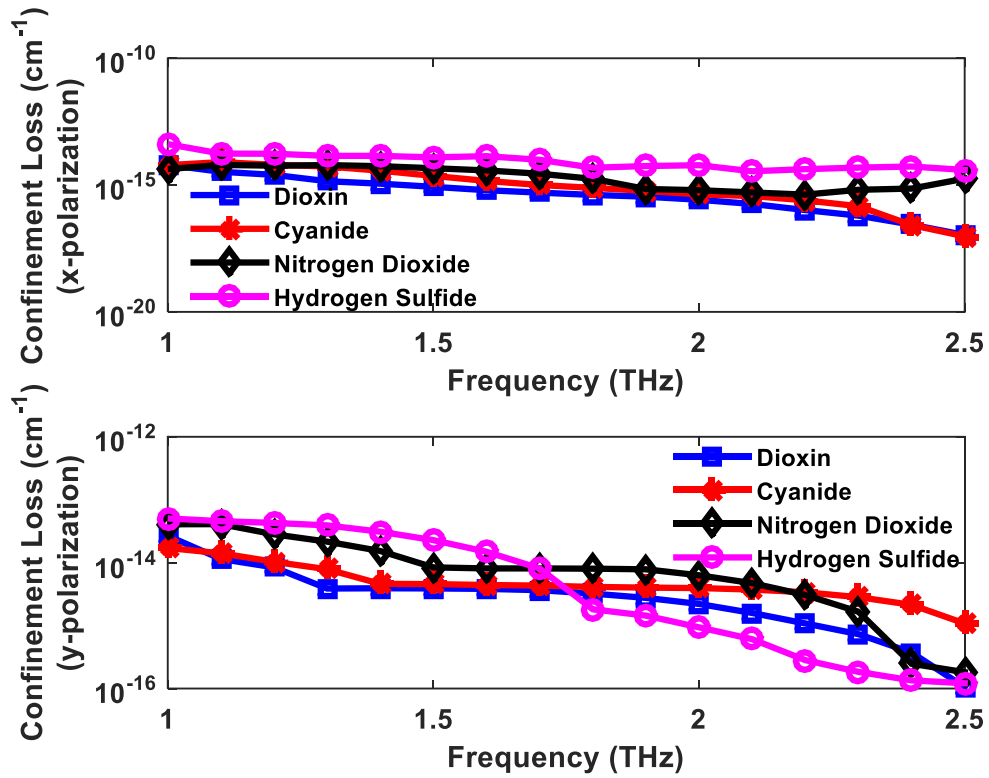
Figure 6.17: Variation of Confinement loss with frequency for different air pollutants at optimum design conditions in *x*-polarization and *y*-polarization.

The reduction in confinement loss is highly comparable with previously presented PCF structures [1-2, 22, 31, 33, 43-45]. At selected geometric condition and working frequency of 2.5 THz, the lowest confinement losses of $(10^{-13} \sim 10^{-16})$ cm^{-1} are observed for *x*-polarization and *y*-polarization in liquid substances detection cases. On the contrary, negligible confinement loss of $(10^{-14} \sim 10^{-16})$ cm^{-1} in *x*-polarization and $(10^{-13} \sim 10^{-15})$ cm-1^1 in *y*-polarization are also noticed for the identification of air toxics.

Light intensity absorption by the background material is presented in Figures 6.18 and 6.19 with frequency for different analytes in *x* and *y* polarization modes at optimum design conditions. For a porous core fiber, EML is directly related to frequency. Increase of frequency improves the compactness of light intensity that creates high interaction environment onto the light and Topas inside the core. Strong light material interaction causes the EML to change in an upward manner as evident in the figures. The proposed PCF performs in a superior manner with an ultra-low EML throughout

137

the detection. For the case of liquid chemicals, the lowest EML achieved is 0.016 ± 0.0015 cm^{-1} in x-polarization and 0.0205 ± 0.0025 cm^{-1} in y polarization modes. Similarly, for evanescent analytes (air pollutants) the lowest EML achieved is 0.015 ± 0.001 cm^{-1} in x mode and 0.02 ± 0.001 in y mode polarizations. These results are quite similar to those reported in the PCF literature [1, 44-45].

Light matter interaction area also related to the frequency and which is clearly demonstrated in Figures 6.20 and 6.21 for various liquids analytes and in evanescent analytes. These figures exhibit that the calculative area gradually decreases with increasing frequency due to close confinement of light at a higher frequency. At optimum design conditions, a moderate effective area is achieved, nearly 4×10^{-8} m^2 in both polarization modes for all the cases.

To enhance the sensing capability, polarization preserving property is very important that can be ensured by observing the birefringence profile of proposed PCF. Higher birefringence helps to compensate the PMD as well as propagation loss. Effective refractive index differences between the orthogonal polarization modes indicate the level of birefringence. It can be boosted up by asymmetrical arrangement in the core and cladding. In this context, an asymmetrical core-cladding structured PCF is considered.

Birefringence profiles of both type analytes sensing cases are presented in Figures 6.22 and 6.23 with respect to the frequency at optimum design conditions. It is observed that birefringence declines very slowly with the augmentation of frequency. Although because of the strong interaction between light pulse and analytes at a higher frequency the birefringence decreased slightly, a significant birefringence is noticed within the operating range for all the tested cases. The achieved birefringence by this structure is also comparable with recently design PCF for similar applications [22, 31].
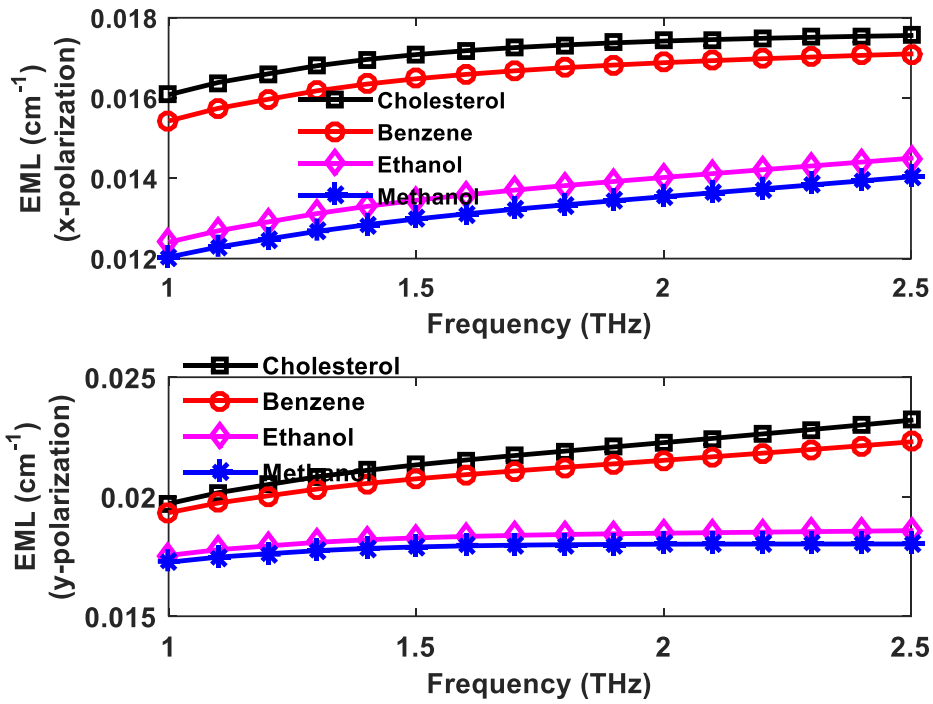
Figure 6.18: EML with respect to frequency for different liquid analytes at optimum design condition in *x*-polarization (top) and *y*-polarization modes (bottom).
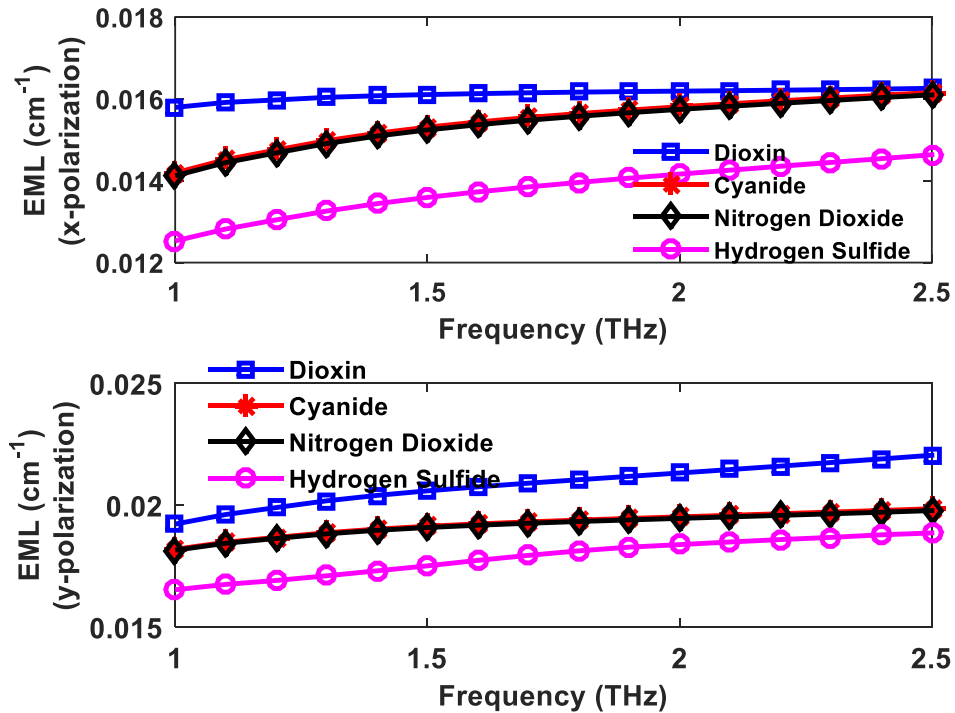
Figure 6.19: EML with respect to frequency for different air toxics at optimum design condition in x-polarization (top) and y-polarization (bottom) modes.
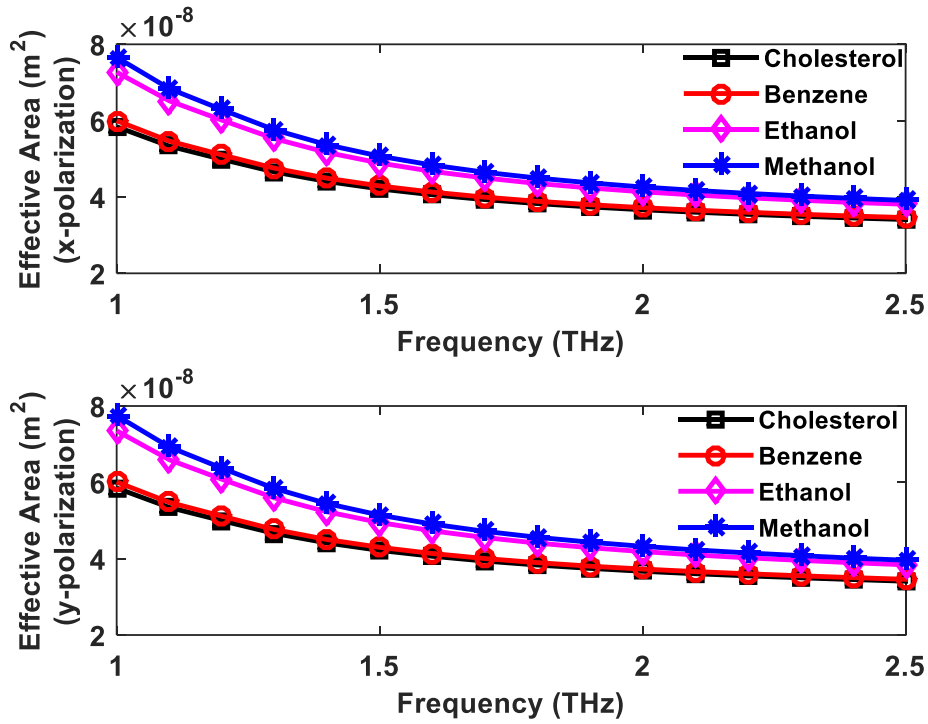
Figure 6.20: Effective Area for different liquid analytes as a function of frequency at optimum design condition in *x*-polarization (top) and *y*-polarization (bottom).
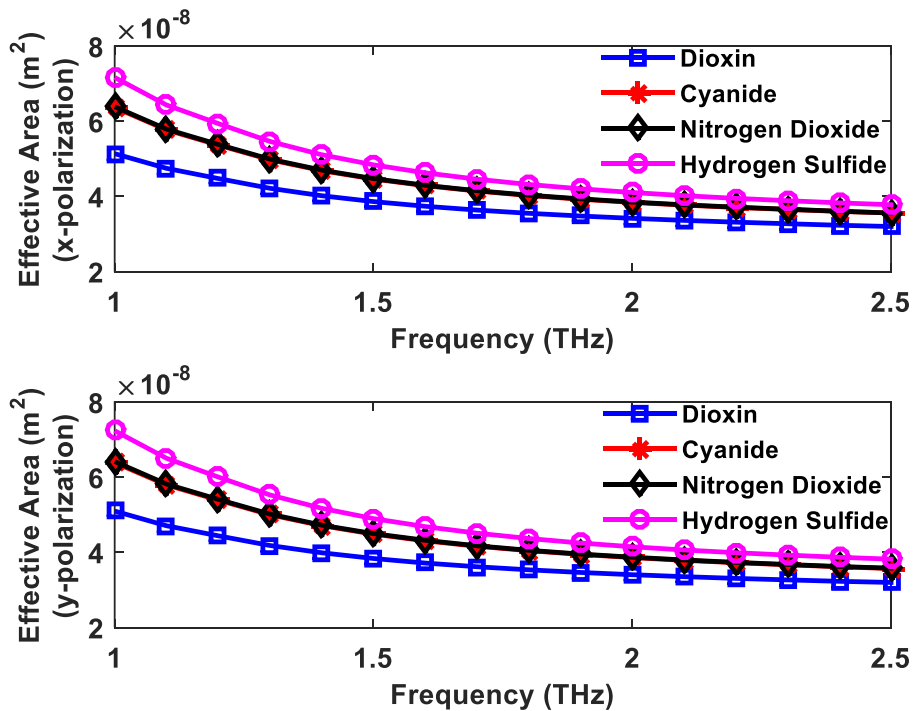
Figure 6.21: Effective Area for different air toxics as a function frequency at optimum design condition in *x*-polarization (top) and *y*-polarization (bottom).

140
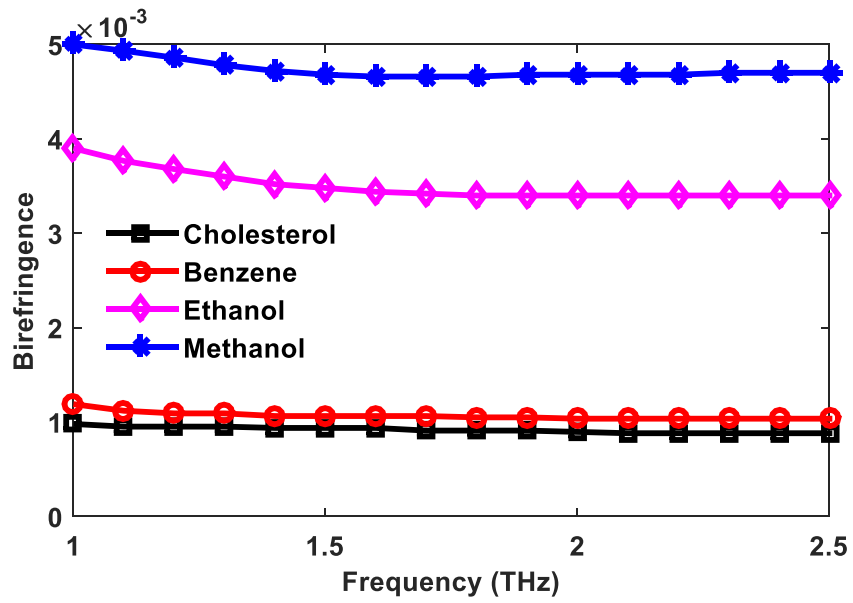
Figure 6.22: Birefringence profile of proposed PCF at optimum design condition for different liquid analytes as a function of frequency.
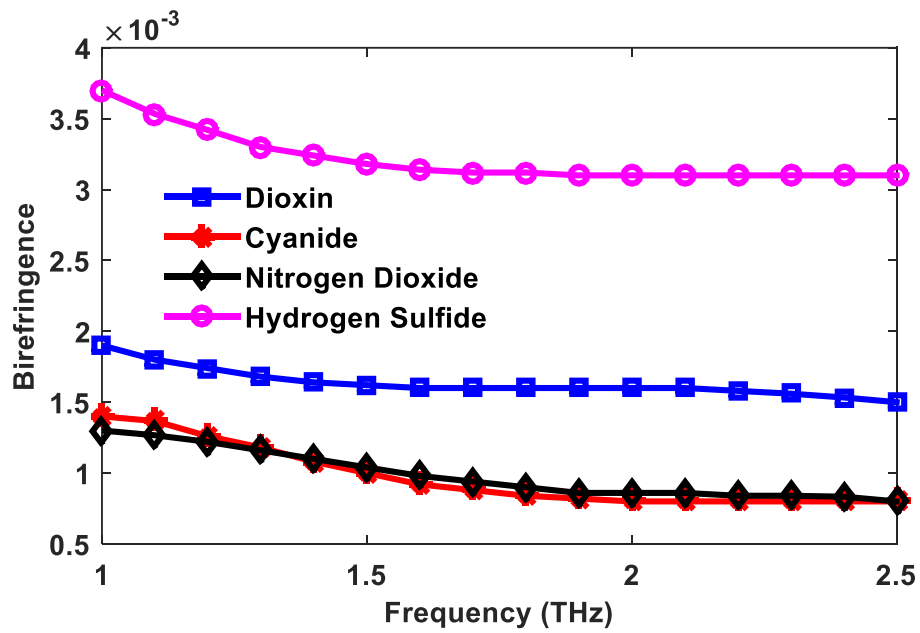
Figure 6.23: Birefringence profile of proposed PCF at optimum design condition for different air pollutants as a function of frequency.

Table 6.2: Comparison with previously proposed works in PCF for THz wave transmission

Ref.	f THz	EML (cm^{-1})	β_2 ps/THz/cm	Geometry	
				Core	Cladding
[6]	1	0.038	± 0.38	Circular	Quasi
[26]	1	0.056	± 0.10 (x) ± 0.18 (y)	Elliptical	Kagome
[27]	0.6	0.066	± 0.60	Hexagonal	Hexahedron
[28]	1.5	0.095	-	Hexagonal	Honeycomb
[29]	1.3	0.03	± 0.01(x) 0.120(y)	Elliptical	Hexagonal
This PCF	**1**	**0.013(x)** **0.020(y)**	**± 0.020 (x)** **± 0.065 (y)**	**Hexagonal**	**Sectored**

Table 6.3: Comparison with previously proposed works for substance detection.

Ref.	Sensitivity (%)	Targeted Substances	L_c	α_{eff} cm^{-1}
[22]	83.4	H_2O	4.5×10^{-9} cm^{-1}	-
	83.1	C_6H_6	1.7×10^{-9} cm^{-1}	
	82.6	C_2H_5OH	1.02×10^{-9} cm^{-1}	
[43]	48.26	Gas	1.26×10^{-5} dB/m	-
[1]	85.8	CN	1.62×10^{-9} cm^{-1}	0.023
[31]	63.5	H_2SO_4	1.42×10^{-17} dB/km	-
[44]	76.44	C_2H_5OH	2.33×10^{-3} dB/m	0.023
	77.16	C_6H_6	3.07×10^{-6} dB/m	
	73.20	H_2O	2.84×10^{-2} dB/m	
[45]	79.8	$C_{17}H_{21}NO_4$	3.108×10^{-13} cm^{-1}	0.003
	80.3	$C_9H_{13}N$	2.583×10^{-13} cm^{-1}	0.003
	82	$C_{13}H_{16}ClNO$	2.5801×10^{-15} cm^{-1}	0.098
[2]	73.78	C_2H_5OH	10^{-8} dB/m	-
This PCF	90.2 ± 0.2 (x-polarization) 88.5 ± 1.5 (y-polarization)	$C_{27}H_{46}O$ C_6H_6 C_2H_5OH CH_3OH	**$(10^{-13} \sim 10^{-16})$** cm^{-1} (x & y polarization modes)	0.014 - 0.022
	90.6 ± 0.5 (x-polarization) 89 ± 1 (y-polarization)	$C_4H_4O_2$ NaCN, NO_2, H_2S	**$(10^{-14} \sim 10^{-16})$** cm^{-1} (x-polarization) **$(10^{-13} \sim 10^{-15})$** cm^{-1} (y-polarization)	0.014 - 0.021

Table 6.4: Comparison of sensitivity between the proposed PCF and that of [140].

Refractive Index of applied analytes	Highest Sensitivity (%)	
	Proposed PCF	[134]
1.562	99.9853	99.56
1.518	99.7546	99.60
1.45	99.9736	99.14
1.366	98.8210	98.36
1.33	98.0505	97.93
1.26	97.7765	97.4

Table 6.2 and Table 6.3 present a comparison with existing PCF literature for the case of THz wave propagation and the detection of substances. It is seen that this proposed PCF improves all the essential optical properties in both cases.

Recently, hexagonal core structured PCF with porous core and sectored-cladding has been reported [24]. But the core-cladding structure of the presented PCF and [24] is different only both the cores are hexagonal in shape. The core-cladding hole's size, position, and shape are totally dissimilar. The objective of our presented work is to propose a PCF structure that can be used for long-distance THz wave guidance as well as for unknown analyte identification cases. The present paper provides an extensive analysis of sensing performance for a number of liquid and gas analytes, as well as for THz wave guidance indicating a wider range of applications. In contrast, the work [24] evaluated the optical properties only for THz wave guidance. Additionally, our proposed PCF shows lower EML than the mentioned work. The achieved EML in [24] is 0.026 cm^{-1} and 0.028 cm^{-1} for TM and TE mode, respectively; on the other hand, our proposed PCF attains 0.013 cm^{-1} & 0.020 cm^{-1} for x and y polarization modes accordingly. Note that EML is the main limiting factor for an optical waveguide in THz transmission. Although there is some similarity between the present work and [140], the latter is employed only for sensing applications with different analytes. For fair comparison, we have tested sensitivity of the proposed PCF with those in [140]. The results are provided in Table 6.4. It is seen that in general the proposed PCF gives better sensitivity.

We also would like to add that several works employ hexagonal-shaped cores as the proposed one [22, 1, 40, 128, 141-142]. However, all the above-mentioned (including our proposed one) PCF structures are unique, only the shape of the core is hexagonal. Some Authors considered the hollow-core structure for their study while others adopted the porous core structure. In the case of a porous core, the air holes' size, shape, and positions differ in all the above-mentioned works. Most importantly all the PCF structures are constructed with almost unique cladding geometry. It is also mentionable that the tested chemicals are different for all the cases. A list of previously developed PCFs with the hexagonal-shaped core is given in Table 6.5. Core hole geometry, cladding structure, sensitivity and EML of this PCF are also listed in Table 6.5.

The proposed PCF is constructed with asymmetric sectored cladding and two types of air holes in the hexagonal-shaped core, indicating limited design similarity with the existing work. It is also seen that apart from the proposed PCF, other PCF structures were not tested for both sensing and waveguiding applications. For example, in [22] the PCF geometry is designed using rectangular structured air holes in the hexagonal core with a Kagome structured cladding, and only liquid analytes are investigated for sensing. On the other hand, the present paper provides an extensive analysis of sensing performance for a number of liquid and gas analytes, as well as for THz wave guidance indicating a wider range of applications. Additionally, our proposed work renders better sensitivity than [23]. For example, the highest sensitivity attained in [23] is 85.6% for RI = 1.33, in contrast our proposed PCF attained 89.9 % for RI = 1.33 where RI denotes refractive index. It should be mentioned that the proposed PCF renders lower EML than the previously proposed hexagonal-shaped core PCFs for THz waveguiding (listed in Table 6.5). The present PCF also provides better sensitivity than the previous works except [128, 142]. Because of the hollow core structure selection in [128, 142], higher sensitivity is obtained. In general, the hollow core PCF shows comparatively higher sensitivity than the porous core PCF due to the large interactive area in the core section with the absence of the background material.

Table 6.5: Comparison of geometry and performance among various hexagonal-shaped core PCF

Ref.	Geometry		Tested for		EML (cm^{-1}) (for waveguiding)	Sensitivity (%) (for sensing)
	Core	Cladding	Waveguiding	Sensing		
[22]	Hexagonal shaped with rectangular holes	Kagome	No	Yes	-	85.7
[1]	Hexagonal shaped with circular holes	Suspended	No	Yes	-	85.8
[24]	Hexagonal shaped with symmetric slotted holes	Rectangular Strips	Yes	No	0.026 ~ 0.028	-
[141]	Hexagonal shaped with hexagonal shaped holes	Hexagonal	Yes	No	0.021	-
[40]	Hexagonal shaped with hexagonal shaped holes	Kagome	Yes	No	0.029	-
[142]	Hexagonal Hollow	Hexagonal	No	Yes	-	94.124
[128]	Hexagonal Hollow	Hexagonal	No	Yes	-	99
This Work	**Hexagonal shaped with asymmetric holes**	**Sectored**	**Yes**	**Yes**	**0.013 ~ 0.020**	**91.1 (porous core) 99.98 (hollow core)**

6.3 Summary

The objective of this Chapter is to introduce a PCF structure that can be used for long-distance THz wave guidance as well as for unknown analyte identification cases. In the case of long-distance wave guidance, single-mode operation of the PCF is important but in hollow-core structured PCF with a core radius of 150µm, it is quite impossible to operate in single mode. On the other hand, a lower core radius will reduce the sensitivity as well as core infiltration process will be more challenging. Concerning our objectives and considering the above-mentioned facts, the present paper employs a porous core PCF, not only for sensing but also for satisfactory THz communication. For a fair comparison, we have tested the sensitivity of our proposed PCF using a porous as well as a hollow-core structure. It is seen that with a porous core, the sensitivity is higher than those of [22, 24], and with a hollow core, a very high sensitivity of 99.98 % is achieved which is better than those of [128, 142]. As compared

to existing works, superior performance in terms of low losses, flattened waveguide dispersion, high core power fraction, and large effective area have been obtained in THz wave propagation. For the liquid chemical and air pollutant analytes, a number of improvements have been demonstrated that include negligible confinement loss, ultra-low EML, and moderate effective area, as compared to several recently reported results. Overall, the designed PCF has a good degree of potential for diverse applications in the THz domain including wave transmission and sensing of different harmful substances.

Apart from the PCF's geometry development, practical implementation is a challenging task. In the context of current developments in fabrications, suggestions have been provided regarding the potential for fabricating the proposed PCFs in Chapter 7.

Chapter 7

Fabrication Potential of PCF and Experimental Setup

7.1   Introduction

Besides geometry selection and evaluation of optical properties, fabrication potential of a PCF structure is an important concern for PCF development. Some existing fabrication techniques and their fabrication process will be discussed in this Chapter. In addition, scopes of fabricating the proposed designs will be described briefly considering the present fabrication technologies for the PCF structures introduced.

7.2   Different fabrication techniques

At the initial stage, stack and draw was the most successful technique for PCF fabrication [143-144]. Presently, several advanced fabrication techniques such as sol-gel [109], capillary stacking [145], drilling [146], extrusion[147-148], and 3D printing [110, 149-150] have been developed for manufacturing the symmetrical or asymmetrical structured PCF. Among these techniques some are not suitable for asymmetrical geometry and some others well suited for any structural conditions. Some of the existing fabrication techniques are discussed in the following sections.

7.2.1 Stack and draw

Stack and draw is one of the most favorable fabrication process for fabricating a PCF structure. Four simple steps need to follow to construct the PCF geometry [143]. The first step of this process is to construct the capillaries as per the design. The next step of this process is called preform making. It is basically, stacking process of capillaries. The capillaries are stacked to make a preform as per the PCF design. After that the preform stack needs to be inserted in a glass tube. By fusing in the drawing process a microstructured preform or cane can be obtained. The final step of the fabrication

process is the cane drawing into the fiber including desired dimension fixing, cladding pitch, outer fiber diameter, etc. Air holes size and their regularities can be controlled by applying air pressure inside the preform. Temperature, preform feed rate, as well as drawing speed can be tuned in this fabrication process [151]. Fabrication steps of stack and draw process are displayed in Figure 7.1. Porous core and hollow core PCF fabrication process are almost similar but in case of hollow core only some capillaries are omitted from the center of the PCF [151]. The major drawback of the stack and draw process is that this process is labor intensive and quality depends on the craft of preform making [151].
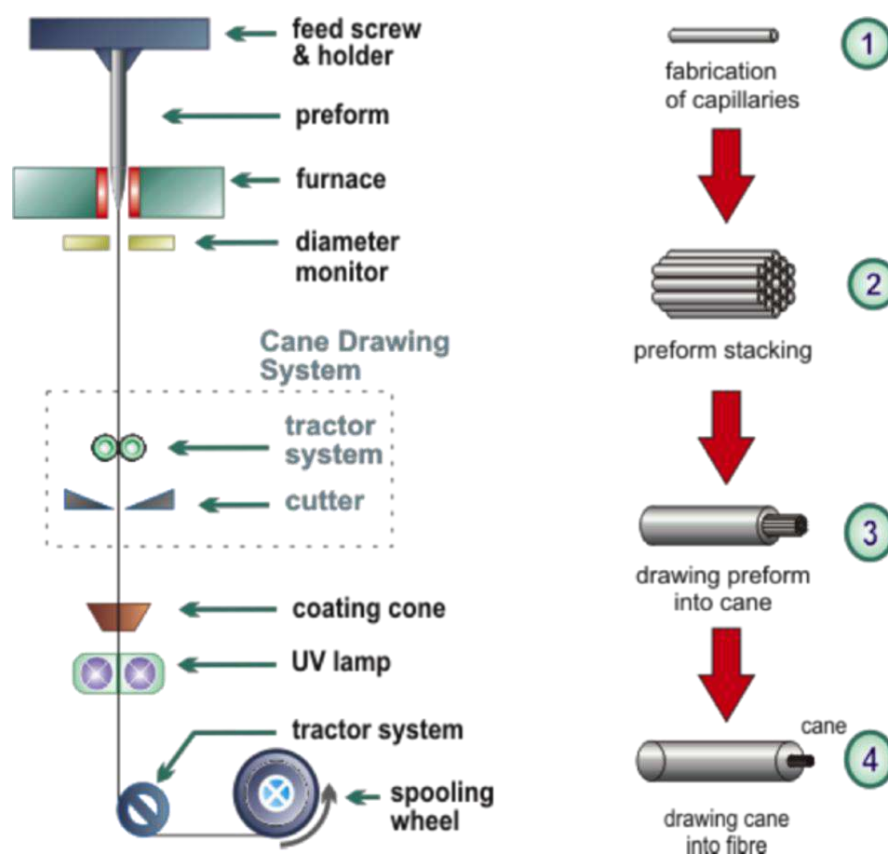
Figure 7.1 Fabrication process of PCF using stack and draw [151]

7.2.2 Sol-gel

Sol-gel fabrication technique was introduced in the Bell labs for fabricating optical fiber [153]. This technique has been used for decades for fiber fabrication. Recently it has

148

been used for various glasses and ceramic processing [153,154]. Two steps are involve in this technique and the name sol-gel coined from these steps. First step of this process is the preparation of solution (sol) which contains small pieces of ion that indicates that the mixture is uniform in nanoscale. Gelling (gel) is the second step of this process. In this step the solution is solidified. The solution will be poured on the shape of the mold. The shape of the mold will be constructed as per the PCF design. It is to be noted that this solution has a unique advantage is that the solution is homogeneous with multi-components. This method provides the facility to control the homogeneity, the composition and high concentration of dopants [155]. Another advantages of this method is that the gelling process takes place through the chemical reaction at room temperature and this process does not require high temperature like other methods [155].

7.2.3 Extrusion

Extrusion is one of the superior techniques for complex PCF geometries fabrication. In this process the PCF can be produced by a single step, where the fiber can be drawn directly from the bulk glass. Extrusion technique allows to produce any shape (complex or simplex) if a die is present. Still, there is an issue, selective doping of rare-earth ions is a complex task [156]. In the case of silica, this technique will not be suitable because no such die materials exist that can bear up the operating temperature during processing without contaminating the glass. The extrusion technique is well suited for several materials at comparatively low softening temperature such as compound silica glasses [157], soft glasses (including sulfur hexafluoride (SF6) [158], lead silicate (SF57) [159, 160], chalcogenides [161] and tellurites [162]) and polymers [163]. Extrusion technique already proved the potentiality for fabricating different structures by using all the above-mentioned materials. In some cases, during the thermal process due to the formation of crystals, it may enhance the fiber losses.

7.2.4 3D printing

Only two simple steps are involved in this technique. A digital file needs to be prepared first as per the design, the design is then printed by a 3D printer. The printing is done

layer by layer to produce a 3D structure, preform, using powdered metal or plastic material [164]. It shows excellent performance for fabricating PCF because only single material is used in the PCF structure. 3D printer also able to fabricate two material devices by using dual head 3D printer [165]. The most advantageous part of this technique is that any arbitrary design can be fabricated with high accuracy.

7.2.5 Mechanical drilling

This technique is performed by the direct drilling of the material. A large range of geometry specially symmetrical holes with geometric shape PCF fabrication, mechanical drilling is a well stablished fabrication technique. This technique allows a broad range of materials such as chalcogenides glasses, soft-glass [166] and polymer [162], as well as whose hardness is not as high as silica glass [167]. Extra care needs to be taken for controlling the drilling device [167]. Using this technique, it would be difficult to handle when the structure will be constructed with very low strut size, it also introduced roughness at the surface [168].

Selection of fabrication process is not only related to the geometry of PCF, but also dependent on the materials. Thus, some knowledge regarding the properties of different useable materials is a requirement. Some possible materials for PCF development are discussed briefly in the next section.

7.3 Background materials for fabrication of PCF

Compared to silica glass, polymer materials offer several advantages such as lower manufacturing cost, high mechanical strength and higher chemical elasticity. Recently developed polymer like Topas or Zeonex offers minimum losses. Polymer materials can be used for various important and necessary application areas such as THz propagation, bio-sensing, and optical-imaging, etc. Various polymer materials including materials for our proposed PCFs are discussed here.

PMMA: Polymethylmethacrylate (PMMA) was first introduced by the British chemists Rowland Hill and John Crawford in the early 1930s at Imperial Chemical Industries

(ICI) in England. PMMA is a lightweight and shatter-resistant clear thermoplastic [169]. Organic compound methyl methacrylate (MMA) is the raw material of the PMMA which is made in the form of synthetic polymer. Pure PMMA is basically a brittle material. Thus, it can be useable for optical device devolvement where much more mechanical strength is not essential. PMMA also cannot tolerate the toughness and scratches.

TEFLON: Teflon is a synthetic polymer and its chemical name is Polytetrafluoroethylene (PTFE). Carbon and fluorine are the two constituting atoms of forming Teflon. It has higher chemical resistances but heating at over 300 degrees Celsius is injurious for health. Radiation resistance capabilities is very lower and high costs than compared to many of similar materials are the limiting factors of Teflon [169].

TOPAS: Cyclic Olefin Copolymer (COC) TOPAS is ultra-pure, crystal-clear material with a wide range of unique properties. Refractive index of TOPAS considerably fluctuates over a large frequency range, well suited for minimum material dispersion [119]. Bulk material loss is also lower compared to other polymers. Further it is insensitive to environmental aspects such as humidity and water vapor absorption and has chemical inertness with special bio-sensing properties. [87-88].

ZEONEX: The chemical name of Zeonex is Cyclo Olefin Polymer (COP) and this is the most recently introduced material in the polymer group. Several advantageous properties of Zeonex include low water absorption, lower impurities, higher heat resistance, low dielectric constant and loss tangent. Furthermore, zeonex offers excellent chemical resistance capacity, higher transparency, and low absorption loss. The refractive index fluctuations over wide THz frequency is very low that indicates a negligible material dispersion is than enhanced in the THz regime [170].

Topas, Zeonex, Silica, PMMA, Teflon etc. can be used as background material for PCF devices. Among these, Topas and Zeonex have shown lower absorption loss than others. Topas and Zeonex have almost similar glass transition temperature but the refractive index of Topas negligibly fluctuates over a wide range of THz spectrum

[119]. Moreover, Topas is impervious to environmental effects and has chemical idleness with exceptional bio-sensing peculiarity [87-88]. For these reasons, Topas has been chosen as background material for the proposed PCFs geometry.

7.4 Current developments and scopes of PCF fabrication

Fabrication complexity minimization by proper geometrical setting is a key challenge for PCF development. Keeping that in mind, mostly symmetrical, and suspended core cladding PCFs are proposed in this research. It is interesting to note the work of W. Talataisong *et al.* [149] where a novel desktop 3D printing fabrication technique is demonstrated and a suspended structured polymer PCF thereby implemented. Their fabricated polymer optical fiber is presented in Figure 7.2. Z. Liu *et. al.* has implemented a microstructure fiber using a stack and draw process for sensing applications. A hexagonal arrangement of asymmetric circular holes, as well as a suspended-structure fiber have also been accomplished [144]. Schematic diagram of the stacked preform of their proposed PCF geometry is shown in Figure 7.3. Complex spider wave and rectangular shaped holes have been implemented by S. Atakaramians [56], shown in Figure 7.4. Extrusion fabrication technique has been utilized in this case. They have successfully implemented these PCF structures with 71% porosity. Besides, several complex structures including suspended and hollow core PCF fabrication techniques have also been analyzed by A. M. Cubillas *et al*. [171] for chemical sensing and photochemistry. H. Ebendorff-Heidepriem has presented a 3D printed with extrusion dies technique that paves the way of more complex PCF fabrication [110]. For sensing applications, different PCF structures have been implemented including suspended and complex kagome by M. Calcerrada et al. [172]. Suspended, butterfly shaped, even twin-core PCF are implemented by M. De *et al*. [173] and applied for sensing applications.
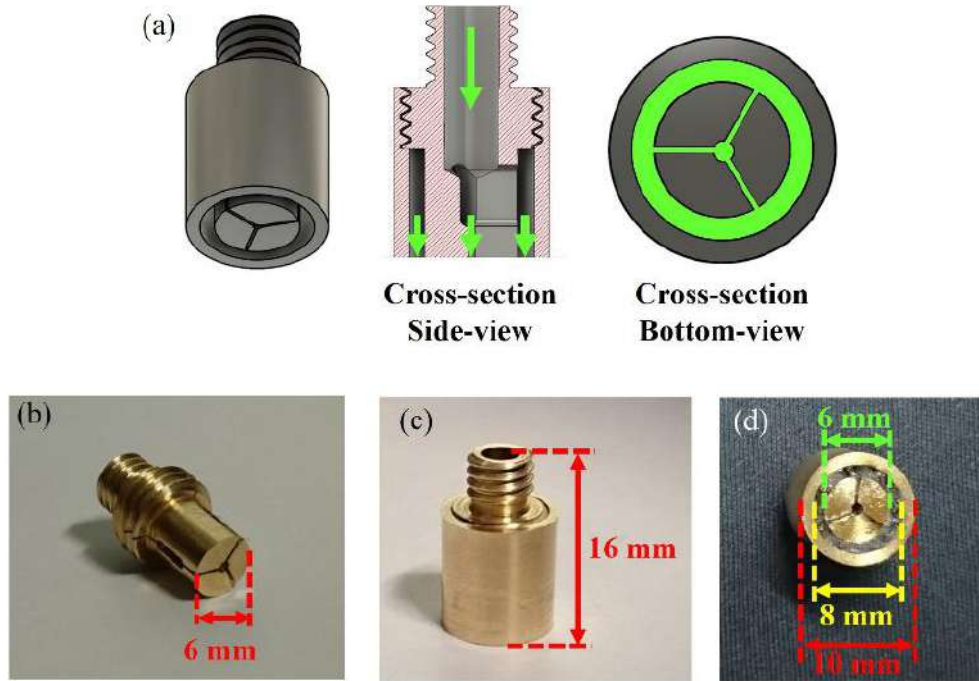
Figure 7.2 Fabricated polymer optical fiber [149].
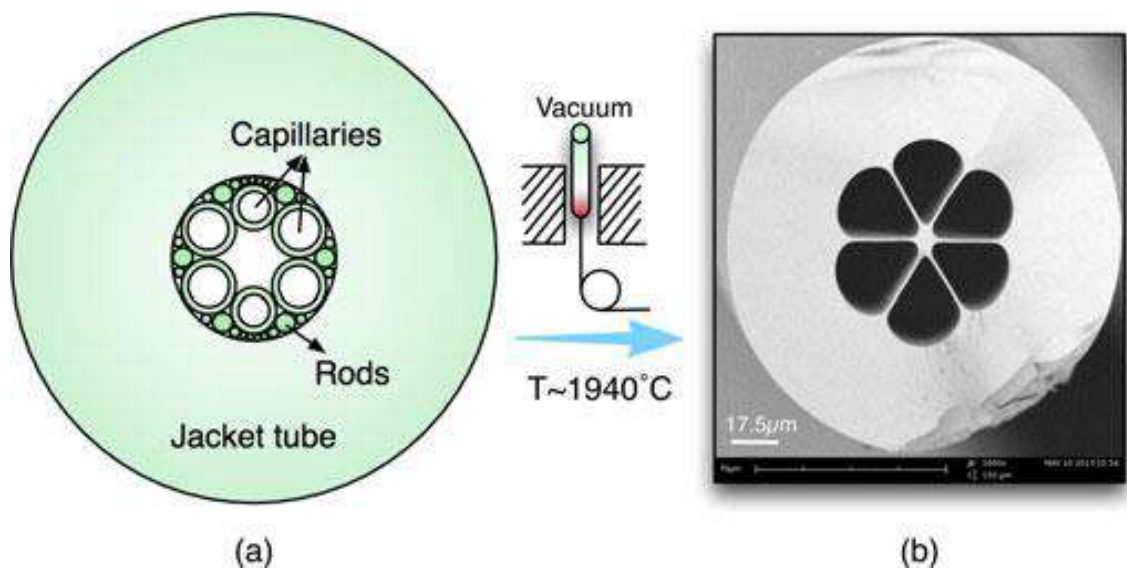
Figure 7.3 Schematic diagram of the stacked preform [144]
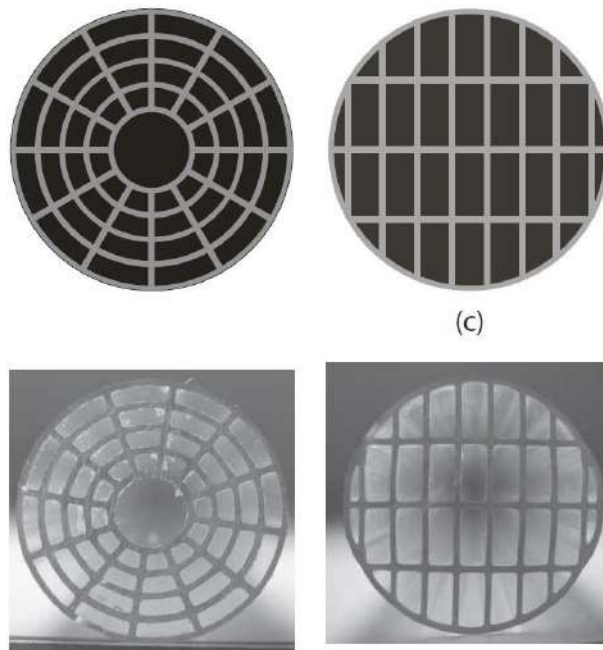
Figure 7.4: The extruded preform of the spider wave and rectangular shaped holes PCF [56]
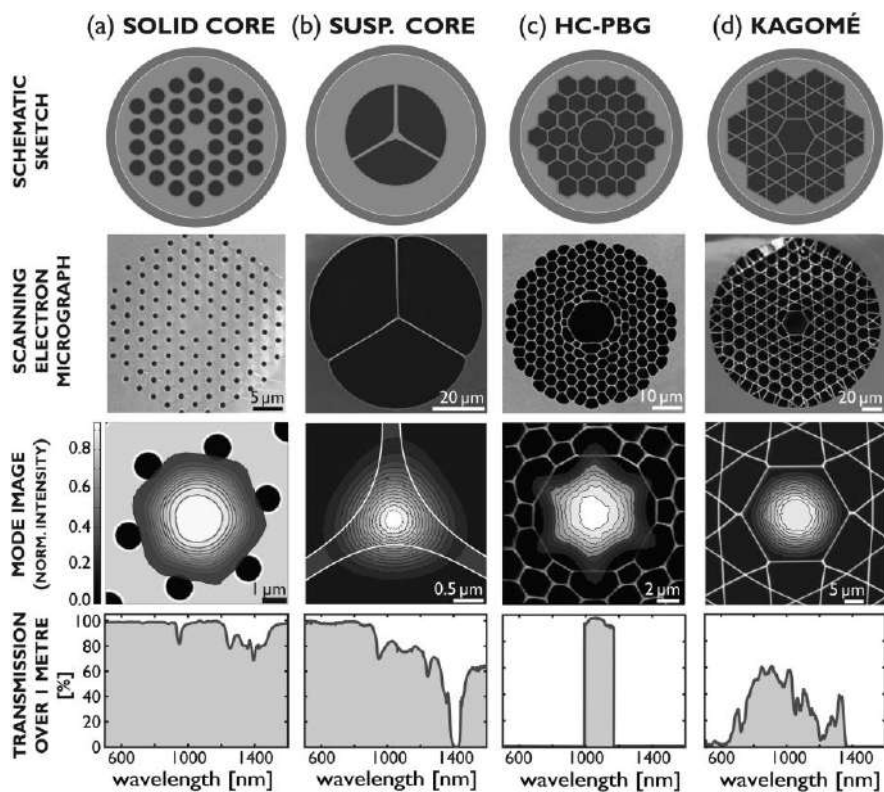
Figure : 7.5 Schematic diagram of some typical structures of PCFs used in chemical sensing [171]
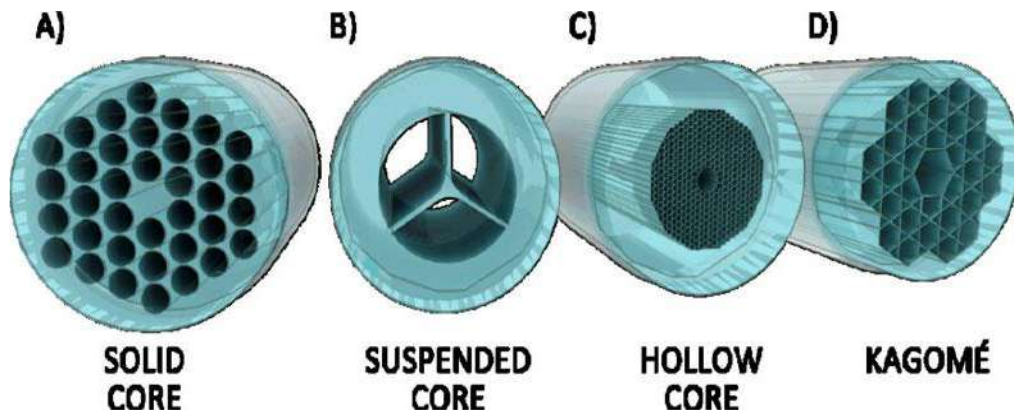
Figure : 7.6 Schematic diagram of some typical structures of PCFs used in chemical sensing, [110]

Based on the above discussion, thus, it is apparent that there is a good potential for fabricating the proposed PCFs using the currently available well-known fabrication processes e.g. stack and draw, 3D printing and extrusion. All our proposed PCFs geometry are displayed in Figure 7.7. Except proposed PCF VIII, all proposed PCFs geometry are constructed with suspended cladding and hexagonal, octagonal, circular, and square-shaped porous and hollow cores. The stack and draw technique has excellent potential for fabricating our proposed PCFs structure. For example, proposed PCF I (see Figure 7.7) constructed with four symmetrical capillaries in the cladding and same number of capillaries in the core section. Fabrication steps for the proposed PCF I using stack and draw technique is shown in Figure 7.8. As per the stack and draw process the first step is capillaries preparation. After making solid rod capillary, an ultrasonic mill can be used for making holes as per desired shape. There is a small difference in shape and size between core and cladding capillaries of our proposed PCF I. After making the core and cladding capillaries as per the design these capillaries need to be stacked together inside a jacket tube. After inserting the preform stack into a glass tube and fusing during the drawing process, one obtains a microstructured preform or "cane". The last step of this fabrication process is drawing the cane into fiber as per the design with desired dimension. Air holes size and their regularities can be controlled by applying air pressure inside the preform. From Figure 7.7 it is seen that our proposed others PCFs constructed with almost similar geometry, just two dissimilarities are there. Firstly, for all proposed design cases the core-cladding capillaries are not symmetrical.

So, different shapes of capillaries are to be prepared for a PCF. Secondly, in the case of hollow core fabrication, the fabrication process is almost similar but only some capillaries need to omits from the center of the PCF. Thus, it can be pronounced that for other proposed designs (II-VII) also can be fabricable using stack and drawing technique.

3D printing techniques also can be applicable for our proposed designs. For example for the proposed PCF III, as per the 3D printing technique a digital file needs to be prepared first as per the design. The schematic view of the proposed design III is shown in Figure 7.9. After making the digital file then one just needs to print the design by 3D printer.

All our proposed designs constructed with suspended cladding except proposed design VIII. But this proposed design will also be suitable for fabricating using stack and draw process. The schematic diagram of the fabrication process for the proposed design III using stack and draw process are shown in Figure 7.10. The fabrication process is same as the previously discussed.

Stack and draw, and 3D printing both techniques have the good potential for fabricating the proposed PCF structures.
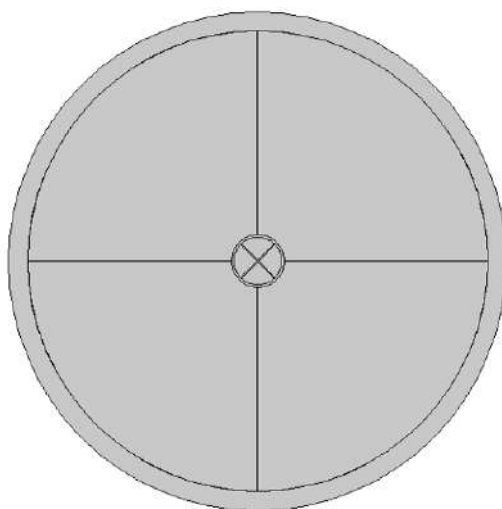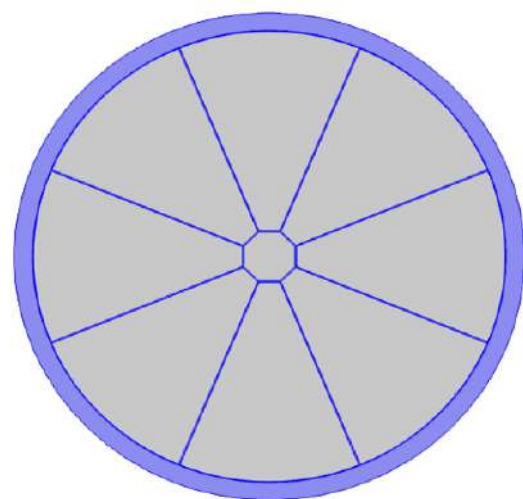
| Proposed PCF I | Proposed PCF II |
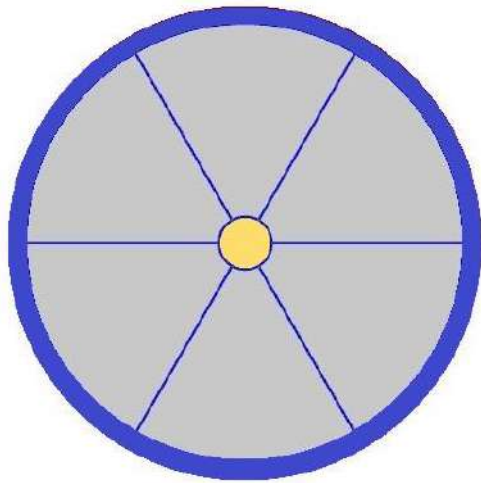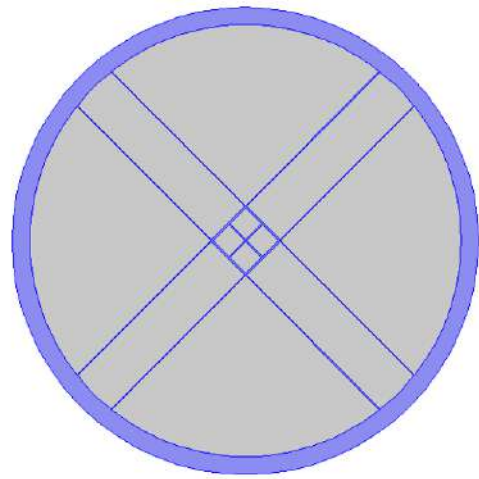
Proposed PCF III   Proposed PCF IV
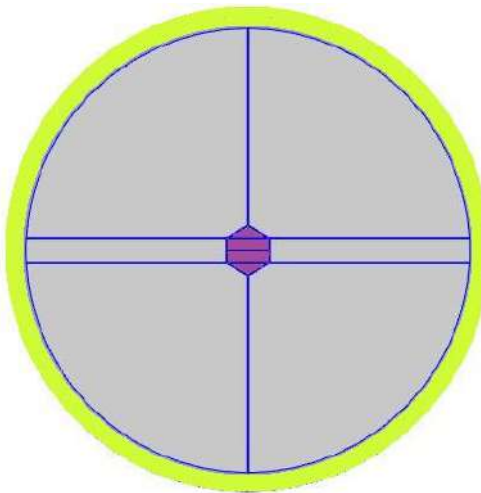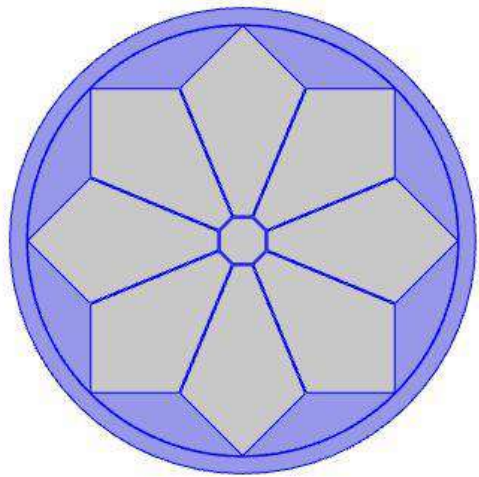
Proposed PCF V   Proposed PCF VI
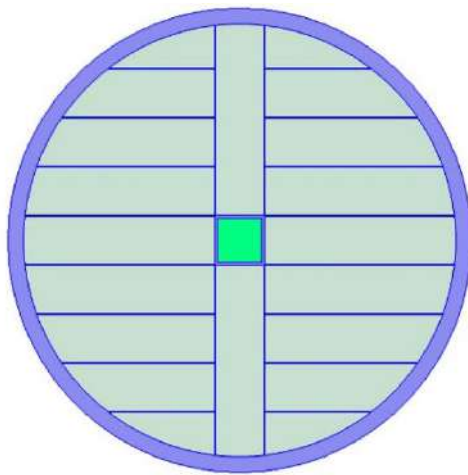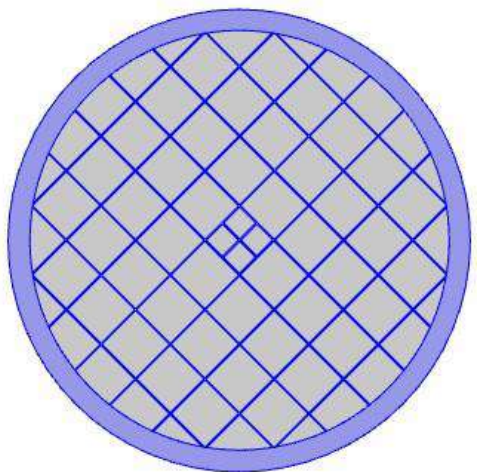
Proposed PCF VII   Proposed PCF VIII

Figure 7.7: Proposed PCF structures.
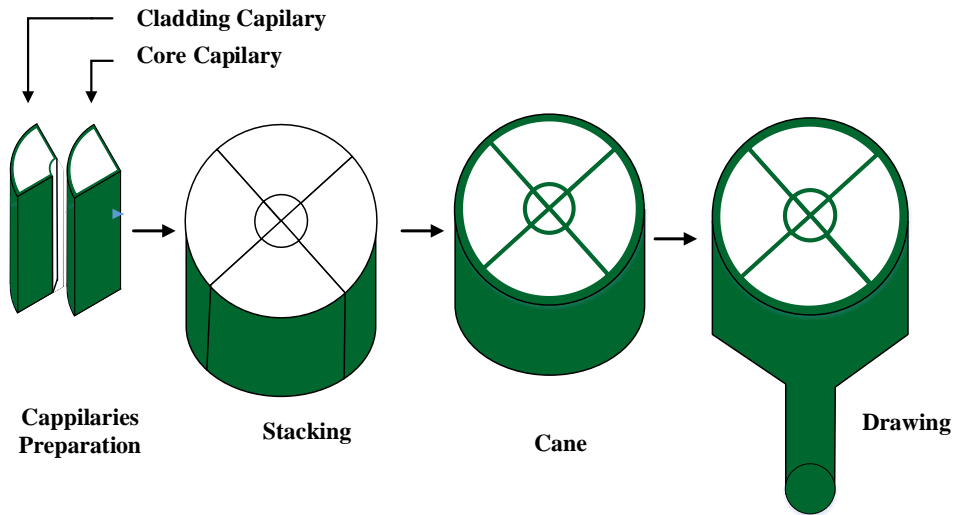
Figure 7.8: Fabrication processing steps for proposed PCF I using stack and draw technique.
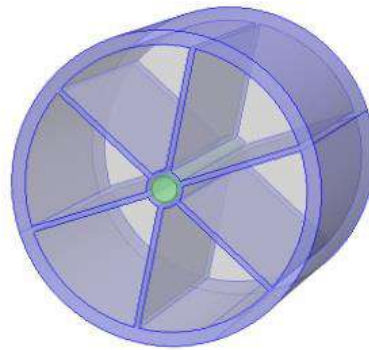
Figure 7.9: The schematic view of the proposed design III for using 3D printing technique.
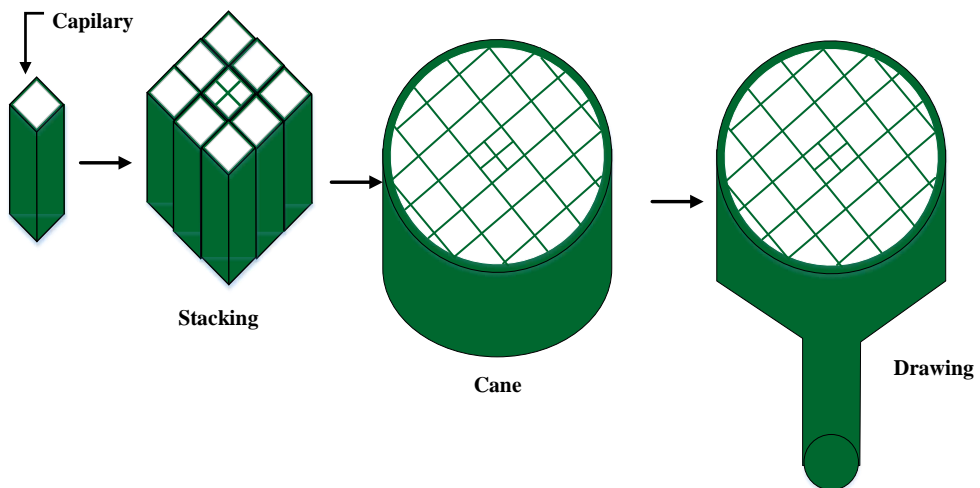
Figure 7.10: Fabrication processing steps for proposed PCF VIII using stack and draw technique.

7.5 Experimental Setup

For testing the proposed PCF sensor in practice several additional arrangements are required. A possible arrangement for testing the PCF sensor is presented in Figure 7.11. First, a supercontinuum light source is required which has a frequency range from 0.6 - 5.6 THz (all our proposed PCFs are evaluated within this frequency range). For this purpose a SuperK compact, NKTPhotonics™ can be utilized [174]. A single-mode-fiber (SMF-28) needs to be coupled between the light source and sensor through the polarizer (that is accompanied by a polarizer controller) to transport the light to the sensor. A splicing method can be used to couple the sensor with SMF-28. Vytran FFS-2000 splicer can be utilized for splicing by using the filament fusion technique. Manual-mode translational and rotational alignment methods can be used for aligning the PCF and SMF [175]. Furthermore, SMF and PCF also can be connected by inserting an etched SMF tip into the PCF. As per the current reports, this splicing method has a coupling efficiency of more than 80% [176]. Also, free space coupling, fiber-to-fiber coupling, etc. techniques can be also utilized for coupling purposes [177-178]. After passing the sensor the light needs to pass through an Optical Spectrum Analyzer which analyzes the responses of different analytes. Yokokawa™, AQ6370C optical spectrum analyzer can
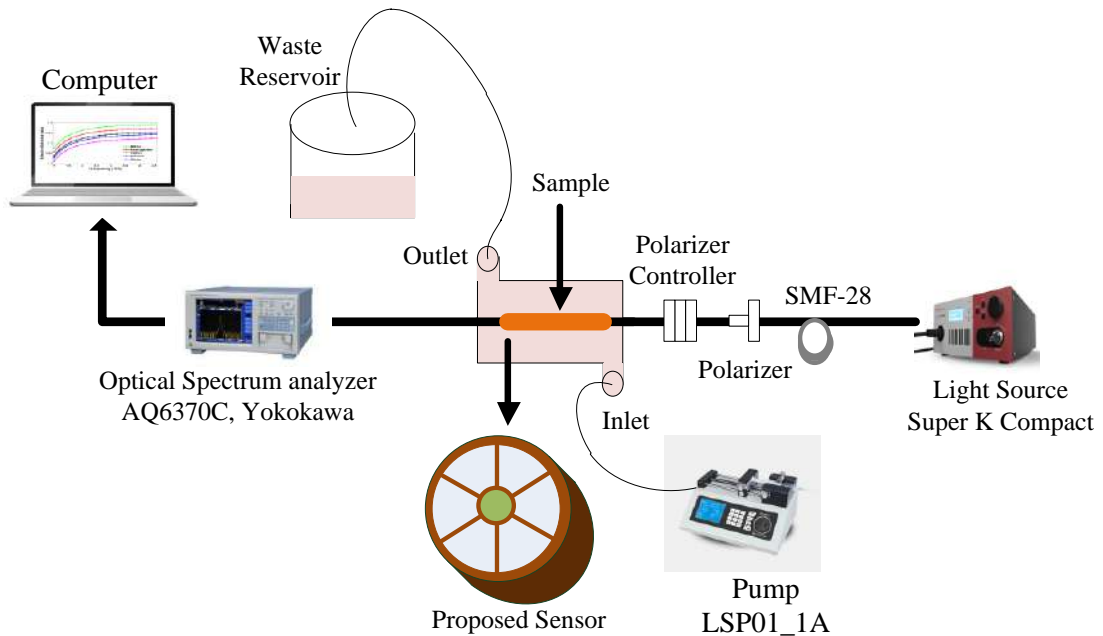
Figure 7.11: Experimental setup schematic of proposed PCF sensors for practical sensing applications.

159

be employed [174]. For injecting the analyte into the sensor, a programmable micro injector pump would be required. LongerPump™, LSP01-1A can be considered for this purpose [174]. A waste reservoir needs to be connected with an outlet channel where the used analyte will be stored. The existence of several unknown analytes causes peak shifts. These shifting can be identified by the spectrum analyzer and can be graphically exhibited in the computer which will be connected to the output of the spectrum analyzer.

7.6 Summary

Existing fabrication techniques have a great potential for fabricating simple or complex, symmetrical, or asymmetrical structured PCFs. For simple and symmetrical shaped PCF fabrication, different fabrication processes are mature enough including capillary stacking, stack and draw and sole-gel techniques. For complex and asymmetrical structured PCF, the stack and draw, extrusion and 3D printing fabrication techniques can be used. Among different materials for PCF, refractive index of TOPAS is considerably fluctuated over a large frequency range, and well suited for minimum material dispersion. Bulk material loss is also lower compared to other polymers. Further it is insensitive to environmental aspects such as humidity and water vapor absorption and has chemical inertness with special bio-sensing properties. Zeonex also provides almost similar characteristics. Thus, Topas or Zeonox both can be used as a background material depending on the availability.

Chapter 8

Conclusion

8.1 Conclusion

The key objective of this research is to design and analysis of simple and novel PCF geometry, that can only to provide high-quality THz transmission, but also render superior sensing of different analytes.

Firstly, for efficient THz waveguiding, three different PCF geometries have been developed. Circular and square shaped core with suspended cladding structured PCF with minimum number of air fragments are proposed, which increasing the air area in the core and cladding section. Higher air fraction in the core cladding region helps to minimize the effective material loss, as well as waveguide dispersion fluctuations. The presented PCFs have been shown to give an impressive low EML of (0.013-0.0153) cm^{-1} and very flat dispersion variation of (±0.010 to ±0.05) ps/THz/cm at 1 THz operating frequency. Moreover, the other wave guiding properties for THz wave propagation including confinement loss, core power fraction, effective area, bending loss of the proposed PCFs have revealed superior performance as compared to several recent designs reported in the literature. Mode test results of the proposed PCFs have shown single mode characteristics which indicate that the proposed PCF's are suitable for long distance communication in the THz regime.

Secondly, three hollow core and suspended cladding PCF have been proposed for different analyte sensing, several harmful and well-known liquid chemicals, biological components, and air pollutants. The various geometrical parameters of the PCFs have been optimized and the optical properties of tuned PCF structure numerically investigated for sensing purposes. Significant improvements have been noticed in different test cases. The proposed alcohol sensor exhibits almost 90% sensitivity and ultra-low confinement loss of 10^{-14} cm^{-1}. The proposed cholesterol sensor renders a

very high sensitivity 98.75% at 2.2 THz. Moreover, a very negligible confinement loss of 3.14×10^{-20} cm^{-1} and very low effective material loss of 0.0008 cm^{-1} have been found for the proposed PCF in case of cholesterol detection. The proposed blood components PCF sensor demonstrates a sensitivity of 99.18 % for RBCs, 99.02 % for hemoglobin, 98.81 % for WBCs, 98.68 % for plasma, and 98.35 % for water in the 4.5 THz operating region. Alongside, negligible confinement losses, $10^{-16\pm1}$ dB/cm have been obtained for all the studied components of blood. In the case of albumin detection in urine, the proposed PCF geometry has been investigated for different levels of albumin concentration and the sensing performances of proposed PCF has been shown to give more than 98.5% sensitivity with a low confinement loss of 10^{-16} cm^{-1} at 4.3 THz operating conditions for all the tested cases.

Finally, a PCF structure has been developed for both waveguiding and analytes sensing in the THz regime. The presented PCF structure exhibits notable advancement in all the experimented cases due to strategic selection of geometrical parameters and proper optimization. It can provide a sensitivity of (90 ± 1) % for detecting substances in liquid and evanescent at 2.5 THz operating point, and give an ultra-low effective material loss of 0.013 cm^{-1} and 0.020 cm^{-1} in x and y polarization mode, respectively in the THz regime for the operating frequency of 1 THz. Additionally, the developed PCF has been shown to have a very low confinement loss and large effective area.

Overall, the study of optical properties for both THz waveguiding and sensing cases indicates that proposed PCFs have good potential for diverse applications. Practical implementation potential in the existing manufacturing technologies has been also discussed in detail.

8.2 Limitations and future scopes

In this research we have designed several PCF structures and analyzed the optical properties of PCFs for THz wave transmission and for different analytes sensing. A superior performance has been achieved for all the tested cases due to strategic

geometrical parameters selection and proper optimization than the existing works. Still there is ample scope to develop new PCF structure for several necessary analyte detection cases. Practical implementation feasibility study needs to be addressed strongly using current fabrication techniques. Due to the absence of necessary resources in the laboratory a prototype development and performance evaluation of the proposed PCFs in practical has been not addressed in this research. A comparative analysis with the practical data after developing a practical setup in the lab should be explored in future.

In addition, when the refractive index changes are very small, the PCF sensor responses with almost similar result. Thus, it can give rise a problem for accurate detection when refractive index changes are very close among different analytes. Surface Plasmon Resonance (SPR) based sensor, small changes in RI results renders noticeable changes in outputs [179-180]. Resonance wavelength and peak confinement loss are very sensitive to RI of the analytes in the SPR-PCF platform [179-180]. As a result, a slight change in RI of the analytes forces to the resonance wavelength to shift right or left and the peak of the confinement loss to higher or lower level [179-180]. Thus, it could be easier to identify the unknown analyte with very tiny changes of RI in SPR platform. Therefore, SPR based PCF sensor development and analysis for identification of different analytes can be a potential research area.

List of Publications

1. **Md. Moshiur Rahman**, and M. I. H. Bhuiyan, "Refractometric Sensing of Urine Protein by Photonic Crystal Fiber Biosensor in the THz Regime," 2023. [**Submitted**].

2. **Md. Moshiur Rahman**, F. A. Mou, M. I. H. Bhuiyan, M. A. A, Mahmud, & M. R. Islam, "Design and characterization of a photonic crystal fiber for improved THz wave propagation and analytes sensing," *Opt Quant Electron,* 54, 669 (2022).

3. **Md. Moshiur Rahman**, F. A. Mou, M. I. H. Bhuiyan, and M. R. Islam, "Refractometric THz Sensing of Blood Components in a Photonic Crystal Fiber Platform," *Braz J Phys,* 52, 47 (2022).

4. **Md. Moshiur Rahman**, F. A. Mou, M. I. H. Bhuiyan, and M. R. Islam, "Photonic crystal fiber-based terahertz sensor for cholesterol detection in human blood and liquid foodstuffs," *Sensing and Bio-Sensing Research*, Vol. 29, 100356. 2020.

5. **Md. Moshiur Rahman,** F. A. Mou, M. I. H. Bhuiyan, and M. R. Islam, "Design and characterization of a circular sectored core cladding structured photonic crystal fiber with ultra-low EML and flattened dispersion in the THz regime," *Optical Fiber Technology*, Vol. 55, 102158, 2020.

6. **Md. Moshiur Rahman**, F. A. Mou, A. A. Mahmud, M. I. H. Bhuiyan, and M. R. Islam, "Photonic Crystal Fiber based Terahertz Sensor for Alcohol Detection in Beverages: Design and Analysis," *IEEE International Conference of Communication and Photonics (ICTP' 2019)*, 28-30 December, Dhaka, Bangladesh, 2019.

7. **Md. Moshiur Rahman,** F. A. Mou, A. A. Mahmud, and M. I. H. Bhuiyan, "Single Mode Porous Core Photonic Crystal Fiber for Terahertz Wave Propagation with Extremely Low Losses," *IEEE R10 Humanitarian Technology Conference (IEEE R10 HTC'2019)*, 12-14 November, Depok, Indonesia, 2019.

8. **Md. Moshiur Rahman,** F. A. Mou, M. I. H. Bhuiyan, and M. R. Islam, "Extremely low effective Material loss of air core photonic crystal fiber for THz guidance," *IEEE region 10 symposium (TENSYMP)*, India, June, 2019.

Bibliography

[1]. Islam, M. S., Sultana, J., Dinovitser A., Ahmed, K., Brian, W.-H. Ng, and Abbott, D., "Sensing of toxic chemicals using polarized photonic crystal fiber in the terahertz regime," *Optics Communications*, 426, pp. 341–347, 2018.

[2]. Paul, B. K., Ahmed, K., Dhasarathan, V., and Nguyen, T. K., "Oligoporous-core Quasi cladding photonic crystal fiber based microsensorfor alcohol detection," *Physica B: Physics of Condensed Matter*, 412104, 2020.

[3]. Liu, H. B., Chen, Y., Bastiaans, G. J., and Zhang, X. C., "Detection and identification of explosive RDX by THz diffuse reflection spectroscopy," *Opt. Express* 14, pp. 415–423, 2006.

[4]. Elayan, H., Amin, O., Shihada, B., Shubair, R. M. and Alouini, M., "Terahertz Band: The Last Piece of RF Spectrum Puzzle for Communication Systems," *IEEE Open Journal of the Communications Society*, vol. 1, pp.1-32, 2019.

[5]. Islam, M. S., Cristiano, M. B., Marcos, A. R., Sultana, J., Alice, L. S., and Derek, A., "Terahertz optical fibers," *Optics Express*, 16089, Vol. 28, No. 11, 2020.

[6]. Paul, B. K., and Ahmed, K., "Analysis of terahertz waveguide properties of Q-PCF based on FEM scheme," *Optical Materials* 100, 109634, 2020.

[7]. Strachan, C. J., Taday, P. F., Newnham, D. A., Gordon, K. C., Zeitler, J. A., Pepper, M., and Rades, T., "Using terahertz pulsed spectroscopy to quantify pharmaceutical polymorphism and crystallinity," *J. Pharm. Sci.* 94(4), pp. 837–846, 2005.

[8]. Crowe, T. W., Globus ,T., Woolard, D. L., and Hesler, J. L., "Terahertz sources and detectors and their application to biological sensing," *Philos. Trans. R. Soc. A* 362, pp. 365–377, 2004.

[9]. Wallace, V. P., Fitzgerald, A. J., Shankar, S., Flanagan, N., Pye, R., Cluff, J., and Arnone, D. D., "Terahertz pulsed imaging of basal cell carcinoma ex vivo and in vivo," *Br. J. Dermatol.* 151(2), pp. 424-432, 2004.

[10]. Asaduzzaman, S., and Ahmed, K., "Proposal of a gas sensor with high sensitivity, birefringence and nonlinearity for air pollution monitoring," Sensing and Bio-Sensing Research, 10: pp. 20–26, 2016.

[11]. Mendis, R., and Grischkowsky, D., "Plastic ribbon THz waveguides," *J Appl Phys* 88(7): pp. 4449-4451, 2000.

[12]. Mendis, R., and Mittleman, D. M., "An Investigation of Lowest-Order Transverse-Electric (TE1) Mode of the Parallel Plate Waveguide for THz Pulse Propagation," *Josa B*. 26(9), 2009.

[13]. Cia, M. N., Melzer, J. E., Harrington, J. A., and Mitrofanov, O., "Silver-Coated Teflon Tubes for Wave guiding at 1-2 THz," *J. Infrared Millimeter Terahertz Waves*, 36(6), pp. 542-555, 2015.

[14]. Wachter, M., Nagel, M., and Kuruz, H., "Metallic Slit Waveguide for Dispersion free Low Loss terahertz Signal Transmission," *Applied Physics letter*, 90(6), 2007.

[15]. Jeon, T. I., Zhang, J., and Grischkowsky, D., "THz Sommerfield Wave Propagation on a Single Metal Wire," *Appl. Phys. Lett.* 86, 161904, 2005.

[16]. Islam, M. S., Rana, S., Islam, M. R., Faisal, M., Rahman, H., and Sultana, J., "Porous core photonic crystal fiber for ultra-low material loss in THz regime," *IET Communications*, 10(16), 2016.

[17]. Srinivasan, K., Radhakrishnan, G., Mohammadd, N., Amin R., Ahmed, K., Bui, F. M., Ibrahim, S. M., and Alsalem, K. A. J., "Ultra-high negative dispersion compensating circular–shaped PCF with highly birefringent and nonlinear characteristics for optical applications," *Opt Quant Electron* 54, 834, 2022.

[18]. Islam, M. S., Islam, M. R., Faisal, M., Arefin, A. S. M. S., Rahman, H., Sultana, J., and Rana, S., "Extremely low-loss, dispersion flattened porous-core photonic crystal fiber for terahertz regime," *Optical Engineering* 55(7), 076117, 2016.

[19]. Sadath, M. A., Rahman, M. M., Islam, M. S., Hossain, M. S., and Faisal, M., "Design optimization of suspended core photonic crystal fiber for polarization maintaining applications", *Optical Fiber Technology* 65, 102613, 2021.

[20]. Islam, M. S., Sultana, J., Rifat, A. A., Dinovitser, A., B. W.-H. Ng, and Derek, A., "Terahertz Sensing in a Hollow Core Photonic Crystal Fiber," *IEEE Sensor Journal*, 1558-1748 (c), 2018.

[21]. Ahmed, K., Ahmed, F., Roy, S., Paul, B. K., Aktar, M. N., Vigneswaran, D., and Islam, M. S., "Refractive Index Based Blood Components Sensing in Terahertz Spectrum," *IEEE Sensor Journal*, Vol. 19 , no. 9, 2019.

[22]. Islam, M. S., Sultana, J., Ahmed, K., Islam, M. R., Dinovitser, A., B. Wai-Him Ng, and Derek, A., "A novel approach for spectroscopic chemical identification using photonic crystal fiber in the terahertz regime," *IEEE Sensors J.*, vol. 18, no. 2, pp. 575–582, 2018.

[23]. Hasanuzzaman, G. K. M., Habib, M. S., Razzak, S. M. A., Hossain, M. A., and Namihira, Y., "Low loss single mode porous-core Kagome Photonic crystal fiber for THz wave guidance," *J. Light-Wave Technol*. 33 (19), 15400618, 2015.

[24]. Singer, A. M., Hameed, M. F. O., and Heikal, A.M., " Highly birefringent slotted core photonic crystal fiber for terahertz waveguiding," *Opt Quant Electron* **53**, 9, 2021.

[25]. Wu ,Z., Shi, Z., Xia, H., Zhou, X., Deng, Q., Huang, J., Jiang, X., and Wu, W., "Design of highly birefringent and low-loss oligoporous-core THz photonic crystal fiber with single circular air-hole unit," *IEEE Photonics J.* 8, 4502711, 2016.

[26]. Islam, M. S., Faisal, M., and Razzak, S. M. A., "Dispersion flattened extremely high-birefringent kagome lattice elliptic core photonic crystal fiber in THz regime," *Optical and Quantum Electronics*, 51:35, 2019.

[27]. Paul, B. K., Haque, M. A., Ahmed, K., and Sen, S., "A Novel Hexahedron Photonic Crystal Fiber in Terahertz Propagation: Design and Analysis," *Photonics*, 6, 32, 2019.

[28]. Islam, M. R., Kabir, M. F., Talha, K. M. A. and Arefin, M. S., "Highly birefringent honeycomb cladding terahertz fiber for polarization-maintaining applications," *Optical Engineering*, 59(1), 016113, 2020.

[29]. Yakasai, I. K., Abas, P. E., Suhaimi, H., and Begum, F., "Low loss and highly birefringent photonic crystal fibre for terahertz applications," *Optik - International Journal for Light and Electron Optics* ,206, 2020.

[30]. Eid, M. M. A., Habib, M. A., Anower, M. S., and Rashed, A. N. Z., "Highly sensitive nonlinear photonic crystal fiber-based sensor for chemical sensing applications," *Microsyst Technol* 27, 1007–1014, 2021.

[31]. Podder, E., Hossain, M. B., Jibon, R. H., and Bulbul, A. A. M., "Chemical sensing through photonic crystal fiber: sulfuric acid detection," *Frontiers of Optoelectronics* vol. 12, pp. 372–38, 2019.

[32]. Britto, E.C., Nizar, S. M., and Krishnan, P. A., "Highly Sensitive Photonic Crystal Fiber Gas Sensor for the Detection of Sulfur Dioxide", *Silicon* 14, 12665–12674, 2022.

[33]. Rabee, A. S. H., Hameed, M. F. O., Heikal, A. M., and Obayya, S. S. A., "Highly Sensitive Photonic Crystal Fiber Gas Sensor", *Optik*, Vol. 188, pp. 78-86, 2019.

[34]. Hossain, M. B., and Podder, E., "Design and investigation of PCF based blood components sensor in terahertz regime," *Applied Physics A*, 125:861, 2019.

[35]. Sen, S., Islam, M. S., Paul, B. K., Islam, C. M. I., Ahmed K., Hasan M. R., Uddin, M. S. and Asaduzzaman, S., "Ultra-Low Loss with Single Mode Polymer Based Photonic Crystal Fiber for THZ Waveguide," *J. Opt. Commun.* 2017.

[36]. Habib, M. A., Anower, M. S., and Hasan, M. R., "Ultrahigh Birefringence and Extremely Low Loss Slotted Core Microstructure Fiber in Terahertz Regime," *Current Optics and Photonics*, Vol. 1, No. 6, pp. 567-572, 2017.

[37]. Islam, M. S., Sultana, J., Dinovitser, A., Faisal, M., Islam, M. R., B. W-H. Ng, and Abbott, D., "Zeonex Based Asymmetrical Terahertz Photonic Crystal Fiber for Multichannel Communication and Polarization Maintaining Applications," *Applied Optics*, Vol. 57, No. 4, 2018.

[38]. Islam ,M. S., Sultana, J.. Faisal, M., Islam, M. R., Dinovitser, A., B. W-H. Ng, and Abbott, D., "A Modified Hexagonal Photonic Crystal Fiber for Terahertz Applications," *Optical Materials*, 79, pp. 336-339, 2018.

[39]. Faisal, M. and Islam, M. S., "Extremely High Birefringent Terahertz Fiber using a Suspended Elliptic Core With Slotted Air Holes," *Applied Optics*, Vol. 57, No. 13, 2018.

[40]. Rana, S., Rakin, A. S., Hasan, M. R., Reza, M. S., Leonhardt, R., Abbott, D., and Subbaraman, H., "Low Loss and Flat Dispersion Kagome Photonic Crystal Fiber in the Terahertz Regime," *Optics Communication*, 410, pp. 452-456, 2018.

[41]. Islam, M. S., Faisal, M. and Razzak, S. M. A., "Dispersion Flattened Extremely High Birefrringent Kagome Lattice Elliptical Core Photonic Crystal Fiber," *Optical and Quantum Electronics*, 2019.

[42]. Ahmed, F., Roy S., Paul, B. K., Ahmed, K. and Bahar, A. N., "Extremely Low loss of Photonic Crystal fiber for Terahertz Wave Propagation in Optical Communication Application," *J. Opt. Commun.* 2018.

[43]. Paul, B. K., Rajesh, E., Asaduzzaman, S., Islam, M. S., Ahmed, K. and Amiri, I.S., "Design and Analysis of Slotted Core Photonic Crystal Fiber for Gas sensing Application," *Results in Physics*, 2018.

[44]. Sen, S. and Ahmed, K., "Design of terahertz spectroscopy based optical sensor for chemical detection," *SN Applied Science*, 1:1215, 2020.

[45]. Tahhan, S. R. and Aljobouri, H. K., "Sensing of Illegal Drugs by Using Photonic Crystal Fiber in Terahertz Regime," J. *Opt. Commun.* 2020.

[46]. Singh, S., and Kaur, V., "Photonic crystal fiber sensor based on sensing ring for different blood components: design and analysis," *IEEE Ninth International Conference on Ubiquitous and Future Networks (ICUFN)*, pp. 399–403, 2017.

[47]. Kaur, V., and Singh, S., "Design approach of solid-core photonic crystal fiber sensor with sensing ring for blood component detection," *J. Nanophoton.* 13(2), 026011, 2019.

[48]. Hossain, M. B., and Podder, E., "Design and investigation of PCF-based blood components sensor in terahertz regime," *Applied Physics A*, 125:861, 2019.

[49]. Hossain, M. B., Podder, E., Bulbul, A. A. M., and Mondal, H. S., "Bane chemicals detection through photonic crystal fiber in THz regime," *Optical Fiber Technology*, 54, 102102, 2020.

[50]. Hasan, M. M., Sen, S., M. Rana, J., Paul, B. K., Habib, M. A., Daiyan, G. M., and Ahmed, K., "Heptagonal Photonic Crystal Fiber Based Chemical Sensor in THz Regime," *2019 Joint 8th International Conference on Informatics, Electronics & Vision (ICIEV) and 2019 3rd International Conference on Imaging, Vision & Pattern Recognition (icIVPR),* 2019.

[51]. Paul, B. K., Islam, M. S., Ahmed, K., and Asaduzzaman, S., "Alcohol sensing over O+E+S+C+L+U transmission band based on porous cored octagonal photonic crystal fiber," *Photon. Sensors*, vol. 7, no. 2, pp. 123–130, 2017.

[52]. Sultana, J.. . Islam, M. S, Ahmed, K. , Dinovitser, A., Brian W.-H. NG, and Abbott, D., "Terahertz detection of alcohol using a photonic crystal fiber sensor," *Applied Optics*, Vol. 57, No. 10 ,1, 2018.

[53]. Islam, M. S. , Paul, B. K., Ahmed, K., and Asaduzzaman, S., "Rhombic core photonic crystal fiber for sensing applications: Modeling and analysis," *Optik,* vol. 157. Pp. 1357–1365, 2018.

[54]. Knight, J. C., "Photonic crystal fibres," *Nature*, vol. 424, pp. 847-851, Aug. 2003.

[55]. Wang, Y., Couny, F., Roberts, P. J., and Benabid, F., "Low Loss Broadband Transmission in Optimized Core-shape Kagome Hollow-core PCF," in *Conf. Lasers and Electro-Optics*, San Jones, CA, 2010.

[56]. Atakaramians, S., Afshar, V. S., Nagel, M., Ebendorff-Heidepriem, H., Fischer, B. M., Abbott, D., and Monro, T. M., "THz porous fibers: design, fabrication and experimental characterization," *Opt. Express*, vol. 17, pp. 14053–14062, 2009.

[57]. Knight, J. C., Birks, T. A., Russell, P. S., and de Sandro, J. P., "Properties of photonic crystal fiber and the effective index model," *Journal of the Optical Society of America A*, vol. 15, no. 3, pp. 748–752, 1998.

[58]. Russell, P. S. J., "Photonic crystal fibers," *Journal of Lightwave Technology*, vol. 24, no. 12, pp. 4729–4749, 2006.

[59]. Belardi, W. and Knight, J. C., "Effect of core boundary curvature on the confinement losses of hollow antiresonant fibers," *Optics Express*, vol. 21, no. 19, pp. 21912–21917, 2013.

[60]. SIEGEL-P. H., "Terahertz technology, IEEE Transactions on Microwave Theory and Techniques, 50(3), pp. 910–928, 2022.

[61]. Woolard-D. L., Brown-R., Pepper-M., And Kemp-M., "Terahertz frequency sensing and imaging: A time of reckoning future applications?, Proceedings of the IEEE, **93**(10), pp. 1722–1743, 2005.

[62]. Terahertz Sources, RP Photonics Encyclopaedia [online]. Available: https://www.rp-photonics.com/terahertz_sources.html, 2020.

[63]. Charrada, K. Zissis G and Aubes, M, "Two-temperature,two-dimensional fluid modelling of mercury plasma in high-pressure lamps", J. Phys. D: Appl. Phys., vol. 29, pp.2432–8, 1996.

[64]. Shin, Y M, Park, G S, Scheitrum, G P and Caryotakis, G, "Circuit analysis of an extended interaction klystron." J. Korean Phys. Soc., vol. 44, pp. 1239–1245, 2004.

[65]. Bhattacharjee, S., "Folded waveguide traveling-wave tube sources for terahertz radiation.", IEEE Trans. Plasma Sci., vol. 32, pp. 1002–1014, 2004.

[66]. Knyazev, B. A., Kulipanov, G. N. and Novosibirsk, N. A., "terahertz free electron laser: instrumentation development and experimental achievements.", *Meas. Sci. Technol*., vol. 21, pp. 054017, 2010.

[67]. Yang, L. A., Hao Y., Yao, Q. and Zhang, J., "Improved negative differential mobility model of GaN and AlGaN for a, terahertz Gunn diode.", *IEEE Trans. Electron Devices*, vol. 58, pp. 1076–83, 2011.

[68]. Knap, W., Lusakowski, J., Parenty, T., Bollaert, S., Cappy, A., and Shur, M. S.,"Terahertz emission by plasma waves in 60 nm gate high electron mobility transistors." Appl. Phys. Lett., vol. 84, pp. 2331–2333, 2004.

[69]. Ubers, H., Pavlov, S. G. and Shastin, V. N., "Terahertz lasers based on germanium and silicon." Semicond. Sci.Technol., vol. 20, pp. 211–21, 2005.

[70]. Dodel, G., "On the history of far-infrared (FIR) gas lasers: Thirty-five years of research and application Infrared.", Phys. Technol., vol. 40, pp. 127–39, 1999.

[71]. Hoffmann, and Hofmann, S. M. R., "Generation of Terahertz radiation with two colour semiconductor lasers", Laser & Photon. Rev., vol. 44, 2007.

168

[72]. Sizov, F., "THz radiation sensors.", Opto-Electron. Rev., vol. 18, 2010.

[73]. Bakker, H. J., G. Cho C., Kurz, H., Wu, Q., and Zhang, X.C., "Distortion of terahertz pulses in electro-optic sampling.", Journal of the Optical Society of America B, vol. 15, Issue 6, pp. 1795-1801, 1998.

[74]. Cole, B., Williams, J., King, B., Sherwin, M., And Stanley, C, "Coherent manipulation of semiconductor quantum bits with terahertz radiation, Nature, 410(6824), pp. 60–63, 2001.

[75]. Huber, R., Tauser, F., Brodschelm, A., Bichler, M., Abstreiter, G., and Leitenstorfer, A., "How many-particle interactions develop after ultrafast excitation of an electron–hole plasma, Nature, 414(6861), pp. 286–289, 2001.

[76]. Cooke, D., Macdonald, A., Hryciw, A., Wang, J., Li, Q., Meldrum, A., and Hegmann, F., " Transient terahertz conductivity in photoexcited silicon nanocrystal films, Physical Review B, 73(19), Art. No. 193311, 2006.

[77]. Beard, M. C., Turner, G. M., and Schmuttenmaer, C. A., "Measuring intramolecular charge transfer via coherent generation of THz radiation, The Journal of Physical Chemistry A, 106(6), pp. 878–883, 2002.

[78]. Schall, M., Walther, M., and Jepsen, P. U., Fundamental and second-order phonon processes in CdTe and ZnTe, Physical Review B, 64(9), Art. No. 094301, 2011.

[79]. Walther, M., Fischer, B. M., and Jepsen, P. U., Noncovalent intermolecular forces in polycrystalline and amorphous saccharides in the far infrared, Chemical Physics, 288(3), pp. 261–26, 2003.

[80]. Ronne, C., Thrane, L., A° Strand, P.-O., Wallqvist, A., Mikkelsen, K. V., and Keiding, S. R. Investigation of the temperature dependence of dielectric relaxation in liquid water by THz reflection spectroscopy and molecular dynamics simulation, *The Journal of chemical physics*, 107(14), pp. 5319–5331, 1997.

[81]. Whitmire, S., Wolpert, D., Markelz, A., Hillebrecht, J., Galan, J., and Birge, R. Protein flexibility and conformational state: A comparison of collective vibrational modes of wild-type and D96N bacteriorhodopsin, *Biophysical Journal*, 85(2), pp. 1269–1277, 2003.

[82]. Kawase, K., Ogawa, Y., Watanabe, Y. and Inoue, H., "Non-Destrctive Terahertz Imaging of Illicit drug using Spectral Fingerprint," Optical Express, vol. 11, pp. 2549-2554, 2003.

[83]. Strachan, C. J., Taday, P. F., Newnham, D. A., Gordon, K. C., Zeitler, J. Pepper, A., M. and Rades,T. "Using Terahertz Pulsed Spectroscopy to Quantify Phamaceutical Polymorphism and Crystallinity," Journal of Phamaceutical Science, Vol. 94, Pp. 837- 846, 2005.

[84]. Pawar, A. y., Sonawane, D. D. and Erande, K. B., "Terahertz Technology and its Applications," *Drug Invent. Today*, pp. 157-163, 2013.

[85]. Balakrishnan, J., Fischer, B. M. and Abbott, D., "Sensing the Hygroscopicity of Polymer and Copolymer materials using Terahertz Time Domain Spectroscopy," *Applied Optics,* 48(12), pp. 2262-2266, 2009.

[86]. Snyder, A.W., Love, J., "Optical Waveguide Theory", *Springer Science and Business Media*, 1983.

[87]. Emiliyanov, G., Hiby, P. E., Pedersen, L. H., Bang, O., "Selective serial multi-antibody biosensing with TOPAS microstructured polymer optical fibers", *Sensors*, vol. 13, no. 3, pp. 3242-3251, 2013.

[88]. Emiliyanov, G., Jensen, J. B., Bang, O., Hoiby, P. E., Pedersen, L. H., Kjr E. M., Lindvold, L., "Localized biosensing with Topas microstructured polymer optical fiber", *Opt. Lett.*, vol. 32, no. 5, pp. 460-462, 2007.

[89]. Nielsen, M. D., Jacob, R. S. and Hansen K. P., "Modal cut-off and the V –parameter in photonic crystal fibers," *Optics Letters*, vol. 28, pp. 1879-1881, 2003.

[90]. Khare, R. P., Fiber Optics and Optoelectronic, 1st ed.*, Oxford University Press*, 2004.

[91]. Siddiqui, S. A., Zubair, A., and Alam M. S. "Effect of stress on the characteristics of elliptical hollow core optical fiber", Optical Engineering, 50 (4), 2011.

[92]. Sadiku, M. N., Numerical Techniques in Electromagnetics. *New York: CRC Press*, 2 ed., 2001.

[93]. Matej, R. A., Dmytro, S, and Stanislav, Z., "Modified Octagonal Photonic Crystal Fiber for Residual Dispersion Compensation over Telecommunication Bands", *Rad.Eng. Jounl.*, vol. 27, 2018.

[94]. Garg, R., Analytical and Computational Methods in Electromagnetics, 3rd ed., *Norwood:Artech House*, 2008.

[95]. Rahman, B. M. A. and Agrawal, A., Finite Element Modeling Methods for Photonics, 2nd ed., *London: Artech House*, 2013.

[96]. Azabi, Y. O., "Spiral photonic crystal fibers," Ph.D. dissertation, School of Mathematics, Dept. Computer Science & Engineering, Univ. of London, London, 2017.

[97]. Rahman, B. A., Fernandez F. A., and Davies J. B., "Review of finite element methods for microwave and optical waveguides," *Proceedings of the IEEE*,vol. 79, no. 10, pp. 1442−1448, 1991.

[98]. Yakasai, I. K., Rahman, A., Abas, P. E., and Begum, F., "Theoretical Assessment of a Porous Core Photonic Crystal Fiber for Terahertz Wave Propagation," *Opt. Commun.*, pp. 1−11, 2018.

[99]. Rahman, B. M. A. and Agrawal, A., Finite Element Modeling Methods for Photonics, *London: Artech House*, 2013.

[100]. Berenger, J.-P., "A perfectly matched layer for the absorption of electromagnetic waves," *Journal of Computational Physics*, vol. 114, no. 2, pp. 185–200, 1994.

[101]. Islam, M. S., Sultana, J., Atai, J., Abbott, D., Rana, S. and Islam, M.R., "Ultra Low-loss Hybrid Core Porous Fiber for Broadband Applications", *Applied Optics*, Vol. 56, Issue 4, PP. 1232-1237, 2017.

[102]. Luo, J., Tian, F., Qu, H., Li L., Zhang, J., Yang, X. and Yann, L., "Design and Numerical Analysis of a THz Square Porous Core Photonic Crystal for Low Flattened Dispersion", *Applied Optics*, Vol. 56, Issue. 24, pp. 6993-7001, 2017.

[103]. Hasan, R., Akter, S., Khatun, T., Rifat, A. A. and Anower, S., "Dual Hole Unit Based Kagome Lattice Microstructure Fiber for Low-Loss and Highly Birefringent Terahertz Guidance", *Optical Engineering*, 56(4), 043108, 2017.

[104]. Ali, S., Sarkar, T., Dey, A., Hasan, R., Mou, J. R., Rana, S., Islam, M. and Ahmed, N., " Ultra Low Loss THZ Waveguide with Flat EML and Near Zero Flat Dispersion Properties", *9th International Conference on Electrical and Computer Engineering (ICECE),* pp-114-117, 2016.

[105]. Ahmed, K., Paul, B. K., Chowdhury, S., Sen, S., Islam, M. I., Islam, M. S., Hasan, M. R. and Asaduzzaman, S., "Design of a single-mode photonic crystal fibre with ultra-low material loss and large effective mode area in THz regime," *IET Optoelectronic.*, Vol. 11 Iss. 6, pp. 265-271, 2017.

[106]. Sen, S., Islam, M. S., Paul, B. K., Islam, M. I., Chowdhury, S., Ahmed, K., Hasan, M. R., Uddin, M. S. and Asaduzzaman, S, "Ultra-low Loss with Single Mode Polymer-Based Photonic Crystal Fiber for THz Waveguide," *J. Opt. Commun.* 2017.

[107]. Paul, B. K., Islam, M. S., Sen, S., Ahmed, K., Uddin, M. S., "Low material loss and dispersion flattened fiber for single mode THz-wave transmission applications," *Results in Physics* 11, 638–642, 2018.

[108]. Pysz, D., Kujawa, I., Stepien, R., Klomczaki, M., Filipkowski, A., Franczyk, M., Kociszewski, L., Harasny, K. and Buczynski, R., "Stack and draw fabrication of soft glass microstructured fiber optics," *Bulletin of the polish academy of sci: technical science* , Vol. 62, No. 4, 2014.

[109]. Bise, R. T. and Trevor, D. J., "Sol-gel derived microstructured fiber: Fabrication and characterization," *OFC/NFOEC Technical Digest. Optical Fiber Communication Conference*, 2005.

170

[110]. Ebendorff-Heidepriem H., Schuppich J., Dowler A., Lima- Marques L., and Monro T. M., "3D-printed extrusion dies: A versatile approach to optical material processing," *Opt. Mater. Exp*, vol. 4, no. 8, pp. 1494–1504, 2014.

[111]. Kelishadi, R., Mirghaffari, N., Poursafa, P., and Gidding, S. S., "Lifestyle and environmental factors associated with inflammation, oxidative stress and insulin resistance in children," *Atherosclerosis*, vol. 203, no. 1, pp. 311–319, 2009.

[112]. Kelishadi, R. and Poursafa, P., "Air pollution and non-respiratory health hazards for children," *Archives of Medical Science*, vol. 6, no. 4, pp. 483–495, 2010.

[113]. Cunningham, P. D., Valdes, N. N., Vallejo, F. A., Hayden, L. M., Polishak, B., Zhou, X. H., Luo, J. D., Jen A. K. Y., Williams, J. C., and Twieg, R. J., "Broadband terahertz characterization of the refractive index and absorption of some important polymeric and organic electro-optic materials," *J. Appl. Phys*. 109, 043505, 2011.

[114]. Edward, P.J. P., and Zeitler J. A., "Terahertz Time-Domain and Low-Frequency Raman Spectroscopy of Organic Materials", Applied Spectroscopy, Volume 69, Issue 1, 2015.

[115]. Asaduzzaman, S., Ahmed, K., Bhuyan, T., and Farah, T., "Hybrid photonic crystal fiber in chemical sensing," Springer Plus 5, 748, 2016.

[116]. Arif, M. F. H., Ahmed, K. Asaduzzaman, S. and Azad, M. A. K., "Design and optimization of photonic crystal fiber for liquid sensing applications," *Photon. Sens*. 6, 279–288, 2016.

[117]. Paul, B. K., Ahmed, K., Asaduzzaman, S., and Islam, M. S., "Folded cladding porous shaped photonic crystal fiber with high sensitivity in optical sensing applications: Design and analysis," *Sensing and Bio-Sensing Research*, Volume 12, 2017.

[118]. Ademgil, H., and Haxha, S., "PCF Based Sensor with High Sensitivity, High Birefringence and Low Confinement Losses for Liquid Analyte Sensing Applications," *Sensors, MDPI*, 31833–31842, 2015.

[119]. Nielsen, K., Rasmussen Henrik, K., Aurèle, J. L. Adam, Paul C. M. Planken, Ole Bang, and Peter U. J. "Bendable, low-loss Topas fibers for the terahertz frequency range," *Opt. Express* 17 (10), pp. 8592–8601, 2009.

[120]. Islam, M. R., Kabir, M. F., Talha, K. M. A., and Islam M. S., "A novel hollow core terahertz refractometric sensor," Sensing and Bio-sensing research, Vol. 25, 100295, 2019.

[121]. Zhu, L., Zou, Y., Li, J., and Lui, Q., "Terahertz Spectroscopy of Neurodegenerative Diseases: the Correlation between Terahertz Biophysics and Pathological Analysis", 9th International Symposium on Ultrafast Phenomena and Terahertz Waves, 2018.

[122]. Kiyoung J., Yong-Min H., Sang-Hoon K., Yeonji P., Joo-Hiuk S., Seung Jae O, and Jin-Suck Sub, "Characterization of blood using terahertz waves" *Journal of Biomedical Optics* 18(10), 107008, 2013.

[123]. Caroline B. Reid, George Reese, Adam P. Gibson and Vincent P. Wallace, "Terahertz Time Domain Spectroscopy of Human Blood" *IEEE Journal of Biomedical and Health Informatics,* Vol.17, Issue: 4, 2013.

[124]. Wu, J., Li, S., Wang, X., Shi, M., Feng, X., and Liu, Y., "Ultrahigh sensitivity refractive index sensor of a D-shaped PCF based on surface plasmon resonance," *Applied optics*, vol. 57, no. 15, pp.4002-4007, 2018.

[125]. Ramachandran, A., Babu, P. R., and Senthilnathan, K., "Sensitivity analysis of steering-wheel gas sensor against diverse core air hole sizes and core materials in terahertz wave band," *In IOP Conference Series: Materials Science and Engineering*, vol. 263, no. 5, p. 052036, 2017.

[126]. Ahmed, K., Morshed, M., Asaduzzaman, S., and Arif, M. F. H., "Optimization and enhancement of liquid analyte sensing performance based on square-cored octagonal photonic crystal fiber," *Optik-International Journal for Light and Electron Optics*, vol. 131, pp. 687-696, 2017.

[127]. Islam, M. I., Ahmed, K., Asaduzzaman, S., Paul, B. K., Bhuiyan, T., Sen S., Islam, M. S., and Chowdhury, S., "Design of single mode spiral photonic crystal fiber for gas sensing applications," *Sens. and Bio-Sens. Res.*, vol. 13, pp. 55-62, 2017.

[128]. Islam, M. R., Mou, F. A., Rahman, M. M., and Bhuiyan, M. I. H., "Hollow Core Photonic Crystal Fiber for Chemicals Sensing in Liquid Analytes: Design and Analysis," *International Journal of Modern Physics B*, Vol.34, No. 28, 2020.

[129]. Islam, M. S., Cordeiro, C. M. B., Nine, M. J., Sultana, J., Cruz, A. L. S., Dinovitser, A. , Wai-Him Ng, B., Ebendorff-Heidepriem, H., Losic, D., and Abbott, D., "Experimental Study on Glass and Polymers: Determining the Optimal Material for Potential Use in Terahertz Technology". *IEEE Access*, Vol. 8, pp. 97204-97214, 2022.

[130]. Xue Z., Mao P., Peng, P., Yan, S., Zang, Z., and Yao, C., "Terahertz spectra of proteinuria and non-proteinuria", *Front. Bioeng. Biotechnol.* Vol. 11 , 2023.

[131]. Eid, M. M. A. , Habib, M. A. , Anower, M. S. , and Rashed, A. N. Z. , "Highly sensitive nonlinear photonic crystal fiber based sensor for chemical sensing applications". *Microsyst Technol* 27, 1007–1014, 2021.

[132]. Mou, F. A., Rahman, M. M., Islam, M. R., and Bhuiyan, M. I. H., "Development of a photonic crystal fiber for THz wave guidance and environmental pollutants detection. *Sensing and Bio-Sensing Research*, Vol. 29, 100346, 2020.

[133]. Wu, J., S. Li, Wang, X., Shi, M., Feng, X. and Liu, Y., "Ultrahigh sensitivityrefractive index sensor of a D-shaped PCF based on surface plasmonresonance," *Applied optics*, vol. 57, no. 15, pp.4002-4007, 2018.

[134]. Islam, M.R, and Mamadou, M., "Spider web ultrasensitive terahertz photonic crystal fiber for chemical sensing", *Opt. Eng.* 59(8), 1–13, 2020.

[135]. Huang, Y., Xu Y., and Yariv, A., "Fabrication of functional microstructured optical fibers through a selective-filling technique", *Appl. Phys. Lett.* 85(22), 5182–5184, 2004.

[136]. Sheikholeslami, M., Rezaeianjouybari, B., Darzi, M., Shafee, A. and Nguyen, T. K., "Application of nano-refrigerant for boiling heat transfer enhancement employing an experimental study," *International Journal of Heat and Mass Transfer*, Vol-141, pp. 974-980, 2019.

[137]. Deibel, J. A., Berndsen, N. and Daniel, and Mittleman M., "Design of cylindrical-wire wave guides and other THz devices can be aided by finiteelement models that characterize propagation and interaction characteristics," *Proc. of the IEEE*, vol. 95, no. 8, 2007.

[138]. Luoa, J., Yanga, Q. Q., Lu S., Mhamdi, A., Dong, C., Lyu, S. S., and Heng, Y., "A novel formulation and sequential solution strategy with time-spaceadaptive mesh refinement for efficient reconstruction of local boundaryheat flux," *International Journal of Heat and Mass Transfer*, vol-141, pp. 1288-1300, 2019.

[139]. Zheng, Z. P., Wen, H. F., Yan, H., Liu, J., Yang, W. Z., and Zhu, S. L., "Terahertz and mid-infrared spectroscopy of benzene-1,2-diol", *Journal of Molecular Spectroscopy*, 281, 13–17, 2012.

[140]. Rahman, A., Khaleque, A., Ali, M. Y., and Rahman, M. T., "THz spectroscopic sensing of liquid chemicals using a photonic crystal fiber," *OSA Continuum,* Vol. 3, Issue 11, pp. 2982-2996, 2020.

[141]. Islam, M. S., Faisal, M., and . Razzak, S. M. A., "Extremely low loss porous-core photonic crystal fiber with ultra-flat dispersion in terahertz regime," *Journal of the Optical Society of America B*, Vol. 34, No. 8, 2017.

[142]. Ahmed, S., Mou, J. R., Mollah, M. A., and Debnath, N., "Hollow-core Photonic Crystal Fiber Sensor for Refractive Index Sensing," *2019 IEEE International Conference on Telecommunications and Photonics (ICTP),* 2019.

[143]. Pysz, D., Kujawa, I., Stepien, R., Klomczaki, M., Filipkowski, A., Franczyk, M., Kociszewski, L., Harasny, K., and Buczynski, R., "Stack and draw fabrication of soft glass microstructured fiber optics," *Bulletin of the Polish Academy of Sciences Technical Sciences*, Vol. 62, No. 4, 2014.

[144]. Liu, Z. and Tam, H. Y., "Fabrication and Sensing Applications of Special Microstructured Optical Fibers,"*Selected Topics on Optical Fiber Technologies and Applications, Intech* (2018).

[145]. Guo, W., Zhou, G., Hou, L., Han, Y., Li, Q., and Liu, Y., "The fabrication of micro-structure fiber with the improved stacking-capillary method," *Advanced Laser Technologies*, Vol. 6344 (2005).

[146]. Zhang, P., Zhang, J.,. Yang, P.; Dai, S., Wang, X., and Zhang, W., " Fabrication of chalcogenide glass photonic crystal fibers with mechanical drilling," *Opt. Fiber* Technol. 26, 2015.

[147]. Ghazanfari, A., Li W., Leu, M. C., and Hilmas, G. E., "A novel freeform extrusion fabrication process for producing solid ceramic components with uniform layered radiation drying," *Additive Manufacturing*, vol. 15, pp. 102–112, 2017.

[148]. Kumar, V. V. R. K., George, A. K., Reeves, W. H., Knight, J. C., and Russell, P. St. J., "Extruded soft glass photonic crystal fiber for ultrabroad supercontinuum generation," *Optics Express*, Vol. 10, No. 25, 152016, 2002.

[149]. Talataisong, W., Ismaeel, R., Sandoghchi, S. R., Rutirawut, T., Ntopley, G., Beresnaand, M. and Bambilla, G., "Novel method for manufacturing optical fiber: extrusion and drawing of microstructured polymer optical fibers from a 3D printer," *Optics Express*, Vol. 26, No. 24, 2018.

[150]. Cruz, A. L. S., Cordeiro, C. M. B., and Franco, M. A. R., "3D Printed Hollow-Core Terahertz Fibers," *Fibers*, 6(3), 43, 2018.

[151]. MacChesney, B., Johnson, D. W., Bhandarkar, S., Bohrer M. P., Fleming J. W., Monberg E. M., and Trevor D. J., "Optical fibers using sol–gel silica over cladding tubes," *Electronics Letters*, vol. 33, no. 18, p. 1573–1574, 1997.

[152]. Bhandarkar, S., "Sol–gel processing for optical communication technology," *Journal of the American Ceramic Society*, vol. 87, no. 7, pp. 1180–1199, 2004.

[153]. MacChesney, B., Johnson, D. Bhandarkar, W. S., Bohrer, M. P., Fleming, J. W., Monberg, E. M. and Trevor, D. J., "Optical fibers using sol–gel silica overcladding tubes," *Electronics Letters*, vol. 33, no. 18, p. 1573–1574, 1997.

[154]. MacChesney, J. B., Johnson, D. Bhandarkar, W., S., Bohrer, M. P., Fleming, J. W., Monberg, E. M., and Trevor, D. J., "Optical fiber by a hybrid process using sol-gel silica overcladding tubes," *Journal of Non-Crystalline Solids*, vol. 226, no. 3, p. 232–238, 1998.

[155]. Hamzaoui, H. E., Bigot, L., Bouwmans, G., Razdobreev, I., Bouazaoui, M., and Capoen, B., "From molecular precursors in solution to microstructured optical fiber: a sol-gel polymeric route," *Optical Materials Express*, vol. 1, no. 2, pp. 234–242, 2011.

[156]. Russell, P. S. J., "Photonic crystal fibers," *Journal of Lightwave Technology*, vol. 24, no. 12, pp. 4729–4749, 2006.

[157]. Bass, M., DeCusatis, C., Enoch, J., Lakshminarayanan, V., MacDonald, G. Li, C., Mahajan, V., and Stryland, E. V., Handbook of Optics, Volume V: Atmospheric Optics, Modulators, Fiber Optics, X-Ray and Neutron Optics. 3 ed., 2009.

[158]. Kumar, V. V. R. K, George, A. K., Reeves, W. H., Knight, J. C., Russell, P. S. J., Omenetto, F., and Taylor A. J., "Extruded soft glass photonic crystal fiber for ultrabroad supercontinuum generation," *Optics Express*, vol. 10, no. 25, pp. 1520– 1525, 2002.

[159]. Kiang, K. M., Frampton, K., Monro, T. M., Moore, R., Tucknott, J., Hewak, D. W., Richardson, D. J., and Rutt, H. N., "Extruded singlemode non-silica glass holey optical fibres," *Electronics Letters*, vol. 38, no. 12, pp. 546–547, 2002.

[160]. Monro, T. M., Kiang, K. M., Lee, J. H., Frampton, K., Yusoff, Z. Moore, R., Tucknott, J., Hewak, D. W., Rutt, H. N., and Richardson, D. J., "High nonlinearity extruded single-mode holey optical fibers," in *Optical Fiber Communication Conference and Exhibit*, pp. FA1–1–FA1–3, Mar 2002.

[161]. Monro, T. M., West, Y. D., Hewak, D.W., Broderick, N. G. R., and Richardson, D. J., "Chalcogenide holey fibres," *Electronics Letters*, vol. 36, no. 24, pp. 1998–2000, 2000.

[162]. Kumar, V. V. R. K., George, A. K., Knight, J. C., and Russell, P. S. J., "Tellurite photonic crystal fiber," *Optics Express*, vol. 11, no. 20, pp. 2641–2645, 2003.

[163]. Van Eijkelenborg, M. A., Large, M. C. J., Argyros, A., Zagari, J., Manos, S., Issa, N. A., Bassett, I. Fleming, S., McPhedran, R. C., Sterke, C. M. de, and Nicorovici, N. A., "Microstructured polymer optical fibre," *Optics Express*, vol. 9, no. 7, pp. 319–327, 2001.

[164]. Zhao, Q., Tian, F., Yang, X., S. Li, Zhang, J., Zhu, X., Yang, J., Liu Z., Zhang, Y., Yuan, T., and Yuan, L., "Optical fibers with special shaped cores drawn from 3D printed preforms," *Optik - International Journal for Light and Electron Optics*, vol. 133, pp. 60–65, 2017.

[165]. Cook, K., Balle, G., Canning, J., Chartier, L., Athanaze, T., Hossain, M. A., Han, C., Comatti, J.-E., Luo, Y., and Peng, G.-D. "Step-index optical fiber drawn from 3D printed preforms," *Optics Letters*, vol. 41, no. 19, pp. 4554–4557, 2016.

[166]. Feng, X., Mairaj, A. K., Hewak, D. W., and Monro, T. M., "Nonsilica glasses for holey fibers," *Journal of Lightwave Technology*, vol. 23, no. 6, p. 2046, 2005.

[167]. Zhang, P., Zhang, J., Yang, P., Dai, S., Wang, X., and Zhang, W., "Fabrication of chalcogenide glass photonic crystal fibers with mechanical drilling," *Optical Fiber Technology*, vol. 26, no. Part B, pp. 176–179, 2015.

[168]. Monro, T. M. and Ebendorff-Heidepriem, H., "Progress in microstructured optical fibers," *Annual Review of Materials Research*, vol. 36, no. 1, pp. 467–495, 2006.

[169]. Weber, M. J., Handbook of Optical Materials, 2nd ed., New York: CRC Press, 2003.

[170]. Anthony, J., Leonhardt, R., Argyros, A., and Large, M. C. J., "Characterization of a microstructured Zeonex terahertz fiber," *Journal of the Optical Society of America B*, vol. 28, pp. 1013-1018, 2011.

[171]. Cubillas, A. M., Unterkofler, S., Euser, T. G., Etzold, B. J. M., Jones, A. C., Sadler, P. J., Wasserscheid, P., and Russell, P. St.J., "Photonic crystal fibres for chemical sensing and photochemistry," *Chem. Soc. Rev.*, vol. 42, no. 22, pp. 8629–8648, 2013.

[172]. Calcerrada, M., Ruiz ,C. G., and alez-Herraez, M. G., "Chemical and biochemical sensing applications of microstructured optical fiber-based systems," *Laser Photonics Rev*. 9, No. 6, pp. 604–627, 2015.

[173]. De, M., Gangopadhyay, T. K., and Singh, V. K., "Prospects of Photonic Crystal Fiber as Physical Sensor: An Overview," *Sensors*, 19, 464, 2019.

[174]. Liu Z, Wei Y, Zhang Y, Zhu Z, Zhao E, Zhang Y, " Reflective-distributed SPR sensor based on twin-core fiber", *Opt Commun*, 366, pp. 107–11, 2016.

[175]. Murawski M, Jaroszewicz LR, and Stasiewicz K. "A photonic crystal fiber splice with a standard single mode fiber", *Photonics Letters of Poland*, vol. 1, no. 3, pp. pp. 115–117, Sep. 2009.

[176]. Fan D, Jin Z, Wang G, Xu F, Lu Y, Hu DJJ, "Extremely high-efficiency coupling method for hollow-core photonic crystal fiber", *IEEE Photonics J*, 9, pp. 1-8, 2017.

[177]. Parmar V., Bhatnagar R., and Kapur P., "Optimized butt coupling between single mode fiber and hollow-core photonic crystal fiber," *Opt. Fiber Technol.* 19, pp. 490–494, 2013.

[178]. B. Li, D. Zheng, D. Kong, E. Chen, and J. Wu, "Free space to single mode fiber coupling efficiency improvement using wave-front sensor-less adaptive optics," *Asia Communications and Photonics Conference (ACP),* 2016.

[179]. Islam, M. R., Iftekher, A. N. M., Noor, F. "AZO-coated plasmonic PCF nanosensor for blood constituent detection in near-infrared and visible spectrum", *Appl. Phys. A* 128, 86, 2022.

[180]. Khalaf, M.K., Tahhan, S.R., and Taher, H.J. "Au-TiO2 coated dielectric micro-channel based plasmonic refractive index sensor", *Opt Quant Electron* 55, 612, 2023.